



Thermo-hydro-chemo-mechanical modeling of inner containments of nuclear reactor buildings in prestressed concrete

Ponleu Chhun

► To cite this version:

Ponleu Chhun. Thermo-hydro-chemo-mechanical modeling of inner containments of nuclear reactor buildings in prestressed concrete. Mechanics [physics.med-ph]. University Paul Sabatier Toulouse III; Laboratory LMDC, 2017. English. NNT: . tel-01686711

HAL Id: tel-01686711

<https://hal.science/tel-01686711>

Submitted on 17 Jan 2018

HAL is a multi-disciplinary open access archive for the deposit and dissemination of scientific research documents, whether they are published or not. The documents may come from teaching and research institutions in France or abroad, or from public or private research centers.

L'archive ouverte pluridisciplinaire **HAL**, est destinée au dépôt et à la diffusion de documents scientifiques de niveau recherche, publiés ou non, émanant des établissements d'enseignement et de recherche français ou étrangers, des laboratoires publics ou privés.



THÈSE

En vue de l'obtention du

DOCTORAT DE L'UNIVERSITÉ DE TOULOUSE

Délivré par *l'Université Toulouse 3 Paul Sabatier (UT3 Paul Sabatier)*
Discipline ou spécialité : *Génie Civil*

Présentée et soutenue Le 30 Octobre 2017 par :

Ponleu CHHUN

Titre :

Modélisation du comportement thermo-hydro-chemo-mécanique des enceintes de confinement nucléaire en béton armé-précontraint

JURY

Frédéric DUFOUR
Nicolas BURLION
Farid BENBOUDJEMA
Sylvie MICHEL-PONNELLE
Bruno CAPRA
Sylvain CHATAIGNER
Alain SELLIER
Laurie LACARRIERE
Benoît MASSON
Sharock GHAVAMIAN

Pr. Grenoble INP
Pr. Polytech Lille
Pr. ENS Paris Saclay
Ingénieur chercheur, EDF R&D
Directeur scientifique, OXAND
Ingénieur chercheur, IFSTTAR Nantes
Pr. Université Paul Sabatier
MC Université Paul Sabatier
Ingénieur expert, EDF SEPTEN
Directeur général associé, NECS

Président
Rapporteur
Rapporteur
Examinatrice
Examineur
Examineur
Directeur de thèse
Co-Directrice
Invité
Invité

Ecole doctorale : *MEGEP Génie civil*
Unité de recherche : *Laboratoire Matériaux et Durabilité des Constructions de Toulouse*

Abstract

In the context of life extension and safety demonstration of nuclear reactor buildings following the severe accidents of Chernobyl (in Ukraine, 1986) and Fukushima (in Japan, 2011), the “Confinement Assessment of a vessel during an Accident” (MACENA) project supported by the French National Research Agency (ANR) has been initiated since 2013. The experimental campaigns and modelling works of this project are based on an experimental containment vessel mock-up at scale 1/3 named VeRCoRs which is constructed and monitored by Electricity of France (EDF). The main issues for long-term operation of nuclear power plants that have more than 50 years old consist of ageing mechanisms in concrete and prestressing losses, as the internal concrete wall is prestressed with steel wires. These phenomena influence the cracking occurrence that can be significant if the “Loss-of-coolant accident” (LOCA) induced conditions are maintained for several weeks. The material characteristics of nuclear containment building can be modified by the loading prior to the LOCA, leading possibly to a reduction of tensile strength (early cracking, pre-operational pressurization test). The loadings during the LOCA i.e. increase of temperature and vapour relative pressure can then propagate the cracks. Thus, the material properties depend on the solicitation history since the concrete pouring

In that context, this PhD thesis introduces a computational strategy adopted to consider the damage accumulation using a single mechanical model from the early age until the LOCA. Considering the effect of chemo-physical of the concrete on the response of this mechanical model along the life of the structure requires the preliminary prediction of the evolution of chemical, thermal and hydric state from casting to later ages, including the LOCA. Several multiphysics models are studied, improved or tested in this thesis work: the first model is devoted to predicting the hydration degree, temperature, water content and porosity of concrete at an early age; the second allows to follow the evolution of temperature and water saturation for later ages (ageing period and effects of the LOCA conditions on the thermal and hydric state of concrete). The mechanical model uses the results of the two previous ones to estimate the delayed deformations of concrete, the relaxation of prestressing wires, and the risk of cracking.

This methodology was developed to avoid the loss of information relative to material state throughout the life of the structure. The main advantages of the methodology are the possibility to consider automatically the accumulation of damage until the LOCA on the one hand and on the other hand the improvements made to the material model to be used in the LOCA conditions, which improve the modelling quality, especially during the early age.

Keywords: THCM behaviour of prestressed concrete, (early) crack, nuclear containment, scale effect, wires relaxation, creep, shrinkage, thermal damage, restrained deformation, drying, hydration, distributed reinforcement, high temperature, humidity

Résumé

Dans le cadre de la prolongation de la vie et de la démonstration de la sécurité des bâtiments des réacteurs nucléaires suite aux accidents graves de Tchernobyl (en Ukraine, 1986) et Fukushima (au Japon, 2011), le projet « Maitrise du confinement d'une enceinte en accident » (MACENA) soutenu par l'Agence Nationale de la Recherche (ANR) a été lancé depuis 2013. Les campagnes expérimentales et les travaux de modélisation dans ce projet sont basés sur une maquette expérimentale de confinement à l'échelle 1/3 nommée VeRCoRs qui est construite et surveillée par Electricité de France (EDF). Les principaux problèmes liés à l'exploitation à long terme des centrales nucléaires de plus de 50 ans sont le vieillissement du béton et la perte de précontrainte puisque l'enceinte de confinement est en béton précontraint. Ces phénomènes conduisent à un risque de fissurations qui pourrait être déterminant si les conditions induites par l'"Accident de Perte de Réfrigérant Primaire" (APRP) sont maintenues pendant plusieurs semaines. Les caractéristiques des matériaux de construction de l'enceinte de confinement nucléaire peuvent être également modifiées par les chargements avant l'APRP, conduisant éventuellement à une réduction des propriétés mécaniques (fissuration précoce, test de mises en pression, effet du séchage). Les conditions pendant l'APRP, c'est-à-dire l'augmentation de la température et de la pression relative de la vapeur dans l'enceinte, peuvent ensuite faire propager ces fissures. Ainsi, les capacités de confinement dépendent de l'histoire des sollicitations depuis le coulage du béton.

Dans ce contexte, cette thèse présente une stratégie de calcul pour considérer l'accumulation de l'endommagement en utilisant un seul modèle mécanique depuis le jeune âge jusqu'à l'APRP, ce modèle est toutefois inclu dans un contexte global de modélisation faisant appel à d'autres modèles multiphysiques destinés à fournir les facteurs influents les plus importants tels que le degré d'hydratation, la température ou l'humidité. Ainsi, plusieurs modèles sont étudiés, améliorés ou testés dans ce travail de thèse : le premier modèle est consacré à la prédiction du degré d'hydratation, de la température, de la teneur en eau et de la porosité du béton au jeune âge, le second permet de suivre l'évolution de la température et de la saturation en eau en condition thermo hydrique ambiante ou proche des conditions APRP. Le modèle mécanique utilise les résultats des deux précédents pour estimer les déformations différées du béton, la relaxation des fils précontraints, et le risque de fissuration.

Cette méthodologie d'analyse a été mise au point pour éviter la perte d'information concernant l'état du matériau tout au long de la vie de la structure. Les principaux avantages de la méthodologie sont la possibilité de considérer automatiquement l'accumulation de l'endommagement depuis le jeune âge jusqu'à l'APRP d'une part et d'autre part les améliorations apportées au modèle matériau pour qu'il soit utilisable en conditions APRP, qui améliore la qualité de modélisation, y compris pour le jeune âge.

Mots clés: Comportement THCM du béton précontraint, fissure (précoce), confinement nucléaire, effet d'échelle, relaxation des fils précontraints, fluage, retrait, endommagement thermique, déformation empêchée, séchage, hydratation, armatures réparties, température élevée, humidité

Table of Contents

Abstract.....	i
Résumé	iii
Table of Contents	v
List of Figures.....	xi
List of Tables	xvii
I. GENERAL INTRODUCTION	2
I. 1. Industrial context	4
I. 2. ANR-PIA MACENA project.....	5
I. 3. Problematic of study	7
I. 4. Objectives and Methodology	8
I. 5. Organisation of the thesis manuscript.....	10
CHAPITRE I: THC simulation of early-age concrete nuclear containments.....	12
1. 1. Introduction.....	14
1. 2. State of the art	15
1. 2. 1. Effect of hydration on THC behaviour of concrete at early-age.....	15
1. 2. 2. Modelling of hydration of concrete.....	16
1. 2. 2. 1. Hydration kinetic law	18
1. 2. 2. 2. Water mass balance equation	20
1. 2. 2. 3. Heat balance equation and boundary conditions.....	20
1. 3. Strategy for concreting sequence modelling.....	21
1. 4. Application to the lower part of vessel mock-up VeRCoRs.....	23
1. 4. 1. Presentation of nuclear containment mock-up VeRCoRs.....	23
1. 4. 2. Formulation of VeRCoRs concrete and cement.....	25
1. 4. 3. Environmental conditions	26
1. 4. 4. Identification of model and material parameters.....	27
1. 4. 5. Validation of model on the structure.....	29
1. 5. Conclusion	31
CHAPITRE II: Simulation of Thermo-Hydric behaviour of Concrete at high temperature	32
2. 1. Introduction.....	34
2. 2. State of the art	35

2. 2. 1.	Transport mechanisms and phase changes	35
2. 2. 2.	Heat transfer	36
2. 2. 2. 1.	Heat transfer model	36
2. 2. 2. 2.	Concrete conductivity	37
2. 2. 2. 3.	Thermal capacity	40
2. 2. 2. 4.	Concrete density	41
2. 2. 3.	Moisture transfer	43
2. 2. 3. 1.	Moisture transfer model	43
2. 2. 3. 2.	Influence of temperature on moisture transfer	45
2. 2. 3. 3.	Permeation of concrete	46
2. 2. 3. 4.	Isotherm sorption curves	48
2. 3.	TH modelling of saturated and unsaturated porous media	50
2. 3. 1.	Constitutive model	50
2. 3. 1. 1.	Governing equations	50
2. 3. 1. 2.	Choice of state variables	51
2. 3. 1. 3.	Temperature dependency of the isotherm sorption curve	52
2. 3. 1. 4.	Relationship between p_v and p_l equivalent to the Kelvin-Laplace law ..	53
2. 3. 1. 5.	Heat and hydric balance equations and numerical implementation	55
2. 3. 2.	Evolution of thermal and hydric parameters	57
2. 3. 2. 1.	Evolution of thermal properties of concrete	57
2. 3. 2. 2.	Evolution of water properties	59
2. 4.	Application on MAQBETH mock-up	65
2. 4. 1.	Presentation of MAQBETH structure, mesh and boundary conditions	65
2. 4. 2.	Numerical results	66
2. 4. 3.	Parametrical studies on permeability	69
2. 5.	Conclusion	70
CHAPITRE III: Simulation of reinforced concrete behaviour under different THCM loadings		72
3. 1.	Introduction	74
3. 2.	State of the art	76
3. 2. 1.	Effect of hydration on mechanical behaviour of concrete	76
3. 2. 1. 1.	Mechanical threshold of cementitious materials at early age	76
3. 2. 1. 2.	Cracking at early age	77
3. 2. 2.	Effect of temperature and humidity on hardened concrete mechanical behaviour	79

3. 2. 2. 1.	Effect on elastic modulus and Poisson coefficient.....	80
3. 2. 2. 2.	Effect on tensile strength.....	83
3. 2. 2. 3.	Effect on compressive strength	84
3. 2. 2. 4.	Effect on fracture energy	86
3. 2. 3.	Effect of temperature and humidity on delayed strains of concrete.....	88
3. 2. 3. 1.	Influence of temperature	90
3. 2. 3. 2.	Influence of water content.....	91
3. 2. 3. 3.	Thermal induced damage at material scale	92
3. 2. 4.	Creep modelling	93
3. 2. 5.	Crack modelling	94
3. 2. 5. 1.	Isotropic elastic damage model	95
3. 2. 5. 2.	Orthotropic damage model.....	96
3. 2. 6.	Influence of temperature on reinforcement behaviour	97
3. 2. 6. 1.	Reinforcement behaviour at high temperature	97
3. 2. 6. 2.	Bond behaviour of reinforcement-concrete at high temperature	99
3. 3.	Modelling of reinforced concrete at high temperature and humidity	104
3. 3. 1.	Presentation of concrete model at moderate temperature and humidity	104
3. 3. 1. 1.	Rheological model.....	104
3. 3. 1. 2.	Damage model.....	110
3. 3. 2.	Adaptation for large meshes of massive structures	113
3. 3. 3.	Adaptation for early age concrete	114
3. 3. 4.	Adaptation for concrete at high temperature and humidity.....	116
3. 3. 4. 1.	Effect of temperature and humidity on mechanical strength	116
3. 3. 4. 2.	Effect of temperature and humidity on damage variable	118
3. 3. 4. 3.	Behaviour law of concrete at high temperature	120
3. 3. 5.	Adaptation for reinforced concrete structure	121
3. 4.	Applications of MACENA experiments (LMDC, IPPRA, CERIB).....	126
3. 4. 1.	Formulation of VeRCoRs concrete	126
3. 4. 2.	Identification of model and material parameters.....	126
3. 4. 3.	Validation of new evolution laws with experiments.....	131
3. 4. 3. 1.	Instantaneous behaviour under effect of temperature and humidity	131
3. 4. 3. 2.	Delayed deformations in compression at moderate temperature	132
3. 4. 3. 3.	Delayed deformations in compression at high temperature	133
3. 4. 3. 4.	Delayed deformations in tension at high temperature.....	134
3. 5.	Conclusion	136

CHAPITRE IV: Effect of temperature and prestress ratio on relaxation of prestressing wires	138
4. 1. Introduction.....	140
4. 2. State of the art	141
4. 2. 1. Temperature influence on mechanical properties of prestressing wires	141
4. 2. 2. Temperature influence on the relaxation of prestressing tendons.....	143
4. 3. Development of relaxation model.....	145
4. 3. 1. Model principles.....	145
4. 3. 2. Nonlinear Maxwell level strain	146
4. 3. 2. 1. Non-linear effect of loading ratio.....	147
4. 3. 2. 2. Temperature effect	148
4. 3. 3. Kelvin level strain	149
4. 3. 4. Numerical implementation	150
4. 4. Applications	151
4. 4. 1. Identification of model and material parameters.....	151
4. 4. 2. Validation	154
4. 5. Conclusion	155
CHAPITRE V: Scale effect consideration for application on massive structures.....	156
5. 1. Introduction.....	158
5. 2. State of the art	158
5. 2. 1. Size effect phenomena	158
5. 2. 2. Modelling of probabilistic size effect in tension.....	160
5. 3. Probabilistic scale effect model	161
5. 3. 1. Weibull scale effect.....	161
5. 3. 2. Weakest Link Localization method (WL2).....	162
5. 3. 3. Numerical implementation	163
5. 4. Application to nuclear wall mock-up PACE 1450	164
5. 4. 1. Presentation of PACE 1450 structure.....	164
5. 4. 2. Mesh and boundary conditions	168
5. 4. 3. Thermal and mechanical results	170
5. 5. Application to the lower part of vessel mock-up VeRCoRs.....	172
5. 5. 1. Benchmark VeRCoRs 2015	173
5. 5. 2. Study of the lower part of the whole vessel containment	176
5. 6. Conclusion	179
General conclusion and perspectives	180

Annexes	A-1
Annexe 1: Technical data sheet of cement	A-1
Annexe 2: Technical data sheet of aggregates	A-2
Annexe 3: Technical data sheet of superplasticizer	A-5
References	R-1

List of Figures

Figure I-1: Nuclear Power Plants in France. The numbers indicate the number of reactors at a particular plant site (IAEA, 2016)	4
Figure I-2: Research project in the framework of previous activities (Hermann et al., 2009) ..	5
Figure I-3: Organisation chart of MACENA project (3SR Grenoble, CEA, IFSTTAR, IPRA Pau, LMDC Toulouse, CERIB, EDF R&D, NECS and OXAND, 2012)	6
Figure I-4: Phenomena to consider for a LOCA analysis (Sellier et al., 2016)	9
Figure I-5: Framework and methodology for the envisioned modelling	9
Figure I-6: Global scheme of THCM model.....	10
Figure 1-1: Equivalent convective coefficient with formwork	21
Figure 1-2: Modelling of concreting sequence during the gusset construction (piece of VeRCoRs structure) (a) heating phase, (b) formwork removal phase	22
Figure 1-3: Nuclear reactor building VeRCoRs mock-up (EDF, 2014)	23
Figure 1-4: Axisymmetric section of structure VeRCoRs	24
Figure 1-5: 3D mesh of whole structure VeRCoRs with soil (only a half of the structure is presented here)	24
Figure 1-6: Evolution of air temperature and heating temperature during gusset formwork ($t = 0$ corresponds to calculation time 834h) (EDF, 2014)	26
Figure 1-7: Calibration of heat of hydration of pure Portland cement (Isothermal calorimeter test at 20°C and 40°C)	28
Figure 1-8: Prediction of temperature evolution of concrete in adiabatic condition (Adiabatic calorimeter test by CEBTP)	28
Figure 1-9: Numerical and experimental results for thermal evolution of gusset	29
Figure 1-10: Model's responses in terms of (a) temperature, (b) porosity, (c) water content, (d) hydration degree obtained at 16h after gusset casting.....	30
Figure 1-11: Temperature fields at different instance of construction sequence	31
Figure 2-1: Schematic representation of water transport and phase changes in cement paste (Benboudjema, 2002).....	35
Figure 2-2: Dehydration of concrete with temperature (Wang, 2016)	36
Figure 2-3: Thermal conductivity Vs Temperature (* TPS = Transient Plane Source)	38
Figure 2-4: Dependence of thermal conductivity on temperature	39
Figure 2-5: Thermal Capacity Vs Temperature and Saturation degree	41
Figure 2-6: Effect of temperature on the density of concrete made from different types of aggregates (a) expanded clay (light aggregates) (b) silico-calcars (c) quartzite and (d) basalt (Bazant and Kaplan, 1996)	42
Figure 2-7: Evolution of density of different concretes with temperature (Schneider, 1988) ..	42
Figure 2-8: Evolution of mass of different concretes with temperature (Kodur, 2014)	42
Figure 2-9: Evolution of concrete density with temperature (Anderberg, 2003; Nguyen, 2013)	42
Figure 2-10: Schema of moisture movement within heated concrete element	46
Figure 2-11: Permeability measures on ordinary concrete (Picandet, 2001)	47
Figure 2-12: Isotherm sorption curves at different temperatures	49
Figure 2-13: Evolution of m_{shr} with the temperature	52

Figure 2-14: Influence of temperature on isotherm sorption curves (thick lines are the curves from the proposed model)	53
Figure 2-15: Comparison of relation p_v, p_l to the Kelvin-Laplace's law	54
Figure 2-16: Continuous description of moisture diffusion for saturated-unsaturated media at 20°C and 100°C	56
Figure 2-17: Outline of the thermo-hydric analysis.....	57
Figure 2-18: Dependence of thermal properties of concrete on temperature	58
Figure 2-19: Water density Vs Temperature ((Raznjevic, 1970) cited by (Hassen, 2006))	59
Figure 2-20: Liquid dynamic viscosity Vs Temperature	60
Figure 2-21: Gas dynamic viscosity Vs Temperature.....	60
Figure 2-22: Relative permeability versus saturation degree (van Genuchten, 1980; KALLEL, 2016; Kameche et al., 2014; Monlouis-Bonnaire et al., 2004; Sogbossi, 2017)	61
Figure 2-23: Evolution of Klinkenberg coefficient with saturation degree of concrete (Kameche et al., 2014).....	62
Figure 2-24: Saturated vapour pressure Vs Temperature	63
Figure 2-25: Geometrical characteristics of MAQBETH mock-up (concrete hollow cylinder) (a) and schematic description of experimental conditions (b) (Bary et al., 2012).....	66
Figure 2-26: Thermal loading history on the inner surface (left) and initial conditions and boundary conditions applied to the 2D axial symmetric model (right) (Bary et al., 2012)	66
Figure 2-27: Comparison of radial temperature profiles at different times (hours) between the simulation (lines) and experimental measurements (symbols) (Bary et al., 2012).....	67
Figure 2-28: Comparison of radial relative humidity $hr(a)$ and liquid saturation $Sl(b)$ profiles at different times (hours) between the simulation (lines) and experimental measurements (symbols) (Bary et al., 2012)	68
Figure 2-29: Comparison of radial gas pressure profiles p_v at different times (hours) between the simulation (lines) and experimental measurements (symbols) (Bary et al., 2012).....	68
Figure 2-30: Comparison of kg and kl effects on p_v responses	70
Figure 3-1: Scheme of percolation threshold during hydration (Stefan et al., 2010)	77
Figure 3-2: Evolution of Young's modulus with different w_c (experiment issued from (Boumiz, 1995)).....	77
Figure 3-3: 3D mesh of restrained shrinkage structure RG8 (Buffo-Lacarrière et al., 2014)..	78
Figure 3-4: Evolution of instantaneous characteristics with hydration degree (Buffo-Lacarrière et al., 2014).....	78
Figure 3-5: Damage field during heating and cooling phase (Buffo-Lacarrière et al., 2014) .	79
Figure 3-6: Crack pattern (Buffo-Lacarrière et al., 2014)	79
Figure 3-7: Evolution of (residual) elastic modulus according to the temperature	81
Figure 3-8: Evolution of elastic modulus with saturation degree (Kallel, 2016; Shoukry et al., 2011)	82
Figure 3-9: Evolution of Poisson coefficient with temperature and moisture content	82
Figure 3-10: Evolution of tensile strength with temperature	83
Figure 3-11: Evolution of tensile strength with moisture levels.....	84
Figure 3-12: Evolution of residual compressive strength with temperatures	85
Figure 3-13: Evolution of residual compressive strength with moisture levels (Shoukry et al., 2011)	86
Figure 3-14: Evolution of fracture energy according to the temperature	87
Figure 3-15: Evolution of fracture energy with saturation degree (Kallel, 2016)	88

Figure 3-16: Scheme of various time-dependent strains of concrete (ACI Committee 209, 2005)	89
Figure 3-17: Evolution of time dependent specific basic creep of concrete at different temperatures (20°C, 50°C and 80°C) under uniaxial compression test of (Ladaoui, 2010)....	90
Figure 3-18: Evolution of time dependent basic creep of concrete at different temperatures (20°C, 40°C and 70°C) under uniaxial compression (15 MPa applied after heating) at LMDC in MACENA project (Nguyen et al., 2017b).....	91
Figure 3-19: Evolution of time dependent basic creep of concrete at different temperatures (20°C, 100°C and 180°C) under uniaxial tension (13.5 MPa applied after heating) at CERIB in MACENA project (Daval, 2016).....	91
Figure 3-20: Incompatibility of thermal deformation of cement paste and aggregates	92
Figure 3-21: Mechanisms of basic creep (a) short-term micro-diffusion of water and (b) sliding of C-S-H sheets (Ulm and Acker, 1998).....	93
Figure 3-22: Softening behaviour of concrete under a tension test	94
Figure 3-23: Scheme of effective stress	95
Figure 3-24: Scheme of tensile tests on rebars (a) and temperature evolution along heated section (b) (Toumi Ajimi et al., 2017)	98
Figure 3-25: Influence of temperature on the tensile behaviour of rebars and comparison with (Eurocode 2, 2005) and (Li et al., 2003).....	98
Figure 3-26: Scheme of the pull-out tests(a) and temperature evolution at the interface before tests at 40, 100 and 140°C (b) (Toumi Ajimi et al., 2017)	99
Figure 3-27: Degradation mechanism of steel-concrete bond (Dominguez Ramirez, 2005) 100	
Figure 3-28: Evolution of ultimate shear stress with temperature for HA12/HA16 (a) and obtained interfacial behaviours at different temperatures for HA12 (b) (Toumi Ajimi et al., 2017)	100
Figure 3-29: Water flow along rebar during heating at 100 and 140°C (Toumi Ajimi et al., 2015)	101
Figure 3-30: Cracks observed for concrete at 100 and 140°C (Toumi Ajimi et al., 2015)....	101
Figure 3-31: Bond stress-slip curve defined by (FIB, 2000)	101
Figure 3-32: Bond-slip model (Rolland, 2015).....	101
Figure 3-33: Interfacial zone model with thickness. Steel bar with bar element (a) (Hameed, 2010), (b) (Kolani et al., 2012), (c) heterogeneity consideration (Michou, 2015) and (d) steel bar with volumetric element (Handika, 2017)	103
Figure 3-34: Interface model without thickness (lineic element) (Mang et al., 2015)	103
Figure 3-35: 1D-3D model of steel cross section inside concrete (Llau et al., 2016)	103
Figure 3-36: Rheological scheme of the creep model	105
Figure 3-37: Evolution of water viscosity (inverse function of CwT).....	108
Figure 3-38: Evolution of coefficient C_p^T	108
Figure 3-39: Idealised cracking pattern used to compute tensile damage (Sellier et al 2013a)	112
Figure 3-40: Behaviour law of hardened concrete under tension-compression cycles with damage ($R_t = 3\text{ MPa}$, $R_c = 30\text{ MPa}$, $G_{ft} = 100\text{ J/m}^2$, $G_{fr} = 100\text{ J/m}^2$) (Sellier, 2015) 112	
Figure 3-41: Uniaxial tensile behaviour modelling (softening part given for different element sizes)	114
Figure 3-42: Effect of hydration on the behaviour law of evolutive concrete under tension-compression cyclic ($R_t = 3\text{ MPa}$, $R_c = 30\text{ MPa}$, $G_{ft} = 100\text{ J/m}^2$, $G_{fr} = 100\text{ J/m}^2$)	116

Figure 3-43: Response under cyclic tension loading	116
Figure 3-44: Evolution of relative tensile strength with temperature and degree of saturation	117
Figure 3-45: Evolution of coefficient $C^{Pc,T}$ at $T_{ref} = 20^{\circ}\text{C}$	118
Figure 3-46: Evolution of coefficient C_p^T	119
Figure 3-47: Evolution of coefficient A^{TH}	119
Figure 3-48: Evolution of thermohydric damage coefficient D^{TH}	120
Figure 3-49: Effect of temperature on behaviour law of hardened concrete under tension-compression cycle test	121
Figure 3-50: Idealized scheme for modelling reinforced concrete	122
Figure 3-51: Concrete mesh and mechanical boundary conditions	124
Figure 3-52: (a), (b), (c) Steel ratio in three directions X, Y, Z and (d) Comparison of experimental crack pattern (below) and computed damage pattern (above) for load 90kN..	125
Figure 3-53: Comparison of experimental and calculated force-deflection curves	125
Figure 3-54: Hydration development at centre of 11 x 22 cm specimen obtained from hydration model (points represent ages of concrete used for measures)	127
Figure 3-55: Evolution of instantaneous characteristics according to hydration development (a) E , (b) R_c , (c) R_t (experimental results obtained from different laboratories in MACENA project)	127
Figure 3-56: LMDC test of concrete creep under uniaxial compression at 20°C ($f_{cm} \approx 52\text{MPa}$).....	128
Figure 3-57: DCT specimen (a) and its mesh (b)	131
Figure 3-58: Force-displacement evolutions under variable TH conditions	132
Figure 3-59: Strains of concrete at 40°C	133
Figure 3-60: Uniaxial drying creeps of concrete in compression at 100 and 180°C (CERIB tests) and at 40°C (LMDC test)	134
Figure 3-61: Deformation during the 2 first days of creep tests in temperature.....	134
Figure 3-62: Geometry of specimen for creep tests in tension (Daval, 2015).....	135
Figure 3-63: Uniaxial creep of concrete in tension at 100 and 180°C (CERIB tests)	135
Figure 4-1: Evolution of mechanical tensile behavior of prestressing wires with temperature (Toumi Ajimi et al., 2017) and comparison with (Eurocode 2, 2005) and (Li et al., 2003)..	142
Figure 4-2: Evolution of relaxation with different temperatures and loading ratios (0.7 (a) and 0.8 (b)) (Toumi Ajimi et al., 2017)	144
Figure 4-3: Scheme of relaxation sample with the heating device on the prestressing wire (a) and temperature evolution along the heated section (b) (Toumi Ajimi et al., 2017)	144
Figure 4-4 : Idealized rheological scheme for relaxation model	146
Figure 4-5 : Nonlinear amplification function k^M versus loading level	148
Figure 4-6 : Comparison between model and experimental results of relaxation versus time for different temperatures and loading ratios (0.7 and 0.8)	153
Figure 4-7: Comparison of model with relaxation experiment at stepwise cooling (140°C , 100°C and 20°C).....	153
Figure 4-8 : Comparison of model with test of relaxation with a stepwise heating (20°C , 100°C and 140°C).....	154

Figure 5-1: Experimental dispersion of concrete tensile strength as function of the smallest dimension of the specimen (Clément, 1987; Farra, 1994; Mivelaz, 1996; Rossi et al., 1994; Van Vliet and Van Mier, 2000) cited by (Ghannoum, 2017)	160
Figure 5-2: Scheme of tensile strength (R_t) vs. specimen diameter (D) and compressive strength (f_c) (Rossi et al., 1994))	160
Figure 5-3: Evolution of m as function of Cv (Sellier and Millard, 2014).....	161
Figure 5-4: Dispersion of measures of tensile strength at 28 days from different laboratories in MACENA project	162
Figure 5-5: Evolution of tensile strength due to scale effect (CEOS.fr, 2016).....	163
Figure 5-6: Geometry and dimension of specimen PACE 1450 (Hermann et al., 2009)	165
Figure 5-7: Horizontal section of specimen PACE 1450 (Hermann et al., 2009)	165
Figure 5-8: Vertical section of specimen PACE 1450 (Hermann et al., 2009)	165
Figure 5-9: Mechanical boundary conditions and photo of the set-up (Hermann et al., 2009)	167
Figure 5-10: Pressure scenario for RUN 1 to RUN 3 (left) and test control (right) (Hermann et al., 2009)	167
Figure 5-11: Illustration of external loading on PACE mock-up according to time (effect of creep is assumed neglected between RUN 2 and RUN 6).....	168
Figure 5-12: Mesh of PACE 1450 and its boundary conditions.....	169
Figure 5-13: Scheme of computed V_{max}	169
Figure 5-14: Ratio of distributed reinforcement along radial axe (a), circumferential axe (b), vertical axe (c) and prestressing wire along circumferential axe (d)	169
Figure 5-15: Evolution of temperature at the centre of specimen according to time (experimental results obtained from (Rosparis, 2016))	170
Figure 5-16: Comparison of prestressing force change during RUN 2 (experimental points obtained in (Hermann et al., 2009))	171
Figure 5-17: Comparison of internal strain during RUN 2 (experimental results S1, S5, S10 obtained in (Hermann et al., 2009))	171
Figure 5-18: Comparison of crack pattern at external surface of PACE during RUN 6 with numerical results (crack measure given by (Hermann et al., 2009))	172
Figure 5-19: Mesh of a piece of VeRCoRs structure (angle about 4.5°)	173
Figure 5-20: Representation of computed V_{max} (a) and ratio of distributed reinforcement in radial (b), tangential (c), vertical (d) direction.....	174
Figure 5-21: Comparison of measured (points) and numerical (curves) deformations at different points (red curve= RC modelling, black curve=Concrete modelling without reinforcement).....	175
Figure 5-22: Structural effect of distributed reinforcement on the crack pattern of gusset structure.....	175
Figure 5-23: 3D mesh of lower part of whole vessel VeRCoRs standing on the soil (only a half of modelled structure is presented here).....	176
Figure 5-24: Representation of computed V_{max} (a) and ratio of distributed reinforcement in radial (b), tangential (c), vertical (d) direction for a half of modelled structure.....	177
Figure 5-25: Comparison of measured (points) and numerical (blue curve) deformations at different points	177
Figure 5-26: Comparison of crack patterns from models (concrete and reinforced concrete) with experimental measurements on intrados of gusset 5 days after casting	178

Figure 5-27: Comparison of crack patterns from models (concrete and reinforced concrete) with experimental measurements on extrados of gusset 5 days after casting.....	178
Figure 5-28: Numerical crack pattern of VeRCoRs gusset 5 days after casting (25 cracks in total)	179
Figure A-1: Technical data sheet of cement	A-1
Figure A-2: Technical data sheet of aggregate 0/4	A-2
Figure A-3: Technical data sheet of aggregate 4/11	A-3
Figure A-4: Technical data sheet of aggregate 8/16	A-4
Figure A-5: Technical data sheet of superplasticizer (a)	A-5
Figure A-6: Technical data sheet of superplasticizer (b)	A-6

List of Tables

Table I-1: Experimental campaign program of MACENA project	6
Table 1-1: Number of meshed elements	24
Table 1-2: Chemical oxide composition of Clinker.....	25
Table 1-3: Formulation of VeRCoRs concrete	25
Table 1-4: Construction procedure of VeRCoRs.....	26
Table 1-5: Boundary condition model parameters (EDF, 2014)	27
Table 1-6: Hydration kinetics parameters.....	28
Table 1-7: Thermal parameters of concrete (EDF, 2014)	28
Table 1-8: Hydric parameters of similar concrete (Mensi et al., 1988).....	28
Table 2-1: Transport mechanisms in the concrete	35
Table 2-2: Mass capacity of concrete component (Neville, 2000)	40
Table 2-3: Parameters for Van Genuchten's relation of relative permeability	61
Table 2-4: Main functions introduced for the simulation	63
Table 2-5: Intrinsic parameters of model.....	64
Table 2-6: Material properties	64
Table 2-7: Different case studies of intrinsic permeability.....	69
Table 3-1: Exponents of De-Schutter law for material parameters	115
Table 3-2 : Concrete characteristics.....	124
Table 3-3 : Steel characteristics	124
Table 3-4: Mix design of VeRCoRs concrete.....	126
Table 3-5: Model parameters issued from literature (and common for similar concretes) and material parameters for the VeRCoRs's concrete (in bold and red symbol).....	129
Table 4-1 : Experimental mechanical properties of prestressing wires (tensile tests) (Toumi Ajimi et al., 2017)	142
Table 4-2: Model parameters and material parameters (in bold and red symbol) for prestressing wires T15.2 at $T_{ref} = 20^{\circ}\text{C}$	152
Table 5-1: Test program (RUNs)(Hermann et al., 2009).....	166

GENERAL INTRODUCTION

I. 1.	Industrial context	4
I. 2.	ANR-PIA MACENA project.....	5
I. 3.	Problematic of study	7
I. 4.	Objectives and Methodology	8
I. 5.	Organisation of the thesis manuscript.....	10

I. 1. Industrial context

The first nuclear power plant in France was opened in 1962. Actually, France has 58 nuclear reactors operated by Electricité de France (EDF), with a total capacity of 63.2 GWe, supplying 436 TWh in 2014 equivalent to 77.5% of the electricity used in France (see Figure I-1) (Bottin, 2017).



Figure I-1: Nuclear Power Plants in France. The numbers indicate the number of reactors at a particular plant site (IAEA, 2016)

France becomes then the world's largest electricity producer from nuclear energy after the United States. But the French Nuclear industry has to face with two main problems: first the ageing of its nuclear power plants which some of them arrive at their design lifetime, and secondly there is an increasing demand of safety demonstration following the severe accidents of Chernobyl (in Ukraine, 1986) and Fukushima (in Japan, 2011). Therefore, the different nuclear agencies and the French government work together incessantly to control the nuclear risk. As can be seen in Figure I-2, a number of research programs sorted in dimension and complexity are realised to enhance the knowledge of prestressed concrete in order to predict more accurately the behaviour of a double wall concrete vessel in case of "Loss-of-coolant accident" (LOCA). If such an accident happens, the vapour will be stopped by the double concrete wall system and redirected to filters which work under a 4 bars relative pressure. At this pressure level, the vapour temperature inside the vessel can reach 180°C and be maintained until two weeks. This vapour pressure and temperature loading constitute the internal conditions in the scenario of LOCA.

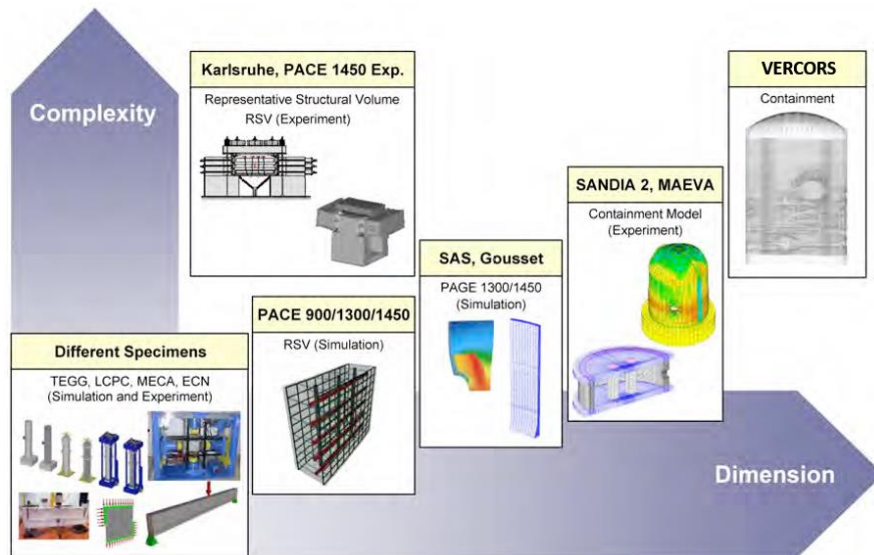


Figure I-2: Research project in the framework of previous activities (Hermann et al., 2009)

In the context of life extension of nuclear containment structures, EDF decided in 2010 to build a 1/3 scaled mock-up VerCoRs (Realistic verification of reactor containment) (EDF, 2014) in order to study the ageing mechanism in concrete and prestressing losses of a 1300 MWe double-wall reactor building, which are the main phenomena that could modify the tightness of an inner containment in prestressed and reinforced concrete.

The French National Project CEOS.fr (2009) has been initiated to further research on the influence of Thermo-Hydro-Mechanical (THM) effect and size effect on the behaviour of massive structures in order to estimate the strains and concrete crack pattern. In this context, the “Non Destructive Evaluation of nuclear plants containment” (ENDE) project and the “Confinement Assessment of a vessel during an Accident” (MACENA) project with nine partners (six research institutes and three industrials) supported by the French National Research Agency (ANR), work on tools to predict accurately the double wall mechanical behaviour in case of LOCA. The experimental campaigns and modelling works of MACENA project are based on VerCoRs mock-up.

I. 2. ANR-PIA MACENA project

The major objective of research project MACENA is to provide an accurate finite element model able to predict if a vapour leakage would be possible in the condition of LOCA scenario. To respond to this objective, the project is organised into four work packages (WPs) (see Figure I-3).

This PhD thesis is funded by the French National Research Agency (ANR) in the framework of this project ANR-PIA MACENA. The present work is a part of WP1 (Assessment of structural state before an accident) and WP2 (Study of instantaneous and delayed mechanical

behaviour of concrete and relaxation of prestressing cables during an accident and simulation of the real structures at a different scale (PACE 1450, VeRCoRs)).

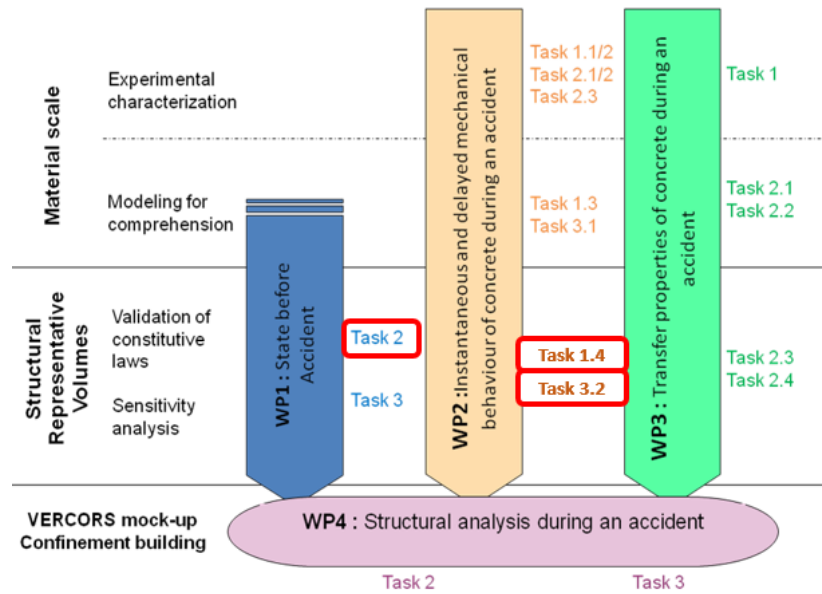


Figure I-3: Organisation chart of MACENA project (3SR Grenoble, CEA, IFSTTAR, IPRA Pau, LMDC Toulouse, CERIB, EDF R&D, NECS and OXAND, 2012)

The experimental campaign program of MACENA project aiming to investigate the behaviour of the prestressed concrete specimen under the conditions envisioned in the LOCA scenario is summarised in Table I-1. The main task of the present thesis is then to develop a THCM model able to cover the phenomena quantified in these experimental campaigns.

Table I-1: Experimental campaign program of MACENA project

Laboratory	Experimental tests
IFSTTAR Nantes (Toumi Ajimi et al., 2017)	Influence of temperature on the interface behaviour of steel-concrete
	Influence of temperature on the relaxation of prestressing cable T15.2
	Influence of temperature on the tensile behaviour of prestressing cable T15.2
	Influence of temperature on the tensile behaviour of reinforced bars HA12 and HA16
SIAME (Kallel et al., 2017)	Influence of temperature and humidity on the instantaneous behaviour of concrete

LMDC (Nguyen et al., 2017a, 2017b)	Creep of concrete cylinder under uniaxial compression (20, 40, 70°C – 50%, 80% HR, endogenous)
	Creep of prestressed concrete beam under four-point bending test (20, 40, 70°C – 50%, 80% HR, endogenous)
	Creep of non-reinforced concrete beam under four-point bending test (20, 40, 70°C – 50%, 80% HR, endogenous)
CERIB (Daval, 2016)	Creep under uniaxial compression and tension (100, 180°C)

I. 3. Problematic of study

This study concerns the double-wall reactor buildings without steel liner representing 24 out of the 58 nuclear reactors of EDF. Ageing mechanisms in concrete, for some nuclear power plants that have more than 50 years old, and prestressing losses have to be considered in the models, particularly because the internal concrete wall is prestressed with steel wires. With time, the prestress force is relaxed and on the other hand, the concrete, constantly compressed by the wires, leading to a concrete shrinkage and creeps in compression which contributes also to the loss of pre-stress. Previous studies about the delayed mechanical behaviour of concrete have indicated an increase of delayed strains with temperature rise: the basic creep can be multiplied by 10 at 80°C, and coupling between creep and heating can lead to damage and to transient thermal creep (Cagnon, 2015; Ladaoui et al., 2013). This phenomenon can be observed also on the relaxation of wires with temperature rise and different initial pre-stress (Toumi Ajimi et al., 2017). These phenomena could be significant if the LOCA induced conditions are maintained for several weeks. So, while the prestress is able to balance the tensile stress induced by the internal pressure in case of LOCA, the leak risk is consequently low. But if the concrete passes in tension even locally due to the loss of prestress, cracks can occur and thus there is a risk of radioactive leakage. Obviously, the concrete can resist itself to a tensile stress of a few MPa, but an estimation of the current tensile strength of a 50-year-old concrete is not so easy to know for different reasons. First, the concrete tensile strength depends on strain, it decreases when the strain exceeds the tensile strain, which leads to a progressive strain localisation and finally causes a localised crack. Therefore, once a tensile strain has been reached, for instance at an early age before the pre-stressing or during a decennial pressurisation test, the apparent tensile strength will be reduced. Another problem is the heterogeneity of concrete. The heterogeneous composition of concrete leads to different measured concrete characteristics of the specimens with the same concrete mix design. The variability (coefficient of variation) of the tensile strength measured on small specimens in several laboratory tests varies from 10 % to 20%. This heterogeneity of concrete leads to a

reduction of the tensile strength, which is known as “scale effect” and it is impossible to neglect in the case of large structures as shown during the CEOS.fr (2009) project.

I. 4. Objectives and Methodology

As mentioned above, several phenomena influencing the cracking occurrence have to be considered to predict the risk of radioactive vapour leak in case of LOCA (summarised in Figure I-4) (Sellier et al., 2016). The material characteristics of nuclear containment building can be modified by the loading prior to the LOCA, leading possibly to a reduction of tensile strength and early age cracking, and the loading during the LOCA, i.e. increase of temperature and vapour relative pressure. Each of these phenomena can occur independently and its consequences in terms of mechanical damage, inelastic strains and chemical evolution are most of the time irreversible. Thus, the material properties just before the LOCA depend on the solicitation history since the concrete pouring. Several computational strategies can be adapted to consider the damage accumulation, for instance several models can be chained, a first one dedicated to the prediction of early age cracking, a second one considering concrete ageing, delayed strains and wires relaxation, and a last one able to take into account the effects of temperature and vapour pressure in order to assess the cracking patterns during the LOCA. Therefore, chaining several models leads rapidly to numerical complications in terms of continuities of material state between two consecutive modelling, particularly when the internal state variables are not exactly the same between two consecutive models (for instance the damage variable can be a tensor in a model and a scalar in another one; the permanent strains can be split in a different number of tensors according to the model used). To avoid these problems of links between elementary models, a better alternative strategy consists to consider all the afore-mentioned phenomena relative to a given material in a single constitutive model. The main advantage is the continuity, along with the numerical modelling, of the internal state variables, which considers then automatically the damage accumulation until the LOCA.

The principal objective of this thesis focuses on the constitutive model clarified in LMDC Toulouse (France) to consider the different phenomena involved in the concrete behaviour since its pouring until the LOCA. These phenomena will be discussed based on the literature review and the experimental campaign. Finally, this finite element model is applied on the real structures at a different scale, i.e. PACE mock-up, and VeRCoRs mock-up.

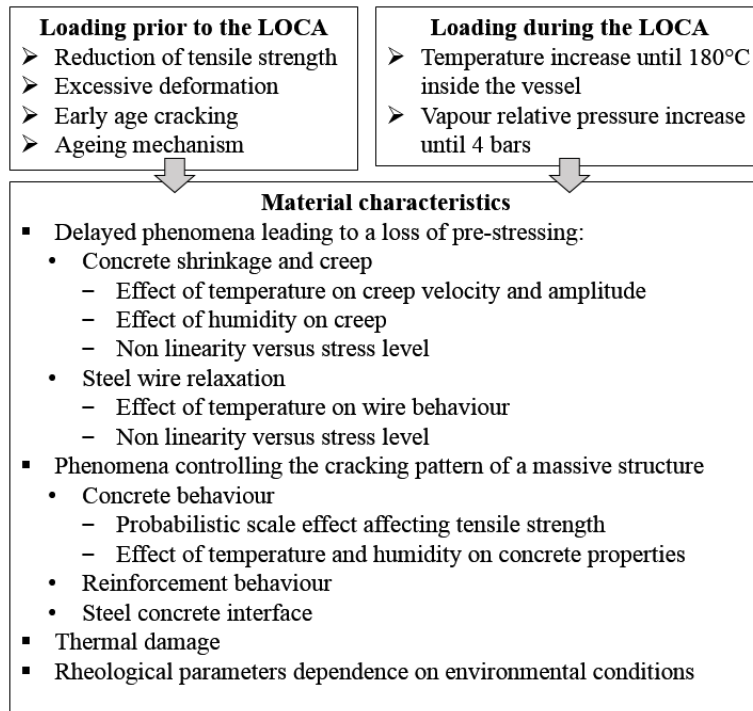


Figure I-4: Phenomena to consider for a LOCA analysis (Sellier et al., 2016)

To achieve this, a scientific approach has been adopted and divided into several studied steps from laboratory tests to large massive structures as shown in Figure I-5. Briefly, the behaviour of concrete, steel and prestressing wires as well as the behaviour of the concrete-reinforcement interface under the effect of temperature and humidity (only on concrete) have been studied separately. Once a coupling of THCM phenomena is achieved, the modelling of different structures can be done. The heterogeneity of structures at different scales will be considered thank to the statistical scale effect method derived from the CEOS.fr works (CEOS.fr, 2016; Sellier and Millard, 2014).

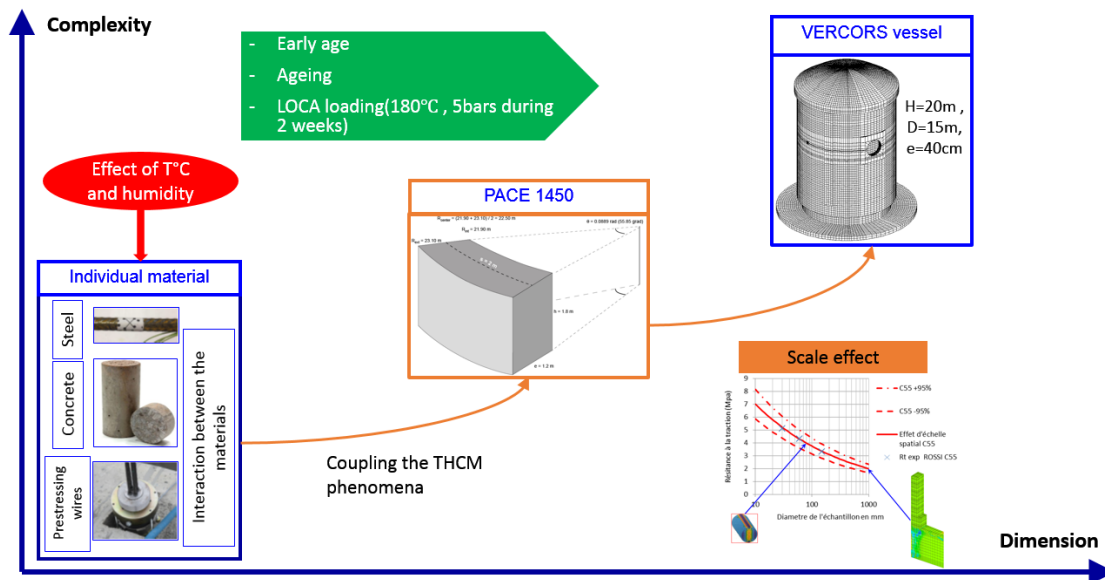


Figure I-5: Framework and methodology for the envisioned modelling

I. 5. Organisation of the thesis manuscript

More specifically, the major objective of this thesis is to propose a THCM model able to simulate to the massive prestressed concrete structures to predict their strains and cracking patterns. Figure I-6 illustrates a numerical methodology adapted to control the structure throughout its entire service lifetime. The chained and weakly coupled THCM model, remaining representative of the multi-physical behaviour of the structure, predicts the spatiotemporal evolution of the temperature, saturation degree and mechanical states since the casting date until the operational visit (VCs and VDs).

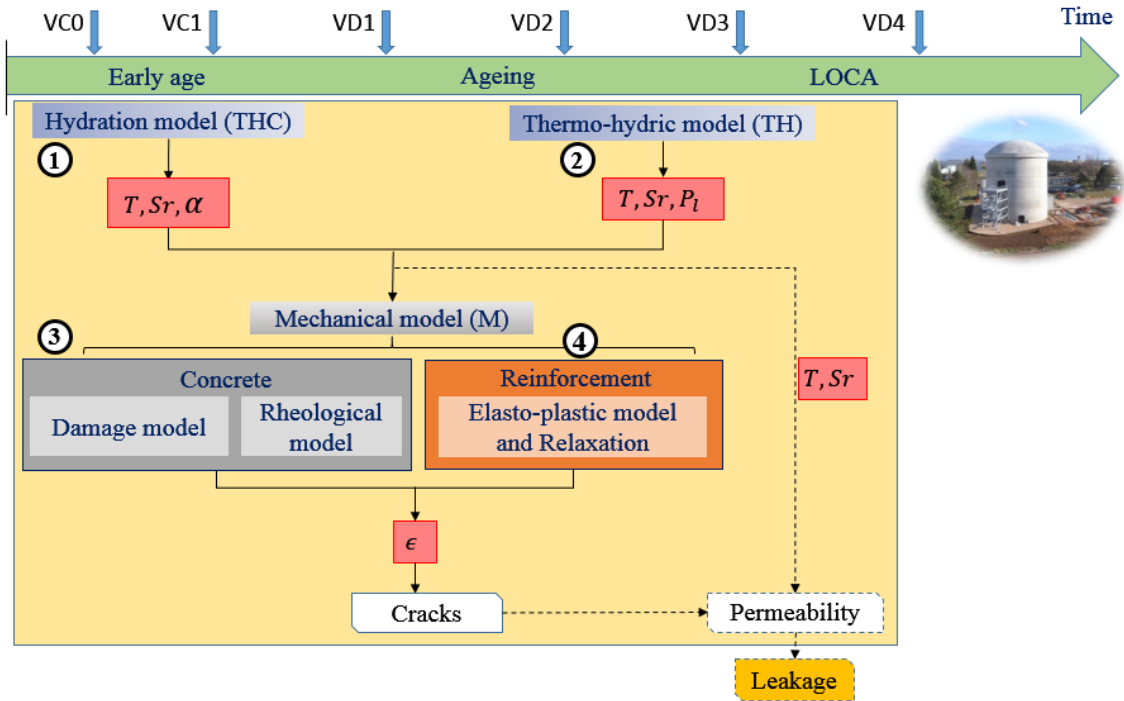


Figure I-6: Global scheme of THCM model

Hence, the manuscript is organised into five chapters:

Chapter 1 deals with the THC behaviour of early age concrete in nuclear containment building using a multiphasic hydration model. The fact that the large/complex structures have to be cast sequentially at a different time is inevitable. So, a proposed approach which consists on modelling the sequential casting of concrete without re-meshing the structure between each stage of casting is described. An inverse analysis with an adiabatic test is done to characterise the model parameters for the VeRCoRs concrete. Furthermore, in order to validate the methodology, it is also applied to concrete mock-up VeRCoRs to compare the evolution of temperature in the structure. The results are the temperature, porosity and water content fields which constitute the entry data for the next chapters.

Chapter 2 is dedicated to the proposal and test of an alternative method for modelling the temperature effect on the thermo-hyric transport in saturated-unsaturated media. Two

particularities are considered in this model: first, the effect of temperature on water retention curves; secondly, a continuous description of saturated and unsaturated media based on a formulation using only the temperature and liquid pressure as a state variable, even in unsaturated conditions. This TH modelling is developed in order to give a fast estimation of the temperature and saturation degree of concrete structures subjected to temperature rise and having a different saturated state. It allows characterising the concrete structure state in various TH conditions, particularly when the LOCA induced conditions occur. For the validation purpose, an experimental campaign found in the literature is considered: a test of MAQBETH mock-up (Ranc et al., 2003) with a variation of temperature up to 200°C close to the LOCA conditions in terms of temperature.

Chapter 3 gathers some literature reviews that studied on the instantaneous and delayed behaviour of concrete subjected to different environmental conditions, a coupling of THCM phenomena and their modelling. Moreover, the experimental campaign of MACENA projects is presented along with the numerical modelling. This chapter leads to three important aspects which have to be considered for an accurate concrete numerical modelling: effect of hydration, effect of humidity on the instantaneous and delayed behaviour of concrete, and damage of concrete subjected to temperature rise. Last but not least, the influence of temperature on the interface of reinforcement-concrete is presented and an alternative method to consider the structural effect of reinforcement in the massive structure, called “Distributed reinforcement” method, will be illustrated with a validation of proposed methodology on a three-point bending beam.

Chapter 4 presents an incremental model for prestressing steel relaxation under the various levels of loading and temperature. It calculates the delayed strain of prestressing wires involved in the relaxation phenomenon and takes the non-linear coupling of temperature and loading effects into account. The constitutive equations of the proposed model and its numerical implementation are described. Furthermore, the simulations of the experimental campaign of IFSTTAR/SMC (carried out in the framework of the MACENA project) for all the kinds of thermo-mechanical conditions envisioned during experiments are shown.

Chapter 5 aims to present the application of the THCM model to prestressed and reinforced concrete real structures of different dimensions. This chapter is divided into two main sections. The first section presents the method to model the scale effect. The second section focuses on the modelling of PACE 1450 structure which is a representative of nuclear containment wall and the nuclear containment vessel VerCoRs.

Finally, there are conclusions and perspectives of the present work.

CHAPITRE I

THC simulation of early-age concrete nuclear containments

« La vie, c'est comme une bicyclette, il faut avancer pour ne pas perdre l'équilibre » Albert Einstein

1. 1.	Introduction.....	14
1. 2.	State of the art	15
1. 2. 1.	Effect of hydration on THC behaviour of concrete at early-age.....	15
1. 2. 2.	Modelling of hydration of concrete.....	16
1. 2. 2. 1.	Hydration kinetic law	18
1. 2. 2. 2.	Water mass balance equation	20
1. 2. 2. 3.	Heat balance equation and boundary conditions.....	20
1. 3.	Strategy for concreting sequence modelling.....	21
1. 4.	Application to the lower part of vessel mock-up VeRCoRs.....	23
1. 4. 1.	Presentation of nuclear containment mock-up VeRCoRs.....	23
1. 4. 2.	Formulation of VeRCoRs concrete and cement.....	25
1. 4. 3.	Environmental conditions	26
1. 4. 4.	Identification of model and material parameters.....	27
1. 4. 5.	Validation of model on the structure.....	29
1. 5.	Conclusion	31

1. 1. Introduction

Concrete generates heat as the cementitious material hydrates, and for thin structures heat dissipates almost as quickly as is generated, but, in case of large-scale structures such as nuclear containment vessels walls, temperature rise due to hydration heat is very important (i.e. more than 50°C), so management of concrete temperatures is necessary to prevent damages, minimize delayed deformations and reaches specifications. In fact, hardening of young concrete is associated with chemical processes accompanied by significant temperature and volume changes. In the early stage, the hydration process is highly exothermal and the generated heat may result in significant temperature changes. Therefore, concrete, for massive structures, are poured in successive layers at a different time to limit the high rise of temperature and facilitate the construction. However, additional checks are also required for the analysis of staged construction because the strains in the young concrete layer are restrained by the previous concrete layers and tensile stresses arise and induce the early cracking if the stress becomes greater than the strength of the material. Consequently, structural damage may occur before the main loading such as during LOCA, and the durability and serviceability of the construction may be significantly reduced.

This chapter is dedicated then to the study and modelling of the early age properties of VeRCoRs structures since setting time, corresponding to work of WP1 (Assessment of structural state before an accident) in the framework of ANR-PIA MACENA project (cf. INTRODUCTION). It is recalled that the 1/3 scale nuclear containment mock-up VeRCoRs is finely instrumented with more than 500 sensors so that the comparison of its behaviour is possible from the beginning of the construction. This nuclear reactor building is constructed in different stages such as pedestal foundation, basement, gusset, wall and dome. The evolution of temperature of this structure was evaluated by means of a thermocouple from the start of construction. Analysis of the temperature field due to hydration of concrete is a highly non-linear problem due to several reasons. The sequential casting is time-dependent and the filling sequences of the formwork are superimposed at different times. The thermal heat exchange between the concrete and the atmosphere is affected by the formwork, wind flow and external temperature. All these transient boundary conditions have to be taken into account in the finite element model. The experimental measurements enable to test and validate the numerical models for reproducing the most likely behaviour of the structure. In this work, a multiphasic hydration model is used to simulate the thermo-hydro-chemical behaviour of early-age

concrete. This study is essential to assess the initial state of the structure before LOCA accident because it provides the input data for the mechanical modelling in the next chapters.

1. 2. State of the art

1. 2. 1. Effect of hydration on THC behaviour of concrete at early-age

Nuclear reactor containments are huge structures where the staged construction is unavoidable. During the construction of the walls, concrete lifts are about 2 m high, and the duration between lifts is about 15 days. The origins of the risk of early cracking for concrete may be distinguished by two features, internal restraint and external restraint. First, the internal restraint is induced by differential thermal dilation between the phases of concrete, cement paste and aggregate characterized by distinct values of the coefficient of thermal expansion. Moreover, it may be induced by the gradient of temperature between the centre and surface of concrete elements caused by the heat release during the hydration reaction. The thermal gradient results in the thermal strains and autogenous strains. While young concrete does not present a sufficient stiffness, stresses induced by these strains are very small compared to the strength. However, as soon as the stiffness increases, stresses appear and cracking may develop. Secondly, new concrete layer presents thermal and autogenous strains, while the strains of the old concrete layer have no more significant. Thus, the strains in the young concrete layer are externally restrained by the old concrete layer and tensile stresses arise.

One of the most important factors associated with thermal cracking in concrete is the evolution and distribution of the temperature increase at any time after casting. The temperature increase is due to the heat released by the hydration of the cement. To measure the heat of hydration of cement, adiabatic or semi-adiabatic calorimeters are used with tested concrete specimens of the same mix that was used on site. Such method aims at determining the evolution of the adiabatic temperature increase under conditions which are very similar to those at the centre of a large structure. The measurement method consists of introducing into the calorimeter a sample of fresh concrete just after the mixing and measuring the temperature of the specimen. Semi-adiabatic calorimeters rely on some form of insulation around the sample to slow down the rate of heat loss. And quasi-adiabatic calorimetry (NF EN 196-9) performed on the concrete specimen is used for the standardized determination of cement hydration heat.

This input is essential for predicting, by numerical simulation, the thermo-hydro-chemical behaviour of structures. Knowing the hydration kinetic is essential to estimate the mechanical and rheological behaviour of concrete during its setting and hardening.

1. 2. 2. Modelling of hydration of concrete

Two levels of numerical models for predicting the development of hydration exist: microscopic and macroscopic model. Model of Jennings (Jennings and Johnson, 1986), DUCOM (MAEKAWA et al., 1996), HYMOSTRUC3D (Van Breugel, 1995), CEMHYD3D (Bentz, 1997; Bentz and Garboczi, 1991) and Wang (Wang et al., 2010) were based on microstructure modelling aiming at describing the microstructure evolution of cement during hardening with great realism but its computation was time-consuming, which is not appropriate for applications in massive structure modelling. As our study focuses on temperature and hydration development in massive structures, macroscopic models would be more interesting.

Several macroscopic models dealing with concrete hydration at the early age have been proposed (De Schutter, 1999; De Schutter and Taerwe, 1996; Kishi and Maekawa, 1994; Powers and Brownyard, 1947). These models can reproduce the combined hydration of concrete but do not explicitly consider the effect of water content on hydration. This effect is essential because it modifies not only the final degree of hydration (Hansen, 1986; Powers and Brownyard, 1947) but also the hydration kinetics (Bentz, 2006). Thus, models coupling hydration development and water content variation were suggested (Bentz, 2006; Oh and Cha, 2003). Waller (Waller, 1999) adapted a chemical affinity model of Ulm and Coussy (Ulm and Coussy, 1998) in order to take the effects of initial W/C ratio and mineral addition content into account. However, this asymptotic method cannot consider the desiccation or rehydration effects during hydration.

These considerations lead us to choose a multiphasic hydration model developed by Lacarrière (Buffo-Lacarrière et al., 2007) and recently extended by (El Bitouri et al., 2016; Kolani et al., 2012). This model considers, at any instant, the effects of temperature and water content on the hydration of several solid phases (clinker and mineral additions) and drying or rehydration effect. It is well suited to the prediction of early age thermo-hydro-chemo-mechanical behaviour because it takes into account coupling between the hydration development and water and temperature variations (which are needed to predict the strains that develop at an early age in concrete in endogenous conditions). It has been validated on several structures (Buffo-

Lacarrière et al., 2007, 2011, 2014) and extended to consider the hydration of slag-bended cement (Kolani et al., 2012) and to take the long-term stoichiometry variation observed in low-pH cement (hydration of silica fume and variation of C/S ratio in C-S-H) into account (El Bitouri et al., 2016). The main interest of using this hydration model is that only three parameters (k, r_k, n) are calibrated for the hydration kinetic law of each phase and they can be characterized easily through Langavant semi-adiabatic calorimeter tests and/or isothermal calorimeter tests.

The hydration kinetic laws for different components, the total water mass balance equation and the heat balance are summarized by Eq. (1-1).

$$\begin{cases} \dot{\alpha}_i = F(\alpha_i, W, T, CH) \\ \dot{W} = -\text{div}(-D_w \cdot \overrightarrow{\text{grad}} W) + \sum (W_{thi} \cdot f_i \cdot \dot{\alpha}_i) \\ \rho c \cdot \dot{T} = -\text{div}(-\lambda \cdot \overrightarrow{\text{grad}} T) + \sum (Q_{thi} \cdot f_i \cdot \dot{\alpha}_i) \end{cases} \quad (1-1)$$

With $i=1$ for the clinker, $i > 1$ for the pozzolanic or hydraulic additions, α is the degree of hydration, W is the total water content of the concrete (in m^3/m^3 of concrete), T is the temperature, CH is the quantity of portlandite of the cement paste, D_w is the water transfer coefficient, W_{thi} is the water needed for total hydration of anhydrous phase i , f_i is the quantity of anhydrous phase i , ρ is density, c is specific heat, λ is thermal conductivity and Q_{thi} is the heat produced by complete hydration of anhydrous phase i .

In addition, in real conditions, the thermal and hydric balance inside the materials is modified by the exchange at the contact between concrete and environment (air, solar radiation, and formwork ...) which can be treated in this model via the boundary conditions.

The necessary input data for this model are: binder composition (including the mineral additions), concrete formulation, thermal characteristics (conductivity, capacity), temperature of the fresh concrete, and environmental conditions (formwork, wind, solar radiation, air temperature).

1. 2. 2. 1. Hydration kinetic law

The hydration kinetic law below (Eq. (1-2)), proposed by (Buffo-Lacarrière et al., 2007) was modified by (Kolani et al., 2012) to simulate the hydration of slag-blended cement. It takes into account not only the thermal activation of the reactions following the Arrhenius law but also the phenomena that control them. At the beginning of hydration, the reactions are driven by dissolution-precipitation phenomena, hydration is accelerated due to supersaturation of interstitial solution (Taylor, 1990). When hydrate formation become preponderant, corresponding to a critical degree of hydration, the hydration kinetics is decreased by the difficulty of contact between water and anhydrous grains surrounded by a hydrated layer.

$$\dot{\alpha}_i = k_i \cdot g_i \cdot \pi_i \cdot h_i \cdot S_i \cdot P_{\text{sup}} \quad (1-2)$$

With k_i is a calibration constant depending on the anhydrous grinding, g_i is the chemical activation term, π_i accounts for the water accessibility to anhydrous phases, h_i is the thermal activation, S_i describes the interaction between portlandite and mineral additions, and P_{sup} accounts for the delayed effect of superplasticizers or is used to reproduce a casting sequence. Regarding the chemical activation, the clinker dissolution is driven by the quantity of clinker present in interstitial solution followed by the precipitation of new hydrates (Taylor, 1990). This effect is modelled by the following expression for each phase “ i ”

$$g_i = \begin{cases} \frac{\alpha_c C_{p0\text{clinker}}}{\min(W_{ps}, W_p)} & i = \text{clinker} \\ \frac{\alpha_c C_{p0\text{clinker}}}{W_p} & i = \text{mineral addition} \end{cases} \quad (1-3)$$

Where α_c is the degree of hydration of clinker, $C_{p0\text{clinker}}$ is the initial volumetric concentration of clinker in the paste, W_p is the volumetric concentration of water in the paste and we define the water content threshold W_{ps} as the maximum volumetric concentration of water in the paste for a water to cement ratio of 0.4. This value is derived from calibration of the proposed model on different types of clinker. When the water content exceeds this value, the water has no additional dilution effect and hence a reduction in kinetics.

When hydration advances, layers of hydration products formed around each anhydrous phase cause the difficulty of the access of free water to anhydrous grains, consequently reduce the hydration kinetics. This phenomenon can be expressed by Eq. (1-4).

$$\pi_i = \exp \left[-\frac{1}{n} \left(\frac{\bar{r}_{m_i}}{r_k} \right)^n \right] \quad (1-4)$$

Where n is a fitting parameter which controls the shape of the hydration kinetic law, r_k is also a fitting parameter that represents the characteristic thickness of hydrate layers beyond which hydration kinetics decrease, and \bar{r}_{m_i} is the current thickness of hydrate layers around anhydrous grains “ i ”. The latter can be evaluated through Eq. (1-5) which considers the influence of porosity, water content and quantity of anhydrous grains.

$$\bar{r}_{m_i} = \frac{C_{P_{hyd_i}}}{W_p \cdot \phi_p \cdot C_{P_{anh_i}}} \quad (1-5)$$

With $C_{P_{anh_i}}$ is anhydrous volumetric concentration in the paste, $C_{P_{hyd_i}}$ is the volumetric concentration of hydrate produced from grains of phase i , Φ_p is the porosity of the paste and W_p is the volumetric concentration of water in the paste. The volumetric concentration of anhydrous phases and hydrates are determined using Eq. (1-6) and (1-7).

$$C_{P_{anh_i}} = (1 - \alpha_i) \cdot \frac{m_i}{V_{paste,0} \cdot \rho_i} \quad (1-6)$$

$$C_{P_{hyd_i}} = R_i \cdot \alpha_i \cdot \frac{m_i}{V_{paste,0} \cdot \rho_i} \quad (1-7)$$

With $V_{paste,0}$ is the initial paste volumetric concentration in concrete, R_i is volume ratio between hydrates and anhydrous phase for grains of phase i , ρ_i is anhydrous phase density, and m_i is the initial mass of anhydrous phase i .

Paste porosity is determined by Eq. (1-8).

$$\Phi_p = 1 - \sum_i (C_{P_{anh_i}} + C_{P_{hyd_i}}) \quad (1-8)$$

The effect of temperature on the hydration kinetics is modelled using the Arrhenius law as followed:

$$h_i = \exp \left(-\frac{Ea_i}{R} \left(\frac{1}{T} - \frac{1}{T_{ref}} \right) \right) \quad (1-9)$$

Where Ea_i is the activation energy of phase i , R is the gas constant (8.314 J/mol.K) and $T_{ref} = 293 \text{ K}$ is the temperature reference.

1. 2. 2. 2. Water mass balance equation

Two important phenomena for water content in concrete are water consumption by hydration or pozzolanic reactions and water exchanges with the environment, which are resolved via the water mass balance equation in Eq. (1-1). The hydric diffusion coefficient governing water transport depends on water content in the paste porosity, which can be modelled using an expression in Eq. proposed by (Mensi et al., 1988) with D_{w0} and p are model parameters.

$$D_w(W) = D_{w0} \exp(p \cdot W) \quad (1-10)$$

Environmental conditions such as drying due to convection or by fixed water content are considered as boundary conditions (Eq. (1-11)):

$$\begin{cases} h_c (W_{air} - W_{face}) \cdot \vec{n} - D_w \cdot \overrightarrow{grad}W = 0 \\ W_{face} - W_{imposed} = 0 \end{cases} \quad (1-11)$$

Where h_c is the convective exchange coefficient, W_{air} is the water content in the ambient air, W_{face} is the water content on the external face of the concrete subjected to exchange and $W_{imposed}$ is the water content imposed on the external face (humid curing for instance).

1. 2. 2. 3. Heat balance equation and boundary conditions

The temperature evolution is affected by heat production from hydration and boundary conditions (imposed temperature, convection, or solar radiation). Exchanges by convection and radiation can be considered using the Eq. (1-12).

$$\begin{cases} \varphi_{c+r} \cdot \vec{n} - \lambda \cdot \overrightarrow{grad}T = 0 \\ \varphi_{c+r} = H_{eq} (T_{ext} - T_{face}) \end{cases} \quad (1-12)$$

Where λ is concrete thermal conductivity, φ_{c+r} is the global convection and radiation flow, T_{ext} is the ambient temperature, T_{face} is the temperature at the face of concrete, and H_{eq} is the equivalent heat transfer coefficient defined by Eq. (1-13). The latter considers convective and radiative exchanges and heat transfer through formwork using classical thermal serial modelling (Figure 1-1). This serial model is used in a steady state as the thermal capacity of formwork material is not integrated.

$$\begin{cases} \frac{1}{H_{eq}} = \frac{1}{H_{c+r}} + \frac{e_f}{\lambda_f} \\ H_{c+r} = H_{rad} + H_{air} \end{cases} \quad (1-13)$$

With λ_f the thermal conductivity of formwork, e_f the formwork thickness, H_{rad} the radiative exchange coefficient, and H_{air} the convective exchange coefficient in the air.

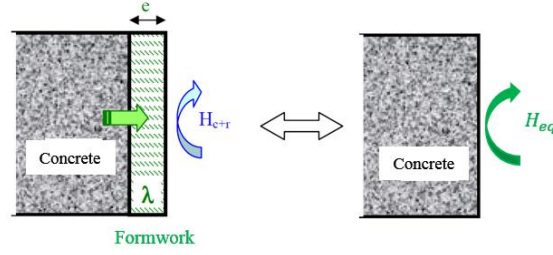


Figure 1-1: Equivalent convective coefficient with formwork

1. 3. Strategy for concreting sequence modelling

As previously presented, the multiphasic hydration model is easy and suitable for applying to large-scale structures. Since the construction of massive structure cannot be completed at one time, the successive construction stage is required to prevent the significant heat released from the hydration reaction, the segregation of aggregates in concrete and facilitate the pouring. Each stage of concrete may be modelled using different meshes by separate analyses. However, separate analyses cannot reproduce the most likely behaviour of each element because the successive elements can effect on each other. To avoid the separate analyses, a better strategy for modelling the sequential casting is introduced here. This method presents several advantages. First, it facilitates the mesh of structure. Each element of the whole structure can be meshed at the same time, but the model is activated once the concrete is casted. Moreover, it takes the behaviour of computed concrete into account for next calculation of new concrete.

The method consists of meshing each element of structure and activating the hydration model only if the element is casted. The activation of the hydration model is made introducing a delayed coefficient P_{sup} in the hydration affinity law (Eq. (1-2)) which is equal to zero when the time t is lower than the casting time $t_{casting}$ of the geometrical zone, and to 1 as soon as the time reach the casting date (see Eq. (1-14))

$$P_{sup} = \begin{cases} 0 & \text{if } t < t_{casting} \\ 1 & \text{if } t \geq t_{casting} \end{cases} \quad (1-14)$$

Using a non-evolutive mesh can induce wrong thermal boundary conditions on the zone lastly casted (which is in contact with “non-active” zones where the hydration kinetic is null). Indeed these non-active zones are supposed to behave thermally like the external temperature. This is achieved by using an artificial huge conductivity in the non-active zones.

Figure 1-2 illustrates the modelling of concreting sequence of a piece of VeRCoRs structure during the construction of gusset on the erected massive basement. It is observed in Figure 1-2(a) that the heating is applied during the gusset formwork, so the equivalent convective coefficient and evolution of heating temperature are applied to the lateral surfaces of gusset and concrete conductivity is used for gusset volume while a huge conductivity is applied to the second and third level of internal wall and free convective coefficient on their lateral surface. Using this strategy, the temperature of the “non-active” zones are equal, at each time step, to the external temperature, which ensures a correct thermal boundary condition on the upper horizontal surface of the “active” zone.

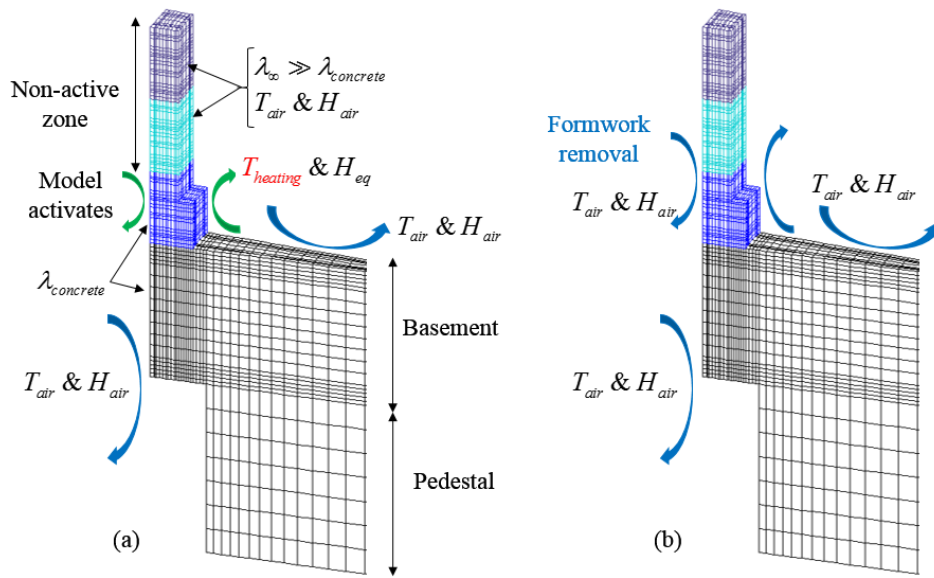


Figure 1-2: Modelling of concreting sequence during the gusset construction (piece of VeRCoRs structure) (a) heating phase, (b) formwork removal phase

Furthermore, a series of computation step is required to take account of formwork and formwork removal process. It can be considered numerically in the modelling through the variation of the convective coefficient. For instance, for the first computation during the formwork of the first element, concrete is protected laterally by the formwork, so the equivalent convective coefficient H_{eq} is applied to the lateral surfaces of this element while the rest of surfaces uses the free convective coefficient H_{air} . After formwork removal, the coefficient H_{eq} will be replaced by H_{air} . The coefficient H_{eq} will be applied during the formwork of second element.

The detailed analysis of entire VeRCoRs is presented in the following section.

1. 4. Application to the lower part of vessel mock-up VeRCoRs

This part is dedicated to an application of the hydration model on a real structure VeRCoRs in order to validate the model through the comparison between the numerical results and experimental measurements of the temperature state variation in the mock-up VeRCoRs.

1. 4. 1. Presentation of nuclear containment mock-up VeRCoRs

In the framework of EDF's continuous effort on the safety and life extensions of nuclear power plants, an experimental mock-up of a reactor containment-building at 1/3 scale was built at Renardieres near Paris. The so-called VeRCoRs mock-up is a double wall containment ($H=30\text{m}$, $\varnothing=16\text{m}$, see Figure 1-3). This mock-up was finely instrumented so that its behaviour could be monitored from the beginning of the construction. The studied structure consists of pedestal, basement, gusset and two levels of internal wall (Figure 1-4). This cylindrical structure is entirely meshed with the soil below where the symmetric vertical cut of the mesh in Figure 1-5 is used to facilitate the illustration. The displacements of lower surface of soil are blocked. The gusset is finely meshed compared to other elements in order to obtain more accurate results. In fact, there are two main reasons behind the choice of this mesh. First, the behaviour of an element may be influenced by the surrounding elements beside the environmental loadings. After hydration modelling, this mesh will be used also for the mechanical modelling in chapter V and the behaviour of massive element i.e. basement affects the behaviour of the gusset particularly in terms of induced strains. Moreover, the soil which performs as the elastic element is also used to provide the most realistic boundary condition for this concrete structure. The second reason is to take into account the statistical size effect highlighted by the CEOS.fr national research project, this size effect will be considered in chapter V. The number of 3D finite elements and 2D elements for convection is summed up in Table 1-1.



Figure 1-3: Nuclear reactor building VeRCoRs mock-up (EDF, 2014)

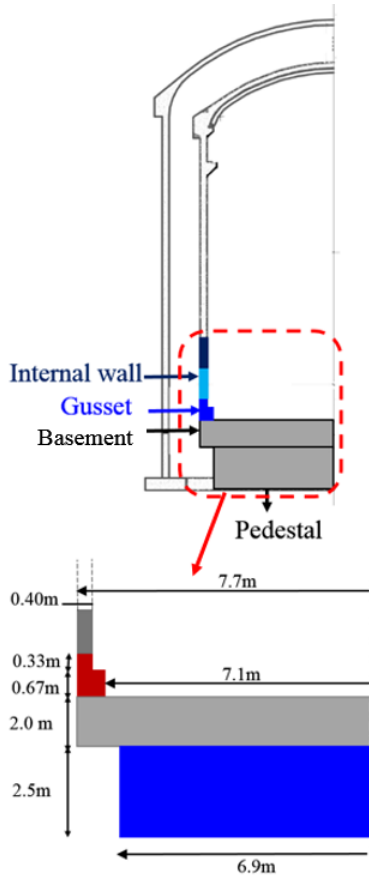


Figure 1-4: Axisymmetric section of structure VeRCoRs

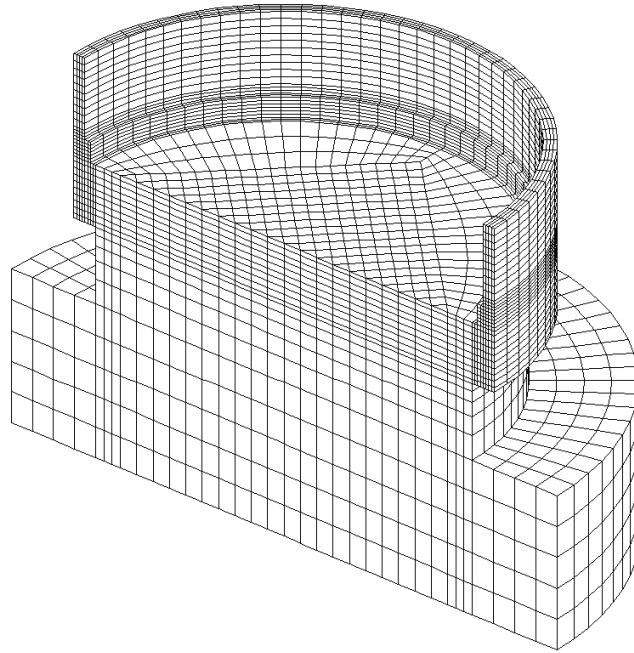


Figure 1-5: 3D mesh of whole structure VeRCoRs with soil (only a half of the structure is presented here)

Table 1-1: Number of meshed elements

Element	Number of 3D elements	Number of 2D elements for convection
Soil	4800	320
Pedestal	3200	400
Basement	12800	4400
Gusset	3840	1600
Internal wall-level 2	1600	800
Internal wall-level 3	1600	1120

1. 4. 2. Formulation of VeRCoRs concrete and cement

The experimental program was performed with a binder composed of Portland cement CEM I 52.5N. The chemical compositions of the clinker used are given in Table 1-2 and the composition of VeRCoRs concrete is given in Table 1-3. (Technical data sheet in Annexe)

Table 1-2: Chemical oxide composition of Clinker

Oxide composition	% by weight
SiO ₂	20.6
Al ₂ O ₃	4.5
Fe ₂ O ₃	2.3
TiO ₂	0.3
MnO	0.1
CaO	63.2
MgO	2.1
SO ₃	3.3
K ₂ O	0.73
Na ₂ O	0.16
P ₂ O ₅	0.3
Loss on ignition	2.1
Density	3.19 g/cm ³
Blaine's specific surface	4150 cm ³ /g

Table 1-3. Formulation of VeRCoRs concrete

	Quantities (kg/m ³)
Cement CEM I 52.5N CE CP2 NF Gaurain	320
Sand 0/4 rec GSM LGP1	830
Gravel 4/11R GSM LGP1	445
Gravel 8/16R Balloy	550
Superplasticizer Techno 80	2.4
Effective water	167.2

1. 4. 3. Environmental conditions

The studied structure was built at Renardieres near Paris during the summer 2014 and the environmental conditions were underwent (temperature, wind flow and formwork) to be considered in the modelling to obtain the most likely evolution of temperature field in the structure. Concrete was casted, for massive structure, at different stages. The initial temperature of concrete for each stage is used in the model as the initial condition (Table 1-4). The daily variation of external temperature was considered directly in the model through convective boundary condition (Figure 1-6(a)). Note that to obtain the most representative behaviour of the nuclear reactor building, the 1/3 scale mock-up has been heated intentionally locally during the gusset formwork (Figure 1-6(b)). The heating curve (red) in Figure 1-6 is imposed by EDF.

Table 1-4: Construction procedure of VeRCoRs

Phase	T°C	Casting	Calculation time	Formwork removal	Calculation time
Basement	27	24/07/14 8h	0	28/07/14 7h	95 h
Gusset	21.7	27/08/14 18h	834 h	29/08/14 7h	871 h
Level 2	23	15/09/14 14h	1286 h	16/09/14 7h	1303 h
Level 3	20.1	25/09/14 14h	1526 h	29/09/14 7h	1615 h
Heating at gusset					
27/08/14 23h (~ 839 h)		29/08/14 7h (~ 871 h)			

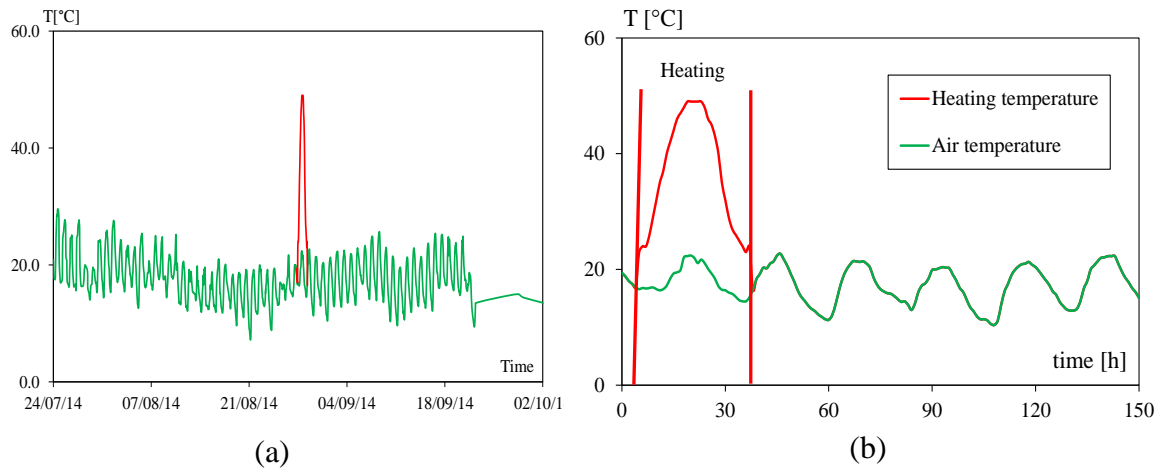


Figure 1-6: Evolution of air temperature and heating temperature during gusset formwork ($t = 0$ corresponds to calculation time 834h) (EDF, 2014)

In term of convection, the air convective coefficient H_{air} is applied to the surfaces of concrete that are free from formwork. During pouring, the lateral surfaces of concrete is protected by the wooden formwork with 3.6 cm of thickness. The convective coefficient with the air is then reduced by the presence of formwork and the equivalent convective coefficient is computed through a serial model (Eq. (1-15)). The value of these parameters is given in Table 1-5.

$$\frac{1}{H_{eq}} = \frac{1}{H_{air}} + \frac{e_f}{\lambda_f} \quad (1-15)$$

Table 1-5: Boundary condition model parameters (EDF, 2014)

Parameters	Value
$H_{air} [W/m^2. ^\circ C]$	8
$\lambda_f [W/m. ^\circ C]$	0.13
$e_f [m]$	0.036
$H_{eq} [W/m^2. ^\circ C]$	2.49

1. 4. 4. Identification of model and material parameters

The three parameters (k, r_k, n) in the hydration model are calibrated using results from an isothermal calorimetry test at 20°C. And the thermal activation energy Ea can be determined through the calibration of heat release in the isothermal calorimetry test at 40°C. The three fitting parameters and the activation energy are listed in Table 1-6 and its calibration results are shown in Figure 1-7. With the gas constant $R = 8.314 J/mol.K$, the thermal activation energy Ea is equal to 28 000 J/mol which is in accordance with the measure obtained from the maturometry test (EDF, 2014). Moreover, it reproduces the temperature increase due to the exothermal reaction of hydration which is similar to results of an adiabatic calorimeter test from CEBTP laboratory in the framework of VeRCoRs project (Figure 1-8). Besides this, the thermal and hydric parameters of concrete needed for thermohydric transfers are listed in Table 1-7 and Table 1-8 respectively.

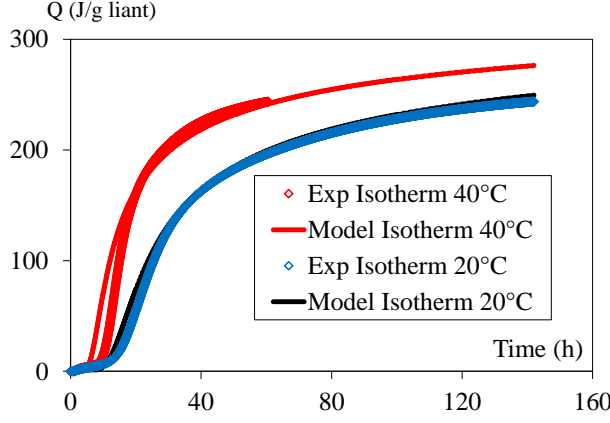


Figure 1-7: Calibration of heat of hydration of pure Portland cement (Isothermal calorimeter test at 20°C and 40°C)

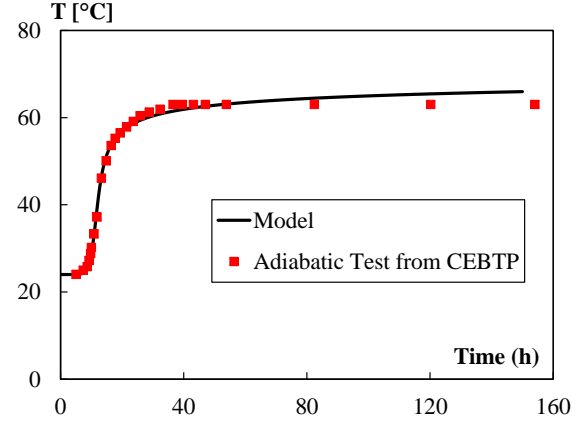


Figure 1-8: Prediction of temperature evolution of concrete in adiabatic condition (Adiabatic calorimeter test by CEBTP)

Table 1-6: Hydration kinetics parameters

Parameters	Value	Technique
k (Eq. (1-2))	1.708	Isothermal
r_k (Eq. (1-4))	1.146	Calorimetry at
n (Eq. (1-4))	0.747	20°C
$Ea/R[K^{-1}]$	3367.6	Iso. Cal. 40°C

Table 1-7. Thermal parameters of concrete (EDF, 2014)

Thermal parameters	Quantities
Thermal conductivity	1.965
$\lambda[W/m. ^\circ C]$	
Concrete density	2370
$\rho[kg/m^3]$	
Thermal capacity	880
$C[J/kg. ^\circ C]$	

Table 1-8: Hydric parameters of similar concrete (Mensi et al., 1988)

Hydric parameters	Quantities
$D_{w0}[m^2/s]$	1.042×10^{-13}
$p[m^3/l]$	0.05

1. 4. 5. Validation of model on the structure

The calculation in this section is performed using the hydration model that is implemented in the finite element code CAST3M (CEA, 2015). Note that in this work, the continuous lines in the figures are derived from modelling, the points correspond to experimental results.

Considering the equivalent and free convective coefficients for the period of formwork and after formwork removal, the external temperature variation plus the heating condition at gusset, the thermal results of modelling are in good agreement with the experimental measurements (Figure 1-9).

The hydration model used in this study was further validated previously on other structures ((Buffo-Lacarrière et al., 2007, 2011, 2014)) and the comparison with the experimental results was only conducted to ensure that the THC loading was correct. Seeing these results (Figure 1-9), we note that it is important to carefully take all the boundary conditions and concrete characteristics into account.

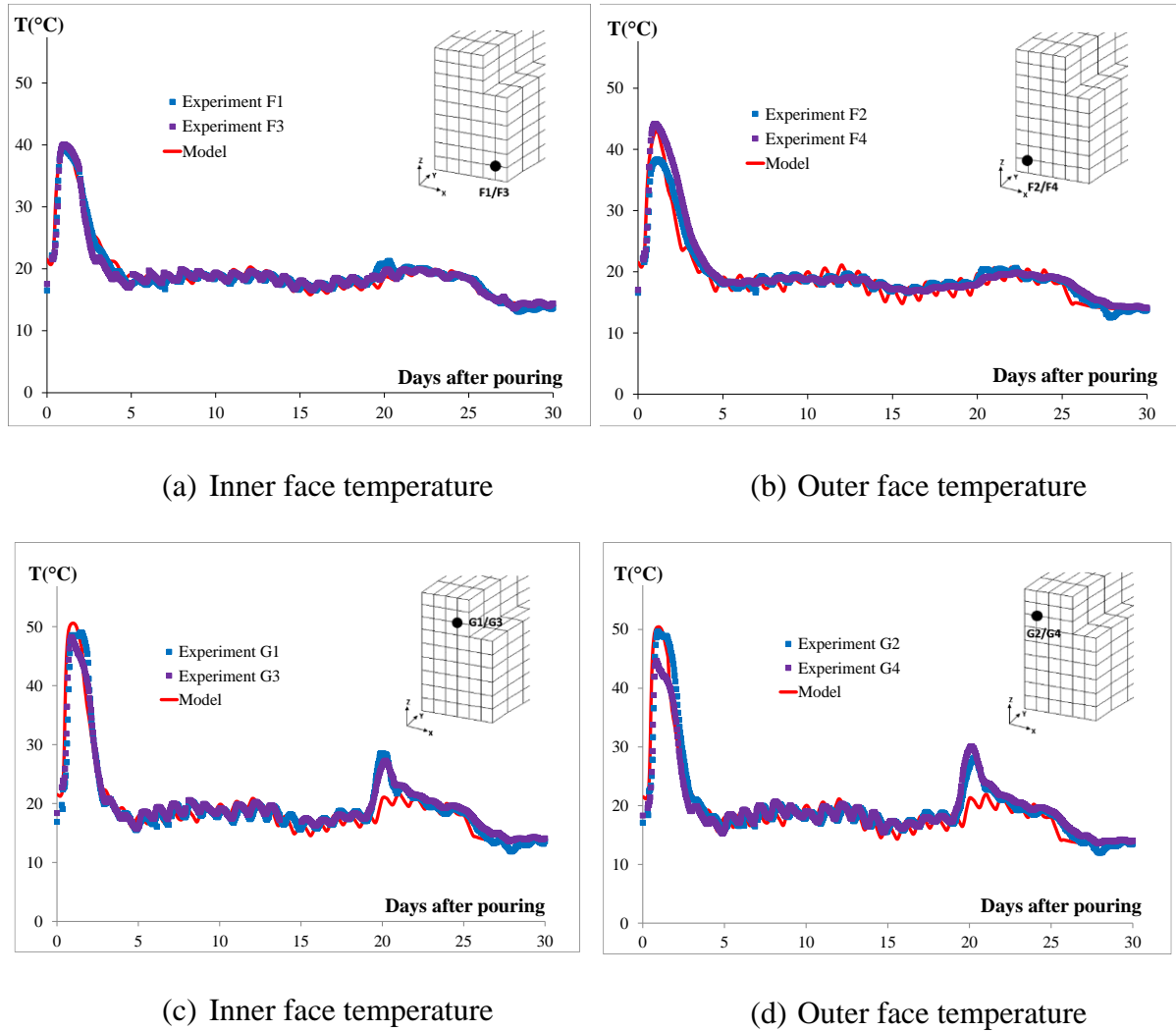


Figure 1-9: Numerical and experimental results for thermal evolution of gusset

As the model can reproduce well the evolution of temperature, its multiphysics characteristic also provides the evolution of porosity ϕ , water content W and hydration degree α , which will be used in the mechanical model in the next section. Figure 1-10 shows the fields of temperature, porosity, water content and hydration degree obtained at 16h after casting gusset. Last but not least, Figure 1-11 highlights the effect of using the concreting sequence method and how the mesh is exploited during the construction sequence. The first scheme shows the temperature field at 42h after casting gusset, the second one corresponds to temperature field at 20h after casting the second level of the internal wall, and the last one corresponds to temperature field at 22h after casting the third level of the internal wall. If we take the first scheme as an example, we see that at 42h after casting gusset, the internal wall above the gusset has not yet been constructed, so the model activates only for gusset and basement but it has not activated yet for the above internal wall. It can be seen clearly through the values of hydration and other parameters. The hydration of above internal wall has not yet developed, so the water content and porosity take its initial values and the temperature takes the value of imposed air temperature.

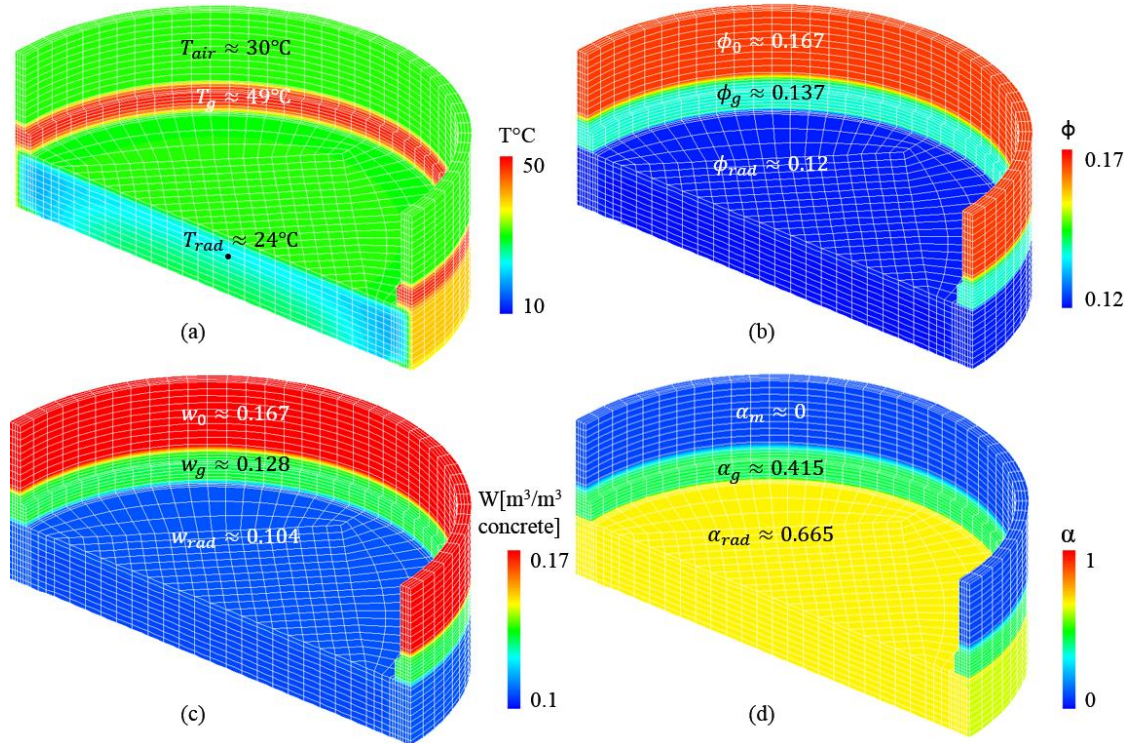


Figure 1-10: Model's responses in terms of (a) temperature, (b) porosity, (c) water content, (d) hydration degree obtained at 16h after gusset casting

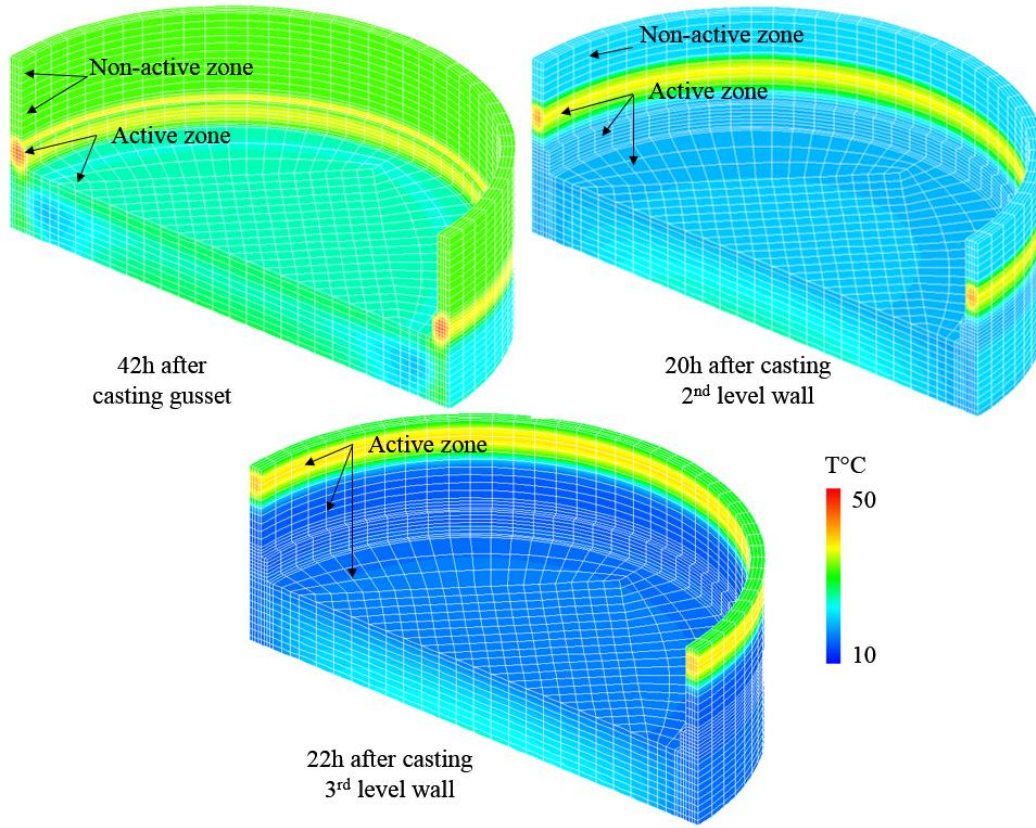


Figure 1-11: Temperature fields at different instance of construction sequence

1. 5. Conclusion

The work presented here related to a numerical approach based on hydration multiphasic model which enables to forecast the temperature state variation in the concrete structure at an early age. This model is well adapted for an application to a massive structure like VeRCoRs.

This approach couples a multiphysics model with a new method avoiding to re-mesh the structure at each stage of casting. The interest of modelling the massive structure using this method allows considering realistically the particularities of large structures, such as the sequential casting of concrete at a different date, the variation of the initial temperature of fresh concrete, the daily variation of external temperature during casting and after formwork removal. Concerning the THC model used for the hydration modelling, it is convenient because the model calibration only requires an adiabatic calorimetry test.

These considerations lead to obtaining a realistic prediction of the temperature evolution in the gusset and provides data for THCM coupling studied in the following chapters, In fact, the temperature, water content and porosity variations obtained from this hydration modelling will be used for the prediction of the mechanical and rheological behaviour of concrete since the beginning of construction (and consequently its early age cracking which will be presented in chapter V) until the long term.

CHAPITRE II

Simulation of Thermo-Hydric behaviour of Concrete at high temperature

« On passe une moitié de sa vie à attendre ceux qu'on aimera et l'autre moitié à quitter ceux qu'on aime » Victor Hugo

2. 1.	Introduction.....	34
2. 2.	State of the art	35
2. 2. 1.	Transport mechanisms and phase changes	35
2. 2. 2.	Heat transfer	36
2. 2. 2. 1.	Heat transfer model	36
2. 2. 2. 2.	Concrete conductivity	37
2. 2. 2. 3.	Thermal capacity	40
2. 2. 2. 4.	Concrete density	41
2. 2. 3.	Moisture transfer	43
2. 2. 3. 1.	Moisture transfer model	43
2. 2. 3. 2.	Influence of temperature on moisture transfer	45
2. 2. 3. 3.	Permeation of concrete	46
2. 2. 3. 4.	Isotherm sorption curves	48
2. 3.	TH modelling of saturated and unsaturated porous media	50
2. 3. 1.	Constitutive model	50
2. 3. 1. 1.	Governing equations	50
2. 3. 1. 2.	Choice of state variables	51
2. 3. 1. 3.	Temperature dependency of the isotherm sorption curve	52
2. 3. 1. 4.	Relationship between p_v and p_l equivalent to the Kelvin-Laplace law ..	53
2. 3. 1. 5.	Heat and hydric balance equations and numerical implementation	55
2. 3. 2.	Evolution of thermal and hydric parameters	57
2. 3. 2. 1.	Evolution of thermal properties of concrete	57
2. 3. 2. 2.	Evolution of water properties	59
2. 4.	Application on MAQBETH mock-up	65

2. 4. 1.	Presentation of MAQBETH structure, mesh and boundary conditions	65
2. 4. 2.	Numerical results.....	66
2. 4. 3.	Parametrical studies on permeability	69
2. 5.	Conclusion	70

2. 1. Introduction

Concrete is a porous material whose accurate description of its long-term behaviour under thermal loading is important in the context of nuclear reactor containment building. Water in concrete is the main factor influencing the concrete material properties such as drying shrinkage, creep, durability and fire resistance. Thus it is essential to forecast the moisture variation state in concrete structures. The water movement within concrete is more complex than other porous media because a number of pore structures are presented in cement paste and they change with age. In concrete structures exposed to ambient air, the moisture content decreases in both space and time due to water consumption (called self-desiccation) during hydration reaction in concrete at an early age and moisture transfer during drying of concrete. Thus the variation of moisture content can be obtained by considering the effect of self-desiccation, which is presented in chapter 1, and moisture transfer in concrete, which is presented in this chapter. The moisture distribution of a cross section of concrete is not uniform. This non-uniform moisture distribution causes the differential drying shrinkage, then tensile stress may occur on the exposed surface of concrete structures and may result in crack formation. Therefore, an assessment of the effects of concrete ageing is very important in performing safety and evaluations of the concrete structure under long-term exposure especially during a thermal excursion resulting from a design-basis accident condition.

This study focuses on the heat and moisture transfers in concrete subjected to high temperature. A rapid increase in temperature inside a thick element provokes a moisture clog characterized by a saturated state due to the fact that the condensed water in the cold zone of the wall does not have enough time to evacuate to the ambient. This explains the interest of this chapter that describes the saturated and unsaturated conditions into a single analytical model. A simplified coupled thermo-hydric model is proposed with the assumption that the gaseous phase is composed uniquely of vapour. The influence of temperature on the isothermal sorption curves and a new expression of vapour pressure dependent on liquid pressure which is equivalent to the Kelvin-Laplace's law are explicitly underlined. In addition, a literature review of thermal and hydric properties of concrete under temperature effect is described. A simplified TH model is then developed in this work. For validation purposes, the model is applied to simulate MAQBETH mock-up, developed at the French Atomic Energy Commission (CEA Saclay) (Ranc et al., 2003), subjected to a variation of temperature until 200°C.

2. 2. State of the art

2. 2. 1. Transport mechanisms and phase changes

Concrete is here considered to be a multiphase material where the voids of the solid skeleton can be filled with a various combination of liquid and gaseous phases. The liquid phases comprise capillary water (or free water), physically bound ‘adsorbed’ water and chemically bound water which is part of the solid skeleton (it can be released at certain high temperature, this is well known as “*Dehydration*”). The gas phases (i.e. water vapour and dry air) are assumed to behave as ideal gases. Transport mechanisms in the concrete consist of the transport of heat, fluid and solid. These are summarised in Table 2-1.

Table 2-1: Transport mechanisms in the concrete

Component		Mechanism
Heat		<ul style="list-style-type: none"> - Conduction within the porous medium - Convection and radiation at external surfaces
Solid skeleton		<ul style="list-style-type: none"> - Mechanical displacement
Liquid water		<ul style="list-style-type: none"> - Darcian flow (pressure gradient)
Gas	Water vapour	<ul style="list-style-type: none"> - Darcian and Diffusional Fick’s flow
	Dry air	<ul style="list-style-type: none"> - Darcian and Diffusional Fick’s flow

The drying of the material involves many complex mechanisms that are more or less coupled (Coussy et al., 2001; Daïan, 2001; Mainguy et al., 2001). In a cementitious material, several phenomena of water transport and phase changes are involved (Figure 2-1).

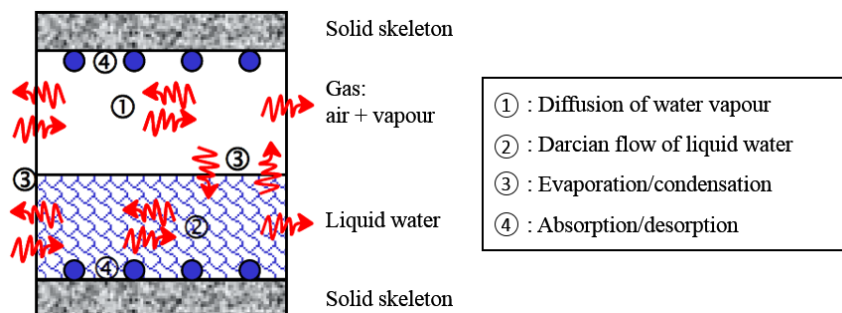


Figure 2-1: Schematic representation of water transport and phase changes in cement paste (Benboudjema, 2002)

They depend on the internal relative humidity in the material. The mechanisms of moisture transport in cementitious materials can be described in four modes (Baroghel-Bouny, 1994; Benboudjema, 2002; Nguyen, 2009; Xi et al., 1994): capillary transport, molecular diffusion, Knudsen type diffusion, and surface diffusion.

Phase changes that take place in concrete can be physical or chemical i.e. dehydration/hydration, evaporation/condensation, physical phase changes (eg. α – β transformation of quartz at 573°C) and decarbonation of calcium carbonate above 650°C. They are strongly influenced by temperature.

In fact, the dehydration has impacts on the physical and mechanical properties of concrete. It becomes significant from the temperature of 105°C for C-S-H and between 450-500°C for the Portlandite. It provokes the loss of mass of cement paste. Based on a recent study of concrete dehydration of (Wang, 2016), there is a slight loss of concrete masse about 5-10% for the temperature rise until 180°C (Figure 2-2). Therefore, for sake of simplification, the effect of dehydration (loss of “structural” water in hydrates) will be considered negligible in comparison to water exchanges by moisture transport and loss of adsorbed water (managed by water retention curves) in the study in the following section in order to simplify the problem for the low elevated temperature induced during LOCA.

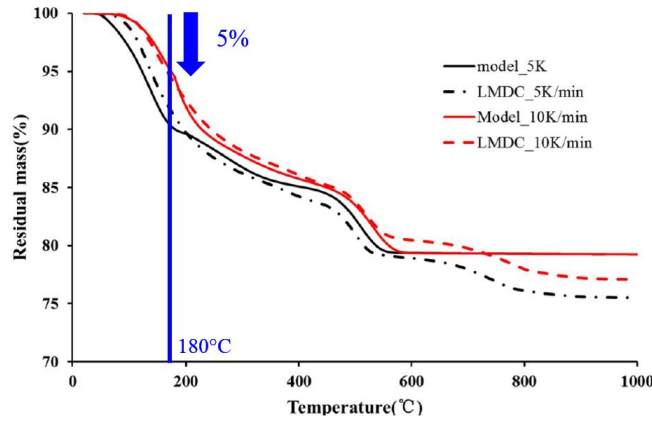


Figure 2-2: Dehydration of concrete with temperature (Wang, 2016)

2. 2. 2. Heat transfer

2. 2. 2. 1. Heat transfer model

Concrete’s thermal properties are more complex than for most materials because the concrete is not only a heterogeneous composite material whose constituents have different properties, but its properties also depend on moisture and porosity. The thermal properties that influence the temperature rise and distribution in a concrete structural section are thermal conductivity; specific heat and mass loss.

Heat transport can be modelled by Fourier’s law (Fourier, 1822) assuming that all the constituents of concrete are in thermodynamic equilibrium in the representative elementary volume (REV). The governing partial differential equation for heat transfer in concrete without internal heat source is given by Eq. (2-1)

$$\rho \cdot C \cdot \frac{\partial T}{\partial t} = -\text{div}(-\lambda \cdot \overrightarrow{\text{grad}T}) + \dot{Q} \quad (2-1)$$

Where $\rho (kg/m^3)$ is concrete density, $C (J/(kg.K))$ is thermal capacity, $\lambda (W/(m.K))$ is concrete conductivity, $T (K)$ is temperature and \dot{Q} is the heat source due to water evaporation-condensation.

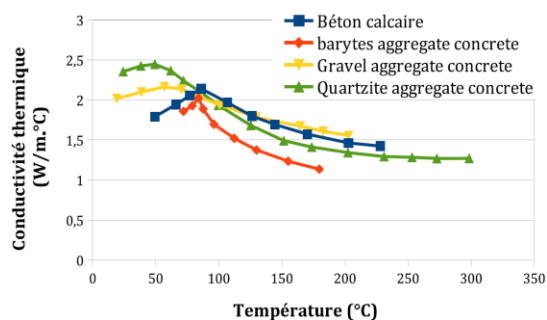
It is difficult to determine intrinsically the thermal properties of concrete as a function of temperature. This difficulty is due mainly due to the fact that the thermal properties are highly influenced by the water content of concrete. When the concrete is subjected to increasing temperatures, some drying will occur that will modify the water content. It is thus difficult to distinguish, in the experiments, the effect of temperature on the thermal properties of the solid skeleton from the effect of water content evolution. Thus, a unique relation valid in all situations cannot be established to describe the variations of these properties as a function of temperature. However, for the purposes of modelling, some empirical formulas for thermal properties of different types of concrete based on experimental data can be adopted.

2. 2. 2. 2. Concrete conductivity

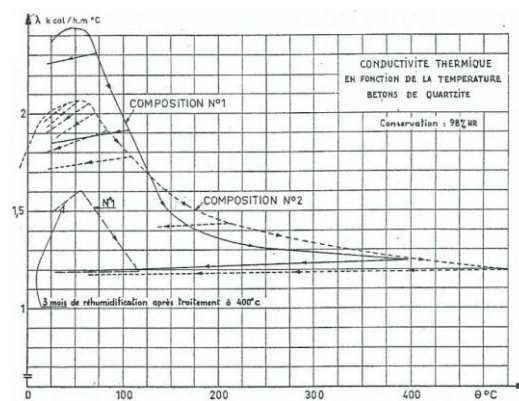
This parameter is influenced by the water content, type of aggregates and cement, the pore volume and distribution, and concrete mix design (Kim et al., 2003; Naus, 2006). Generally, the thermal conductivity of concrete decreases with the rise of temperature (Haniche, 2011; Mindeguia, 2009; Morabito, 1989; Xing, 2011). This can be attributed by the progressive departure of water which is a good thermal conductor and, in a lesser extent, by the creation of voids (increase in pore size and cracking) which induces the good thermal insulation.

It is noted for the concrete not previously dried before the test that its thermal conductivity slightly increases until the temperature 50°C and 90°C, mainly due to an increase of thermal conductivity of water (it varies from 0.6 W/m°C at 25°C to 0.68 W/m°C at 130°C) before it decreases with temperature rise because concrete begins to lose water by evaporation. These phenomena can be seen clearly in Figure 2-3 (a), (b), (c) (Bazant and Kaplan, 1996; KALLEL, 2016; Marechal, 1970).

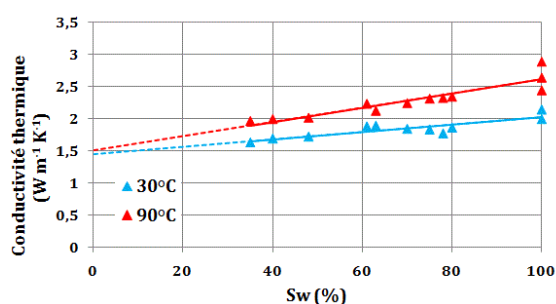
In the case of partially pre-dried concretes, a slight decrease of thermal conductivity is also observed, whatever the type of aggregates ((Kalifa and Menneteau, 2000) on Figure 2-3(d)) and (Al Najim, 2004) on Figure 2-3(e)). It is also confirmed on concrete with low W/C ratio (0.4) on Figure 2-3(f) (Kim et al., 2003).



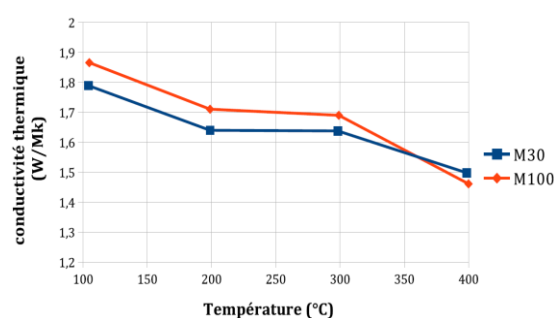
(a) (Bazant and Kaplan, 1996)



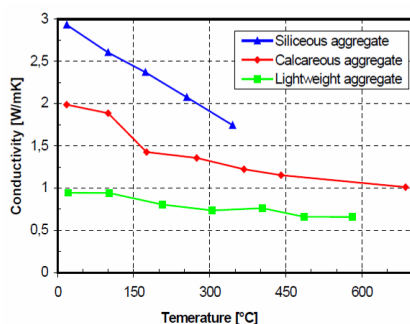
(b) (Marechal, 1970)



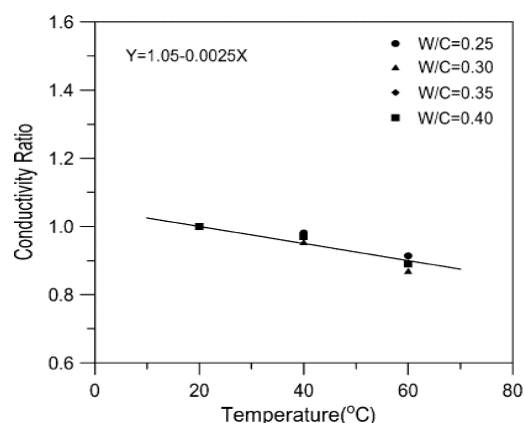
(c) (KALLEL, 2016) using TPS* technique



(d) (Kalifa and Menneteau, 2000)



(e) (Al Najim, 2004)



(f) (Kim et al., 2003)

Figure 2-3: Thermal conductivity Vs Temperature (* TPS = Transient Plane Source)

For the modelling of coupled heat-water transport, some laws could be found for the variation of thermal conductivity according to both water content and temperature (where the temperature effect will only be the one on the solid skeleton) equation (Gawin et al., 1999, 2003; Perre and Degiovanni, 1990; Pesavento, 2000). Results as the one of (Kallel 2016) can be used. But as the effect of water is very difficult to isolate from the other effect (especially for other thermal properties as thermal capacity where the heat of state change can be included)

it seems more adapted to structural modelling to adopt a general law globally expressed according to temperature and taking into account both effect simultaneously.

As mentioned previously, it can be assumed that the trend of thermal conductivity declines with temperature. In the modelling point of view, the evolution of thermal conductivity with temperature can be described by a linear regression using empirical formulas, for instance, the regulatory standard of (Eurocode 4, 1994) by Eq. (2-2) and (DTU, 1987) by Eq. (2-3). Kim et al. (2003) proposed, for a ratio of thermal conductivity, a linear equation via Eq. (2-4) in which the reference conductivity λ_0 is measured at ambient temperature. In these equations, the temperature T is expressed in °C. The comparison of the ratio of conductivity using these models is illustrated in Figure 2-4 where the conductivity measured at 20°C is selected as a base. The trend marked by the two regulatory standards are roughly the same. Moreover, the experimental result of thermal conductivity of a siliceous aggregate concrete from the French Penly Nuclear Power Plant based 40 measurements at different temperatures (30, 60, 90, 150, and 200°C) ((Vodák et al., 1997) cited by (Naus, 2006)) are plotted in the same figure. They are compared with the experimental results presented in (Bary et al., 2012) and realised on the concrete tested on the MAQBETH mock-up (which will be used for the validation)

$$\lambda_b = 2 - 0.24 \left(\frac{T}{120} \right) + 0.012 \left(\frac{T}{120} \right)^2 \quad 20^\circ\text{C} < T < 1200^\circ\text{C} \quad (2-2)$$

$$\begin{cases} \lambda_b = 1.628 - 0.14 \left(\frac{T}{100} \right) & 0^\circ\text{C} < T < 500^\circ\text{C} \\ \lambda_b = 0.928 - 0.07 \left(\frac{T}{100} \right) & 500^\circ\text{C} < T < 1000^\circ\text{C} \end{cases} \quad (2-3)$$

$$\lambda / \lambda_0 = 1.05 - 0.0025T \quad (2-4)$$

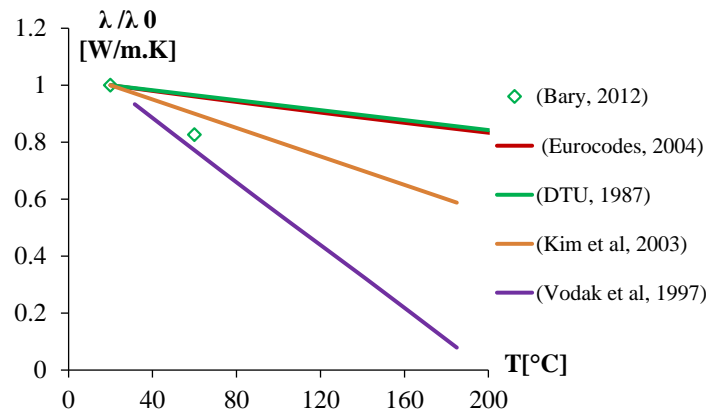


Figure 2-4: Dependence of thermal conductivity on temperature

2. 2. 2. 3. *Thermal capacity*

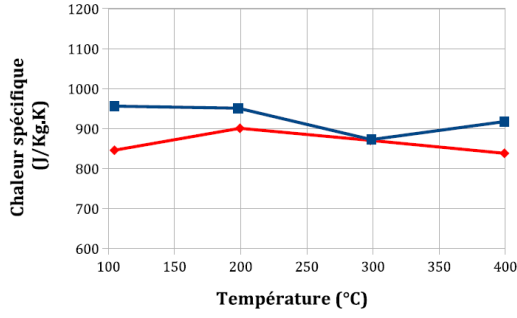
Thermal capacity or heat capacity refers to the amount of heat needed to raise the temperature of one kilogram of mass by 1 K. The heat capacity of concrete can be determined from the heat capacity of each constituent and their volume fraction in mix design ($C = \sum_i f_i \cdot C_i$). The classical value of mass heat capacity of the concrete component can be found in Table 2-2 (Neville, 2000). When the temperature increases, this parameter is strongly modified by the different physicochemical transformations, the drying of material (departure of water) and dehydration of C-S-H and Portlandite. Figure 2-5(a) (Kalifa and Menneteau, 2000) shows that the values of heat capacity obtained from test during heating are slightly influenced by the temperature while Figure 2-5(b) (Bazant and Kaplan, 1996) shows that the values of this parameter obtained from different test after cooling are significantly influenced by the temperature. It is difficult to compare these experimental results as they are conducted on different types of concrete and different configuration of tests. By the way, a common point can be deduced from these tests for low elevated temperature under 180°C that the effect of temperature tends to increase the heat capacity of concrete which is in a good agreement with (Eurocode 2, 2004). This property depends on not only the temperature but also the moisture content. The influence of moisture content on heat capacity has been studied by (KALLEL, 2016) at 20°C and 90°C (Figure 2-5(c)).

Table 2-2: Mass capacity of concrete component (Neville, 2000)

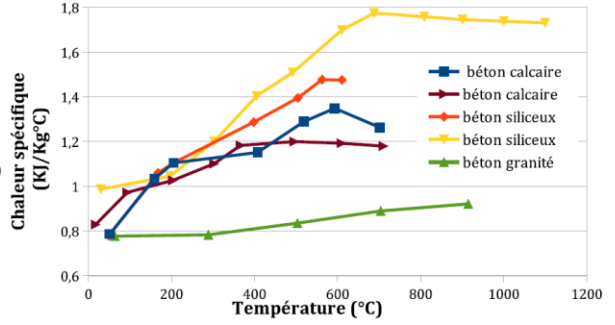
Phase i	Mass capacity (J/kg.K)
Anhydrous cement	750
Aggregate	800
Free water	4184
Bound water	3760
Water vapour	1805
Dried air	1005

In the regulatory point of view, the evolution of thermal capacity with temperature is proposed to be constant (921 J/Kg. °C) for all temperature by (DTU, 1987) and to be slightly increased with temperature rise by (Eurocode 2, 2004) in Eq. (2-5) which is illustrated in Figure 2-5(d).

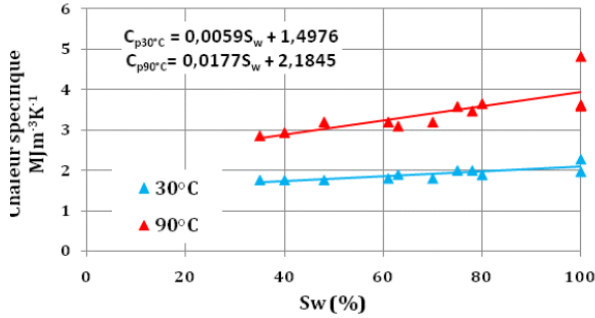
$$C_b = 900 + 80 \left(\frac{T}{120} \right) - 4 \left(\frac{T}{120} \right)^2 \quad 20^\circ\text{C} < T < 1200^\circ\text{C} \quad (2-5)$$



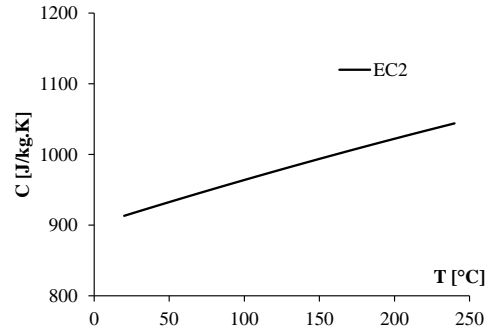
(a) (Kalifa and Menneteau, 2000)
Test during heating



(b) (Bazant and Kaplan, 1996)
Test after cooling



(c) (KALLEL, 2016)



(d) (Eurocode 2, 2004)

Figure 2-5: Thermal Capacity Vs Temperature and Saturation degree

2. 2. 2. 4. Concrete density

At ambient temperature, concrete density is about 2300 kg/m^3 . This propriety maybe modified due to the temperature rise and different physico-chemical transformations:

- Water departure by drying and dehydration of C-S-H and Portlandite decreases the density of concrete
- Thermal expansion of concrete decreases its density
- High expansion at 573°C of the quartz-containing aggregates decreases the density of concrete
- Strong release of CO_2 which accompanies the decomposition of calcium carbonate from 700°C greatly reduces the density of concrete
- Melting of concrete densifies the material, consequently increasing its density

According to the experimental results from different authors (Bazant and Kaplan, 1996; Kodur, 2014; Schneider, 1988) shown in Figure 2-6, Figure 2-7 and Figure 2-8, we observe, for all kinds of concrete, a slight decrease of its density for temperature range from ambient temperature to 400°C because of the thermal expansion of material and departure of water. For modelling, (Anderberg, 2003) proposed a relation between concrete density and temperature with Eq. (2-6) in which the reference density ρ_0 is measured at ambient temperature and the

temperature T is expressed in $^{\circ}\text{C}$. The experimental results of (Nguyen, 2013) on the measure of concrete density at various temperatures are also plotted in the same figure (Figure 2-9).

$$\rho_b = \begin{cases} \rho_0 & , 20^{\circ}\text{C} \leq T \leq 115^{\circ}\text{C} \\ \rho_0 \left[1 - \frac{0.02(T - 115)}{85} \right] & , 115^{\circ}\text{C} \leq T \leq 200^{\circ}\text{C} \\ \rho_0 \left[0.98 - \frac{0.03(T - 200)}{200} \right] & , 200^{\circ}\text{C} \leq T \leq 400^{\circ}\text{C} \\ \rho_0 \left[0.95 - \frac{0.07(T - 400)}{800} \right] & , 400^{\circ}\text{C} \leq T \leq 1200^{\circ}\text{C} \end{cases} \quad (2-6)$$

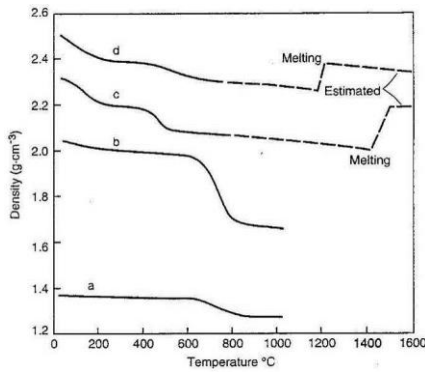


Figure 2-6: Effect of temperature on the density of concrete made from different types of aggregates (a) expanded clay (light aggregates) (b) silico-calcars (c) quartzite and (d) basalt (Bazant and Kaplan, 1996)

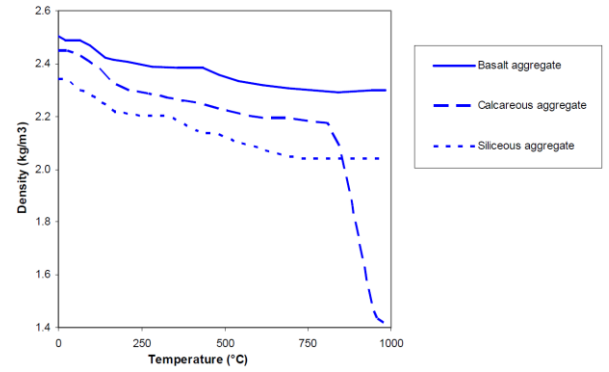


Figure 2-7: Evolution of density of different concretes with temperature (Schneider, 1988)

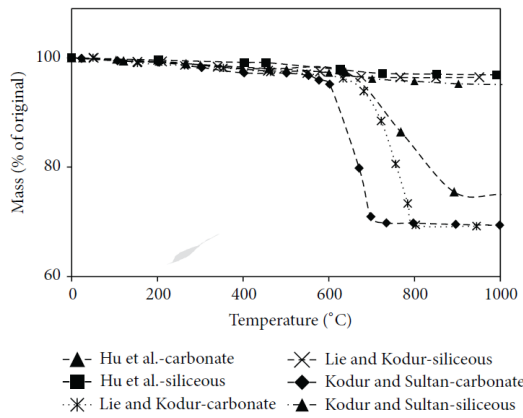


Figure 2-8: Evolution of mass of different concretes with temperature (Kodur, 2014)

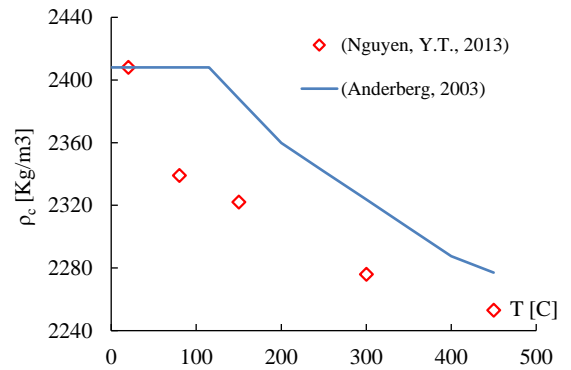


Figure 2-9: Evolution of concrete density with temperature (Anderberg, 2003; Nguyen, 2013)

2. 2. 3. Moisture transfer

2. 2. 3. 1. Moisture transfer model

From the theoretical point of view, Philip and De Vries (1957) and Luikov (1975) were among the first to propose a model of coupled partial differential equations governing the heat and moisture transfer in porous media. On the basis of Luikov's theory, Bazant and Thonguthai (1978) developed a mathematical model for drying of concrete at high temperatures. An extended bibliography review of numerical modelling of the behaviour of concrete under high/moderate temperature may be found in (AbdelRahman and Ahmed, 1996; Bary et al., 2008; Bazant and Kaplan, 1996; Davie et al., 2006; De Morais et al., 2009; Gawin et al., 1999; Khoury et al., 2002; Mounajed and Obeid, 2004; Ranc et al., 2003; R. T. Tenchev, 2001; Sercombe, J. et al., 2001; Thiery et al., 2007; Yuen et al., 2007). Sophisticated models involving three interacting fluid phases: liquid water, vapour water, and dry air were developed to cover all the main phenomena that can be observed in porous media such as vapour diffusion, liquid water flow due to pressure gradients and capillary effects, evaporation/condensation phenomena, etc. These models are derived from the coupled formulation of heat and mass transfer conservation equations and state variables of the hydric problem can be capillary pressure, liquid pressure, gas pressure, or saturation degree upon the choice of author. The common features of these models are that they are able to describe coupled water and heat transfers in the porous media and their interactions with the deformable solid matrix.

Modelling of drying is based on the mass balance equations of three constituents in the porous media: liquid water (l), water vapour (v) and dry air (a). This macroscopic approach is expressed via the following form:

$$\begin{cases} \frac{\partial m_l}{\partial t} = -\text{div}(\vec{w}_l) - \dot{\mu} + \dot{d} \\ \frac{\partial m_v}{\partial t} = -\text{div}(\vec{w}_v) + \dot{\mu} \\ \frac{\partial m_a}{\partial t} = -\text{div}(\vec{w}_a) \end{cases} \quad (2-7)$$

With m_i the mass quantity per unit volume $d\Omega$, $i = l, v$ or a index corresponding to liquid water, water vapour and dry air respectively, w_i the mass flux of each constituent, $\dot{\mu}$ the mass quantity exchanged by vaporisation or condensation per unit volume $d\Omega$ and \dot{d} the rate of water released in the porosity.

In Eq. (2-7), the mass flux of each constituent w_i is the product of its mass m_i and its velocity v_i .

$$w_i = m_i \times v_i \quad (2-8)$$

The mass quantity m_i is expressed according to its density, saturation of water S_l and total porosity ϕ by

$$\begin{cases} m_l = \rho_l \cdot \phi \cdot S_l \\ m_v = \rho_v \cdot \phi \cdot (1 - S_l) \\ m_a = \rho_a \cdot \phi \cdot (1 - S_l) \end{cases} \quad (2-9)$$

With $\rho_l(T)$, $\rho_v(T, p_v)$ and $\rho_a(T, p_a)$ the water, vapour and air densities respectively, which depend on temperature T and pressure p_j ($j = v$ or a). If the vapour and dry air behave as the ideal gas, their density ρ_j ($j = v$ or a) can be described by equation of ideal gas, Eq. (2-10), in which M_j is the molar mass, R is the universal gas constant, and T is the temperature.

$$\rho_j = \frac{p_j M_j}{RT} \quad (2-10)$$

Moreover, the velocity of water transfer v_l is supposed to be mainly controlled by the pore-water pressure gradient, which is in agreement with Darcy equation:

$$\vec{v}_l = -\frac{k_l}{\eta_l} k_{rl} \overrightarrow{\text{grad}} p_l \quad (2-11)$$

With k_l is the intrinsic permeability of concrete, η_l is the dynamic viscosity of liquid, k_{rl} is the relative permeability of concrete to the liquid.

And the transfer velocity of gas in vapour or air phase v_j ($j = v$ or a) is controlled by the gas pressure gradient (via the convection) and gas concentration gradient (via the diffusion). The gas transfer via convection is given by Darcy equation:

$$\vec{v}_j^c = -\frac{k_g}{\eta_g} k_{rg} \overrightarrow{\text{grad}} p_g \quad (2-12)$$

With k_g is the intrinsic permeability of concrete, η_g is the dynamic viscosity of gas, k_{rg} is the relative permeability of concrete to the gaz. The equation (2-12) given in (Baroghel-Bouny et al., 1999; Mainguy, 1999) did not consider the gas transfer relative to molecular flow. To take this phenomenon in account, Klinkenberg coefficient Γ (Klinkenberg, 1941) has been proposed and used in (Thiery et al., 2007):

$$\vec{v}_j^c = -\frac{k_g}{\eta_g} \left(k_{rg} + \frac{\Gamma}{P_g} \right) \overrightarrow{\text{grad}} p_g \quad (2-13)$$

Plus, the gas transfer via diffusion is given by Fick equation with D the diffusive coefficient of gas.

$$\vec{v}_j^d = -D \overrightarrow{\text{grad}} C_j = -D \overrightarrow{\text{grad}} \left(\frac{p_j}{p_g} \right) \quad (2-14)$$

So the total gas transfer is obtained through the combination of Eq. (2-13) and Eq. (2-14).

$$\vec{v}_j = \vec{v}_j^c + \vec{v}_j^d = -\frac{k_g}{\eta_g} \left(k_{rg} + \frac{\Gamma}{P_g} \right) \overrightarrow{\text{grad}} p_g - D \overrightarrow{\text{grad}} \left(\frac{p_j}{p_g} \right) \quad (2-15)$$

In order to resolve this problem, there are many phenomena and parameters to be identified and the coupling of the problem becomes thus complex for the resolution and convergence. For sake of simplification, several physical phenomena should be neglected (Gawin et al., 2011a, 2011b). The simplifications may be applied based on the hypothesis on the gas. On the one hand, the gas pressure is supposed constant and equal to the ambient pressure, leading to a simplified model by a diffusion type equation (Benboudjema et al., 2005; Buffo-Lacarrière, 2007; Dal Pont et al., 2005; Mainguy et al., 2001; Ranaivomanana, 2010). This is more likely adapted for modelling the drying at ambient temperature. On the other hand, the gas phase is assumed only composed of vapour, so the gas transfer due to diffusion v_v^d (Eq. (2-14)) does not exist because the fraction of vapour pressure p_v/p_g become constant. Plus, the latter hypothesis allows reducing the two mass conservation equations of water in liquid and gaseous phase into a single one (Bary et al., 2008; Kanema, M. and De Morais, M. V. G., 2007; Ranc et al., 2003; Sercombe, J. et al., 2001). Thus, the single governing equation can be described as in Eq. (2-16) corresponding to a parallel model. According to an exhaustive study of De Morais et al. (2009), these models and complete models predict reasonably well the behaviour of concrete and the use of the simplified models appear to be clearly justified since it provides results comparable to the complete models for much lower CPU time and convergence problems.

$$\frac{\partial}{\partial t} \left(\rho_l \cdot \phi \cdot S_l + \frac{P_v M_v}{RT} \cdot \phi \cdot (1 - S_l) \right) = \text{div} \left(\rho_l \frac{k_l}{\eta_l} k_{rl} \cdot \overrightarrow{\text{grad}} p_l + \frac{P_v M_v}{RT} \cdot \frac{k_g}{\eta_g} \cdot \left(k_{rg} + \frac{\Gamma}{p_v} \right) \overrightarrow{\text{grad}} p_v \right) \quad (2-16)$$

2. 2. 3. 2. Influence of temperature on moisture transfer

With temperature rise, changes in the relative proportions of the liquid and the vapour phase of pore water are induced according to the vapour pressure. As a result, an increased vapour pressure gradient arises near the hot surface, which pushes moisture towards areas of lower pressure.

Thus the migration of moisture in a concrete element subjected to a non-uniform heating is a complex phenomenon because it depends on several parameters and their interactions. England and Khoylou (England and Khoylou, 1995) have shown that for high temperature ($T > 105^\circ\text{C}$), the infiltration (fluid induced by pressure) is a dominant transport phenomenon. The heating

leads to an evaporation of water and non-negligible pressurization of vapour inside the pores. When the surface of a concrete element undergoes a temperature rise, the preceding phenomena leads to a release of vapour at the boundaries of the structure and a migration of liquid water from the hotter to the cooler zone.

If the concrete element is thin enough i.e. thickness 15 cm, moisture easily escapes through the unexposed surface without forming a moisture zone (Kang et al., 2016). However, it is relatively difficult for the moisture to move through the thicker elements whose thickness more than 20 cm, as illustrated in Figure 2-10, and a moisture clog (Hager, 2013; Hamarthy, 1965) is formed inside the concrete element. This fully saturated layer is characterized by a low permeability to the gas and acts as an impermeable barrier for gases. In parallel, the temperature rise changes the water into steam which cannot escape due to water clog presence and results in a high internal pressure in the concrete.

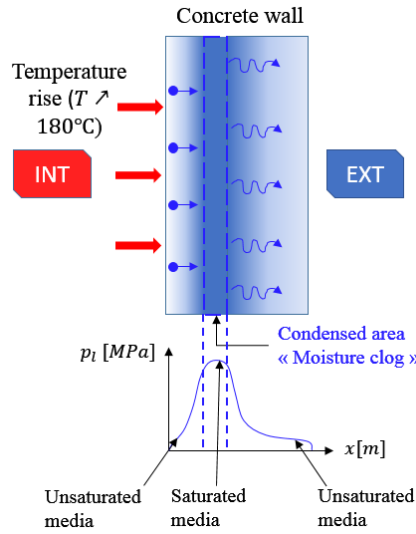


Figure 2-10: Schema of moisture movement within heated concrete element

2. 2. 3. 3. Permeation of concrete

The permeation, defined as the movement of fluid through a porous medium under an applied pressure load, is characterized by the coefficient of permeability which is the most important property governing the long-term durability of concrete. Therefore, water and gas permeabilities of concrete are then major indicators to characterise the transfer of water vapour due to drying of material as well as to evaluate the ability of this material to prevent the penetration of aggressive agents such as carbon dioxide or chlorides. As reported by Darcy, the permeability is measured in water saturated materials and the effective permeability k_{eff} is the product of intrinsic permeability k_i and relative permeability $k_{r,i}$ where $i = l$ or g for water liquid and gas phase respectively.

$$k_{eff} = k_i \times k_{ri} \quad (2-17)$$

The relative permeability k_{ri} depends on the capillary pressure, so it is not the intrinsic property of material (see section 2. 3. 2. 2). The intrinsic permeability k_i can be determined thanks to Klinkenberg method (Klinkenberg, 1941). The gas permeability obtained experimentally is the apparent value. Figure 2-11 indicates that the intrinsic permeability K_i corresponds only to the viscous flow. It is assumed that the intrinsic permeability is measured on dry material.

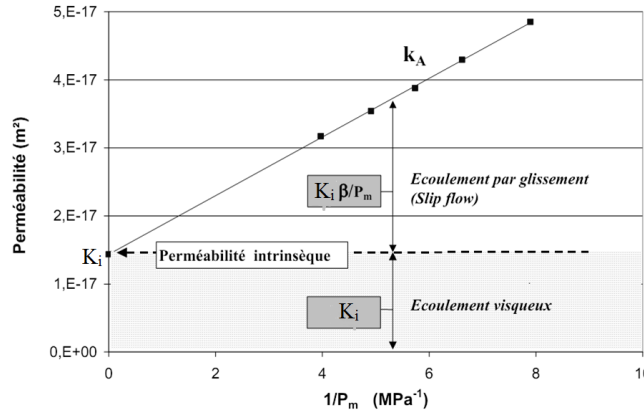


Figure 2-11: Permeability measures on ordinary concrete (Picandet, 2001)

The intrinsic permeability, also known as absolute permeability, is a material characteristic describing the penetration of gases or liquid through a porous material due to pressure. It is usually measured with a constant head CEMBUREAU permeameter (Kollek, 1989). The problem concerning this measure is more complex if the temperature is not constant, in particular, temperature above 100°C. During heating of concrete, its intrinsic permeability may increase by up to 4 orders of magnitude when compared to its initial value at ambient temperature (Bazant and Kaplan, 1996; Bazant and Thonguthai, 1978; England and Khoylou, 1995). In classical phenomenological approach, it is assumed that intrinsic permeability depends only on temperature and moisture content (Bazant and Thonguthai, 1978; England and Khoylou, 1995), but it also depends on the nature of fluids (Coussy et al., 2001) and the damage state of material (Bary, 1996; Gawin et al., 2002, 2005a, 2005b).

The liquid and gas permeability coefficient are essential parameters for modelling the transfer phenomena and the characterization of the porous structure. The value of gas permeability mainly depends on the degree of saturation of the materials, it is about $10^{-17} m^2$ for the ordinary concretes and between $10^{-18} - 10^{-19} m^2$ for the high strength concretes (Villain et al., 2001). But there is not yet still a consensus on the value of liquid permeability. Some authors (Dal Pont et al., 2007; Gawin et al., 2005a; Schrefler et al., 2002) did not distinguish these parameters using only a value of intrinsic permeability of order of $10^{-17} m^2$. While other authors (Bary et al., 2012; Coussy et al., 2001; Kanema, M. and De Moraes, M. V. G., 2007) used different values for these parameters. The value of liquid permeability used by the latter

authors is greatly lower than that of gas permeability. (Coussy et al., 2001) explained the difference by the presence of physical forces between the water molecules and cement matrix which significantly reduce the velocity of the water molecules near the surface of the pores where the flows take place.

As mentioned earlier in section 2. 2. 1, for sake of simplification of the problem at elevated temperature induced during LOCA, the effect of dehydration will be considered negligible, so the intrinsic permeability in this study is supposed to be constant according to temperature.

2. 2. 3. 4. *Isotherm sorption curves*

In the scientific literature review, there are only a few results about the influence of temperature on the concrete water retention curves (Chen et al., 2012; Ishida et al., 2007; KALLEL, 2016; Poyet, 2009; Radjy et al., 2003; Ranaivomanana, 2010). These studies, in which the maximal temperature is 80°C, have been reported an important impact of temperature on the retention curves as shown in Figure 2-12. For modelling the drying of concrete at high temperature, the evolution of relative humidity to the saturation degree represented by the isotherm sorption curve at various temperatures can be obtained using the measured data. The numerical model considering the influence of temperature on the isotherm sorption curve is initially developed by (Bazant and Kaplan, 1996; Bazant and Thonguthai, 1978) with an empirical expression:

$$S_l(p_v, T) = \left(\frac{p_v}{p_{vs}(T)} \right)^{\frac{1}{b(T)}} \quad (2-18)$$

$$b(T) = 1.04 - \frac{T_1}{22.34 + T_1} \quad ; \quad T_1 = \left(\frac{T + 10}{T_0 + 10} \right)^2 \quad (2-19)$$

Where T is the temperature (°C) and $T_0 = 25^\circ\text{C}$.

Lately, (Bary et al., 2012) also proposed a model, based on the Guggenheim-Anderson-de Boer (GAB) model and Clausius-Clapeyron relation, for describing the water sorption curve with temperature. These models are also plotted in the same figure (Figure 2-12). It is remarkable that the isotherm curves become flattered and approach 0 for high temperature. Note that in these approaches, the model curves have been modified for $HR > 0.96$ to reduce the abrupt transition saturated – partially saturated state near $HR = 1$.

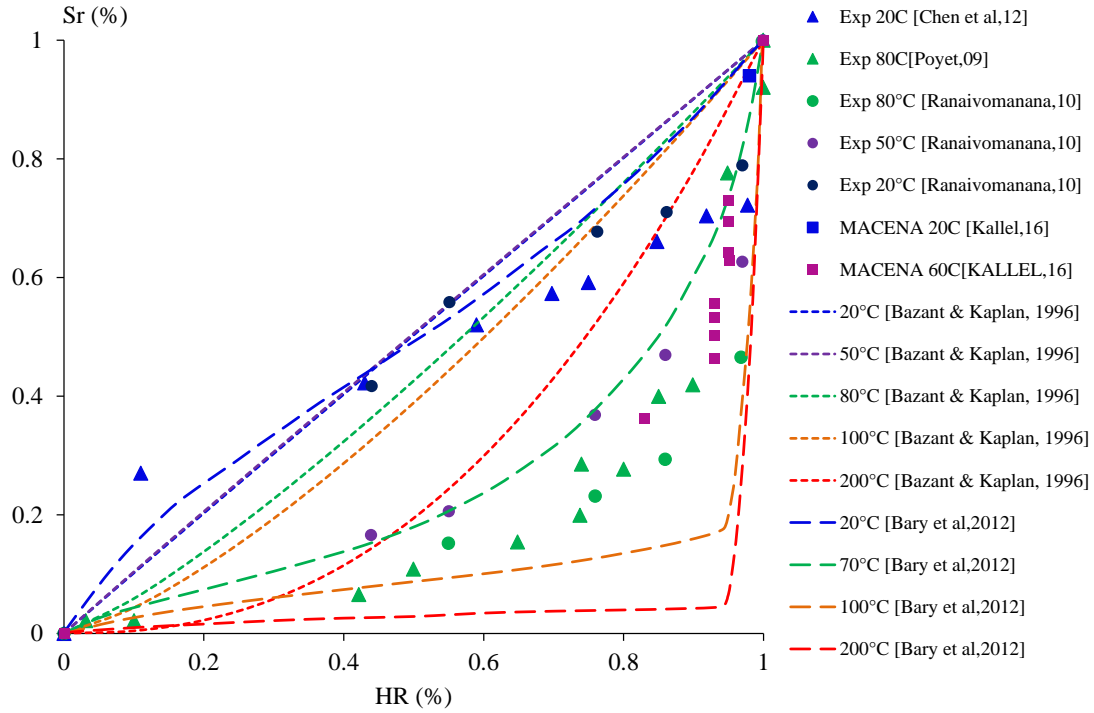


Figure 2-12: Isotherm sorption curves at different temperatures

After study of transfer mechanisms particularly heat and moisture transfers, the next paragraph will focus on a new development of TH model for saturated and unsaturated porous media envisioned for high temperature conditions.

2. 3. TH modelling of saturated and unsaturated porous media

2. 3. 1. Constitutive model

2. 3. 1. 1. Governing equations

In this work, TH model is developed with a hypothesis that the gas phase is only composed of vapour, leading to a combination of two mass conservation equations for liquid water and gas into a single one. It implies that the dry air is neglected, so $m_w = m_l + m_v$ and $\vec{w}_w = \vec{w}_l + \vec{w}_v$. Moreover, the vapour transfer due to diffusion can be neglected (see Eq. (2-14)) (no vapour gradient when the gas is supposed only composed of vapour). The effect of dehydration is not considered for the temperature range from 20°C-180°C, and the thermo-hydric phenomena are weakly coupled with the unilateral effect of temperature on moisture transport.

The governing equations for heat transport and water mass transfer balance can be described by Eq. (2-20).

$$\begin{cases} \rho(T) \cdot C(T) \cdot \frac{\partial T}{\partial t} = -\text{div}(-\lambda(T) \cdot \overrightarrow{\text{grad}T}) \\ \frac{\partial m_w}{\partial t} = -\text{div}(\vec{w}_w) \end{cases} \quad (2-20)$$

The parameters of heat equation depend on temperature and their evolutions are detailed in the next section 2. 3. 2. 1. The mass transfer equations for water can be distinguished for the saturated and unsaturated condition.

a. Saturated media

Normally a formulation based on the Biot theory of saturated porous media extended to the unsaturated conditions is employed to reproduce the solid-fluid interactions because the thermodynamic equilibrium of liquid and vapour fluids is no longer valid. For the saturated media undergoes the heating, it is submitted to the interstitial overpressures ($p_l \geq 0$) that provoke the swelling within the pores. Based on the state law of liquid water, the liquid pressure p_l can be expressed as follows:

$$p_l = M_l \left(\frac{m_l}{\rho_l} - \phi_l \right) \quad (2-21)$$

with M_l Biot's modulus account for the effect of the presence of water in the pores on the macroscopic behaviour of the material and the value of $\frac{1}{M_l} = \frac{1}{K_f} = 0.45 \text{GPa}^{-1}$ according to

(Dormieux et al., 2006; Tognevi, 2012).

Integrating the state law of liquid water, Eq. (2-21), into the water balance equation, Eq. (2-20), we obtain the following equation:

$$\frac{\partial m_l}{\partial t} = \text{div} \left(\rho_l \frac{k_l}{\eta_l} \cdot \text{grad } p_l \right) \quad (2-22)$$

$$\frac{1}{M_l} \frac{\partial p_l}{\partial t} = \text{div} \left(\frac{k_l}{\eta_l} \cdot \text{grad } p_l \right) \quad (2-23)$$

b. Unsaturated media

For the partially saturated media where $0 \leq S_l < 1$, the thermodynamic equilibrium such as the Kelvin-Laplace's law and isotherm sorption curves as well as Darcy equation can be applied to liquid and vapour phase. Based on the hypothesis that gas phase is only composed of vapour, we can combine the liquid and vapour transfers into a single model as can be seen in section 2. 2. 3. 1. The following balance equation is recalled from the governing equation in Eq. (2-16) in which the first term corresponds to the variation of liquid and vapour mass quantities and second term the gradient due to liquid and vapour transfer, respectively.

$$\frac{\partial}{\partial t} \left(\rho_l \cdot \phi \cdot S_l + \frac{p_v M_v}{RT} \cdot \phi \cdot (1 - S_l) \right) = \text{div} \left(\rho_l \frac{k_l}{\eta_l} \cdot \text{grad } p_l + \frac{p_v M_v}{RT} \cdot \frac{k_g}{\eta_g} \cdot \left(k_{rg} + \frac{\Gamma}{p_v} \right) \text{grad } p_v \right) \quad (2-24)$$

2. 3. 1. 2. Choice of state variables

To describe the long-term behaviour (temperature field and moisture migration) of concrete undergoing thermal loadings, the use of coupled TH models involving heat conduction, liquid and vapour flow is therefore necessary. The temperature T is a main variable for heat equation. For hydric equation, as the thermodynamic equilibrium such as the Kelvin-Laplace's law and isotherm sorption curves are valid only for the partially saturated media and not for the saturated media, the state law of liquid water is needed to consider the overpressure of liquid water. In order to consider both conditions into a single model, the liquid pressure p_l has been chosen as the state variable retained in the hydric model because it can be negative for unsaturated media and positive for saturated media and is the only variable able to ensure continuity between saturated and unsaturated cases. In order to express the governing equation Eq. (2-24) with a single state variable p_l , it is necessary to express all the variables as a function of p_l , for instance the relationship between p_v and p_l and the isothermal curves which depend on the temperature. The following sections will present these calculation steps.

2. 3. 1. 3. Temperature dependency of the isotherm sorption curve

As studied previously in the literature review, the isothermal sorption curve is greatly influenced by temperature. To describe this phenomenon, an analytical expression, derived from Van-Genuchten, is proposed using the experimental data by Eq. (2-25) in which the parameter M_{shr} varies with the temperature to take the influence of temperature into account.

$$S_l = \left(1 + \left(\frac{p_c}{M_{shr}} \right)^{\frac{1}{1-m_{vgn}}} \right)^{-m_{vgn}} \quad (2-25)$$

Based on the available data in the literature, we can adjust the numerical curves to the experimental data at 20°C, 50°C and 80°C by fixing the value of exponent coefficient m_{vgn} and varying the value of parameter M_{shr} . After obtaining the three values of M_{shr} at different temperatures, an exponential expression is proposed to reproduce the evolution of M_{shr} with temperature using only two parameters: M_{shr0} is measured at the reference temperature $T_{ref} = 20^\circ\text{C}$. And T_{kvgn} is obtained from calibrating the exponential equation of $M_{shr}(T)$ in Eq. (2-26) with the fitting values of M_{shr} used to reproduce the isothermal curves at 20, 50 and 80°C (see

Table 2-5 and Figure 2-13). The results of the new relation of Van Genuchten are illustrated in Figure 2-14. Indeed, these curves show that, for a given S_l , HR tends to increase upon heating. For the zone where $HR > 0.96$ in particular at high temperature ($T > 150^\circ\text{C}$), the saturation degree exhibits a significant abrupt front which shows a strong variation of S_l and this problem remains uncertain due to the lake of experimental data and physical explanations. So, to predict more accurately the isotherm sorption curve at high temperature, the experimental works in this field study are demanded.

$$M_{shr}(T) = M_{shr0} \exp\left(-\frac{T - T_0}{T_{kvgn} - T_0}\right) \quad (2-26)$$

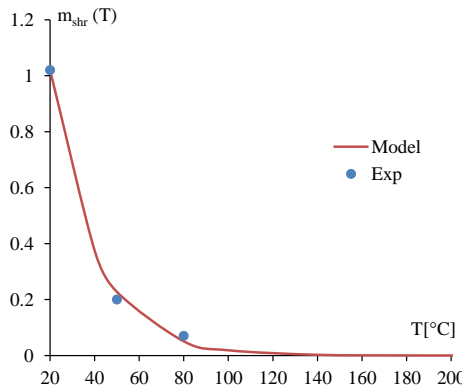


Figure 2-13: Evolution of m_{shr} with the temperature

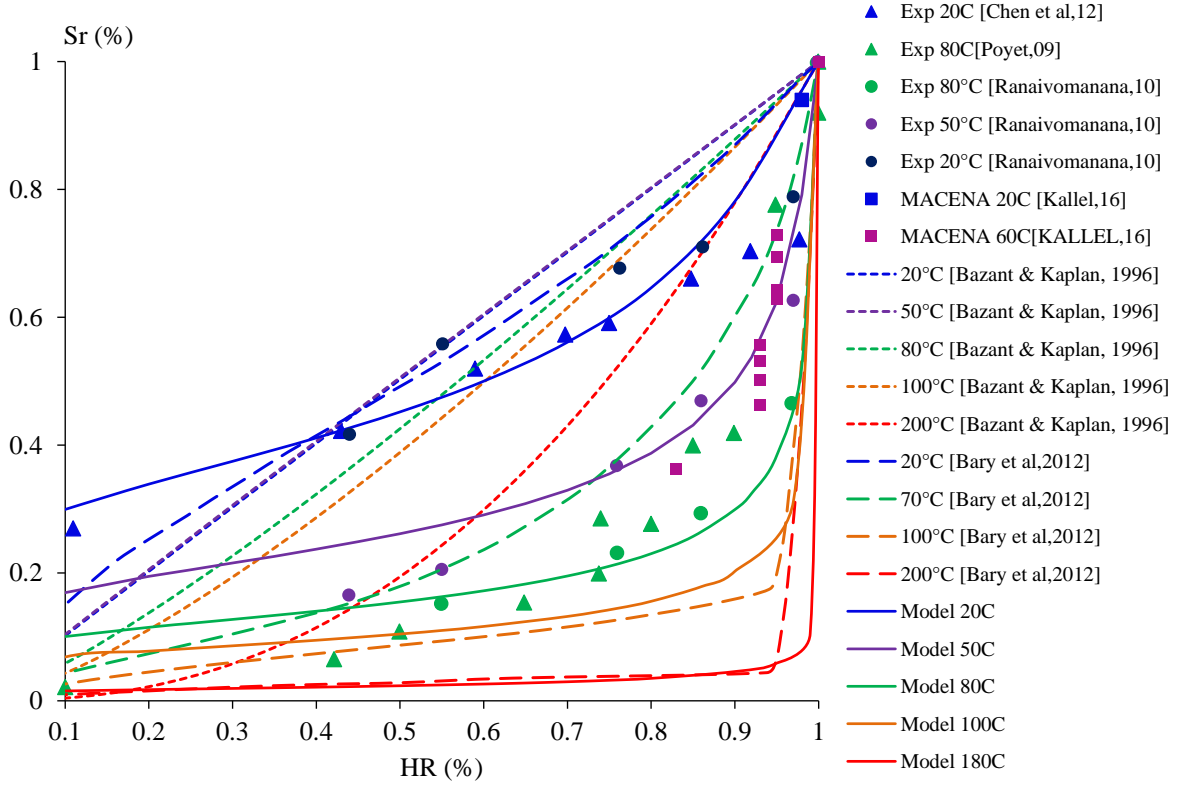


Figure 2-14: Influence of temperature on isotherm sorption curves (thick lines are the curves from the proposed model)

2. 3. 1. 4. Relationship between p_v and p_l equivalent to the Kelvin-Laplace law

In order to express the governing equation (2-15) for unsaturated condition with the state variable p_l , we need replace p_v by p_l through a relationship of Kelvin-Laplace.

The capillary pressure is linked to the relative humidity defined by $HR = p_v / p_{vs}$, with p_{vs} the vapour pressure at saturation, via the Kelvin-Laplace's law which describes the equilibrium between gas pressure and liquid pressure (Eq. (2-27))

$$p_c = p_g - p_l = -\rho_l \frac{RT}{M_v} \ln HR \quad (2-27)$$

With M_v is the molar mass of water, R is the gas constant ($8.3145 \text{ J}/(\text{K} \cdot \text{mol})$), ρ_l is the liquid water density and here $p_g = p_v$ as we neglect the dry air pressure.

Once p_g replaced by p_v , the relation in Eq. (2-27) cannot be inversed analytically to obtain an expression of p_v according to p_l . To overcome this difficulty, an exponential expression is proposed in Eq. (2-28) and the functions $A(T)$ et $B(T)$ are identified by inverse analysis to respect the Kelvin-Laplace's law. Figure 2-15 shows the compatibility of the proposed relationship with the law's Kelvin-Laplace at different temperatures. In this figure, the points

are obtained by exact Kelvin-Laplace law while the circles are deduced from the proposed relationships.

$$p_v = A(T) \cdot \exp[B(T) \cdot p_l] \quad (2-28)$$

$$A(T) = A_0 \exp\left[\left(\frac{T - T_0}{\Delta T_{A1}}\right)^{k_1}\right] + A_1 \exp\left[-\left(\frac{T - T_{cal1}}{\Delta T_{A2}}\right)^2\right] \left[1 - \exp\left(-\frac{T - T_0}{\Delta T_{A3}}\right)\right] \quad (2-29)$$

$$B(T) = B_0 \left[1 + \left(\frac{T - T_0}{\Delta T_{B1}}\right)^2 + \left(\frac{T - T_0}{\Delta T_{B2}}\right)\right] \quad (2-30)$$

The parameters found in Eq. (2-29) and (2-30) are listed in the summary table of parameters (Table 2-5) at the end of this section 2.3.

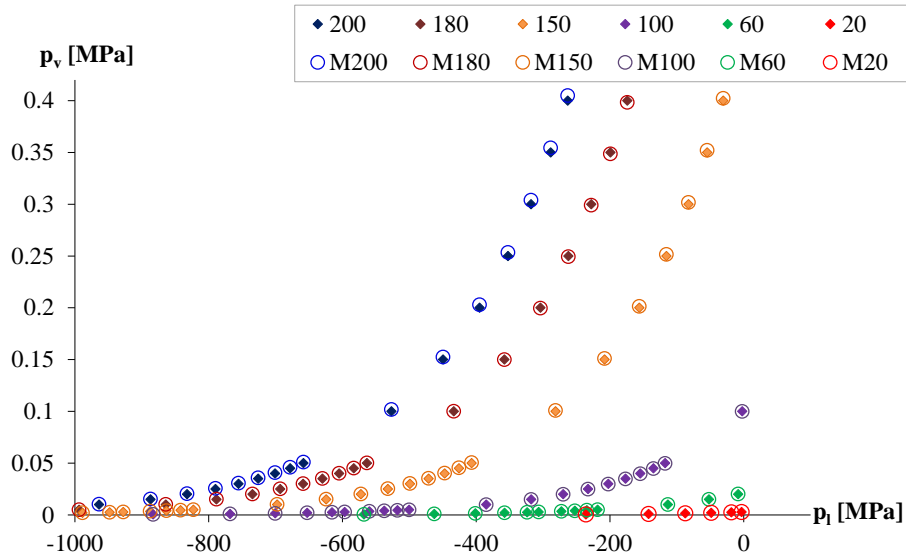


Figure 2-15: Comparison of relation $p_v(T, p_l)$ to the Kelvin-Laplace's law

2. 3. 1. 5. Heat and hydric balance equations and numerical implementation

The heat and hydric balance equations in Eq. (2-31) are derived from Eq. (2-20) using the two main variables, and the complementary assumption that the heat source due water evaporation-condensation is neglected compared to the heat flow due to the gradient of temperature: T and p_l .

$$\begin{cases} \rho(T) \cdot C(T) \cdot \frac{\partial T}{\partial t} = -\text{div}(-\lambda(T) \cdot \text{grad} T) \\ C_l(p_l, T) \frac{\partial p_l}{\partial t} = \text{div}(D(p_l, T) \cdot \text{grad} p_l) \end{cases} \quad (2-31)$$

The main advantage of this equation's set is that the Thermal problem is solved first, and next the liquid pressure problem can be solved using this last, this second problem can itself be solved with a nonlinear thermal analogy.

For unsaturated condition, according to Eq. (2-16) and the introduction of the functions in Eq. (2-25) and Eq. (2-28), the water mass balance equation can be rewritten using the mathematical deduction in a form of Eq. (2-31) with the following coefficients:

$$C_l = \left(\rho_l - \frac{p_v M_v}{RT} \right) \phi \frac{m_{vgn}}{1 - m_{vgn}} \frac{B}{m_{shr}} \frac{\rho_l RT}{M_v} \left[1 + \left(\frac{p_c}{m_{shr}} \right)^{\frac{1}{1 - m_{vgn}}} \right]^{-m_{vgn} - 1} \left(\frac{p_c}{m_{shr}} \right)^{\frac{m_{vgn}}{1 - m_{vgn}}} + \frac{\phi M_v}{RT} (1 - S_l) B p_v \quad (2-32)$$

$$D = \rho_l \frac{k_l}{\eta_l} k_{rl} + \frac{p_v M_v}{RT} \cdot \frac{k_g}{\eta_g} \cdot \left(k_{rg} + \frac{\Gamma}{p_v} \right) p_v B \quad (2-33)$$

The coefficient of diffusion thus highlights the sum of two terms associating the different modes of moisture transport. The first term relates to the moisture transport by Darcy in liquid form while the second relates to the diffusive transport of moisture in gaseous form. In this modelling, these two modes of moisture transfer are necessarily linked and active simultaneously.

For saturated condition, the obtained equation (2-23) keep the same form as Eq. (2-31) with the coefficients:

$$C_l = \frac{1}{M_l} \quad (2-34)$$

$$D = \frac{k_l}{\eta_l} \quad (2-35)$$

Therefore, the continuous description of the moisture transfer between saturated and unsaturated condition can be expressed in a single TH model (see Figure 2-16).

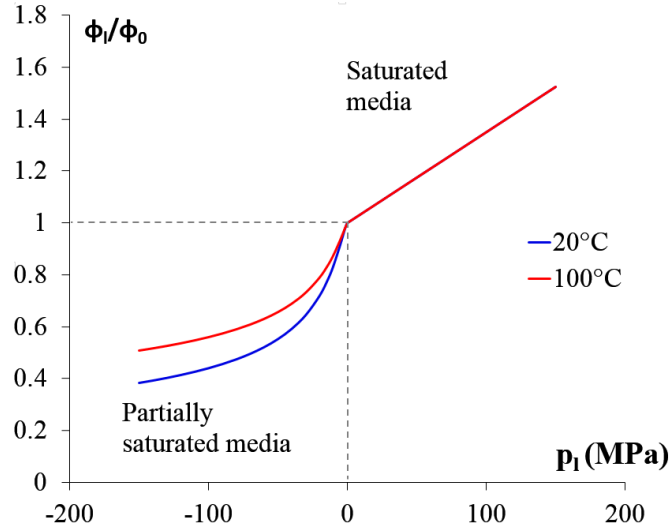


Figure 2-16: Continuous description of moisture diffusion for saturated-unsaturated media at 20°C and 100°C

The governing equations of the TH model are solved numerically by the finite element (FE) method for the discretization of the space domain. The following structures are simulated using the FE code Cast3M developed by the French Atomic Energy Agency (CEA, 2016). The model is implemented in a module written in object-oriented programming language named Gibiane and takes advantage of the Cast3M thermal and diffusion formulation for solving both balance equations, i.e. heat and water mass balance equations. A brief outline of the overall procedure for a thermo-hydric analysis is illustrated in Figure 2-17 where the state variables, i.e. temperature T and liquid pressure p_l , are resolved for every time step using the mid-point (theta) method since in unsaturated conditions the capacity and conductivity terms associated to the liquid pressure equation depend on this liquid pressure.

For validation purposes, the experimental campaign found in the literature is considered: a test of MAQBETH mock-up with a variation of temperature until 200°C performed by the French Atomic Energy Commission (CEA Saclay) (Ranc et al., 2003). It is presented in next section 2. 4.

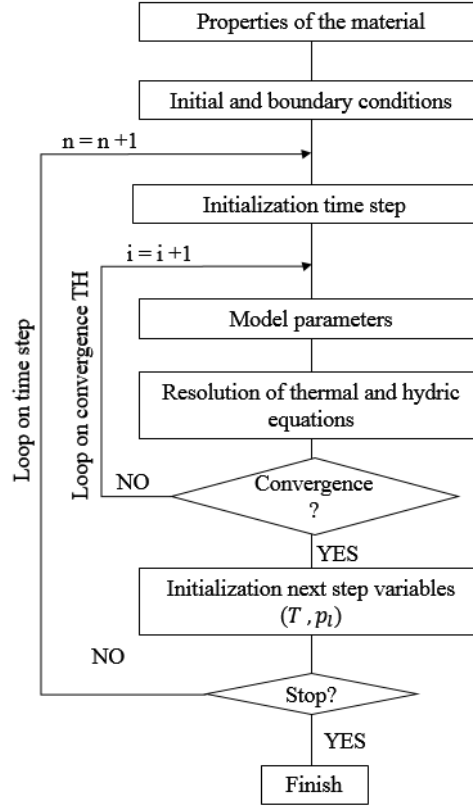


Figure 2-17: Outline of the thermo-hydric analysis

2. 3. 2. Evolution of thermal and hydric parameters

2. 3. 2. 1. Evolution of thermal properties of concrete

As presented previously in the literature review, the three main characteristics of concrete i.e. thermal conductivity, thermal capacity and density, have been represented by the empirical relations with only the value of characteristics at 20°C (DTU, 1987; Eurocode 2, 2004, etc.). Therefore, we propose in this work new expressions that are more generalised and able to describe the evolution from the referential characteristics of material measured at the referential temperature.

First, the thermal conductivity decreases with temperature. This is mainly attributed to the variation of thermal conductivity affected by the pastes. By a linear regression, the following equation was obtained to estimate the effect of temperature change on the thermal conductivity:

$$\lambda(T) = \lambda_{ref} \left(1 - 3.26 \times 10^{-3} (T - T_{ref}) \right) \quad (2-36)$$

With $\lambda_{ref} = 2.3 \text{ W} / \text{m.K}$ is thermal conductivity measured at $T_{ref} = 20^\circ \text{C}$ which is selected as a base. The proposed model represents the average of the existing data as illustrated in Figure 2-18(a).

Regarding the thermal capacity of concrete, we propose a linear function reproducing the same trend of (Eurocode 2, 2004): (see Figure 2-18(b))

$$C(T) = C_{ref} \left(1 - 6.65 \times 10^{-4} (T - T_{ref}) \right) \quad (2-37)$$

Where $C_{ref} = 913 \text{ J} / \text{kg.K}$ is measured at $T_{ref} = 20^\circ \text{C}$

Besides these properties, concrete density also decreases when the temperature rises, mainly due to the departure of water. An experimental function of concrete density was proposed by Eq. (2-38) using the experimental data of (Nguyen, 2013) where $\rho_{ref} = 2408 \text{ kg} / \text{m}^3$ is the concrete density measured at moderate temperature $T_{ref} = 20^\circ \text{C}$ (Figure 2-18(c)):

$$\rho(T) = \rho_{ref} \left(1 - 3.25 e^{-3} (T - T_{ref})^{1/2} \right) \quad (2-38)$$

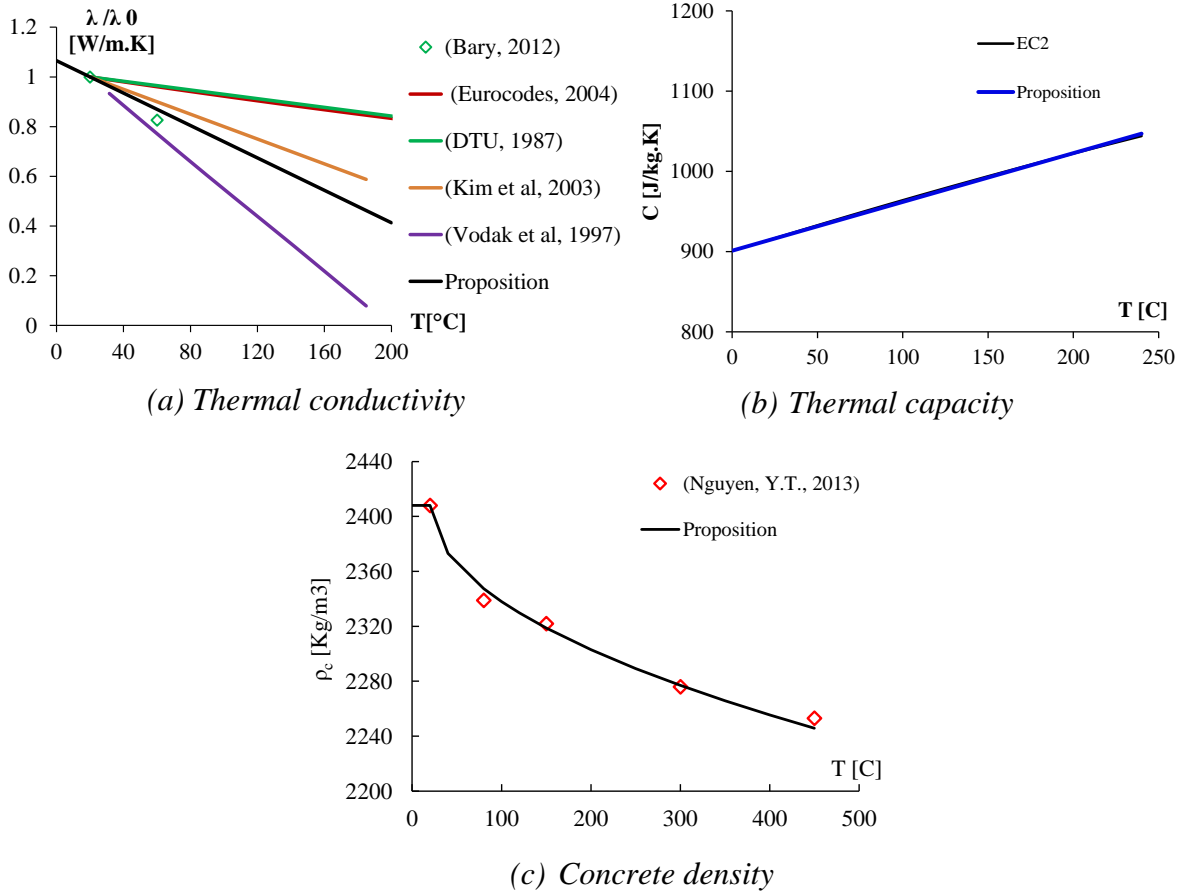


Figure 2-18: Dependence of thermal properties of concrete on temperature

2. 3. 2. 2. Evolution of water properties

a. Water density

Water plays an important role in the hydric transfer inside porous material like concrete. Due to thermal dilation, its density at ambient pressure decreases when the temperature rises. Ranznjevica (Raznjevic, 1970) proposed an expression (Eq. (2-39)) for its evolution versus temperature based on his experimental results (Figure 2-19) which is widely used in other recent studies (Hassen, 2006; Kanema, 2007; Nguyen, 2013) and will be used as well in this study.

$$\rho_l = 314.4 + 685.6 \left[1 - \left(\frac{T - 273.15}{374.14} \right)^{\frac{1}{0.55}} \right]^{0.55} \quad (2-39)$$

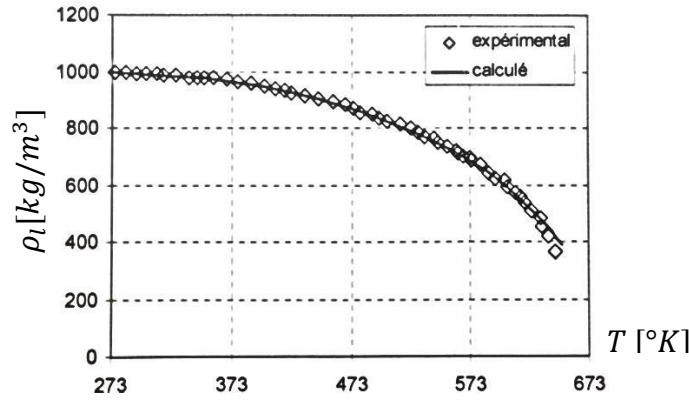


Figure 2-19: Water density Vs Temperature ((Raznjevic, 1970) cited by (Hassen, 2006))

b. Dynamic viscosity

A temperature-dependent parameter, liquid dynamic viscosity (η_l [Pa.s or kg/(m.s)]), can be modelled using the experimental data (Reid, 1987) by an empirical expression: Eq.(2-40) by Thomas and Sansom (1995) cited by (Hassen, 2006; Kanema, 2007; Stefano Dal Pont, 2004) or Eq. (2-41) by Bary et al. (2012). These two functions are able to reproduce the trend of experimental results as can be seen in Figure 2-20.

$$\eta_l(T) = 0.6612(T - 229)^{-1.562} \quad (2-40)$$

$$\eta_l(T) = 2.414 \times 10^5 \exp\left(\frac{570.58058}{T + 133.15}\right) \quad (2-41)$$

Furthermore, the dynamic viscosity of moist air, which depends upon the temperature and ratio of the dry air and gas pressures ($x = p_a/p_g$), using the data from (ASHRAE, 1993) cited by (Gawin et al., 1999), can be approximated using the following expression (Feraille Fresnet and Ehrlacher, 2000; Pierre PERROT, 1992) cited by (Stefano Dal Pont, 2004): (see Figure 2-21)

$$\eta_g(T) = 3.85 \times 10^{-8} \cdot T \quad (2-42)$$

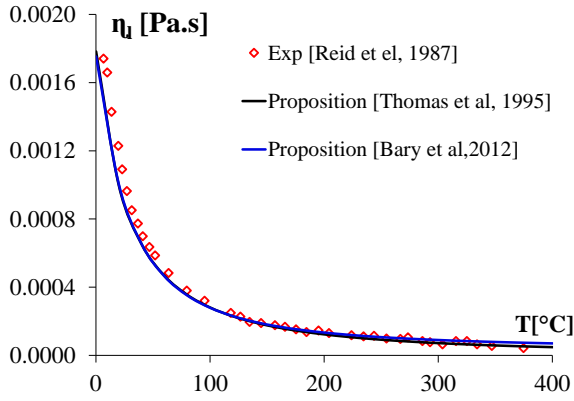


Figure 2-20: Liquid dynamic viscosity Vs Temperature

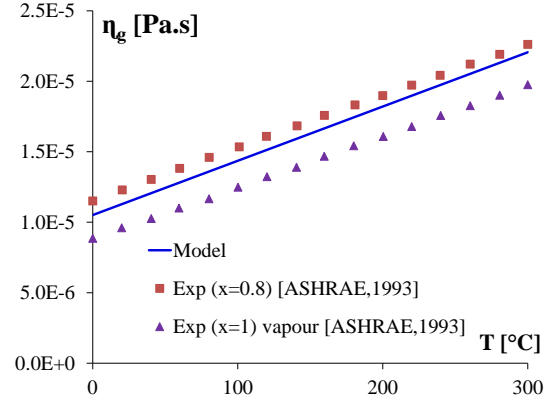


Figure 2-21: Gas dynamic viscosity Vs Temperature

c. Relative permeability

The relative permeability to liquid and to gas are used to take into account, for the unsaturated media, the fact that pores are partially filled by another phase. They are highly dependent on the liquid saturation of the porous media. Van Genuchten (van Genuchten, 1980) cited by (Stefano Dal Pont, 2004) proposed an analytical expression linking relative permeability to the saturation degree, based on the works of (Mualem, 1976). When the porous media become saturated ($S_l = 1$), the relative permeability k_{rl} and k_{rg} tend to 1 and 0 respectively.

$$k_{rg}(S_l) = (1 - S_l)^p \left(1 - S_l^{1/m}\right)^{2m} \quad (2-43)$$

$$k_{rl}(S_l) = S_l^q \left[1 - \left(1 - S_l^{1/m}\right)^m\right]^2 \quad (2-44)$$

With p, q are the material parameters and m is a parameter to be determined from the isothermal sorption or capillary pressure curve of the material at the ambient temperature.

Unlike gas permeability, a limited number of experimental studies on liquid water permeability of partially saturated cement paste are available due to the difficulty of measurement. According to (Li et al., 2015), the only available data dealing with water permeability of cement-based materials is found in the recent studies of (Kameche et al., 2014). Figure 2-22 illustrates the experimental results of relative permeability of gas measured by (KALLEL, 2016; Kameche et al., 2014; Monlouis-Bonnaire et al., 2004; Sogbossi, 2017) along with numerical models of (van Genuchten, 1980) for relative permeability of gas and liquid. According to an intensive study of the relative permeability to gas flow of cement-based materials, Monlouis-Bonnaire et al. (2004) have reported that for concrete k_{rg} decreases very rapidly with S_l . The first pores that are filled with water seem to have a significant effect on

the air transport through the material for cement-based materials, but this is not exactly the case for soils. The best values of exponent coefficients for the soils correspond to $p = 0.5$ and $m = 0.5$, while the adjusted values of Van Genuchten's relation for unsaturated Portland cement concrete correspond to $p = 2.5$ to 5.5 , which have been verified with the experimental results of concrete (Kameche et al., 2014; Monlouis-Bonnaire et al., 2004; Sogbossi, 2017). The chosen values for different types of concrete are listed in Table 2-3. However, there is a remarkable dispersion in the experimental results of (KALLEL, 2016) which worked on the same composition concrete than (Sogbossi, 2017) in project ENDE (another project in relation with this PIA, in which the LMDC is involved).

Therefore in this work, the value of p and q equal to 4.5 and 0.5 have been chosen according to (Sogbossi, 2017) and $m = 0.26$ has been also chosen for isothermal calibration at $20\text{ }^{\circ}\text{C}$ according to (Chen et al., 2012).

Table 2-3: Parameters for Van Genuchten's relation of relative permeability

Material	p	q	m	References
Soil	0.5	0.5	0.5	(van Genuchten, 1980; Mualem, 1976)
Cement concrete	3.5	0.5	0.5	(Kameche et al., 2014)
	4.5	0.5	0.5	(Sogbossi, 2017)
	5.5	0.5	0.56	(Monlouis-Bonnaire et al., 2004)

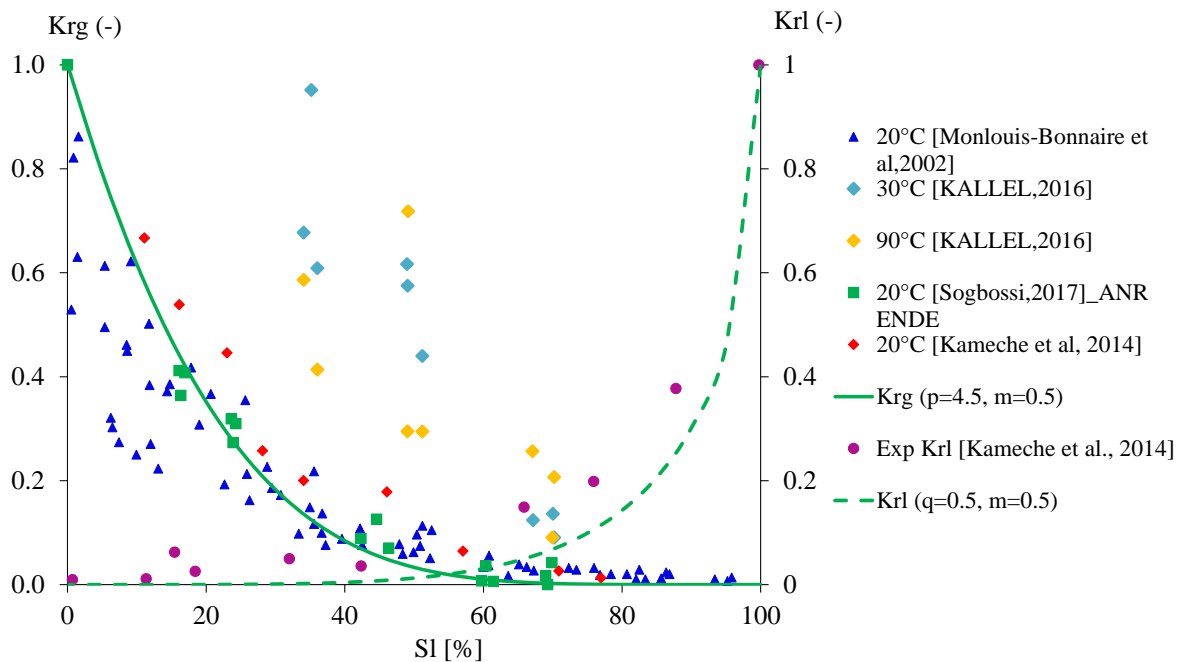


Figure 2-22: Relative permeability versus saturation degree (van Genuchten, 1980; KALLEL, 2016; Kameche et al., 2014; Monlouis-Bonnaire et al., 2004; Sogbossi, 2017)

d. Klinkenberg coefficient

The coefficient Γ , known as Klinkenberg constant (Klinkenberg, 1941), varies with the degree of saturation. Kameche et al. (2014) have reported using the experimental data on different size specimens that this coefficient decreases when the degree of saturation increases (see Figure 2-23). The evolution of Klinkenberg constant can be obtained using a linear regression:

$$[\text{Pa}] \quad \Gamma = 3.12 \times 10^5 (1 - S_l) \quad (2-45)$$

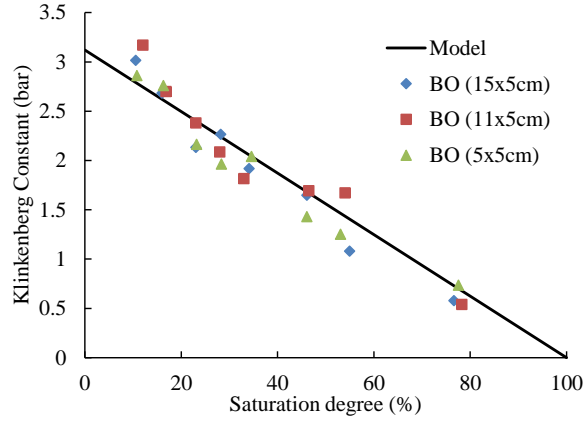


Figure 2-23: Evolution of Klinkenberg coefficient with saturation degree of concrete (Kameche et al., 2014)

e. Saturated vapour pressure

The saturated vapour pressure refers to the pressure of vapour when it is in equilibrium with the liquid phase. It is solely dependent on the temperature. As temperature rises, the saturation vapour pressure increases as well. In the literature review, there are many models proposed to estimate the evolution of saturated vapour pressure with temperature such as: a regulatory standard of (NF EN ISO 13788, 2013) by Eq. (2-46), model of (Raznjevic, 1970) by Eq. (2-47) for temperature lower than 374°C with a complementary model of (Ju, J. W. and Zhang, 1998) in Eq. (2-48) for higher temperature, cited by (Hassen, 2006) and model used in (Bary et al., 2012; Nguyen, 2013) by Eq. (2-49). The comparison of these models with the experimental measures by (KALLEL, 2016) at various temperatures has been plotted in Figure 2-24. The trend marked by these models are roughly the same and can reproduce the experimental data.

$$[Pa, K] \quad p_{vs}(T) = 610.5 \times \exp\left(\frac{17.269 \times T - 4717.03}{T - 35.85}\right) \quad (2-46)$$

$$[Pa, ^\circ C] \quad p_{vs}(T) = \exp\left(6.4075 + \frac{16.82669T}{228.73733 + T}\right) \quad (2-47)$$

$$[Pa, K] \quad p_{vs}(T) = p_{vs,Cr} \left[L_0 + L_1 \frac{T}{647.15} + L_2 \left(\frac{T}{647.15} \right)^2 \right] \quad (2-48)$$

With $L_0 = 15.74373327$, $L_1 = -34.17061978$, $L_2 = 19.31380707$ and $p_{vs,Cr} \approx 20792261.4 Pa$ is measured at the critical temperature (647.15K).

$$[Pa, ^\circ C] \quad p_{vs}(T) = p_{atm} \cdot \exp \left[\frac{40500}{R} \left(\frac{T - 100}{373.15(T + 273.15)} \right) \right] \quad (2-49)$$

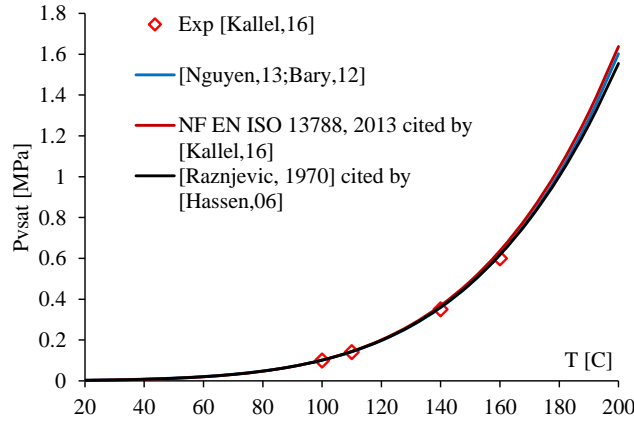


Figure 2-24: Saturated vapour pressure Vs Temperature

f. Summary of model and material parameters

Table 2-4: Main functions introduced for the simulation

Data	Expression	Eq.	Reference
Liquid water density	$\rho_l = 314.4 + 685.6 \left[1 - \left(\frac{T - 273.15}{374.14} \right)^{0.55} \right]^{0.55}$	(2-39)	(Raznjevic, 1970)
Klinkenberg coefficient	$\Gamma = \Gamma_0 (1 - S_l)$	(2-45)	(Kameche et al., 2014)
Vapour relative permeability	$k_{rg}(S_l) = (1 - S_l)^p \left(1 - S_l^{1/m_{vgn}} \right)^{2m_{vgn}}$	(2-43)	(van Genuchten, 1980)
Liquid relative permeability	$k_{rl}(S_l) = S_l^q \left[1 - \left(1 - S_l^{1/m_{vgn}} \right)^{m_{vgn}} \right]^2$	(2-44)	(van Genuchten, 1980)
Saturated vapour pressure	$p_{vs}(T) = p_{atm} \exp \left[\frac{40500}{R} \frac{(T - 373)}{373T} \right]$	(2-49)	(Bary et al., 2012; Nguyen, 2013)

Vapour dynamic viscosity	$\eta_g(T) = 3.85 \times 10^{-8} T$	(2-42)	(Feraille Fresnet and Ehrlacher, 2000; Pierre PERROT, 1992)
Liquid dynamic viscosity	$\eta_l(T) = 0.6612(T - 229)^{-1.562}$	(2-40)	(Thomas and Sansom, 1995)

Table 2-5: Intrinsic parameters of model

Data	Value	Data	Value
A_0	$28.65 \times 10^{-4} \text{ MPa}$	B_0	$7.4 \times 10^{-3} \text{ MPa}$
A_1	$-18.5 \times 10^{-3} \text{ MPa}$	ΔT_{B1}	384.7 K
k_A	0.653	ΔT_{B2}	-352.4 K
ΔT_{A1}	10.7 K	T_{kvgn}	313 K
ΔT_{A2}	19.66 K	M_v	0.018 Kg / mol
ΔT_{A3}	5 K	R	8.314 J / K.mol
T_{cal}	365.7 K		

Table 2-6: Material properties

Data	Value	Reference
Initial porosity ϕ	0.13	(EDF, 2014)
Constant of Van Genuchten m_{shr0}	10 MPa	(van Genuchten, 1980)
Isothermal exponent m_{vgn0}	0.26	(Chen et al., 2012)
Exponent of relative permeability to gas p	4.5	(Sogbossi, 2017)
Exponent of relative permeability to liquid q	0.5	(Monlouis-Bonnaire et al., 2004; Sogbossi, 2017)
Coefficient of Klinkenberg Γ_0	$3.12 \times 10^5 \text{ Pa}$	(Kameche et al., 2014)

Note: Index “0” represent the value measured at ambient temperature (20°C)

2. 4. Application on MAQBETH mock-up

2. 4. 1. Presentation of MAQBETH structure, mesh and boundary conditions

For validation purpose, the proposed TH model has been applied to the MAQBETH mock-up. A detailed comparison was made between simulation results and data from a large-scale reinforced concrete heating experiment performed by the French Atomic Energy Commission (CEA Saclay) (Ranc et al., 2003). The MAQBETH mock-up is a reinforced hollow concrete cylinder with an inner and outer diameter of 1 and 2.2 m, respectively, and a height of 3 m (see Figure 2-25). It is laid on a 60 mm thick wooden plate and its top is covered with a 200 mm thick insulator layer and a 30 mm thick wooden layer.

The simulation of the thermo-hydric behaviour of MAQBETH has been performed with a particular mesh for modelling the concrete structure. Indeed, significant gradients of the unknowns T and p_l arise near the structures surfaces during the thermal loading and these gradients require a fine mesh in the direction perpendicular to theses surfaces to achieve convergence and obtain an accurate solution, particularly for the water mass conservation equation. However, there is no gradient in the height of structure as its bottom and top are insulated. Therefore, the adopted TH mesh contains many elements in the thickness (see Figure 2-26 right).

Regarding the thermal boundary conditions, there is a heating source at the internal surface that is imposed by an evolution of temperature given in Figure 2-26 (left). For sake of realistic imposed initial conditions, the convection has been applied with a high value of exchange coefficient, allowing to achieve rapidly an equilibrium at the surface.

In term of hydric boundary conditions, as the state variable of model is p_l , it is handled internally in the program using the Kelvin-Laplace's law in order to respect at every time step p_v constant and equal to 2500 Pa. Besides, the optimal values of intrinsic permeability of gas and liquid for this concrete are $k_g = 1.5 \times 10^{-17} m^2$ and $k_l = 1 \times 10^{-19} m^2$, respectively.

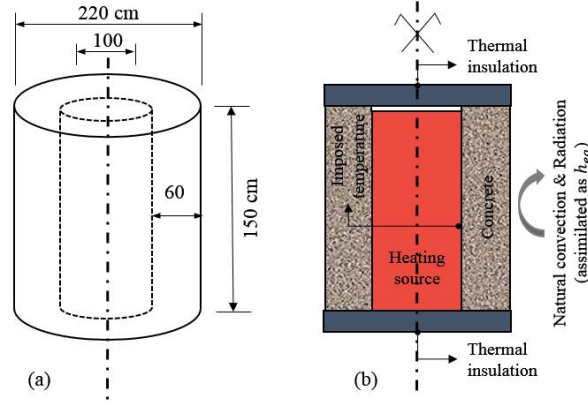


Figure 2-25: Geometrical characteristics of MAQBETH mock-up (half of concrete hollow cylinder) (a) and schematic description of experimental conditions (b) (Bary et al., 2012)

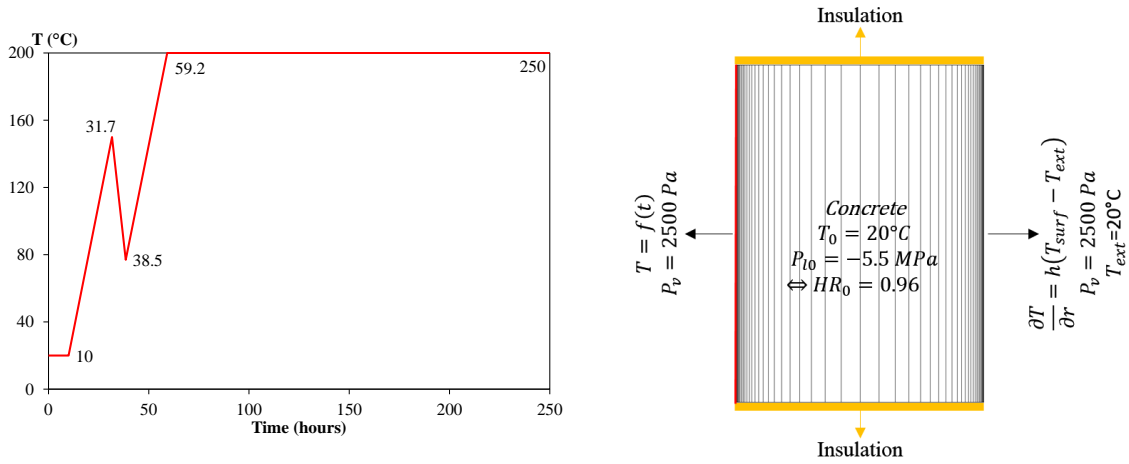


Figure 2-26: Thermal loading history on the inner surface (left) and initial conditions and boundary conditions applied to the 2D axial symmetric model (right) (Bary et al., 2012)

2. 4. 2. Numerical results

Figure 2-27, Figure 2-28 and Figure 2-29 illustrate the comparisons of the temperature, relative humidity, saturation degree and vapour pressure profiles obtained from the experiment and simulation at various times. On these figures, the distance $r = 0$ and $r = 0.6 \text{ m}$ correspond to the inner and outer surface of the structure, respectively. According to these satisfying confrontation, the global thermo-hydric behaviour of the structures is well reproduced by the model.

First, we observed that the model can reproduce the temperature evolutions inside the structure (see Figure 2-27).

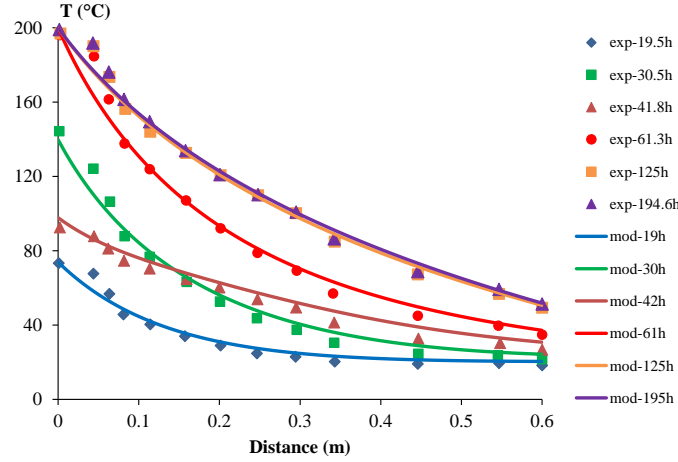


Figure 2-27: Comparison of radial temperature profiles at different times (hours) between the simulation (lines) and experimental measurements (symbols) (Bary et al., 2012)

The profiles of relative humidity given by the model are also in a good agreement with the experiments (Figure 2-28(a)). As the inner surface was heated up, the concrete near the inner surface started to dry out, with reducing moisture content and relative humidity. Meanwhile; the strong nonlinear dependence of moisture diffusivity on the relative humidity leads to a great reduction of the moisture diffusivity near the heated inner surface, consequently a strong gradient in the relative humidity (or equivalently the saturation degree) occurs near the heated surface (HR approaches 0), and a sharp gradient of relative humidity also exists over a short distance about 1-2 cm from the outer surface.

For the profiles of saturation degree on Figure 2-28(b), there is no experiment to compare, however we remind that the evolution of S_i in the heated zone is very sensitive due to a very abrupt front representing a strong variation of S_i in the temperature-dependent sorption curves of Figure 2-14 for $HR > 0.94$ (more details in section 2. 3. 1. 3). Such behaviour is problematic for the numerical modelling due to convergence difficulties and it requires a very fine mesh. The difference of the saturation profiles obtained by this model and from (Bary et al., 2012) can be mainly explained by the different temperature-dependent desorption curves.

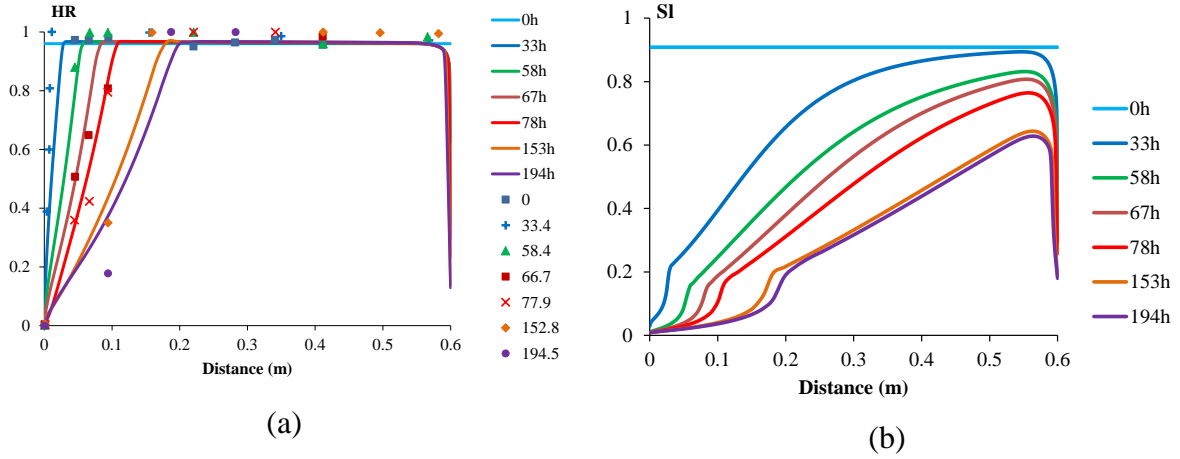


Figure 2-28: Comparison of radial relative humidity h_r (a) and liquid saturation S_l (b) profiles at different times (hours) between the simulation (lines) and experimental measurements (symbols) (Bary et al., 2012)

Moreover, the comparison of radial profiles of gas pressure (or vapour pressure) from the model and experiments on Figure 2-29 shows that the simulation globally reproduces the similar trend but underestimates the experimental data. If we focus on the experimental data at 25.1h and 41.7h for which temperature is less than 100 °C, the measured values of p_v are greater than the value of p_{vs} , which means that the media is completely saturated. In this case, the measures of p_v does not make sense because p_v does not exist for saturated condition. Whilst the numerical results of p_v present the value more coherent because the media is highly saturated but not yet fully saturated. Despite these, the experimental measures of p_v do not seem very precise because the data exhibit quite important deviations. After 60h of heating, the numerical results and the experimental ones are more in accordance.

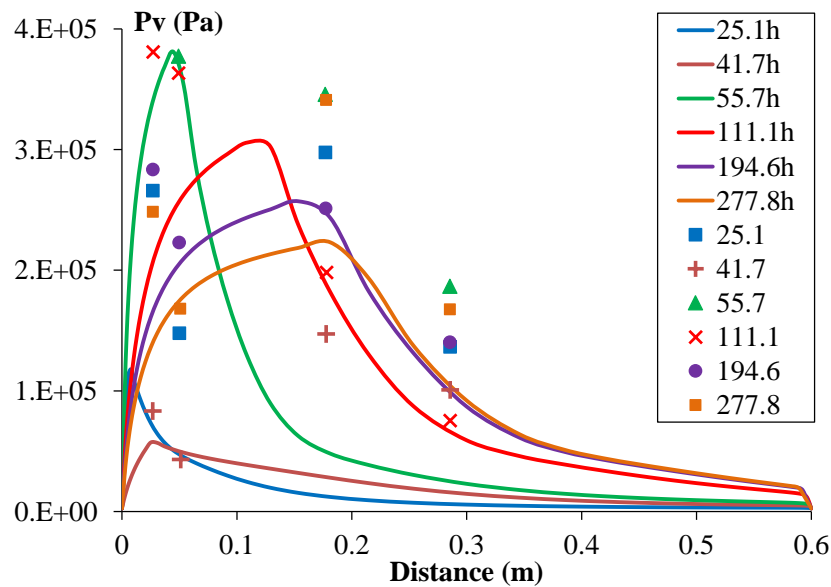


Figure 2-29: Comparison of radial gas pressure profiles p_v at different times (hours) between the simulation (lines) and experimental measurements (symbols) (Bary et al., 2012)

2. 4. 3. Parametrical studies on permeability

Permeability is an important indicator for the diffusion of pressure inside the material, but it is difficult to measure its real value despite a number of experimental campaigns. In the literature review, some studies (Dal Pont et al., 2005; Gawin et al., 2005a) assume that the intrinsic permeability is the same for both liquid and gas, whilst other studies (Bary et al., 2012; Coussy et al., 2001) distinguish between these values (cf. section 2. 2. 3. 3). The value of liquid permeability is found out to be lower than that of gas permeability. This part focuses on the parametrical studies of the parameters to see their sensitivity. The studied values of k_{g0} and k_{l0} are listed in Table 2-7. As mentioned in previous section, the optimal values of permeability for MAQBETH concrete are $k_g = 1.5 \times 10^{-17} m^2$ and $k_l = 1 \times 10^{-19} m^2$. Figure 2-30 compares the effects of k_g and k_l on the p_v results. It is observed that the decrease of gas or liquid permeability provokes an increase of vapour pressure because material with low permeability prevents the flow of fluids towards the exterior and then induces the condensation of vapour. Noted that gas permeability is more sensitive than liquid permeability.

Table 2-7: Different case studies of intrinsic permeability

Intrinsic permeability [m^2]	(a)	(b)	(c)	(d)
k_g	2×10^{-17}	1×10^{-17}	1.5×10^{-17}	1.5×10^{-17}
k_l	1×10^{-19}	1×10^{-19}	1.5×10^{-17}	1.5×10^{-20}

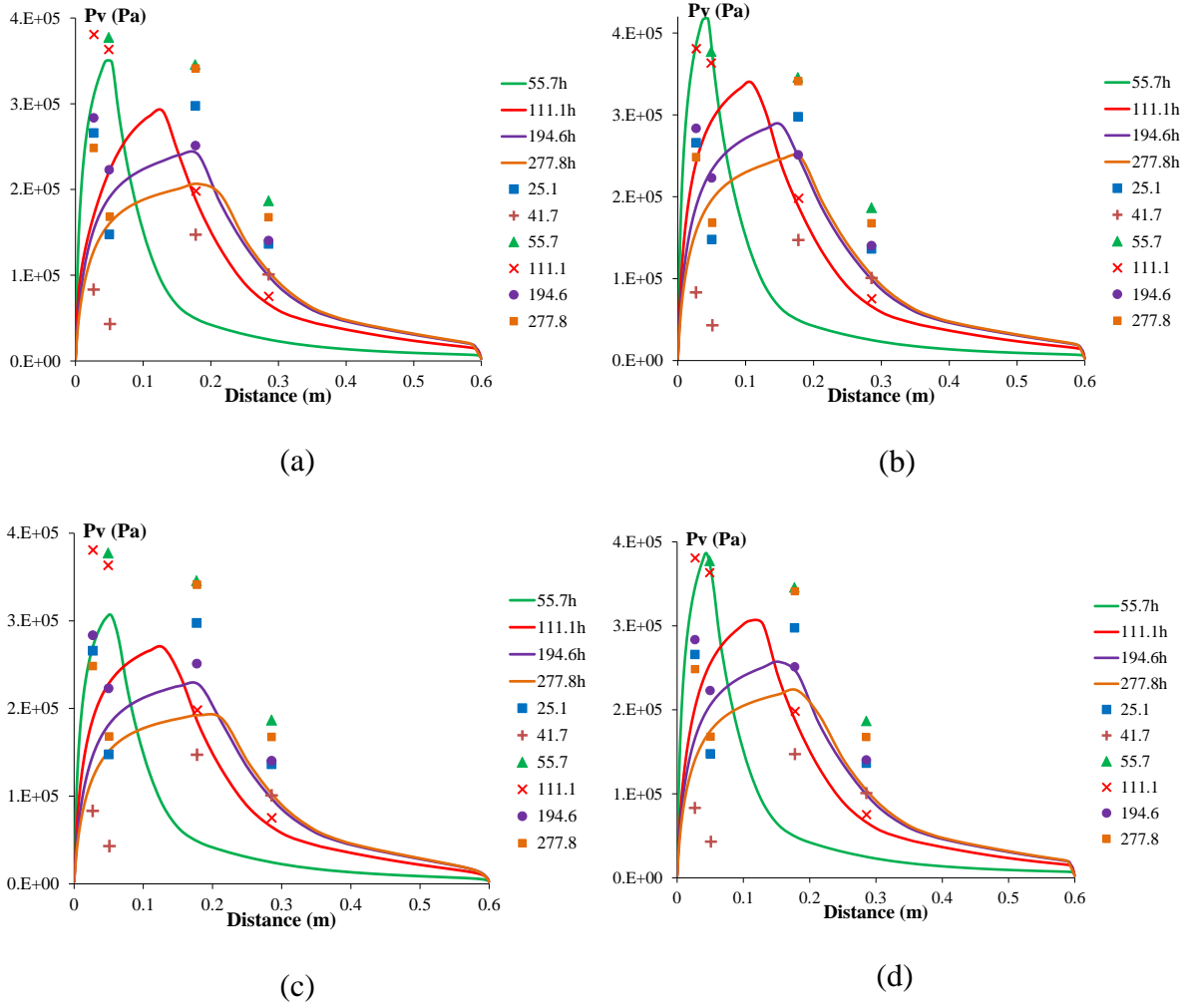


Figure 2-30: Comparison of k_g and k_l effects on p_v responses

2. 5. Conclusion

The simulations of the thermo-hydric behaviour of concrete structures subjected to heating can be carried out by means of a simplified coupled moisture and heat transfer model. This TH model is developed by considering the influence of temperature on the isotherm sorption curves and the continuous description of the saturated and unsaturated state of the material through a single state variable chosen as the liquid pressure. Moreover, it is suitable for the massive structure application to predict the temperature and moisture fields inside the massive structure thanks to a short computation time. It can be implemented in any finite element programmes. The comparison of simulations with experimental data in terms of profiles of temperature, relative humidity, saturation degree and gas pressure as a function of time and space illustrates, in general, a reasonable agreement, mainly when the high gradient of pressure near the heating surface is past.

We remark that the temperature-dependent sorption curves influence greatly the relative humidity and saturation degree, in particular for $HR > 0.94$ and high temperature. The

necessity of experimental data in this zone of isotherms are needed to improve the TH modelling. Moreover, the intrinsic permeability to gas and liquid are very important parameters of materials that need to be measured precisely for each concrete.

CHAPITRE III

Simulation of reinforced concrete behaviour under different THCM loadings

« Sous un bon gouvernement, la pauvreté est une honte ; sous un mauvais gouvernement, la richesses est aussi une honte. » Confucius

3. 1.	Introduction.....	74
3. 2.	State of the art	76
3. 2. 1.	Effect of hydration on mechanical behaviour of concrete	76
3. 2. 1. 1.	Mechanical threshold of cementitious materials at early age	76
3. 2. 1. 2.	Cracking at early age.....	77
3. 2. 2.	Effect of temperature and humidity on hardened concrete mechanical behaviour 79	
3. 2. 2. 1.	Effect on elastic modulus and Poisson coefficient.....	80
3. 2. 2. 2.	Effect on tensile strength.....	83
3. 2. 2. 3.	Effect on compressive strength	84
3. 2. 2. 4.	Effect on fracture energy	86
3. 2. 3.	Effect of temperature and humidity on delayed strains of concrete.....	88
3. 2. 3. 1.	Influence of temperature	90
3. 2. 3. 2.	Influence of water content.....	91
3. 2. 3. 3.	Thermal induced damage at material scale	92
3. 2. 4.	Creep modelling	93
3. 2. 5.	Crack modelling	94
3. 2. 5. 1.	Isotropic elastic damage model	95
3. 2. 5. 2.	Orthotropic damage model.....	96
3. 2. 6.	Influence of temperature on reinforcement behaviour.....	97
3. 2. 6. 1.	Reinforcement behaviour at high temperature	97
3. 2. 6. 2.	Bond behaviour of reinforcement-concrete at high temperature	99
3. 3.	Modelling of reinforced concrete at high temperature and humidity	104

3. 3. 1.	Presentation of concrete model at moderate temperature and humidity	104
3. 3. 1. 1.	Rheological model.....	104
3. 3. 1. 2.	Damage model.....	110
3. 3. 2.	Adaptation for large meshes of massive structures	113
3. 3. 3.	Adaptation for early age concrete	114
3. 3. 4.	Adaptation for concrete at high temperature and humidity.....	116
3. 3. 4. 1.	Effect of temperature and humidity on mechanical strength	116
3. 3. 4. 2.	Effect of temperature and humidity on damage variable	118
3. 3. 4. 3.	Behaviour law of concrete at high temperature	120
3. 3. 5.	Adaptation for reinforced concrete structure	121
3. 4.	Applications of MACENA experiments (LMDC, IPPRA, CERIB).....	126
3. 4. 1.	Formulation of VeRCoRs concrete	126
3. 4. 2.	Identification of model and material parameters.....	126
3. 4. 3.	Validation of new evolution laws with experiments	131
3. 4. 3. 1.	Instantaneous behaviour under effect of temperature and humidity	131
3. 4. 3. 2.	Delayed deformations in compression at moderate temperature	132
3. 4. 3. 3.	Delayed deformations in compression at high temperature	133
3. 4. 3. 4.	Delayed deformations in tension at high temperature.....	134
3. 5.	Conclusion	136

3. 1. Introduction

The material properties are negatively affected by the influence of high temperatures. Changes in the microstructure of concrete during a high-temperature exposure result in changes in mechanical and physical properties. Concrete behaviour at high temperature becomes a subject of concerns following the recent nuclear accidents in nuclear power plants (Chernobyl in 1986 and Fukushima in 2011). In the present work, the scenario of the loss-of-coolant accident (LOCA) leads to the rise of temperature up to 140 °C and pressure 5 bars, the degradation of prestressed-concrete containment could then be observed leading to cracking and possibly to radioactive leakages. The prediction of the structural behaviour during this type of loading is therefore crucial and can be possible only with a good understanding of the different mechanisms of damage and mechanical behaviours of concrete subjected to temperatures. Three main mechanisms of concrete damage at high temperatures can be classified at different levels:

- At the macroscopic level, the thermal gradient between the inner surface (subjected to heating due to the LOCA) and the outer surface of the structure creates the differential expansion by inducing differential stresses.
- At the mesoscopic level, the incompatibility of thermal expansion between cement paste and aggregates causes damages at the interface.
- At the microscopic level, physicochemical degradation such as dehydration of concrete alters the cement matrix. Moreover, at this scale, an increase of temperature to high values change the favourable effect capillary pressure in possible deleterious over pressure of vapour.

Within the framework of the ANR-PIA MACENA project, several phenomena are identified and studied for concrete subjected to different loads at high temperatures. Our work consists in developing behaviour laws for the delayed behaviour of concrete structures at high temperatures. Disregarding in a first time the structural and chemical modifications in the studied material, creep is already a complex phenomenon since it depends on five factors: creep kinetics, duration of the loading, stress level, temperature and hygrometric states (taking into account the drying effect and the dependence of creep kinetic on water saturation). Previous studies (Bazant et al., 2004; Cagnon, 2015; Ladaoui, 2010; Vidal et al., 2014) about the delayed behaviour of concrete have pointed out a significant increase of delayed strains with the temperature rise. The different analyses (Briffaut et al., 2012; Harmathy, 1967; Nguyen et al., 2017a; Sellier et al., 2016) have enabled the development of some creep laws which need to be calibrated based on experimental results. Therefore, the analysis of the concrete creep at high temperatures requires a good understanding of the physical phenomena observed from the experiments.

In order to model the delayed behaviour of the concrete during the temperature rise, it is necessary to know the influence of the temperature on the creep rate. The influence of temperature variation and loading rate on the behaviour of the concrete can be relatively complex, thus using incremental numerical models may be necessary to evaluate the delayed deformations of the concrete. The models have also to take into account the different observations from the experimental campaigns in the ANR-PIA MACENA project. The coupled phenomena can be modelled adapting the LMDC concrete model, built in the framework of poromechanics, to consider the effects of high temperature and humidity.

The objective of this chapter is to study the influence of the variation of temperature and humidity from casting to the LOCA (included) on the mechanical behaviour of concrete, the structural effects of reinforcement and to propose a method to consider these phenomena into the numerical model. The mechanical behaviour of early age concrete will thus be first recalled. Indeed, the aim of this work is to be able to predict the evolution of damage all along the structure life with continuity in this evolution for the early age to the LOCA. Concerning the effect of temperature and humidity variations during the LOCA, the experimental campaigns in the framework of MACENA were designed to assess these phenomena and are used in this study to adapt the existing model. For some of them, their comparisons with numerical results will allow validating our approach.

3. 2. State of the art

This section is the summary of the literature that has been identified addressing the general behaviour and pertinent mechanical properties of concrete and reinforcement materials under elevated temperature (up to 180°C) corresponding to LOCA induced conditions. As the model will be applied to reinforced concrete elements from early age until the LOCA, the section starts with a brief recall of the classical methods used to link the hydration state and the mechanical properties, next effects of temperature and moisture are given, followed by a review of damage theory to model effects of cracking. An overview of some important complementary phenomena concerning the reinforcement behaviour and the interaction of reinforcement with the concrete matrix closes the state of the art section.

3. 2. 1. Effect of hydration on mechanical behaviour of concrete

Hydration reactions play an important role at early-age when the rates of water consumption and of released heat are important and the tensile strength of the hardening material is low. The thermal and moisture variations caused by autogenous conditions during hydration resulted in the volume changes which under restraint may cause tensile stresses to develop. When these stresses are greater than the tensile strength of hardening material, there is a risk of cracking. Thus, the effect of hydration on the mechanical behaviour of concrete becomes crucial towards predicting early-age stresses and cracking risks assessment.

3. 2. 1. 1. *Mechanical threshold of cementitious materials at early age*

It is necessary to identify the early-age transition from fluid-to-solid of a cement-based material, which occurs at the setting time and is known as the **percolation threshold**. It involves a threshold of the degree of hydration (α_{thr}) below which the stiffness of the material can be neglected. According to (Stefan et al., 2010), the percolation threshold corresponds to the connectivity between the solid phases (considered to be the anhydrous cement and the hydrates) (see Figure 3-1). For high w/c ratio, an important quantity of hydration products is required to reach the percolation threshold (Figure 3-1A) while a small quantity of hydration products is needed when anhydrous grains are closer to each other in a cement paste with low w/c ratio (Figure 3-1B). These phenomena can be observed on the experimental results of Young's modulus evolution obtained by (Boumiz, 1995) for cement pastes of different w/c ratios using ultrasonic measurements (Figure 3-2). Thus, mechanical percolation threshold can be identified by monitoring the evolution of mechanical properties (Maia et al., 2012; Torrenti and Benboudjema, 2005).

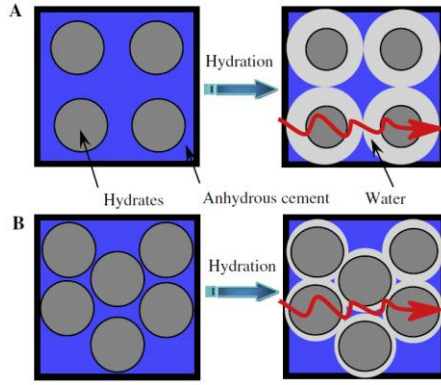


Figure 3-1: Scheme of percolation threshold during hydration (Stefan et al., 2010)

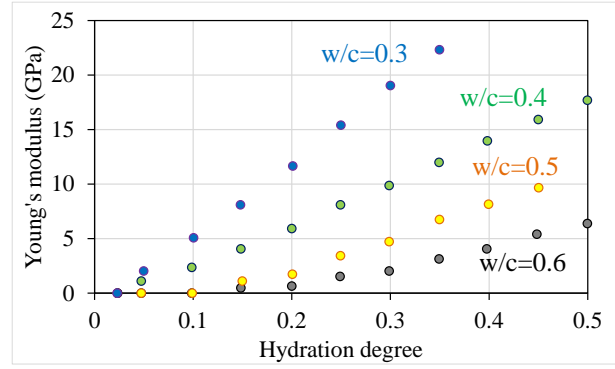


Figure 3-2: Evolution of Young's modulus with different w/c (experiment issued from (Boumiz, 1995))

For structural applications, the mechanical behaviour of concrete at early age can be expressed as a function of degree of reaction thanks to the De Schutter's evolution law (Schutter and Taerwe, 1996):

$$\frac{X(r)}{X(r=1)} = \left(\frac{r - r_0}{1 - r_0} \right)^a \quad (3-1)$$

With $X(r)$ strength at degree of reaction r , $X(r=1)$ strength at degree of reaction $r=1$, r_0 and a parameters. In this formulation, it is assumed that no strength development occurs below a certain value r_0 .

3. 2. 1. 2. Cracking at early age

Early age cracking can be appeared under the effects of two kind of stresses: the auto equilibrated stress system between surface and core due thermal gradient between core and surface during the heating period (exothermie of hydration reactions); and the stress induced by an external restraint that limit the global contraction of the concrete during the cooling phase. This external restraint is observed mainly on the sequential casting structures because the strains in the young concrete layer are restrained by the old concrete and tensile stresses arise (Benboudjema and Torrenti, 2008; Buffo-Lacarrière, 2007; CEOS.fr, 2016; Kolani, 2012). In this context, massive restrained shrinkage structures have been studied in the French national project CEOS.fr to understand the early-age cracking of this kind of structure (see Figure 3-3) (Buffo-Lacarrière et al., 2014). The evolution of instantaneous characteristics according to hydration development is shown in Figure 3-4.

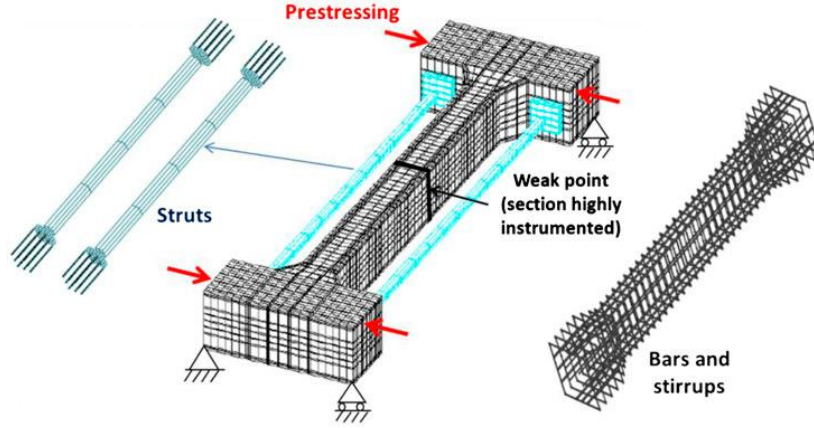


Figure 3-3: 3D mesh of restrained shrinkage structure RG8 (Buffo-Lacarrière et al., 2014)

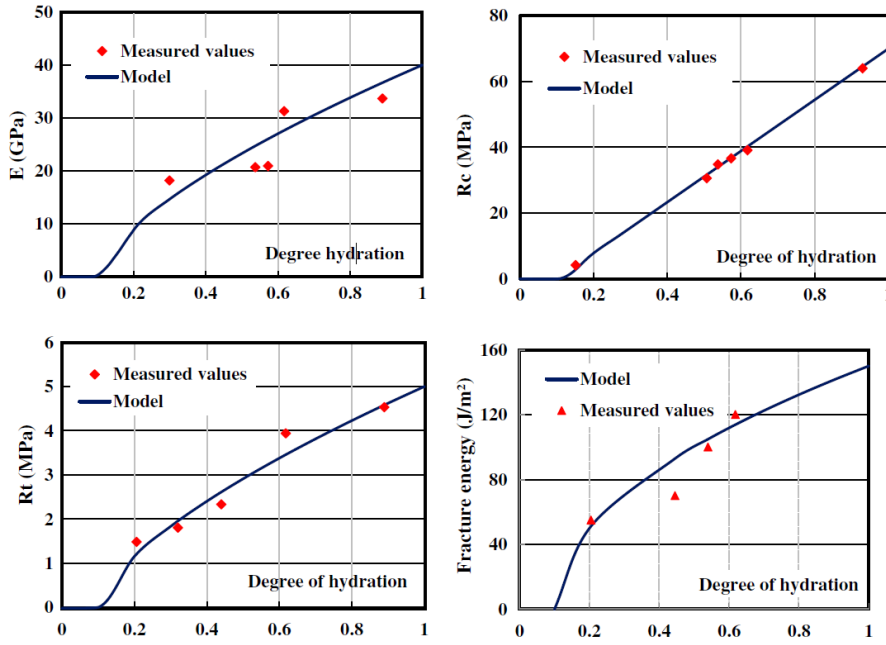


Figure 3-4: Evolution of instantaneous characteristics with hydration degree (Buffo-Lacarrière et al., 2014)

Figure 3-5 illustrates the evolution of damage in the structure for the heating phase (a) and the cooling phase (b). During heating phase, damage was developed at the extreme faces due to a flexion of the heads (under the effect of the dilation of the central part of the beam), whilst damage and cracking are localised at the central part during the cooling phase (due to the restraint of the contraction of the central part by the metallic struts). The cracks firstly occur at 70 h after casting at the central part of beam (Figure 3-6).

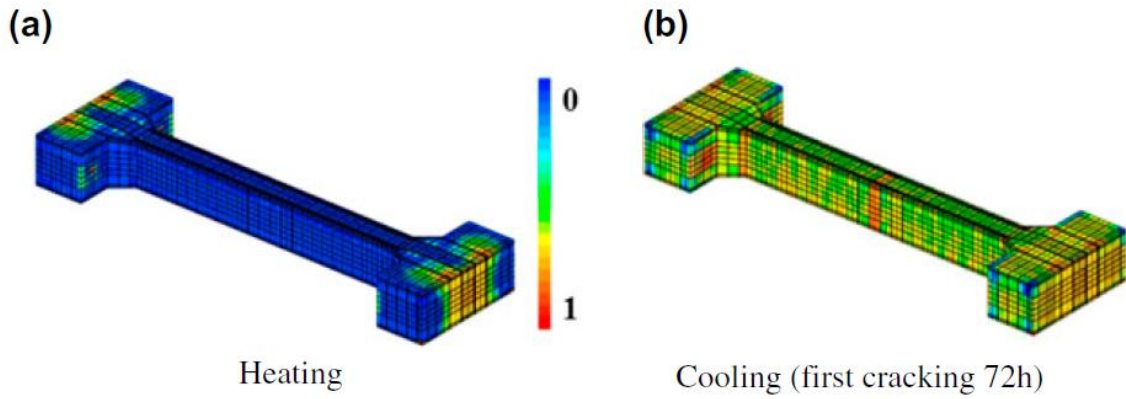


Figure 3-5: Damage field during heating and cooling phase (Buffo-Lacarrière et al., 2014)

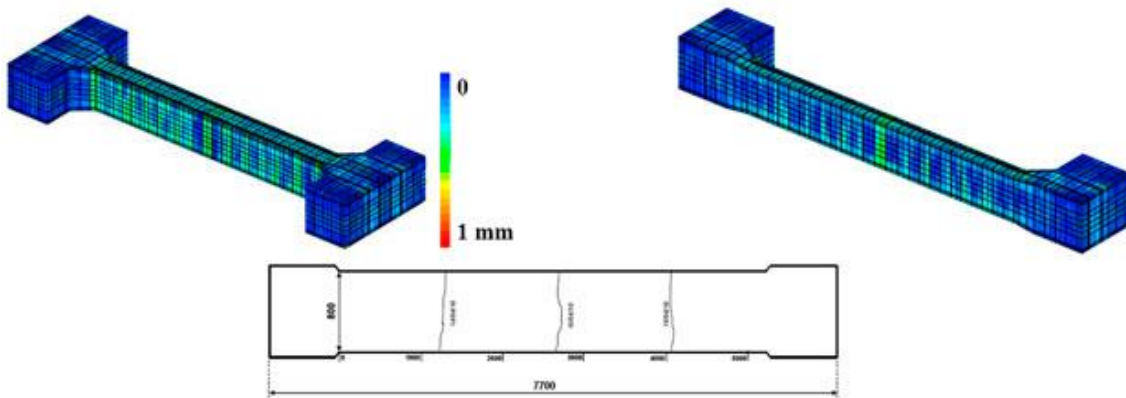


Figure 3-6: Crack pattern (Buffo-Lacarrière et al., 2014)

3. 2. 2. Effect of temperature and humidity on hardened concrete mechanical behaviour

The influence of temperature on mechanical properties of concrete has been widely studied (Abdel-Fattah and Hamoush, 1997; Bazant and Kaplan, 1996; Brue, 2009; Cagnon, 2015; Djaknoun et al., 2012; Felicetti and Gambarova, 1998; Hager, 2004a; Kalifa and Menneteau, 2000; Ladaoui, 2010; Mindeguia et al., 2012).

Most of that studies mention the effect of high temperature on concrete but few of them focus on the properties of concrete subjected to “lower elevated temperature” (from 20°C to 180°C) such as the thermal loading during the LOCA conditions. Under elevated-temperature, the Portland cement paste presents physical and chemical changes that contribute to the development of shrinkage, transient creep, and changes in mechanical properties. Non-linearity in concrete behaviour at high temperature depends on exposure conditions i.e. temperature-moisture-load-time regime. It has been reported that the mechanical properties of concrete are adversely affected by the elevated-temperature exposure (Bazant and Kaplan, 1996; Cülfik and Özturan, 2010; Diederichs et al., 1992; Felicetti and Gambarova, 1998; Hager, 2013; Kallel,

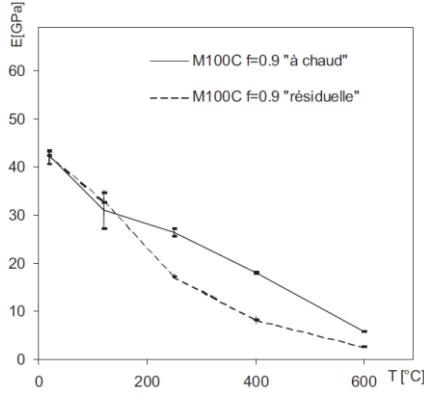
2016; Matsuzawa et al., 2016). However, quantitative interpretation of available data is difficult because test conditions can be very different.

The methods investigating the concrete properties at high temperature can be categorised by the cold or hot test. In cold testing, specimens are heated to a specified temperature, stabilised at that temperature for a prescribed period of time, gradually cooled to ambient temperature, and then tested to determine residual mechanical properties. While in hot testing, the mechanical measurements are conducted when the specimens are thermally stable at the specified temperature. During testing, specimens are maintained in either an open environment where moisture exchange occurs (unsealed) or a closed environment where moisture exchange is restricted (sealed). During heating or cooling, the specimens may be either loaded or unloaded. Mechanical properties in which the specimens have been permitted to return to ambient temperature prior to testing are referred to as residual properties.

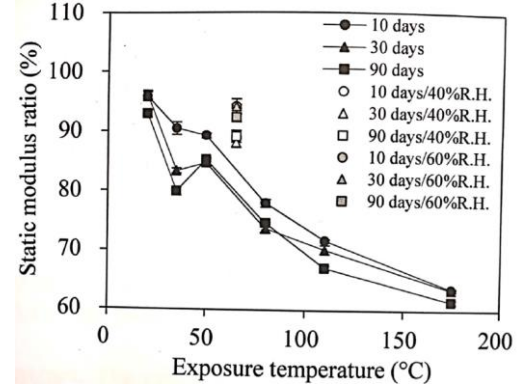
Furthermore, a variation of moisture content has a considerable effect on the mechanical properties of concrete (Brue, 2009; Burlion et al., 2005; Popovics, 1986; Shoukry et al., 2011; Zhang, 2011). Concrete that has been dried has the higher compressive strength and lower elastic modulus than concrete with a high moisture content taken from the same mix and subjected to an identical curing process, according to (Burlion et al., 2005; Li, 2004).

3. 2. 2. 1. Effect on elastic modulus and Poisson coefficient

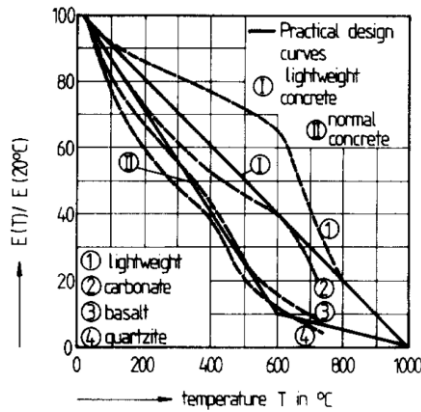
It has been reported in the literature that the elastic modulus decreases when the temperature increases (Hager, 2004b; Noumowé, 1995; Pimienta, 1999; Sa, 2007; Schneider, 1988). This phenomenon exists in both cold and hot testing (see Figure 3-7(a), (b)) for any type of aggregates (Figure 3-7(c)) and it becomes predominant for rapid heating (Gross, 1973). But in these tests (contrary to the ones issued from (Kallel, 2016) presented in Figure 3-7(d), it is difficult to distinguish the only effect of temperature from the one of drying induced by the heating.



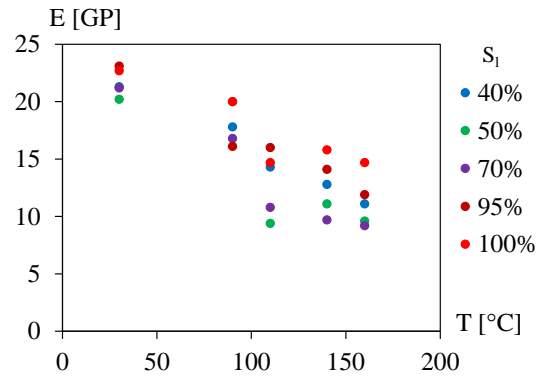
(a) (Hager, 2004b)



(b) (Matsuzawa et al., 2016)



(c) (Schneider, 1988)



(d) (Kallel, 2016)

Figure 3-7: Evolution of (residual) elastic modulus according to the temperature

The measurements of the elastic modulus of concrete under the control of saturation degree are still limited in the literature. (Shoukry et al., 2011) has investigated the variation of elastic modulus with a degree of saturation at ambient temperature. Recently, an experiment in the framework of ANR-PIA MACENA research project has been carried out to study the influence of saturation degree on the behaviour of concrete at various temperatures i.e. elastic modulus, strength and fracture energy (Kallel, 2016). The evolution of the ratio of elastic modulus with saturation degree is treated in Figure 3-8 where the elastic modulus measured at the saturated condition is selected as a base. We observe that the evolution of the elastic modulus fluctuates with the degree of saturation, which globally follows a constant linear trend. It is thus assumed the degree of saturation has a moderate impact on the elastic modulus.

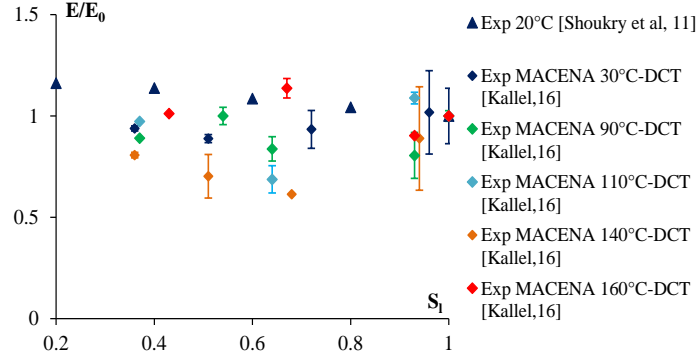


Figure 3-8: Evolution of elastic modulus with saturation degree (Kallel, 2016; Shoukry et al., 2011)

Indeed, there is only few literature focused on the evolution of Poisson coefficient with temperature. (Marechal, 1972) has shown that Poisson coefficient decreases at high-temperature because of the rupture of the internal bonds in the microstructures and the development of micro-cracking during heating (Figure 3-9(b)). According to Shoukry (Shoukry et al., 2011), the effect of both temperature and moisture on Poisson's ratio seemed to be negligible after the concrete had cured, as shown in Figure 3-9(a),(c). The value of Poisson coefficient is generally close to 0.2 for concrete.

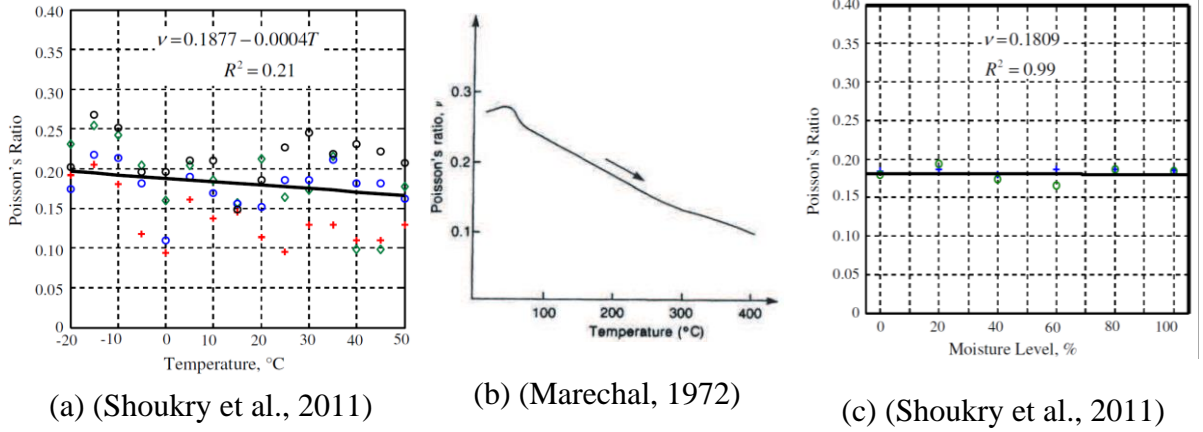
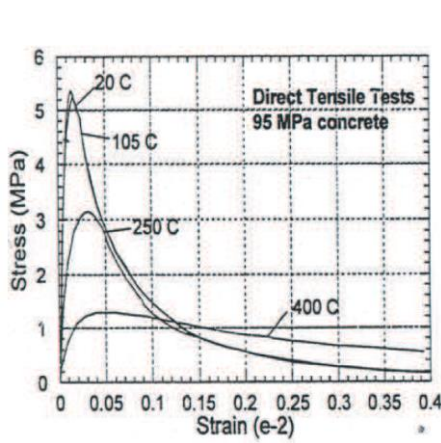


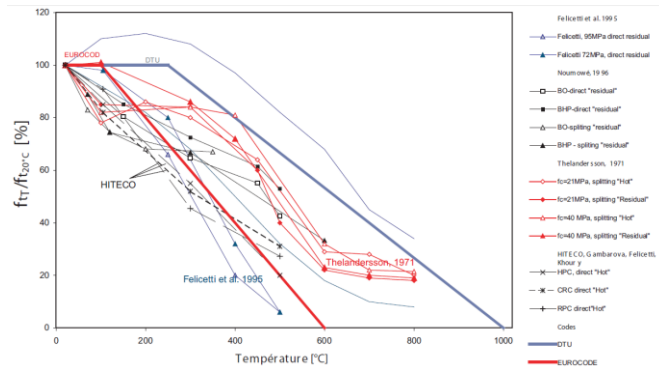
Figure 3-9: Evolution of Poisson coefficient with temperature and moisture content

3. 2. 2. 2. Effect on tensile strength

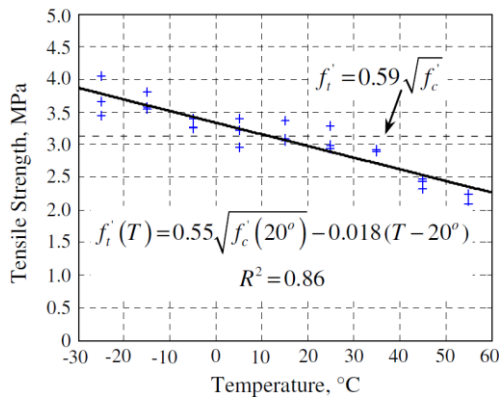
Measurement of tensile strength at high temperature is more complex than the measurement for compression. According to (Felecitti and Gambarova, 1999), the tensile stress-strain curves are affected by the temperature especially from 250°C (Figure 3-10(a)). The mechanical degradation is found to be more severe for concrete at 250°C, mainly associated with transport of evaporable water and accelerated hydration during heating. The pic of tensile strength moves slightly until 105°C but it drops significantly after 250°C. Moreover (Pimienta, 1999) has plotted the works relative to the evolution of tensile strength with temperature from different kinds of tests (hot, cold, direct tensile, splitting test...) in the same graph and we observe the general trend of tensile strength that declines with temperature (Figure 3-10(b, c)).



(a) (Felecitti and Gambarova, 1999)



(b) (Pimienta, 1999)



(c) (Shoukry et al., 2011)

Figure 3-10: Evolution of tensile strength with temperature

Similarly, concrete specimens were found stronger at lower degrees of saturation as shown in Figure 3-11(a) according to (Shoukry et al., 2011). The strength increase due to drying mechanism can be explained as a consequence of both developed capillary forces and confinement effect of the core of specimen by the auto-equilibrated stress system due to drying

of the surface (Burlion et al., 2005; Pihlajavaara, 1974; Popovics, 1986). The first phenomenon is the capillary suction effect that leads to an almost isotropic compression of the solid skeleton, consequently material behaves like a prestressed concrete of higher strength. The second phenomenon is relative to hydrous gradients which occur and involve a contraction of the external part of the sample as well as a confinement of samples inside the body (Bartlett and MacGregor, 1994). This confining lateral pressure will then induce an increase of strength in the perpendicular direction, the sample is self-reinforced. This is also in a good agreement with the recent experimental campaigns in the framework of ANR MOSAIC project (Bucher et al., 2016) on three-point and four-point bending tests of concrete at 20°C under various degrees of saturation and experimental results of DCT tests on concrete at 30°C and 90°C under various degrees of saturation in the framework of ANR PIA-MACENA project (Kallel, 2016) (Figure 3-11(b)). Therefore, it is observed that the tensile strength increases when the material is dry, but this effect is less pronounced on the material subjected simultaneously to the elevated temperature.

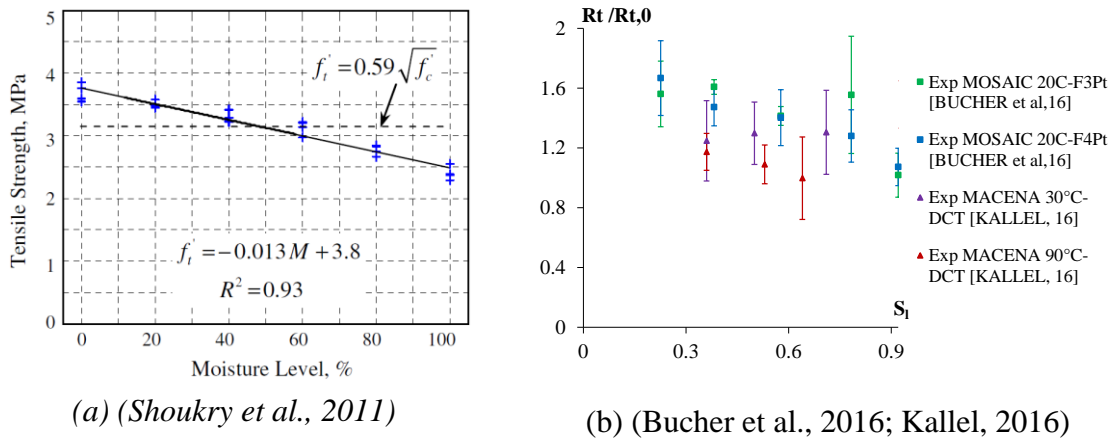
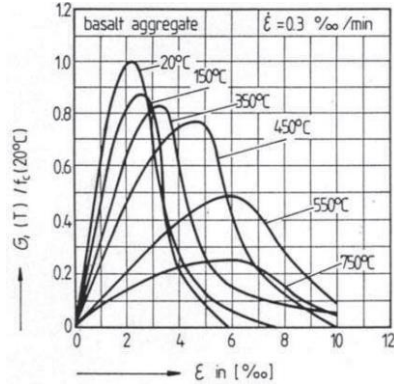


Figure 3-11: Evolution of tensile strength with moisture levels

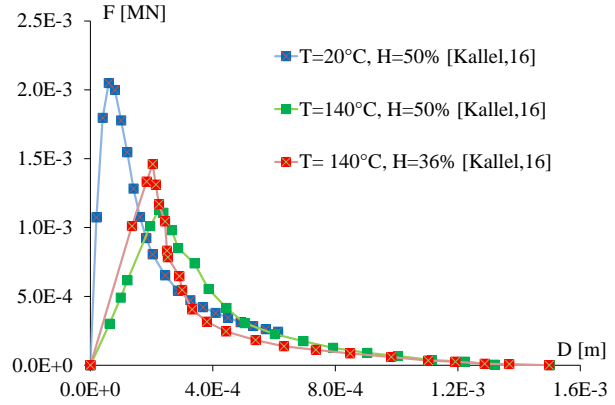
3. 2. 2. 3. Effect on compressive strength

Previous studies indicated that concrete would permanently lose its compressive strength when the temperature rises. According to the compressive stress-strain curves of (Schneider, 1988) in Figure 3-12(a) and the force-displacement curves of (Kallel, 2016) on Figure 3-12(b) at various temperatures, we observe a decrease in the rigidity of the material during the rise in temperature due to the decrease in the elastic modulus and compressive strength. Moreover, (Harada et al., 1972) who worked on hot and cool testing found out that the compressive strengths from the hot testing were greater than the residual strengths and they decrease when temperature rises (Figure 3-12(c)). Furthermore, the data in Figure 3-12(d) indicate that increasing the concrete temperature by 60°C results in decrease the compressive strength by 23% (Shoukry et al., 2011) which is in agreement with (Lawson et al., 2000; Phan and Carino, 2003) who reported that concrete loses up to 50% of its compressive strength as the temperature

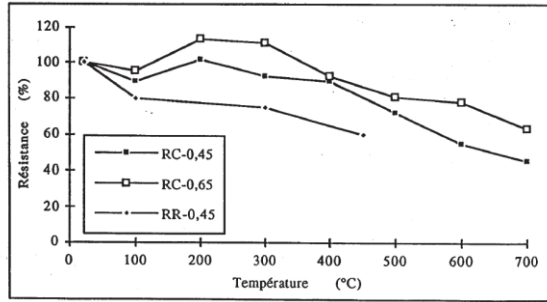
increases by 100°C. This phenomenon can be seen also in Figure 3-12(e), (f) from (Mindess et al., 2002) and (Matsuzawa et al., 2016) respectively. This was attributed to the formation of shrinkage cracks when concrete is exposed to hot dry conditions.



(a) Compressive stress-strain curves at different temperatures (Schneider, 1988)

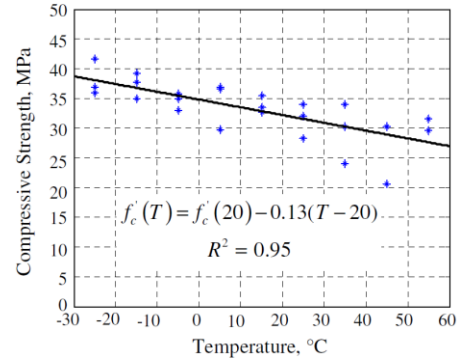


(b) (Kallel, 2016)

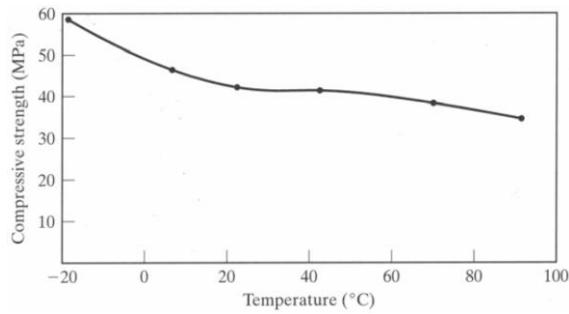


RC-0,45 ==> Résistance à chaud d'un béton avec E/C= 0,45
RC-0,65 ==> Résistance à chaud d'un béton avec E/C= 0,65
RR-0,45 ==> Résistance résiduelle du béton avec E/C= 0,45

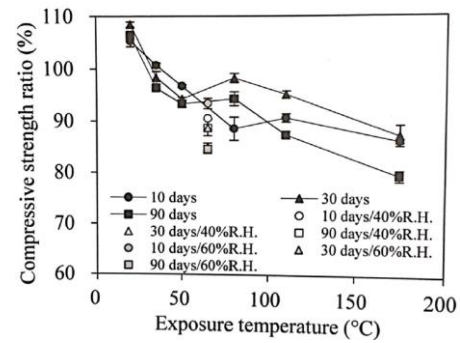
(c) (Harada et al., 1972)



(d) (Shoukry et al., 2011)



(e) (Mindess et al., 2002)



(f) (Matsuzawa et al., 2016)

Figure 3-12: Evolution of residual compressive strength with temperatures

Furthermore, concrete specimens were found slightly stronger at lower degrees of saturation as shown in Figure 3-13 (Shoukry et al., 2011).

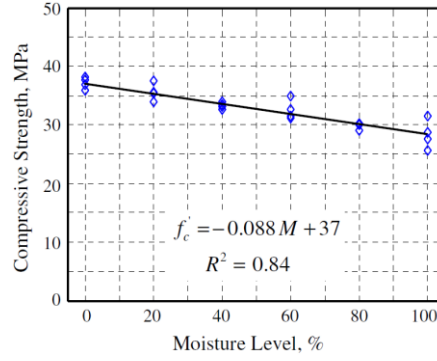
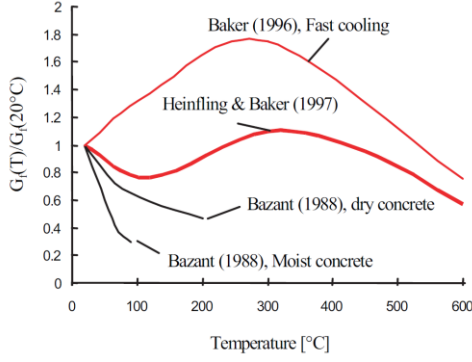


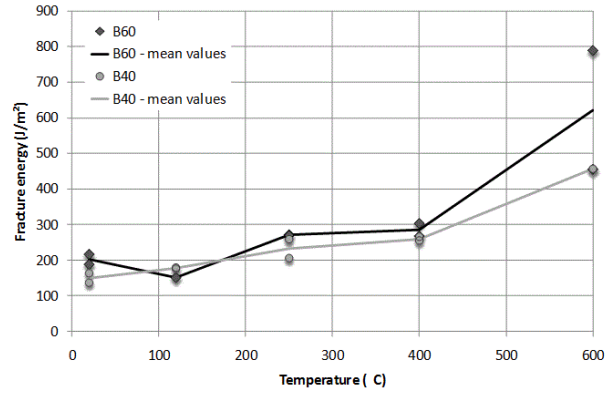
Figure 3-13: Evolution of residual compressive strength with moisture levels (Shoukry et al., 2011)

3. 2. 2. 4. Effect on fracture energy

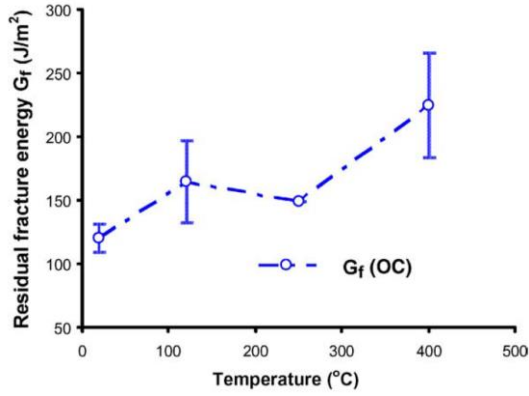
There is no consensus on the variation of fracture energy with temperature in the literature (see Figure 3-14(a)) for instance, it increases with temperature according to (Baker, 1996; Carré and Pimienta, 2012; Kallel, 2016; Menou et al., 2006)(see Figure 3-14(b,c,d)) which is a contrast to (Bazant and Prat, 1988). (Menou et al., 2006) has carried out an investigation on the cement paste, mortar and concrete specimens using the three-point bending test after heating/cooling cycles (Figure 3-14(c)). He also explained the main mechanism responsible for the observed increase in the fracture energy is the thermal damage making the crack surface more tortuous going around the aggregates rather than through them. This indicates that the ductility of concrete increases as temperature increases.



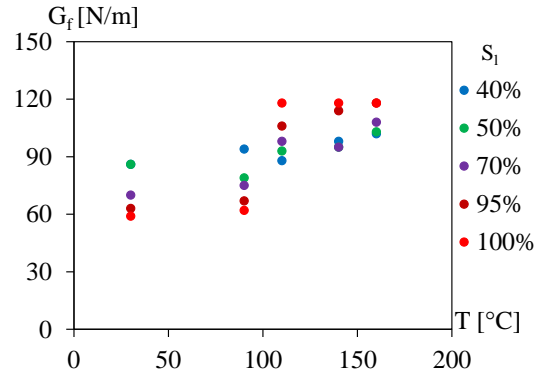
(a) (Bazant and Prat, 1988;
HEINFLING, 1998; Marechal, 1972)
cited by (Sa, 2007)



(b) (Carré and Pimienta, 2012)



(c) (Menou et al., 2006)



(d) (Kallel, 2016)

Figure 3-14: Evolution of fracture energy according to the temperature

In a literature review, very few studies focused on both temperature and humidity conditions. (Bazant and Prat, 1988) studied the fracture energy of concrete in dry and saturated conditions and at different temperatures (under 200°C) (Figure 3-14(a)). Some other works are available but the experiments were not performed under homogeneous water content conditions. Recently (Kallel, 2016) has investigated the mechanical behaviour of concrete under homogeneous conditions of moisture and temperature in the framework of MACENA project. The experimental works were carried out on DCT (Disk-shaped Compact Tension) sample at 30, 90, 110 and 140°C and with different levels of degree of liquid water saturation between 36 and 100%. Figure 3-15 illustrates the evolution of the ratio of fracture energy with saturation degree where the fracture energy measured at the saturated condition is selected as a base. Noted that the method of determination of (Kallel, 2016) is particular because all the mechanical proprieties are obtained from the same DCT test using inverse analysis. Moreover, it is difficult to define, for these DCT tests at elevated temperature, a real humidity at the crack front which is believed greater than other area of specimen.

(Bazant and Prat, 1988; Kallel, 2016) explained that the fracture energy for dry concrete is greater than for moist concrete due to the capillary pressure which increases as the degree of saturation decreases. This induces local compressive stresses between the pores, then the propagation of cracks is harder and greater energy is necessary for the creation of cracks. But there is still no exact explanation of an increase of the fracture energy with the degree of saturation for temperature higher than 110°C. This seems relative to the departure of free water at this temperature but also to a possible beginning of dehydration of some hydrates such as C-S-H (Wang, 2016).

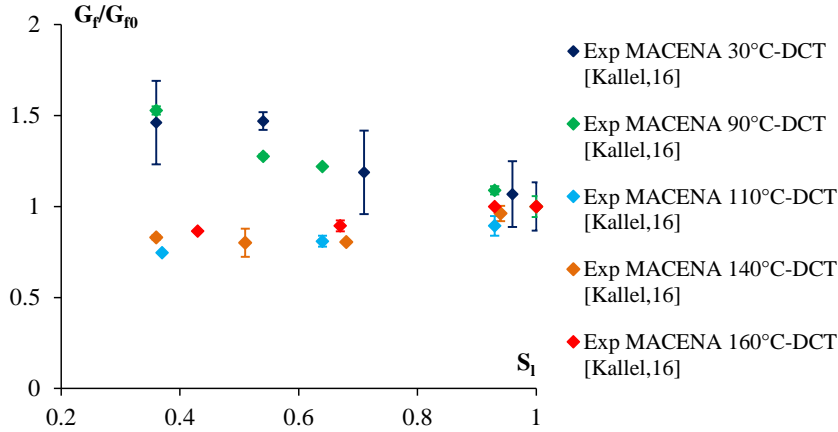


Figure 3-15: Evolution of fracture energy with saturation degree (Kallel, 2016)

3. 2. 3. Effect of temperature and humidity on delayed strains of concrete

Deformations due to creep and shrinkage are normally several times greater than elastic deformations in concrete structures. These deformations frequently cause excessive cracking and deflections or possible failure in serviceability, durability and long-term safety of massive concrete structures like nuclear containment buildings. In the scientific literature, many efforts have tried incessantly to study creep and shrinkage phenomena especially for concrete structures under variable environmental conditions. When a structure is subjected to elevated temperature, most of the delayed strains illustrated in (Figure 3-16) are significantly affected, so the failure of assessment of these strains would lead to a large error in stresses.

The negative strain measured on a load-free concrete specimen is called *shrinkage*, which is distinguished into two types depending on its exposure to the environment. For a sealed concrete specimen, the shrinkage occurring in the absence of moisture exchange due to the hydration reactions taking place inside the cement paste is termed *autogenous shrinkage*. Shrinkage occurring in a specimen that has moisture exchange with the environment is called *drying shrinkage*. Besides these, creep strain represents the time-dependent increase in strain under sustained constant load taking place after the initial strain at loading. The creep strain is also subdivided into *drying and basic creep* for a drying and a non-drying component respectively. The delayed behaviour of concrete in terms of shrinkage and creep of concrete is

influenced by several factors such as concrete mixture, volumes and properties of aggregates, ambient conditions (temperature and moisture), stress, shape and size of the specimen, construction procedures. The effects of these factors are analysed in detail in the document (ACI Committee 209, 2005). Undertaking the study of the delayed behaviour of concrete related to thermo-hygrometric solicitations seems to be a challenge. However, the shrinkage and creep analysis have been gradually progressed thanks to experimental results.

The experimental setup for basic creep tests (Figure 3-16) can be varied with the investigators but the process is generally as follows: the concrete specimens were unmoulded one day after casting and were cured under water at ambient temperature during long variable duration over three months minimum. This long water curing aims to prevent the influence of capillary depression, and the coupling of hydration and self-desiccation with basic creep. To limit the desiccation, the specimens are sealed by three layers of waterproof adhesive aluminium and covered in a waterproof plastic film. Concrete samples are then placed in the test device and then heated until satisfied temperature, leading to thermal dilatation. When they are thermally stabilised in the whole sample the load corresponding to 30% or 60% of the compressive strength is applied and the instantaneous deformation is also measured. This moment is taken as the origin of the creep. Simultaneously, other identical samples placed in another device are used to measure the shrinkage at the same temperature. This complement measure of shrinkage is used to deduce only the creep.

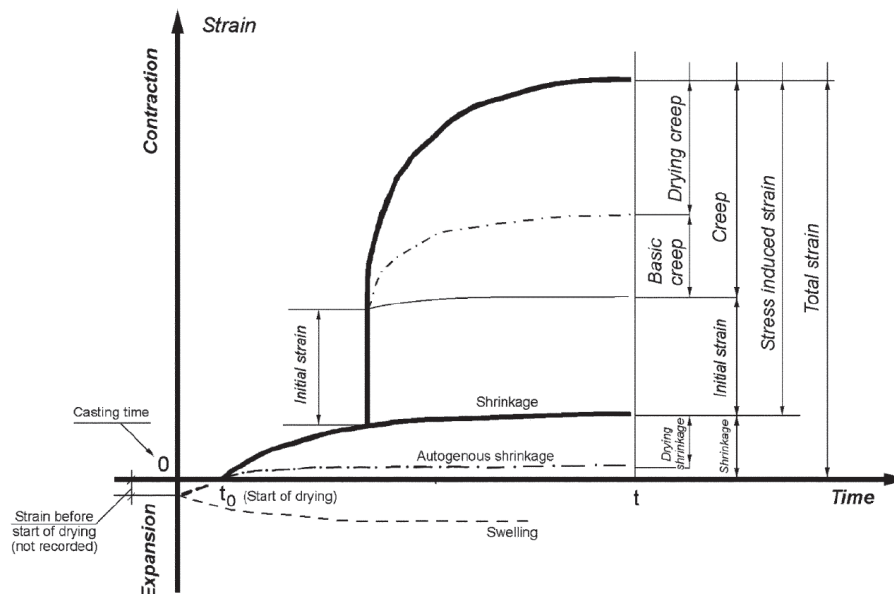


Figure 3-16: Scheme of various time-dependent strains of concrete (ACI Committee 209, 2005)

3. 2. 3. 1. Influence of temperature

It has been reported that the temperature rise increases the amplitude and velocity of the delayed strains based on the ANDRA experimental campaign of creep tests (Cagnon, 2015; Ladaoui, 2010). It has been pointed out an increase of specific basic creep deformation with the temperature rise, as shown in Figure 3-17, the basic creep can be multiplied by a factor 2.5 at 50°C and factor 7 at 80°C. The coupling between creep and heating can lead to damage and to transient thermal creep (Cagnon, 2015). Moreover, based on the recent investigations of ANR-PIA MACENA project in the context of safety and durability of nuclear containment during LOCA conditions, (Nguyen et al., 2017a, 2017b) has conducted an experimental campaign of concrete creep at different temperatures (20°C, 40°C and 70°C) at LMDC and (Daval, 2016) has also conducted the creep tests at higher temperatures (100°C and 180°C) at CERIB. The influence of temperature on creep behaviour of concrete can be observed clearly in Figure 3-18 and Figure 3-19, which illustrates the evolution of specific basic creep under compressive tests at 20°C, 40°C and 70°C and the evolution of basic creep under tensile tests at 20°C, 100°C and 180°C, respectively.

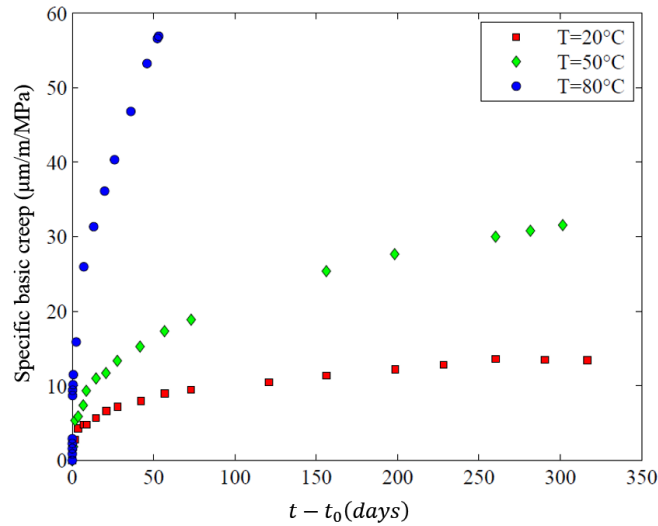


Figure 3-17: Evolution of time dependent specific basic creep of concrete at different temperatures (20°C, 50°C and 80°C) under uniaxial compression test of (Ladaoui, 2010)

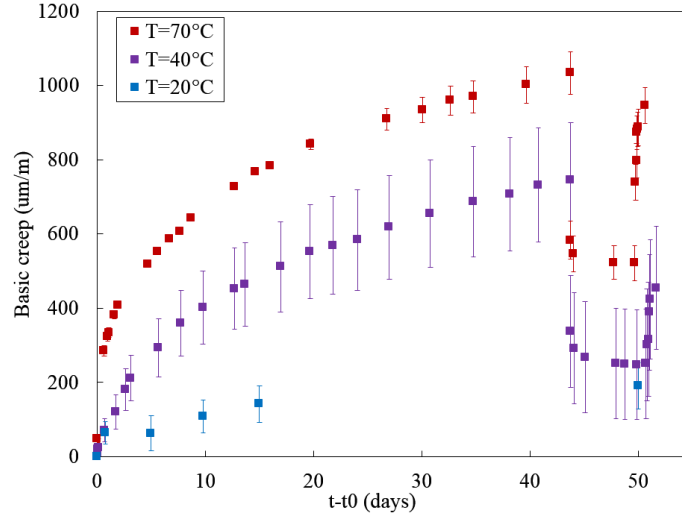


Figure 3-18: Evolution of time dependent basic creep of concrete at different temperatures (20°C, 40°C and 70°C) under uniaxial compression (15 MPa applied after heating) at LMDC in MACENA project (Nguyen et al., 2017b)

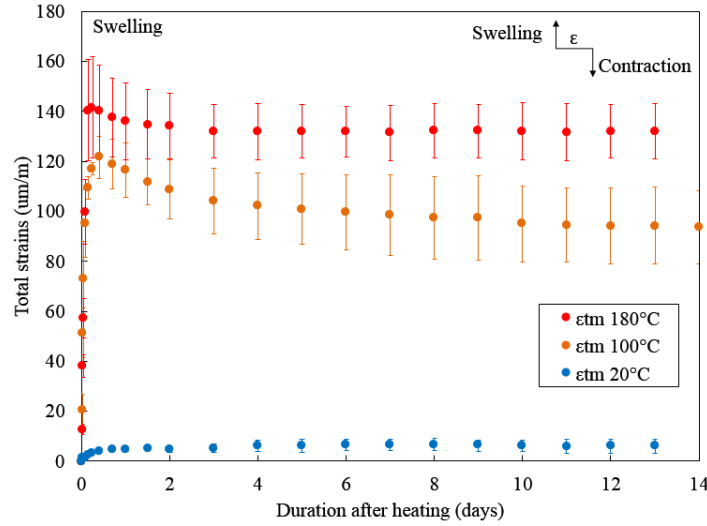


Figure 3-19: Evolution of time dependent basic creep of concrete at different temperatures (20°C, 100°C and 180°C) under uniaxial tension (13.5 MPa applied after heating) at CERIB in MACENA project (Daval, 2016)

3. 2. 3. 2. Influence of water content

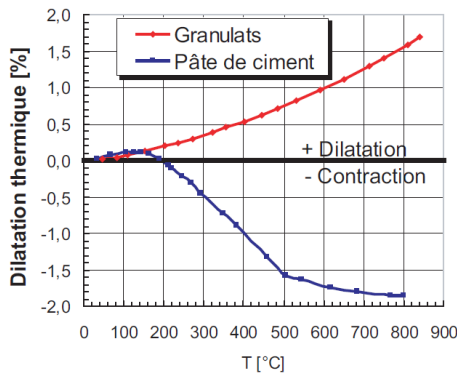
Water has a significant influence on the performance of concrete as it contributes, since an early age to later age, to the properties of concrete such as mechanical strength and elastic modulus (Hover, 2011; Yao and Wei, 2014) and plays an important role in concrete creep (Frech-Baronet et al., 2017; He and Qian, 2011; Tamtsia and Beaudoin, 2000; Wittmann, 1970). The moisture change in concrete with surrounding ambient is generally represented by internal relative humidity or degree of saturation. The magnitude of creep and shrinkage deformation is believed to depend on the water content of concrete. It has been investigated

that the creep deformation decreases linearly when the internal relative humidity increases (He and Qian, 2011) and it is the same case for shrinkage (Jiang et al., 2005).

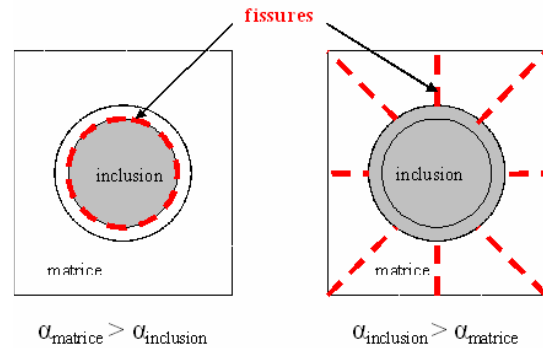
According to (Bazant et al., 1976), the acceleration of creep due to a change in lower relative humidity (<50%) is smaller and extends for a longer period than it does at higher relative humidity (>50%). Furthermore, water effect on C-S-H interlayer cohesion and disjoining forces is sensitive to the water saturation degree as explained in (Bazant et al., 1976; Jennings et al., 2013; Vandamme et al., 2013).

3. 2. 3. 3. Thermal induced damage at material scale

The increase of temperature at a structural scale can induce macroscopic damage by thermal gradient for instance. This kind of “structural” effect is generally assessed by a thermos-mechanical modelling of the structure and does not imply modification of the mechanical properties at material scale. But even at this scale (mesoscopic scale), the temperature can causes damage due to differential thermal dilation between the phases of concrete. Indeed, cement paste and aggregate are characterised by distinct values of the coefficient of thermal expansion (Figure 3-20(a)). It results in the restrained deformation for temperature up to 150°C and micro-cracks occur. For higher temperature range, only the expansion of aggregates is the main cause for the expansion of concrete despite the contraction of cement paste due to its dehydration (Bazant and Kaplan, 1996). This mechanism can be explained by the model of the spherical inclusion of (Hettema, 1996). The tangential cracks develop at the interface by incoherence between the matrix (cement paste) and the inclusion (aggregate) for temperature range up to 150°C, while the radial cracks generate within the cement paste for higher temperature range (Figure 3-20(b)). The more heterogeneous the material is, the more the thermal expansion values for the cement paste and aggregate differ (Menou, 2004). These coefficients vary with the temperature and the type of constituents used (Diederichs et al., 1992).



(a) (Castellote et al., 2004)



(b) (Hettema, 1996)

Figure 3-20: Incompatibility of thermal deformation of cement paste and aggregates

3.2.4. Creep modelling

The mechanisms of concrete creep have been widely studied in the literature (Benboudjema, 2002; Jordaán and Illston, 1969; Rossi et al., 2013; Sellier and Buffo-Lacarrière, 2009; Ulm and Acker, 1998), but here only the most common phenomena of creep is presented. Basic creep of concrete is provoked by two physical processes with different kinetics, the short-term micro-diffusion of water between capillary pores and the long-term sliding of C-S-H sheets (Figure 3-21). At short term, the stress is transmitted to water adsorbed in the intrinsic porosity of the hydrates, which migrates to the capillary pores due to capillary tensions. This contraction provokes a deformation of the solid skeleton. At long term, it concerns the irreversible mechanism of C-S-H sheet sliding.

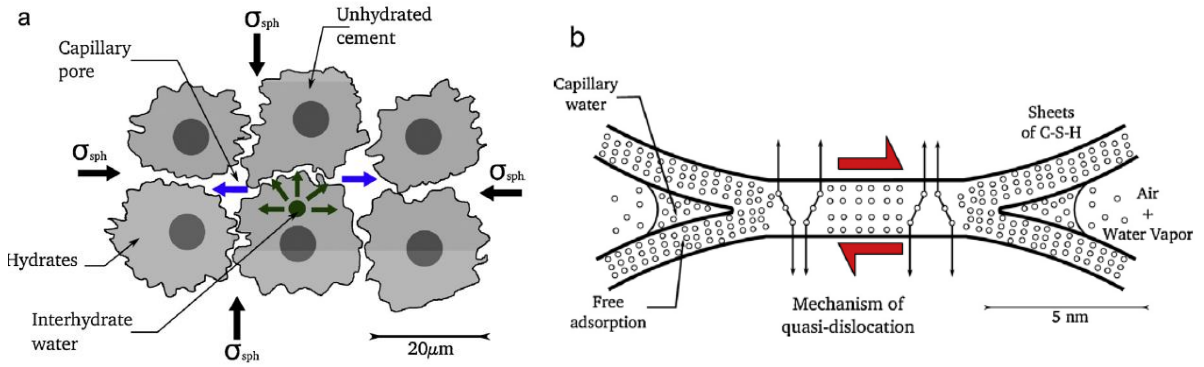


Figure 3-21: Mechanisms of basic creep (a) short-term micro-diffusion of water and (b) sliding of C-S-H sheets (Ulm and Acker, 1998)

In term of creep modelling, these two mechanisms have been considered through the spherical and deviatoric part of the stress tensor (Benboudjema et al., 2001; Sellier and Buffo-Lacarrière, 2009; Ulm and Coussy, 1998). The total strains are the sum of an elasto-damaged strain ε_e and a (basic) creep ε_{cr} (Eq. (3-2)). And creep strains are split into reversible and irreversible and then into their spherical and deviatoric strains (Eq. (3-3)). So the state variables of the creep model are $\varepsilon_{cr}^{sr}, \varepsilon_{cr}^{si}, \varepsilon_{cr}^{dr}, \varepsilon_{cr}^{di}$ corresponding to spherical reversible, spherical irreversible, deviatoric reversible and deviatoric irreversible strain tensors, respectively.

$$\varepsilon = \varepsilon_e + \varepsilon_{cr} \quad (3-2)$$

$$\varepsilon_{cr} = \varepsilon_{cr}^{sr} + \varepsilon_{cr}^{si} + \varepsilon_{cr}^{dr} + \varepsilon_{cr}^{di} \quad (3-3)$$

This basic creep model has been improved by (Buffo-Lacarrière, 2007; Hilaire et al., 2014) to adapt to the concrete at an early age by linking to the degree of hydration.

Under the drying condition, loaded concrete specimens present the drying creep which is greater than the sum of drying shrinkage and basic creep. (Bazant and Chern, 1985) proposed to model the drying creep using the Maxwell module in which the viscosity depends on relative

humidity. Then (Benboudjema, 2002) replace the Maxwell module by the Kelvin-Voigt module in which the visco-elastic characteristics depend on the water content variation speed within the material. Even if these models consider a complementary creep due to the variation of relative humidity they cannot be considered as a real coupling between shrinkage and creep because they used a chaining of independent models: shrinkage + basic creep + drying creep. Therefore, a rheological model developed at LMDC (Sellier et al., 2016) has been chosen for this study as it allows to couple these deformations into a single model. This model will be presented in the next paragraph.

3. 2. 5. Crack modelling

The crack of concrete is modelled in the framework of continuum mechanics. Damage theory has been initially introduced by (Kachanov, 1958) who focused on the rupture phenomena induced by creep. This notion was later generalised using the thermodynamic principle of irreversible processes by (Lemaitre and Chaboche, 1985) who reported that damage origin occurs in the creation of cavities in the material, which come along with plastic phenomena. For geomaterial like concrete, the damage theory is usually applied until failure, which comprises the stage of void nucleation, as in the original theory of Kachanov, and the void coalescence until apparition of macro-cracks (see Figure 3-22). Accordingly, numerous damage models have been developed to describe the crack opening based on strain extension phenomena (strain softening character of geomaterial) (La Borderie et al., 2007; Mazars, 1986; Pijaudier-Cabot and Bazant, 1987; Sellier et al., 2013a).

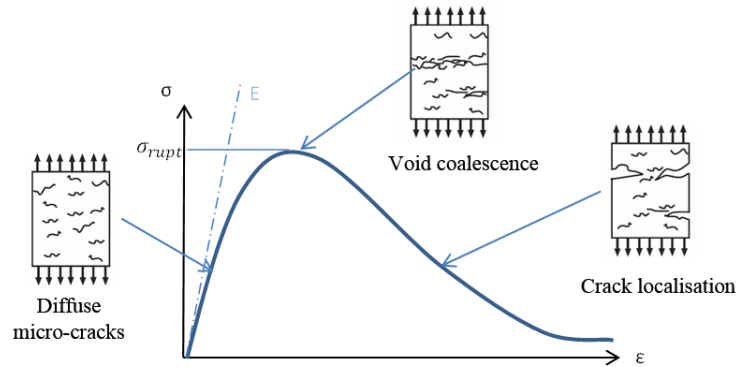


Figure 3-22: Softening behaviour of concrete under a tension test

In the damage model, the damaged material is considered as a continuous, homogeneous and anisotropic medium. The damage is quantified by the damage variable which varies from 0 for virgin material to 1 for completely damaged material (Eq. (3-4), Figure 3-23). S_D is the damage part within a damaged material whose S is its apparent area, thus the effective undamaged area is deduced as $\tilde{S} = S - S_D$. Based on the strain-equivalent principle, an effective stress $\tilde{\sigma}$ is applied on the equivalent virgin material S in order to obtain the same strain for damaged

material subjected to a total stress σ . Accordingly, the effective stress $\tilde{\sigma}$ can be as defined as in Eq.(3-5) and the elastic modulus of damaged material as in Eq.(3-6).

$$D = \frac{S_D}{S} \quad (3-4)$$

$$\tilde{\sigma} = \frac{\sigma}{1 - D} \quad (3-5)$$

$$E = (1 - D)E_0 \quad (3-6)$$

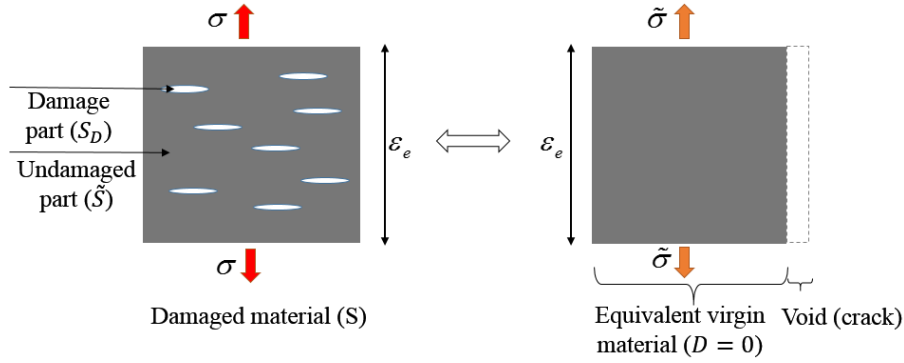


Figure 3-23: Scheme of effective stress

3. 2. 5. 1. Isotropic elastic damage model

(Mazars, 1986) developed an isotropic elastic damage model for concrete to describe the loss of concrete stiffness due to the micro-cracks occurrence. The model has been used as a reference for other damage models thereafter (Hamon and Mazars, 2012; La Borderie, 1991; de Vree et al., 1995). Mazars introduced a scalar damage variable $D(\varepsilon_{eq})$ ($\in [0,1]$) to describe the isotropic elastic damage but distinguish between tensile and compressive damage. The total stress depends on the deformation ε , stiffness S and damage state D (Eq. (3-7)). In Eq. (3-8), an equivalent strain ε_{eq} translates a triaxial state by an equivalence to a uniaxial state. As the extensions are primordial in the phenomenon of cracking, ε_{eq} considers only the positive values of the tensor of the principle deformations. The dissymmetry of the tensile-compressive behaviour is due to the fact that in the first case, micro cracks are created directly by extensions parallel to the stress and in the second case, extensions are transmitted by the Poisson effect and are perpendicular to the direction of stress. Thus, the damage variable D results from a combination of tensile damage D_t and compressive damage D_c (Eq.(3-9)). In this equation, the coefficient β characterises the shear response of the material when it is greater than 1 and the tensile/compressive damage is defined using the Eq. (3-10) when ε_{eq} is greater than an initial deformation threshold at which the damage appears ε_{d0} . A_r and B_r are the material parameters. The coefficient α_i allows the coupling of tension and damage ($\alpha_i = 0$ for pure compression and

1 for pure tension) (Eq. (3-11)) in which ε_{ii} is deformation induced by positive principle stress (Eq.(3-12)).

$$\sigma = (1 - D(\varepsilon_{eq})) \times S \times \varepsilon \quad (3-7)$$

$$\varepsilon_{eq} = \sqrt{\langle \varepsilon_i \rangle_+ : \langle \varepsilon_i \rangle_+} = \sqrt{\sum_{i=1}^3 \langle \varepsilon_i \rangle_+^2} \quad \text{where} \quad \langle \varepsilon_i \rangle_+ = \begin{cases} \varepsilon_i & \text{if } \varepsilon_i \geq 0 \\ 0 & \text{if not} \end{cases} \quad (3-8)$$

$$D = \alpha_t^\beta D_t + (1 - \alpha_t)^\beta D_c \quad (3-9)$$

$$D_r = 1 - \frac{\varepsilon_{d0}(1 - A_r)}{\varepsilon_{eq}} - \frac{A_r}{\exp[B_r(\varepsilon_{eq} - \varepsilon_{d0})]} \quad (r = t \text{ or } c) \quad (3-10)$$

$$\alpha_t = \frac{\sum_{i=1}^3 [\langle \varepsilon_i \rangle_+ \varepsilon_{ii}]}{\varepsilon_{eq}^2} \quad (\alpha_t \in [0, 1]) \quad (3-11)$$

$$\varepsilon_{ii} = \frac{1 + \nu}{E} \langle \sigma \rangle_+ - \frac{\nu}{E} tr(\langle \sigma \rangle_+) \quad (3-12)$$

Due to its simplicity, this model is easy to implement and is able to reproduce the crack effect in the compression/tension test with monotonous and unidirectional loading. However, it is not suitable for more complex loadings because it is still limited to take into account the phenomenon of reclosing cracks (stiffness restoration) and the possible irreversible plastic deformations or viscous effects that can be observed during the deformation of concrete.

3. 2. 5. 2. Orthotropic damage model

As concrete is characterised by a strain softening behaviour (see Figure 3-22), the micro-cracks diffuse under tension forces in the pre-peak phase and reclose rapidly after the peak. This is the reason why, most often, only localised cracks are modelled. When the material is put under compression forces, the diffuse micro-cracks induced by tension will reclose either partially or completely, which is called the *unilateral effect* (Lemaitre et al., 2009). This effect results in a restoration of material stiffness and a slowdown of crack occurrence. Therefore, the unilateral effect has been considered in the modelling (La Borderie, 1991; Lemaitre et al., 2009; Rouquand and Pontiroli, 2007).

When complex loads are applied on concrete structures, crack openings appear perpendicular to the main extensions and parallel to the direction of compression, so it is more reasonable to describe anisotropic damage with a tensor variable rather than a scalar variable. As there are many damage models using a tensor variable in the literature, we cite only some models that are frequently used without explicit details (Desmorat, 2006; Dufour et al., 2013; Gatuingt et al., 2006; Girya et al., 2011; Hamon and Mazars, 2012; Lemaitre et al., 2009; Sellier et al., 2013a).

3. 2. 6. Influence of temperature on reinforcement behaviour

3. 2. 6. 1. Reinforcement behaviour at high temperature

Bonded reinforcement (i.e. deformed bars) used to control the extent and width of cracks at operating temperatures, resists to tensile stresses and provides structural reinforcement required by design procedures. Bonded reinforcement in nuclear power plant structures is often used in conjunction with high resistance steel prestressed wires. The prestressed steel preserves the structural rigidity and the major part of the strength while the bonded reinforcement distributes cracks by reducing the cracking width, it increases also the ultimate strength, reinforcing the zones not adequately strengthened by the prestressed bars and contributing then to additional safety for unexpected conditions of loading. The structural elements in reinforced concrete have a high thermal inertia that results in relatively slow down the rate of temperature rise through the cross section (Naus, 2006). Reinforced concrete structures generally perform well under elevated-temperature conditions, however, under certain scenarios (e.g. rapid heating until high temperature), spalling of concrete could occur. During heating of steel, crystalline transformations occur depending on the temperature (e.g. perlite at 721°C and Curie point at 768°C) but strength characteristics and mechanical properties of steels are not remarkably changed for temperature ranges under 180°C (Toumi Ajimi et al., 2017).

A literature review indicates that many experimental studies have been conducted on the effect of temperature on strength properties of reinforcing steel (Elghazouli et al., 2009; Felicetti and Gambarova, 1998; Topçu and Karakurt, 2008; 1992). Most of these studies were carried out for evaluating strength and stiffness properties of conventional reinforcing steel bars with a yield strength in the range of 235-520 MPa. According to (Kodur and Dwaikat, 2007), the critical temperature, defined as the temperature at which steel (reinforcement) loses 50% of its ultimate strength, is taken as 593°C for reinforcing steel bars. And it can be observed that between 20°C and 140°C the mechanical tensile behaviour of steel rebars are not affected by temperature. A recent study of (Toumi Ajimi et al., 2017) investigating the evolution of the tensile and bond behaviour of B500B rebars (ultimate strength of 500 MPa) with a diameter of 12 mm and 16 mm and length of 1200 mm. The tensile tests were carried out in the framework of MACENA at an ultimate temperature of 20, 40, 100 and 140°C and the obtained temperature profiles were not constant along the studied length, as illustrated in Figure 3-24. Figure 3-25 shows results for evolution of ultimate tensile strength R_m , characteristic yield stress $R_{p0.2}$ and the elastic tensile modulus E with temperature. It can be observed a slight evolution of R_m , $R_{p0.2}$ and E with temperature according to results of (Li et al., 2003; Toumi Ajimi et al., 2017) which is lower than an estimation expected by (Eurocode 2, 2005). Therefore, the influence of a low elevated temperature (up to 140°C) on the mechanical behaviour of rebars is quite low.

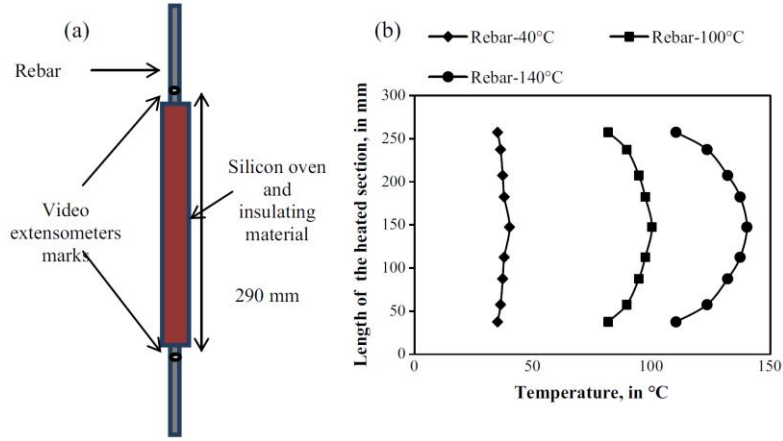


Figure 3-24: Scheme of tensile tests on rebars (a) and temperature evolution along heated section (b) (Toumi Ajimi et al., 2017)

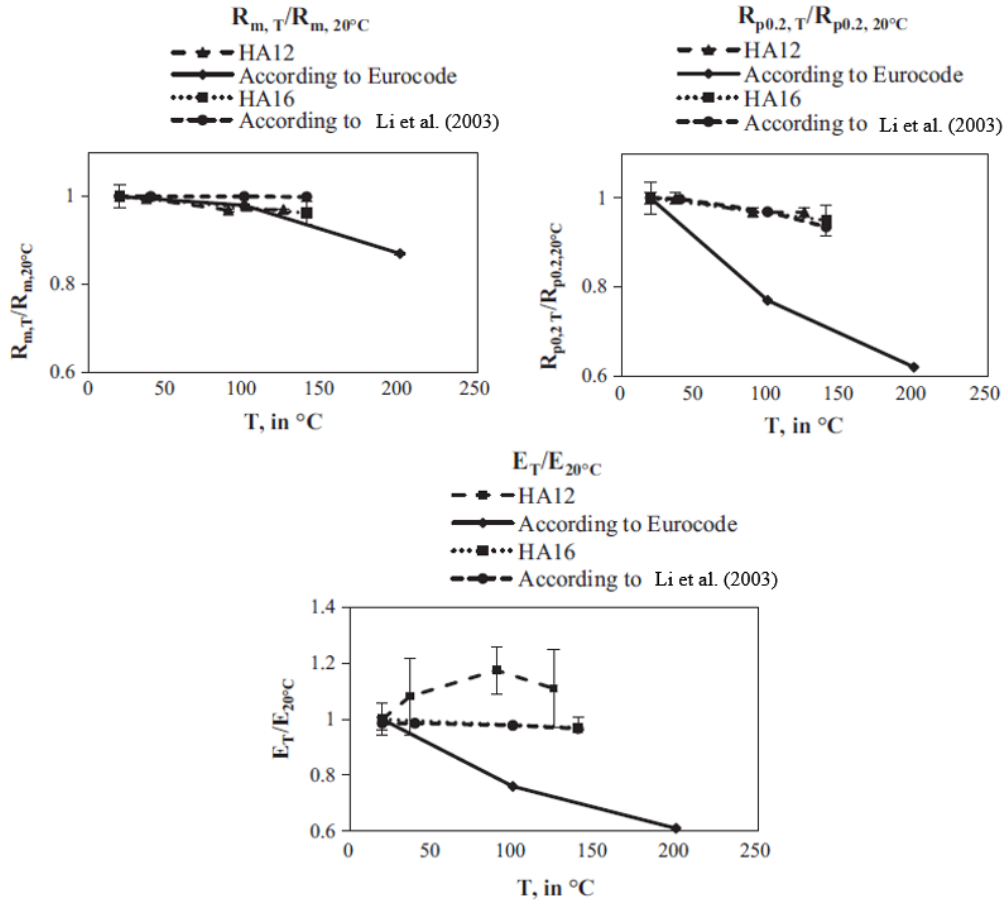


Figure 3-25: Influence of temperature on the tensile behaviour of rebars and comparison with (Eurocode 2, 2005) and (Li et al., 2003)

3. 2. 6. 2. Bond behaviour of reinforcement-concrete at high temperature

The concrete-rebars bond behaviour has been investigated using the pull-out test (ACI 440.3R-04, 2004). The test configuration in (ACI 440.3R-04, 2004) was adopted to dispose of a higher bonded length ($6d$ instead of $5d$) as described in Figure 3-26.

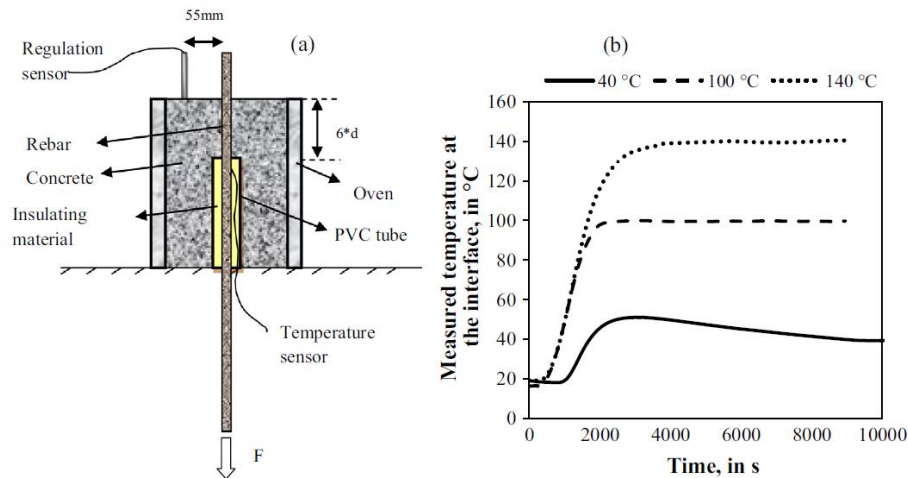


Figure 3-26: Scheme of the pull-out tests(a) and temperature evolution at the interface before tests at 40, 100 and 140 $^{\circ}\text{C}$ (b) (Toumi Ajimi et al., 2017)

Most of the investigations (Clément, 1987; Farra, Bicher, 1995; Gambarova and Rosati, 1996) on the bond between concrete and rebars have been reported in (FIB, 2000). The main factors that influence the bond stress-slip are the temperature (Bazant and Kaplan, 1996; Huang, 2010; Katz et al., 1999), the steel bar diameter (Bouazaoui and Li, 2008) and other influencing factors linked to the test process as the length embedded into the concrete, the concrete strength, the confinement effect, the form of the specimen (cylindrical (Kolani et al., 2012) or prismatic (Handika, 2017)), the steel bar properties (ribbed or non-ribbed bar), the loading application (monotone or cyclic), etc.. Based on the experimental works on the pull-out test (ACI 440.3R-04, 2004; Eligehausen et al., 1983; FIB, 2000; Goto, 1971; Lutz and Gergely, 1967), the degradation mechanism of the steel-concrete bond can be divided into 3 as followed:

- The chemical adhesion of two different materials (concrete and steel)
- The frictional forces based on the roughness of steel-concrete collision, the transverse forces and the relative slip of concrete and steel bar
- The anchorage mechanisms or bearing mechanism of ribs against concrete structures

Figure 3-27 illustrates the mechanism of deterioration of steel-concrete bond under monotonic loading (Dominguez Ramirez, 2005). More detail explanations can be found in (Dominguez Ramirez, 2005; FIB, 2000).

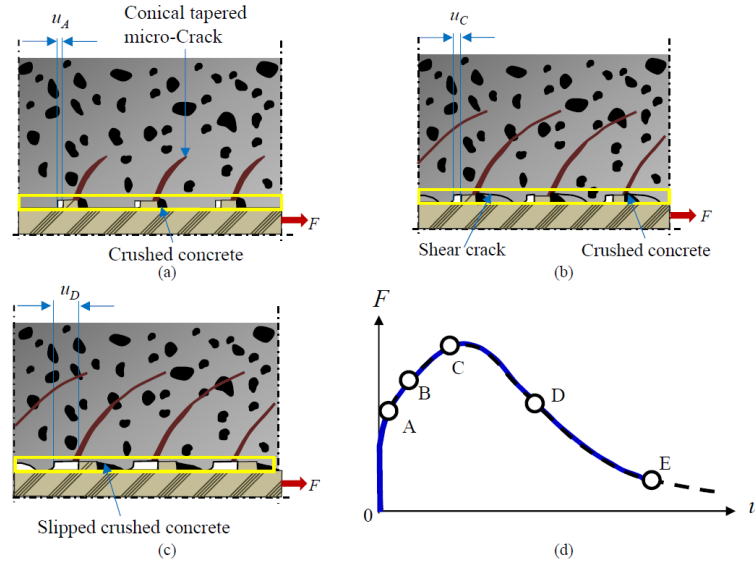


Figure 3-27: Degradation mechanism of steel-concrete bond (Dominguez Ramirez, 2005)

Concerning the influence of temperature on the concrete-rebar bond, very few studies got interested in a temperature range between 20°C and 140°C. Figure 3-28 shows the influence of temperature on the ultimate shear stress for two rebars HA12 and HA16 according the pull-out test of (Toumi Ajimi et al., 2017). It can be seen that the bond strength decreases with a diameter of rebars and with temperature except for high temperature (more than 100°C). In our opinion, the inversion of the curves at 100°C and 140°C is not logic because these experimental results include the tests that are not representative. As we can see clearly in Figure 3-30, the concrete specimens were damaged before reaching the peak of slip curve, so the test measures thus the splitting strength rather than the adhesion strength. Another investigation observed on the high temperature test is the flow of water along the rebar which may be explained by the drying of concrete specimen (Figure 3-29).

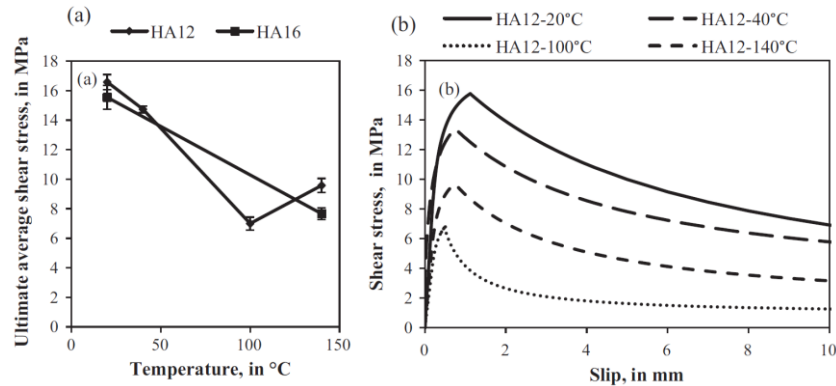


Figure 3-28: Evolution of ultimate shear stress with temperature for HA12/HA16 (a) and obtained interfacial behaviours at different temperatures for HA12 (b) (Toumi Ajimi et al., 2017)



Figure 3-29: Water flow along rebar during heating at 100 and 140°C (Toumi Ajimi et al., 2015)



Figure 3-30: Cracks observed for concrete at 100 and 140°C (Toumi Ajimi et al., 2015)

- **Rebars-concrete bond modelling**

Modelling of the obtained experimental results can be achieved through analytical models or numerical models. Several analytical models have been proposed. For example, an interfacial model (or bond-slip law) in (FIB, 2000) (see Figure 3-31) was suggested from the experimental works of Eligehausen (Eligehausen et al., 1983). And an analytical model for the characteristic interfacial behaviours was proposed by (Rolland, 2015) (Figure 3-32).

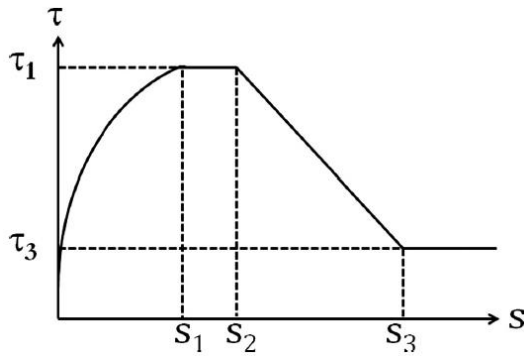


Figure 3-31: Bond stress-slip curve defined by (FIB, 2000)

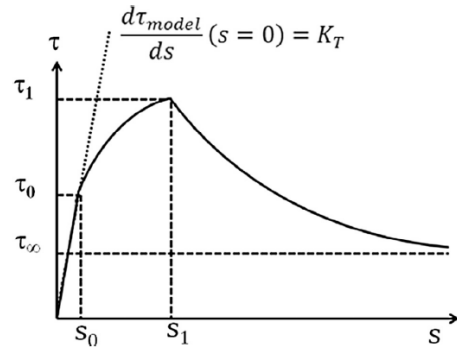


Figure 3-32: Bond-slip model (Rolland, 2015)

For numerical modelling, it can be divided into two categories based on the geometrical representation of interface zone: an interface with a thickness (volumetric element of the interface) and an interface with no thickness (double nodes element of the interface).

For the interface model with thickness, the volumetric element of the interface was used by (Hameed, 2010; Handika, 2017; Kolani et al., 2012; Michou, 2015) as illustrated in Figure 3-33. The steel bar was meshed using bar elements in (Hameed, 2010; Kolani et al., 2012) and using volumetric element in (Handika, 2017). (Michou, 2015) considered the ribs on the reinforcing bar explicitly to take into account the heterogeneity properties of the steel-concrete

interface. In the application on pull-out samples and tie-beam, it shows its capacity to reproduce the stress transfer steel-concrete and also crack opening. However, these methods are not appropriate for large-scale structure because of the explicit mesh complexity required for the interface element and time-consuming calculation.

For the interface model without thickness (using double nodes), it can be a surface element and the lineic element of the interface. The steel bar and surrounding concrete are connected through steel-stress vector with a stiffness matrix or kinematical relations. Millard (Millard and Vivier, 2006) used a surface element called “Joint element”, which was implemented in Cast3M (CEA, 2015) using Eligehausen’s evolution law, to model the degradation of the steel-concrete bond due to corrosion. Recently, Mang (Mang et al., 2015) suggested the lineic element called “coaxial element”, which was also implemented in Cast3M, based on the initial work by (Casanova et al., 2012). This interface element has a zero thickness four-node element (each has three degrees of freedom) that is able to associate steel truss element (1D) with a superimposed segment bonded to the surrounding concrete (3D) through kinematical relation, illustrated in Figure 3-34. This approach can replace the perfect or “no-slip” relation hypothesis between concrete and reinforcement using the bond-slip law from (Casanova et al., 2012) that is enriched for cyclic loading. Though the global bond behaviour of the steel-concrete interface is well reproduced, this may lead to pathological mesh dependency effects due to stress concentration at the singularity (Badel and Lorentz, 2011). In a condition of a sufficiently finer mesh size of concrete surrounding the bar, the stress concentration induced by the bar into the concrete can lead to almost a total deterioration of concrete around the bar. A later development of this method presented by (Llau, 2016) suggested a distribution of the bar force to four nodes using a static condensation method aiming to delocalize the bar force in a sufficient large zone of concrete to avoid concrete damage. The so-called 1D-3D model (1D inclusions / 3D finite elements) creates an equivalent volume from the 1D mesh with static condensation of the stresses and stiffness and it is bounded to the concrete using kinematical relations. Despite this approach can avoid the well-known stress concentration around singularities observed with a 1D model and can reproduce local structural effects, it is still limited for an additional mesh of equivalent volume of the reinforcement and interface nodes. Besides these, in literature, several studies also focused on modelling of bonding between steel rebar and concrete at elevated temperature (Huang, 2010; Pothisiri and Panedpojaman, 2012). These analytical models were rather complex and aiming at modelling of bond behaviour in a fire where the temperature is up to 600°C, they were thus not adopted for an application on large-scale structure and temperature range under 140°C.

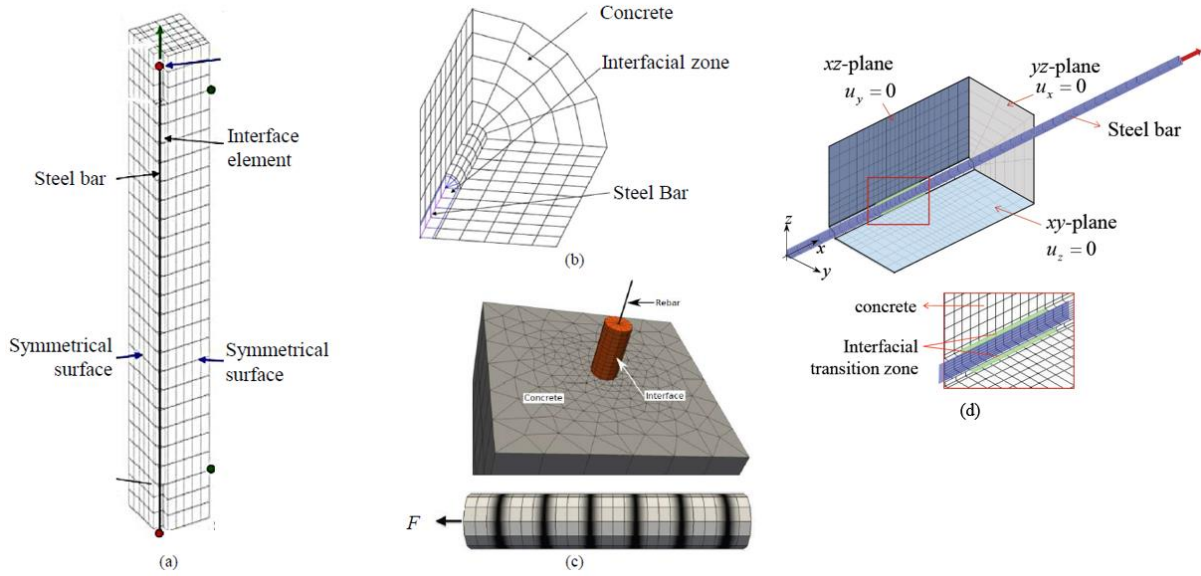


Figure 3-33: Interfacial zone model with thickness. Steel bar with bar element (a) (Hameed, 2010), (b) (Kolani et al., 2012), (c) heterogeneity consideration (Michou, 2015) and (d) steel bar with volumetric element (Handika, 2017)

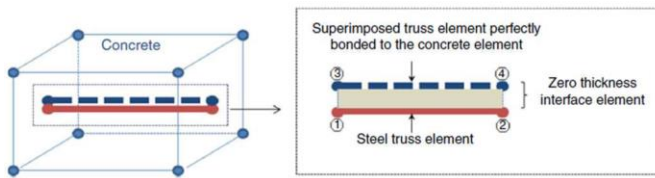


Figure 3-34: Interface model without thickness (lineic element) (Mang et al., 2015)

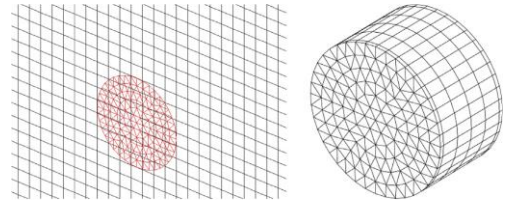


Figure 3-35: 1D-3D model of steel cross section inside concrete (Llau et al., 2016)

3. 3. Modelling of reinforced concrete at high temperature and humidity

After the studies of influence of temperature and humidity on the mechanical behaviour of concrete and the effect of temperature on the reinforcement behaviour, this paragraph will present a new development for modelling the effect of high temperature and humidity on the massive reinforced concrete structure. Noted that in this part, the superscripts m and r represent the properties belongs to concrete and reinforcement, respectively.

This work focuses on the extension of the material model developed at LMDC and its adaptation to elevated temperatures (up to 200°C). The interest of the work is to introduce an analytical strategy adopted to consider the accumulation of damage using a single mechanical model from the young age to the LOCA. This mechanical model uses the results of temperature, humidity, hydration degree and porosity from the two previous models i.e. hydration model (cf. chapter 1) and TH model (cf. chapter 2) in order to estimate the delayed deformations and risk of cracking. First, we present the existing concrete model for moderate temperature and humidity which comprises a damage model (Sellier et al., 2013a) and a rheological creep model (Sellier et al., 2016), which allows the coupling of creep, shrinkage, thermal deformation and damage and thus reproduces the mechanical effects in real structures. Then, the improvements made to the model will be presented such as adaptation for large meshes of the massive structure, for young age concrete, for concrete at high temperature and humidity and for reinforced concrete structure.

3. 3. 1. Presentation of concrete model at moderate temperature and humidity

3. 3. 1. 1. *Rheological model*

Concrete creep is modelled using a Burger chain which is represented by a rheological scheme (Figure 3-36) and implemented in a poromechanical framework. The creep model used here is developed by (Sellier and Buffo-Lacarrière, 2009; Sellier et al., 2016) and have been tested and validated with many real case structures (Buffo-Lacarrière and Sellier, 2011; Buffo-Lacarrière et al., 2011, 2014; Kolani et al., 2012). The originality of the model lies in the consideration of consolidation phenomena to reproduce the irreversible delayed strain which avoids to have multiple Kelvin or Maxwell modules, limiting then the fitting work and including a physical base to the creep velocity decrease with time: When an external loading is applied to the material, an instantaneous elastic response occurs and is modelled by the elastic analysis level. If stress lasts for a long time, a viscous sliding of C-S-H sheets occurs. It provokes a reversible creep corresponding to the reversible arrangement of interlayer water molecules (Benboudjema, 2002; Ulm and Acker, 1998), which is modelled by a viscoelastic Kelvin-Voigt module. If some inter-layer bonds break, leading to a stress concentration in non-viscous phases and a new material configuration, irreversible creep occurs (Acker and Ulm, 2001). This phenomenon is modelled by the nonlinear Maxwell module in which the viscosity depends on

the Maxwell strain through the consolidation function, itself controlled by a parameter characterizing the “creep potential” of concrete. Besides, the effects of hydric forces due to the capillary depression and disjoining forces, influence the drying creep potential and shrinkage of concrete which is modelled through the water pressure (p_l) thanks to the poro-mechanical theory.

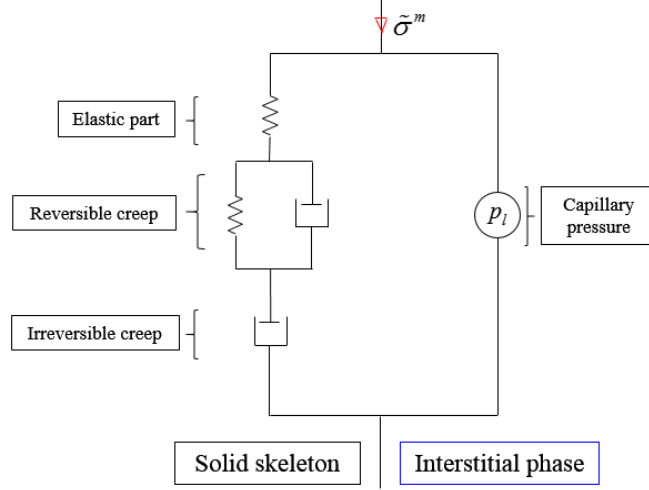


Figure 3-36: Rheological scheme of the creep model

In Eq. (3-30), the effective stress $\tilde{\sigma}_{kl}^m$ may be deduced by the difference between the effect of water (capillary pressure) and solid skeleton (Eq. (3-13)). In the poromechanical theory, the capillary pressure effect is managed by the Biot coefficients (b') which depends on the stress state and the saturation degree (S_l) (Coussy, 1995). The effective stress applied on the solid (in Eq. (3-13)) is determined by integration of the increment of the solid effective stress $\dot{\tilde{\sigma}}_{kl}^m$ obtained from the matrix stiffness $S_{klmn}(\alpha)$ and the elastic strain deduced from total strain increment $\dot{\epsilon}_{mn}^{tot}$, plastic strain increment $\dot{\epsilon}_{mn}^{pl}$, creep increment $\dot{\epsilon}_{mn}^{cr}$, and thermal increment $\dot{\epsilon}_{mn}^{th}$ (Eq. (3-14)). The incremental formulation of this solid behaviour law is needed to be adapted to early age modelling (Buffo-Lacarrière and Sellier, 2011).

$$\tilde{\sigma}_{kl}^m = \tilde{\sigma}_{kl}^m - b'(\sigma_{kl}^m) \times S_l \times P_{l,kl} \quad (3-13)$$

$$\dot{\tilde{\sigma}}_{kl}^m = S_{klmn}(\alpha) \times (\dot{\epsilon}_{mn}^{tot} - \dot{\epsilon}_{mn}^{pl} - \dot{\epsilon}_{mn}^{cr} - \dot{\epsilon}_{mn}^{th} - \dot{\epsilon}_{mn}^{DTT}) \quad (3-14)$$

The material stiffness $S_{klmn} = f(E, \nu, \alpha)$ is a second-order tensor expressed as a function of Young's modulus E , Poisson's ratio ν and degree of hydration α . The stiffness and mechanical properties of material increase with the development of hydration.

a. Creep deformation

The creep deformation consists of permanent and reversible creep which are represented in the left branch of Figure 3-36. As the proportion of reversible and irreversible strain is derived from the corresponding elastic strain in concrete, the proportionality between permanent strain kinetic and elastic strain can be assumed as expressed in Eq. (3-15). Previous experimental works analysed by (Sellier et al., 2016) supports this assumption which corresponds to a Poisson coefficient of creep close to the elastic one while the consolidation does not affect the material state, and an anisotropic evolution of the Maxwell strain tensor when the consolidation occurs. This model is formulated to be usable in finite element codes and able to model the large/complex structures.

$$\frac{\partial \varepsilon_I^M}{\partial t} = \frac{\varepsilon_I^E}{\tau_{ref}^M \cdot C_I^C} \quad (3-15)$$

In this equation τ_{ref}^M is a reference characteristic time at initial state associated with the Maxwell strain ε_I^M , C_I^C is a function standing for a consolidation state of the material and ε_I^E is the elastic strain with index I corresponding to Eigen-direction.

The consolidation function C_I^C follows an exponential evolution (Eq. (3-16)) with a parameter k which is the creep coefficient for the reference temperature. The objective of the consolidation function is to consider the decrease of creep strain velocity with time as experimentally observed during creep tests, explaining the phenomenon by a progressive transfer of viscous stresses from viscous phases (unblocked C-S-H mainly) to non-viscous phases (other constituents of concrete and consolidated C-S-H packets).

$$C_I^C = \frac{1}{k} \exp \left(\frac{1}{k} \left(\frac{\varepsilon_I^M}{\varepsilon_I^E} \right)^+ \right) \quad (3-16)$$

The creep coefficient k is used to consider the THM conditions through the coupling of functions linked to the temperature C^T , humidity C^H and mechanical loading C^M :

$$k = k_{ref} \cdot C^T \cdot C^H \cdot C^M \quad (3-17)$$

With $k_{ref} = \frac{\varepsilon_{ref}^M}{\varepsilon_{ref}^E}$ is the reference coefficient defined as the ratio of a characteristic Maxwell strain ε_I^M and the characteristic elastic strain ε_I^E at the reference THM conditions. The characteristic strain ε_I^M is a fitting parameter of a material called reference creep potential because the creep amplitude is proportional to ε_{ref}^M .

In Eq. (3-17), the function C^T accounts for the influence of temperature on creep potential, C^H stands for the influence of humidity and C^M corresponds to the non-linear effect of mechanical loading.

The reversible creep is modelled with Kelvin module, in which stress is replaced by a reduced elastic strain corresponding to the final strain of Kelvin module (Eq. (3-18)). Like permanent creep, reversible creep depends on temperature and water content, thus the same coefficients, C_w^T and C^H are used and the fitting coefficients τ_{ref}^K and ψ^K are applied.

$$\frac{\partial \varepsilon_l^K}{\partial t} = \frac{1}{\tau_{ref}^K C_w^T C^H} \left(\frac{\varepsilon_l^E}{\psi^K} - \varepsilon_l^K \right) \quad (3-18)$$

b. Temperature effects on creep deformation

Previous studies in the subsection 3. 2. 3. 1 have revealed that heating leads to increase in basic creep kinetics and amplitudes. The temperature affects the intrinsic viscosity of viscous phases containing free water due to the dependence of water viscosity on temperature. Over approximately 45°C, the temperature can modify the microstructure due to the differential thermal dilatation between phases of concrete, cement paste and aggregate characterised by distinct values of the coefficient of thermal expansion. This can increase creep potential by releasing viscous phases and cause thermal damage (Ladaoui et al., 2013; Vidal et al., 2014). Thus the function C^T takes into account these coupled effects through the following equation:

$$C^T = C_w^T \cdot C_p^T \quad (3-19)$$

Where C_w^T and C_p^T express respectively the effect of temperature on water viscosity and creep potential through Eq. (3-20) and Eq. (3-21) thank to Arrhénius law (Figure 3-37 and Figure 3-38).

$$\frac{1}{C_w^T} = \eta_l / \eta_{l,0} = \exp \left[\frac{E_w^a}{R} \left(\frac{1}{T} - \frac{1}{T_{ref}} \right) \right] \quad (3-20)$$

$$C_p^T = \begin{cases} \exp \left[-\frac{E_p^a}{R} \left(\frac{1}{T} - \frac{1}{T_{thr}} \right) \right] & \text{if } T > T_{thr} \\ 1 & \text{if } T \leq T_{thr} \end{cases} \quad (3-21)$$

Where $E_w^a \approx 17000 \text{ J/mol}$ is the activation energy of water viscosity (Grasberger and Meschke, 2004), T_{ref} is the reference temperature for which τ_{ref}^M is fitted, generally 20°C, $E_p^a \approx 25000 \text{ J/mol}$ is the activation energy intrinsic to the materials which control the sensibility of creep to increase with temperature, $T_{thr} \approx 45^\circ \text{C}$ is the threshold temperature

from which thermal damage appears and modifies the creep potential (Ladaoui et al., 2013), $R=8.314 \text{ J}/(\text{mol.K})$ is gas constant.

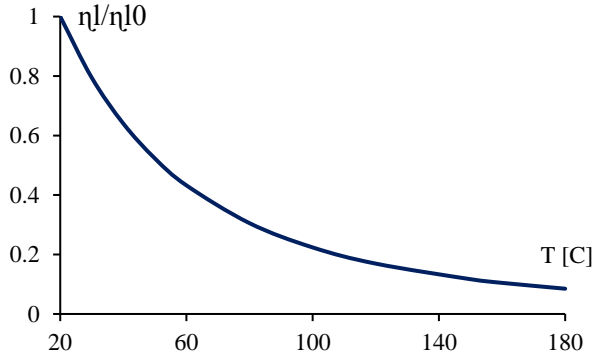


Figure 3-37: Evolution of water viscosity
(inverse function of C_w^T)

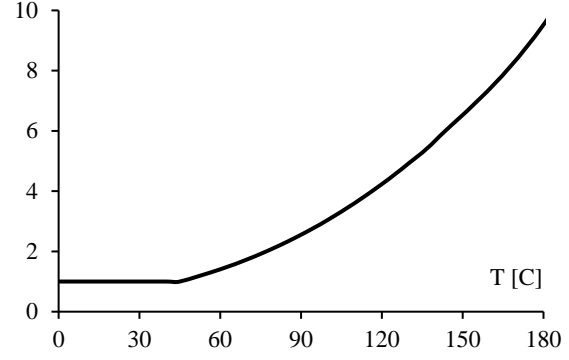


Figure 3-38: Evolution of coefficient C_p^T

c. Humidity effects on creep deformation

As explained in the subsection 3. 2. 3. 2, the influence of humidity on basic creep is sensitive to the water content. (Benboudjema et al., 2005) suggested for structural modelling that only a macroscopic approximation of these complex underlying phenomena can be envisioned. Thus, currently, a linear approximation is applied to consider the reduction of creep velocity when concrete is dry (Eq. (3-22)). It means that the higher the water saturation degree S_l , the higher the specific creep amplitude. Besides this, the effect of hydric forces on shrinkage and drying creep will be explained in the following subsection e.

$$C^H = S_l \quad (3-22)$$

With $S_l = \phi_l / \phi$ is the degree of water saturation (ϕ_l is the volume of water content and ϕ is the total volume of porosity).

d. Nonlinear effects of mechanical loading on basic creep

The nonlinear creep behaviour for high-loading rate may be considered through the function C^M which starts from 1 for unloading material and diverges when the loading level reaches a critical value causing tertiary creep (Eq. (3-23)). As it is assumed that tertiary creep occurs only in case of deviatoric loading, C^M depends on the loading level only through an equivalent shear stress τ^{DP} (Drucker and Prager, 1952). A Drucker Prager formulation of τ^{DP} (Eq. (3-24)) frequently used for plasticity and visco-plasticity, can consider the effect of triaxial confinement that reduces the impacts of deviatoric stresses in term of damage. τ_{cr}^{DP} is the critical stress leading to tertiary creep (Eq. (3-25)) which depends on the confinement effect coefficient δ and the uniaxial critical stress σ_{cr} . The critical stress σ_{cr} is computed from a non-

linear amplification coefficient χ^M according to Eq. (3-26). The fitting parameter χ^M varies from 1 for the linearity of creep under a compression stress to the greater value for the non-linearity of creep. For instance, $\chi^M = 2$ is used by (Sellier et al., 2016).

$$C^M = \frac{\tau_{cr}^{DP}}{\tau_{cr}^{DP} - \tau^{DP}} \quad (3-23)$$

$$\tau^{DP} = \sqrt{\frac{\sigma^d : \sigma^d}{2}} + \delta \frac{Tr(\sigma)}{3} \quad (3-24)$$

$$\tau_{cr}^{DP} = \frac{\sigma_{cr}}{\sqrt{3}} \left(1 - \frac{\delta}{\sqrt{3}} \right) \quad (3-25)$$

$$\sigma_{cr} = \frac{2}{3} \left(\frac{\chi^M}{\chi^M - 1} \right) R_c \quad (3-26)$$

e. Shrinkage and drying creep

The magnitude of shrinkage and drying creep depend on the effect of water change within the material which is described by the effect of capillary pressure. The equivalent capillary pressure can be obtained directly from the thermohydric calculation. In our approach, the pressure p_l is determined in the post-treatment by Eq. (3-27) for the early age calculation (with M_{shr} depends on the degree of hydration α) (cf. Chapter I) and issued directly from the thermohydric transfer model for long term calculation (cf. Chapter II).

$$p_l = M_{shr} \left[1 - S_l^{(-1/m_{vgn})} \right]^{(1-m_{vgn})} \quad (3-27)$$

Moreover, to consider the nonlinear interaction between the solid skeleton and water effects during drying or humidification, a parameter σ_{DC} has been introduced in Eq. (3-13) in such a way that the capillary pressure effect is doubled when the material is subjected to a compression $\sigma_{ij} = -\sigma_{DC}$ (see Eq. (3-28)). In this incremental formulation, the parameter b corresponds to the Biot coefficient when there is no stress. The phenomenon of Biot coefficient variation corresponds to a more or less aptitude of cement matrix to transmit its capillary forces to the structure scale, depending on the micro cracking state of the micro-structure under combination of capillary forces and external forces (Sellier et al 2016).

$$\frac{\partial \sigma_{ij}^m}{\partial t} = \frac{\partial \sigma_{ij}^m}{\partial t} + \frac{\partial (b \cdot S_l \cdot p_l)}{\partial t} \left(1 + \frac{|\sigma_{ij}^m|}{\sigma_{DC}} \right) \quad (3-28)$$

f. Transient thermal creep

Transient thermal creep in Eq. (3-13) is observed only if the material is loaded in compression before heating (Bazant et al., 2004), and if heating is relatively fast. The magnitude of this deformation depends on the consolidation state of material and is proportional to the heating rate (Cagnon, 2015). The transient thermal creep can be modelled by:

$$\frac{\partial \varepsilon_I^{DTT}}{\partial t} = K_{DTT} \frac{\min(\sigma_I, 0)}{C_I^C} \left[\frac{\partial T}{\partial t} \right]^+ \quad (3-29)$$

With $[]^+$ considers only the positive part, C_I^C is the consolidation coefficient in direction of principal stress, K_{DTT} is a parameter to fit the transient thermal creep amplitude.

3.3.1.2. Damage model

In this work, the crack of concrete is modelled using an orthotropic damage model developed at LMDC laboratory (Sellier et al., 2013a). This model considers many aspects of concrete such as dissymmetry of the tensile-compressive behaviour, unilateral effect, hysteric dissipation due to crack re-closing phenomena, etc.

According to (Sellier, 2015), the LMDC model has recently been improved to calculate anisotropic plastic strains. Moreover, two criteria have been also considered: first, Rankine criteria are used to define the tension behaviour which corresponds to localised cracks, but diffuse cracks can also occur due to the propagation of microcracks induced by shear stresses. So a second criterion, Drucker-Prager (DP), is used to manage shear cracking. The general form of the total stress is calculated by a classic combination of the damage and the effective stresses:

$$\sigma_{ij}^m = \underbrace{(1 - D^{TH})}_{\text{Thermal damage}} \underbrace{(1 - D^{cr})}_{\text{Creep damage}} \underbrace{(1 - D^s)}_{\text{Shear damage}} \underbrace{[(1 - D_0^t)(1 - D^t)]_{ijkl}}_{\text{Tensile damage}} \tilde{\sigma}_{kl}^+ + \underbrace{(1 - D^r)_{ijkl}}_{\text{Reclosure damage}} \tilde{\sigma}_{kl}^- \quad (3-30)$$

This damage model is coupled with the creep model when the effective stress $\tilde{\sigma}_{kl}$ used in Eq. (3-30) is derived from the resolution of the creep model in Eq. (3-13).

In Eq. (3-30), several damage phenomena can occur simultaneously in the model such as thermal damage D^{TH} , shear and compression scalar damage D^s , creep damage D^{cr} , tensile damage D^t , and reclosure damage D^r . In this work, it is also noted that a positive stress represents a tension and a negative one for a compression.

The shear damage D^s is linked to Drucker Prager criterion and driven by plastic dilatancy $Tr(\bar{\varepsilon}^{pl,s})$. This dilatancy causes an isotropic damage only if it is greater than a dilatancy threshold ($\varepsilon^{th,s} = Tr(\bar{\varepsilon}_{peak}^{pl,s})$) corresponding to the peak in uniaxial compression test:

$$D^s = \begin{cases} \frac{Tr(\bar{\varepsilon}^{pl,s}) - \varepsilon^{th,s}}{Tr(\bar{\varepsilon}^{pl,s}) - \varepsilon^{th,s} + \varepsilon^{k,s}} & \text{if } \bar{\varepsilon}^{pl,s} > \varepsilon^{th,s} \\ 0 & \text{if } \bar{\varepsilon}^{pl,s} \leq \varepsilon^{th,s} \end{cases} \quad (3-31)$$

With $\varepsilon^{k,s}$ a characteristic strain to control the damage evolution rate versus dilatancy.

The creep damage D^{cr} considers a coupling between creep strain and possible consequences in terms of macroscopic properties such as apparent stiffness or strength. As the final creep damage D_U^{cr} is assumed to be linked to the mechanical loading coefficient C^M (Eq. (3-23)), the current creep damage D^{cr} (Eq. (3-32)) depends both on the consolidation variable C_I^c (Eq. (3-16)) which reflects the current creep strain state and the final creep damage D_U^{cr} (Eq. (3-33)). In Eq. (3-33), D_{max}^{cr} is the maximal possible creep damage that is linked to the compression strength under a long-term loading R_c^{LT} (Eq. (3-34)).

$$D^{cr} = D_U^{cr} \left(1 - \frac{1}{C_I^c} \right) \quad (3-32)$$

$$D_U^{cr} = D_{max}^{cr} \left(\frac{\tau^{DP}}{\tau_{lim}^{DP}} \right) \quad (3-33)$$

$$R_c^{LT} = (1 - D_{max}^{cr}) \times R_c \quad (3-34)$$

The thermal damage D^{TH} allows to consider the effect of temperature. This variable will be improved in the present work to consider the variation of water content within the material and developed in the next section 3.3.4.2.

The tensile damage can be categorised into two types: pre-peak isotropic damage which occurs when tensile peak strain is greater than the elastic strain at the peak R_t/E and an orthotropic damage that occurs during the post-peak phase corresponding to the localisation of tensile cracks (see Figure 3-39). The isotropic pre-peak damage depends on the principal effective stresses:

$$D_0' = 1 - \exp \left[-\frac{1}{m} \left(\frac{\tilde{\sigma}_I}{R_t} \right)^m \right] \quad (3-35)$$

With m and \tilde{R}_t parameters defined such that the behaviour law curve passes through the tensile strength $\tilde{\sigma}_I = R_t$ for the strain equal to $\varepsilon_I = \varepsilon_I^{peak}$. And the localised tensile damage, computed in the principal directions of localised cracks, depend directly on the maximal crack openings $w_I^{pl,t,max}$ for $I \in (I, II, III)$:

$$D_I^t = 1 - \left(\frac{w_I^{k,t}}{w_I^{k,t} + w_I^{pl,t,max}} \right)^2 \quad (3-36)$$

With $w_I^{k,t}$ a characteristic crack opening computed such as the dissipated energy during localised damage (increasing from 0 to 1) is equal to the fracture energy in tension G_f^t (Eq. (3-39)).

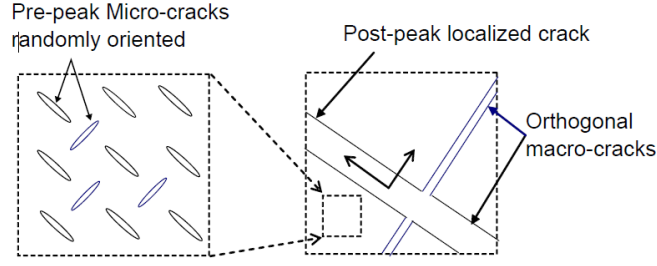


Figure 3-39: Idealised cracking pattern used to compute tensile damage (Sellier et al 2013a)

Reclosure damage D^r is used to consider the decrease of contact number between tensile crack edges. It depends on the crack opening $w_i^{pl,t}$ as follows:

$$D_i^r = \frac{w_i^{pl,t} (w_i^{pl,t} + 2w_i^{k,r})}{(w_i^{pl,t} + w_i^{k,r})^2} \quad (3-37)$$

With $w_i^{k,r}$ a characteristic crack opening computed such to verify that the energy G_f^r is consumed during reclosing process.

$$G_f^r = l_t \int_{w_i^{pl,t}}^0 (1 - D_i^r) \tilde{\sigma}_i^- dw_i^{pl,t} \quad (3-38)$$

Figure 3-40 illustrates an example of the behaviour law obtained from the model under tension-compression cycles. It also shows that the effect of reclosing cracks (unilateral effect). This phenomenon consists in a restoration of the stiffness during the passage of a loading in tension, where this stiffness is initially damaged due to the cracking, to a loading in compression, where the preceding cracks close (Ramtani, 1990).

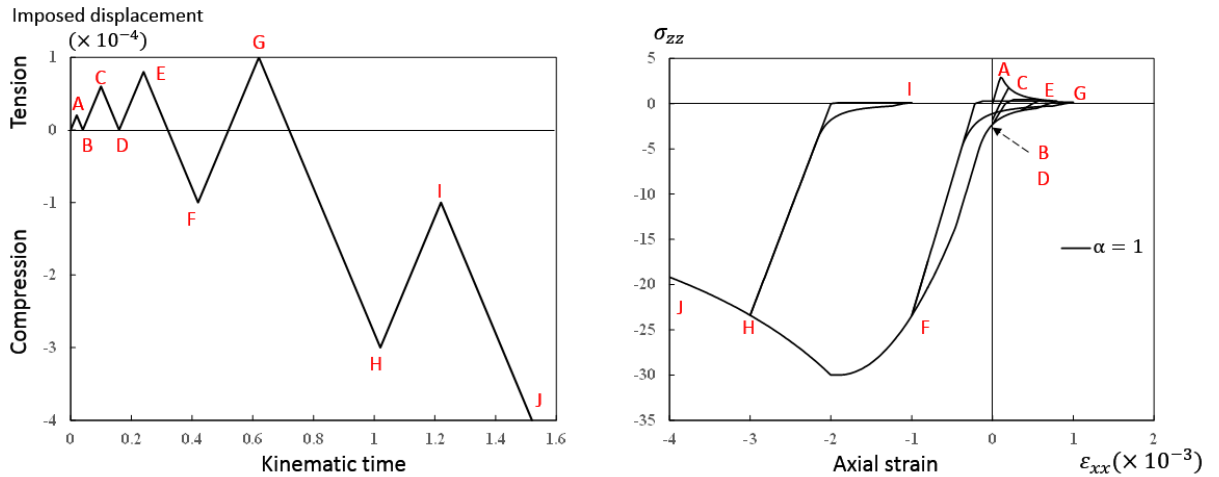


Figure 3-40: Behaviour law of hardened concrete under tension-compression cycles with damage ($R_t = 3 \text{ MPa}$, $R_c = 30 \text{ MPa}$, $G_f^t = 100 \text{ J/m}^2$, $G_f^r = 100 \text{ J/m}^2$) (Sellier, 2015)

3. 3. 2. Adaptation for large meshes of massive structures

In the tension condition, Hillerborg regularisation is used to control the fracture energy dissipation (Hillerborg et al., 1976) and evaluate the crack opening. According to the Hillerborg energy based regularization principle (Hillerborg et al., 1976), the dissipated fracture energy can be defined as follows:

$$G_f^t \approx l_I \frac{(R_t)^2}{2E(1-D_0^t)} + R_{t,I} w_I^{k,t} \quad (3-39)$$

With $R_{t,I}$ the tensile strength and l_I the finite element length in the principal direction of cracking I . The latter term can be assessed by different methods (Stablon et al., 2012). The operator **tail** supplied by Cast3m (CEA, 2015) can provide an approximate value of l_I . This calculus remains possible while the size of the finite element respects the following condition:

$$l_I < \frac{2E(1-D_0^t)G_f^t}{(R_t)^2} \quad (3-40)$$

When the tensile crack localised, the microcrack density approaches 1 ($D_I^t \rightarrow 1$) and the crack widths are computed assuming the tensile plastic strains correspond to the permanent crack's openings (Eq. (3-41)). This approximation is valid as long as $\varepsilon_I^{pl,t}$ is greater than other strains.

$$w_I \approx l_I \cdot \varepsilon_I^{pl,t} \quad (3-41)$$

It is noted that the local damage model is mesh-dependent as the dissipated energy per finite element depends on its size. To avoid dependency of Hillerborg method toward finite element shape, the model uses an anisotropic description of element size. The computed post-peak behaviour of material should vary with the finite element size. For the large mesh of massive structures where the size of the finite element does not verify the condition in Eq. (3-40), the model adopts a fracture energy G_f^{t*} sufficient to avoid a snap-back of the behaviour law, so an overestimation of fracture energy is voluntarily provoked imposing a softening modulus H at the beginning of localised damage such as:

$$\frac{\partial \sigma}{\partial \varepsilon} > -\frac{E_0}{n} \quad (3-42)$$

With $n \approx 6$ an arbitrary factor permitting to control the softening branch whatever the finite element size. This overestimation can provoke an over-dissipation of mechanic energy only if the finite element damages. Thanks to this possibility large finite elements can be meshed in zones where damage remains small enough to avoid localization. Thus, only the zones where the post-peak damage is active have to verify the condition in Eq. (3-40). An error variable is computed to verify if this option is active or not, if it is the case, the mesh should be refined in the corresponding zone. The error variable could then be used in an automatic mesh refinement context, but this possibility has not yet been implemented. Note that for RC elements, greater

than the anchorage length of reinforcements, the number of localised crack increases, increasing automatically the fracture energy at the element scale, so that, the error induced by large RC element damage is finally not so frequent as feared.

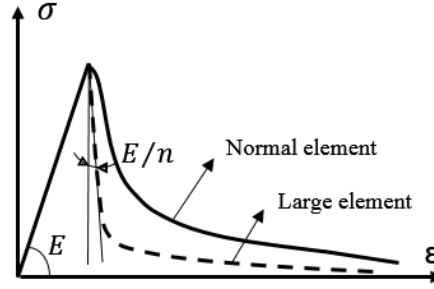


Figure 3-41: Uniaxial tensile behaviour modelling (softening part given for different element sizes)

3. 3. 3. Adaptation for early age concrete

The mechanical model has been adapted to model the early age behaviour of concrete by (Buffo-Lacarrière, 2007). So here we recall only the evolution of mechanical characteristics, then we focus on a new modification for updating of internal variables during the hydration process.

Several material parameters are linked to the degree of hydration α to represent the aging nature adapting the evolution law of De Schutter (Schutter and Taerwe, 1996) in Eq. (3-1) (cf. section 3. 2. 1. 1.):

$$X = X_{ref} \times \left\langle \frac{\alpha - \alpha_{thr}}{\alpha_{ref} - \alpha_{thr}} \right\rangle^{n_x} \quad (3-43)$$

With α_{thr} the solidification threshold, α_{ref} the reference hydration degree for which are determined the material parameter X_{ref} (usually at 28 days), n_x a non-linearity exponent for the material parameter X whose value is listed in Table 3-1. The usual parameters for this law is a threshold close to 0.1 for concrete and exponent close to 0.66, 0.66, 1, 0.5 respectively for Young modulus, tensile strength, compressive strength and fracture energy (Kolani, 2012).

Table 3-1: Exponents of De-Schutter law for material parameters

Parameter X	Symbol	Exponent n_x
Young modulus	E	0.66
Poisson coefficient	$0.45 - \nu$	0.66
Tensile strength	R_t	1.00
Re-closure characteristic stress	σ^r	0.66
Compressive strength	R_c	1.00
Confinement coefficient for Drucker-Prager criterion	δ	0
Dilatancy coefficient for non-associated plasticity	β	0
(1-Biot)	$1 - b$	0.5
Van Genuchten modulus	M_{shr}	1.86
Fracture energy	G_{ft}	0.5
Crack reclosure energy	G_{fr}	0.5

Besides the evolution of mechanical properties, the chemo-mechanical coupling needs specific updating of internal variables (Buffo-Lacarrière and Sellier, 2011). Indeed, as internal variables of the model concern both the hydrated and un-hydrated parts, each of them is considered as the average value between hydrated and un-hydrated parts of the elementary volume of material, this leads to the following updating condition:

$$\frac{\partial V_i}{\partial \alpha} = -\frac{V_i}{\alpha} \quad (3-44)$$

With V_i any mechanical state variable of the model. This updating condition leads to a decrease in mechanical damage under the effect of hydration and is applicable to almost all the internal variables of the mechanical model. When the cracking is localised and opened, the crack opening is also a mechanical internal variable of the model used in the present study (see section 3. 3. 1. 2) while the opening was just assessed by a posttreatment from the damage variable in the previous model. The preceding concepts are available for the macroscopic damage variable (as explained in (Buffo-Lacarrière and Sellier, 2011)) but are not directly applicable on the localised crack opening.

Therefore, a new modification is proposed in this work. For the localised crack opening, the updating is done on the associated internal variable D_I^f then the updated crack opening is deduced by inverting the relationship between the two variables in Eq. (3-36), allowing a decrease of the crack opening when the concrete is hydrating. Figure 3-42 and Figure 3-43 illustrate the modelling of evolutive concrete at three different degrees of hydration under tension-compression cyclic test. Concerning the consolidation coefficient of creep C_I^c , as it

depends on the Maxwell strain in the present version (see Eq. (3-16)), the actualisation (Eq. (3-44)) is directly applied on the strain, leading then to a modification of C_f^c .

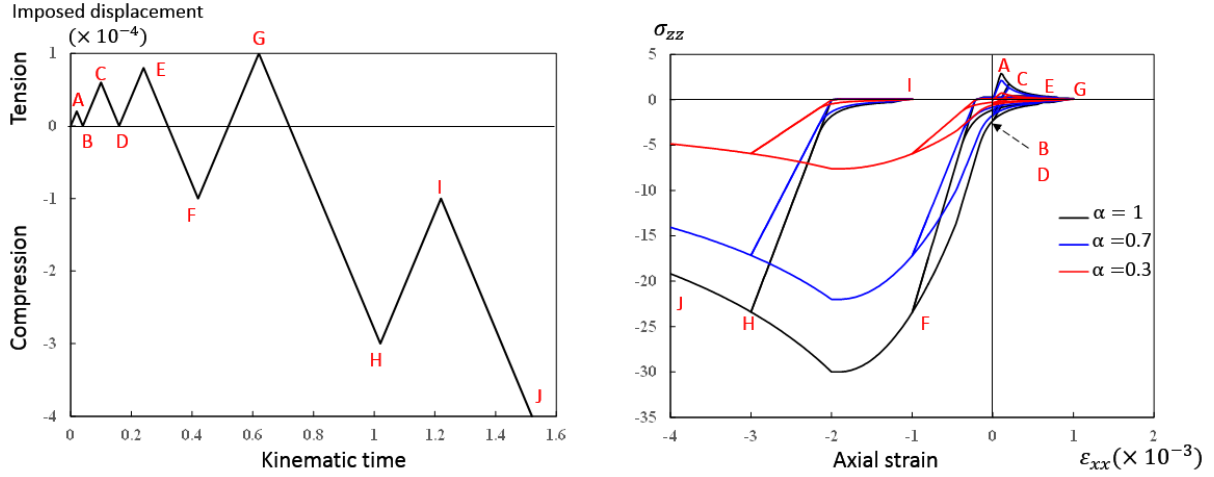


Figure 3-42: Effect of hydration on the behaviour law of evolutive concrete under tension-compression cyclic ($R_t = 3 \text{ MPa}$, $R_c = 30 \text{ MPa}$, $G_f^t = 100 \text{ J/m}^2$, $G_f^r = 100 \text{ J/m}^2$)

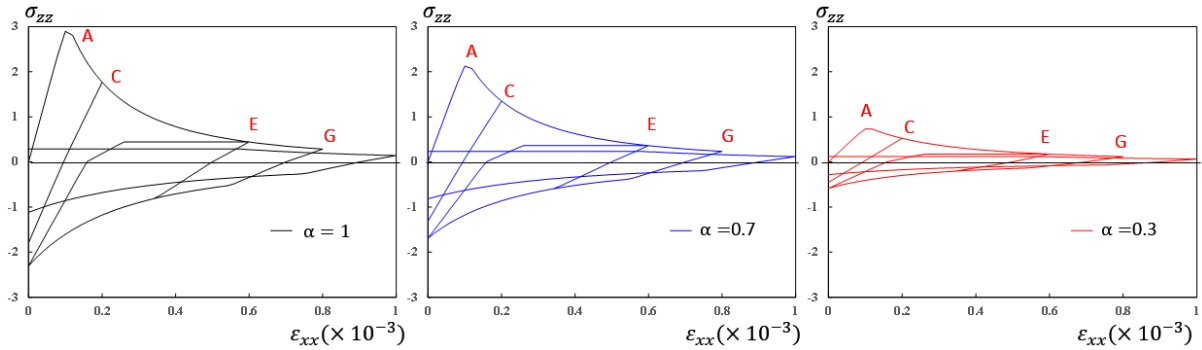


Figure 3-43: Response under cyclic tension loading

3. 3. 4. Adaptation for concrete at high temperature and humidity

3. 3. 4. 1. Effect of temperature and humidity on mechanical strength

As previously discussed in the subsection 3. 2. 2, the instantaneous mechanical behaviour of concrete is influenced by the temperature and humidity. The reduction of these properties such as the elastic modulus, tensile strength and compressive strength, is considered indirectly through the thermal damage in the model. Noted that the effect of temperature on the microstructure that affects the mechanical properties has not yet been taken in account in the present model for elevated temperature. Regarding the influence of humidity on mechanical properties, it is assumed moderate effect of humidity on the evolution of elastic modulus and fracture energy. But it has a significant effect on the evolution of tensile strength, so this phenomenon will be considered in the model.

According to (Burlion et al., 2005; Pihlajavaara, 1974; Popovics, 1986), drying effects improve the strength of material due to the capillary suction effect and the confinement effect of the core of specimen by the auto-equilibrated stress system due to drying of the surface. Thus, the reduction of saturation degree increases the tensile strength. This phenomenon is considered in the model through the effect of capillary pressure by a new relationship of R_t and S_l (see Eq. (3-45)). This evolution law is proposed based on the available experimental data such as the results of three-point and four-point bending tests on concrete at 20°C under various degrees of saturation in the framework of ANR MOSAIC project (Bucher et al., 2016) and the results from DCT tests on concrete at 30°C and 90°C under various degrees of saturation in the framework of ANR PIA-MACENA project (Kallel, 2016). Figure 3-44 shows that the tensile strength increases when the material is dry, but this effect is less pronounced on the material subjected simultaneously to the elevated temperature.

$$\frac{R_t}{R_t^{ref}} = 1 - C^{w,Rt} C^{Pc,T} (S_l - S_l^{ref}) \quad (3-45)$$

$$C^{Pc,T} = \begin{cases} \exp\left(-\frac{T - T_{ref}}{T_k^{vg} - T_{ref}}\right) & \text{if } T > T_{ref} \\ 1 & \text{if } T \leq T_{ref} \end{cases} \quad (3-46)$$

With S_l^{ref} is the reference degree of saturation for which the tensile strength R_t^{ref} is determined at the temperature T_{ref} . According to ANR MOSAIC research program, $C^{w,Rt} \approx 0.85$ at 20°C for concrete (Bucher et al., 2016). $C^{Pc,T}$ takes into account the decrease of the positive effect of capillary pressure on R_t with the temperature rising (Eq. (3-46), Figure 3-45) in which $T_k^{vg} \approx 40^\circ C$ is a fitting parameter same as the one used in the temperature-dependent sorption curves in the chapter II.

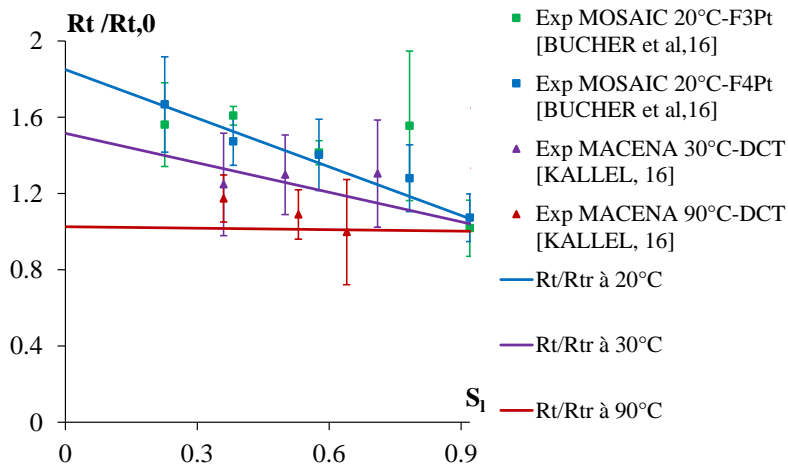


Figure 3-44: Evolution of relative tensile strength with temperature and degree of saturation

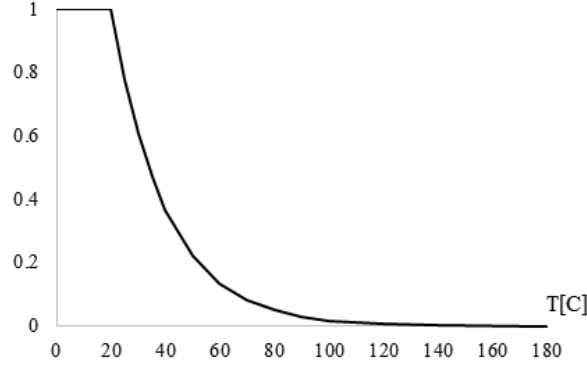


Figure 3-45: Evolution of coefficient $C^{Pc,T}$ at $T_{ref} = 20^\circ\text{C}$

3. 3. 4. 2. Effect of temperature and humidity on damage variable

The thermal activation function C_p^T of creep potential introduced in the creep model (Eq. (3-48) recalled from Eq. (3-21)) amplifies creep if the temperature is above $T_{thr} (\approx 45^\circ\text{C})$. The underlying phenomenon is attributed to the contrast of dilation coefficient between different phases of concrete, cement paste and aggregate, leading to a release of creep sites in temperature. It is possible that this phenomenon comes along with thermal damage, especially if creep site release is due to micro-cracking. In the previous work (Sellier et al., 2013a; Vidal et al., 2014), the thermal damage considers only the effect of temperature. But it is evident that the variation of water content within material affects the damage due to a greater dilation ability compared to other materials, leading to possible overpressure in porous media in autogenous condition or possible micro cracking induced by the complementary shrinkage during the desiccation.

Hence, the effects of water saturation are not only on the mechanical strength but also on the mechanical internal variable i.e. thermal damage variable. Here we present how to consider these effects into the model. The isotropic thermal damage D^{TH} is assumed to link to C_p^T via Eq. (3-47) in accordance with damage theory. In the study area, thermal damage due to physicochemical degradation, particularly the dehydration of the concrete, is considered negligible due to its moderate effect in the temperature range of interest (cf. Chapter 2).

$$D^{TH} = 1 - \frac{1}{A^{Th} (C_p^T - 1) + 1} \quad (3-47)$$

$$C_p^T = \begin{cases} \exp \left[-\frac{E_p^a}{R} \left(\frac{1}{T} - \frac{1}{T_{thr}} \right) \right] & \text{if } T > T_{thr} \\ 1 & \text{if } T \leq T_{thr} \end{cases} \quad (3-48)$$

With $E_p^a \approx 25000 \text{ J/mol}$ the activation energy intrinsic to the materials which control the sensibility of creep to increase with temperature, $R=8.314 \text{ J/(mol.K)}$ is gas constant and $T_{thr} \approx 45^\circ\text{C}$ is the threshold temperature.

A fitting constant A^{TH} accounts for the effect of the saturation degree and controls the damage level at a given temperature (Eq. (3-49)). The latter is computed automatically from the measured thermal damage at 80°C in a saturated state ($D^{TH}(80^\circ\text{C}) \approx 0.15$ based on experimental results of (Ladaoui et al., 2013)) and it can be deduced as follows:

$$A^{Th} = \frac{1}{C_p^T(80^\circ\text{C}) - 1} \left(\frac{S_l \times D^{TH}(80^\circ\text{C})}{1 - S_l \times D^{TH}(80^\circ\text{C})} \right) \quad (3-49)$$

It is noted that the degree of water saturation S_l limits the damage due to temperature if the material is dry.

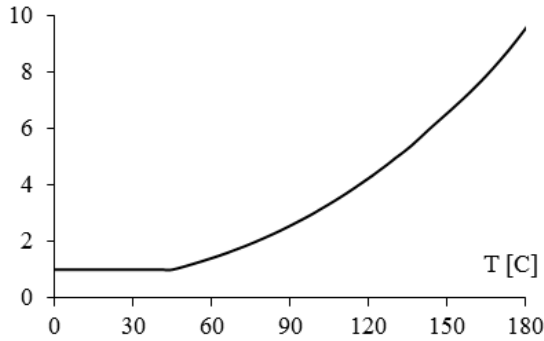


Figure 3-46: Evolution of coefficient C_p^T

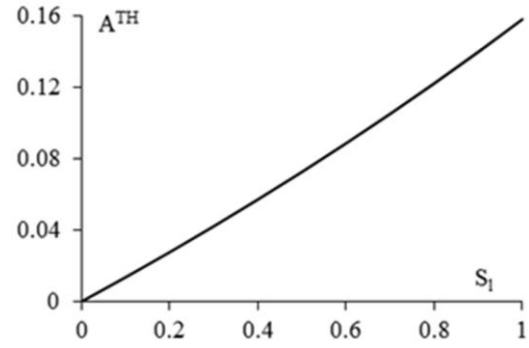


Figure 3-47: Evolution of coefficient A^{TH}

Figure 3-48 illustrates the evolution of thermal damage variable D^{TH} with temperature and degree of saturation. It increases with temperature rise and decreases when the material is dry. An experimental point of thermal damage measured at 80°C in the saturated condition observed from the experimental campaign of (Ladaoui et al., 2013) corresponds to the value of 0.15. Another point measured at 140°C with 50% of S_l obtained from the experimental campaign in the framework of MACENA project (Kallel, 2016) corresponds to value 0.47 instead of 0.3 due to the fact that the notched area seems to be the most humid area in the specimen where the degree of water saturation is potentially high. Besides these, the regulatory standard FIB MC2010 (Vidal et al., 2016) proposed a simplified linear evolution of the thermal damage with the temperature which is also plotted in Figure 3-48 by a dotted line.

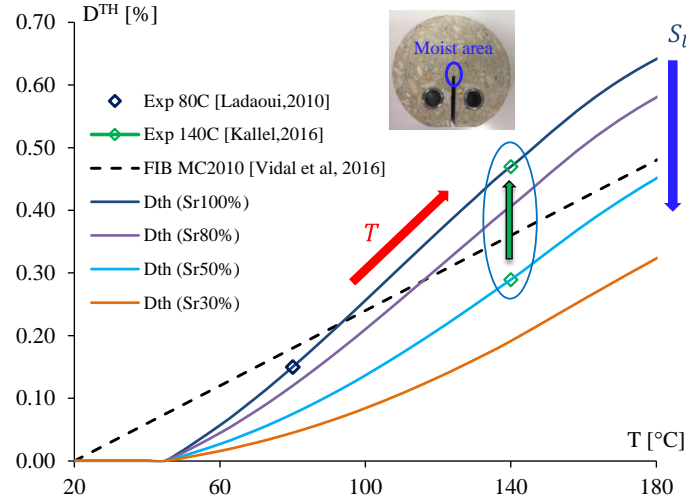


Figure 3-48: Evolution of thermohydric damage coefficient D^{TH}

A new aspect of the model lies in the consideration of the influence of temperature on the effect of capillary depression. The particularity of model is to assume that the drying, which varies with temperature, generates a micro damage that can modify the effect of capillary depression. This micro damage is integrated into a variation of the Biot coefficient which becomes anisotropic under the simultaneous effect of the external stress and the capillary depression. Since the damage is less in the compressed direction, the transmission of the capillary depression is improved, which increases the intensity of the capillary effects in this direction, leading to an additional deformation corresponding to the drying creep (Picket effect).

3. 3. 4. 3. Behaviour law of concrete at high temperature

Figure 3-49 illustrates the stress-strain behaviour of concrete under tension-compression cycles at different temperatures obtained from the numerical model. The weakening of evolution curves at high temperature shows the effect of temperature on the degradation of mechanical properties of concrete in tension as well as in compression.

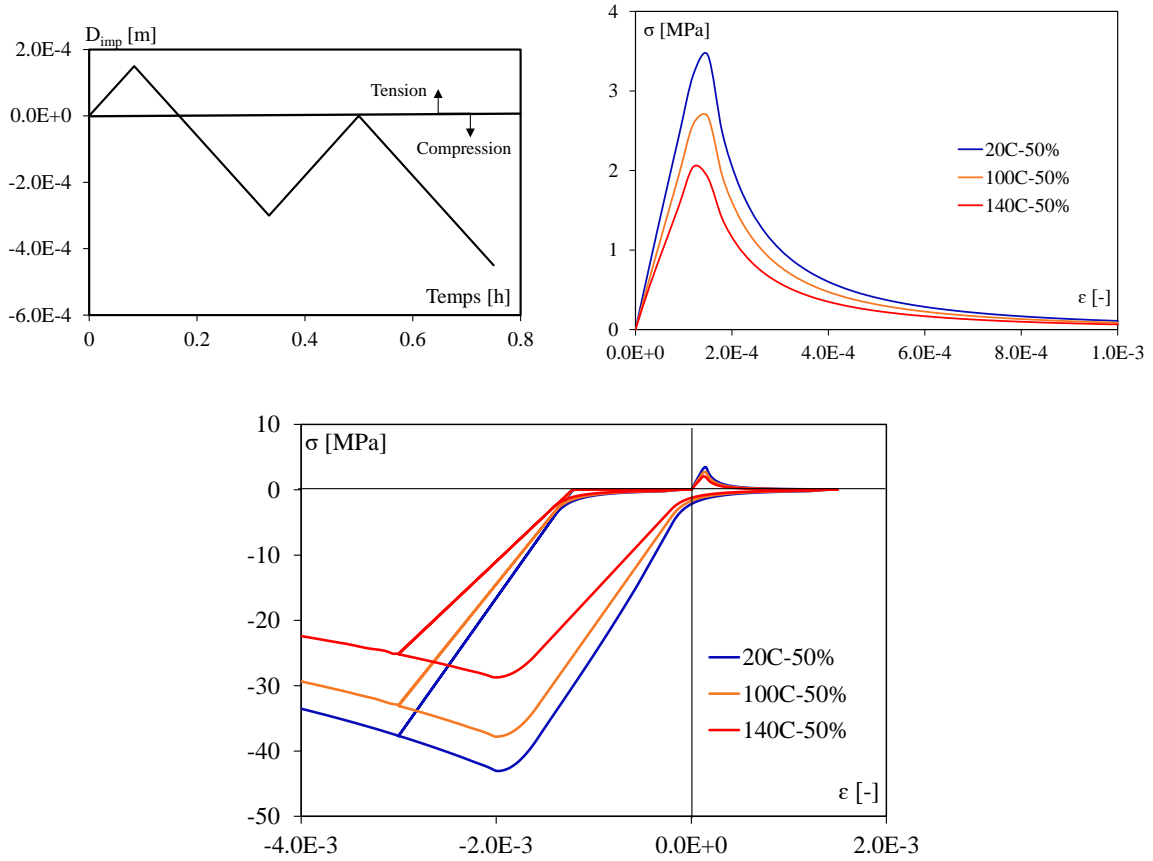


Figure 3-49: Effect of temperature on behaviour law of hardened concrete under tension-compression cycle test

3. 3. 5. Adaptation for reinforced concrete structure

Regarding the limits of the existing approaches (stress concentration, meshing difficulty, and capacity to be applied to either fine or coarse mesh, applicability for large-scale structure...), a new approach is proposed in this contribution which is adapted to concrete model for an application of large-scale structures such as nuclear containment (Figure 3-50). The so-called “Distributed reinforcement” can be used in 3D FE domain using the ratio of steel cross-section inside the concrete in any direction without additional mesh of reinforcements. In particular, it aims at providing the structural effect of reinforcements (without stress concentration) in nonlinear solid mechanics problems involving various types of behaviour laws for the reinforcement and matrix and solved by the finite element method.

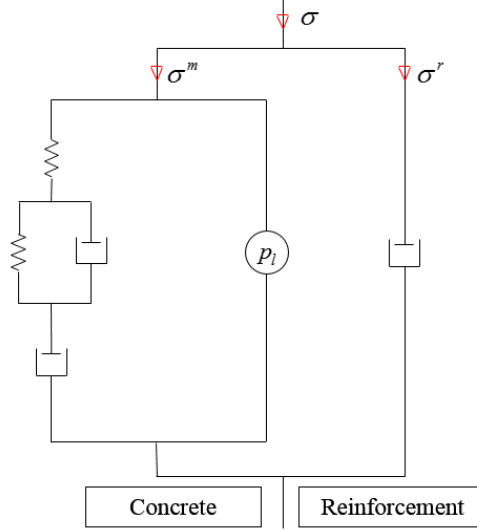


Figure 3-50: Idealized scheme for modelling reinforced concrete

This alternative approach is based on the principle of the homogenized behaviour of the reinforced matrix. It is described via the combination of steel and concrete stresses which are modified upon their directions (\vec{V}^r , with $r \in [1, \dots, n^r]$ and n^r the distributed reinforcement number) and is written by Eq. (3-40).

$$\sigma_{ij} = (1 - \rho^r) \sigma_{ij}^m + \rho^r \sigma^r \quad (3-50)$$

With ρ^r is the cross-section ratio of the reinforcement oriented along the axe \vec{V}^r . σ_{ij}^m is the total stress in the matrix (see Eq.(3-30)) and σ_i^r is the axial stress in the reinforcement computed in each direction of reinforcement by equation (3-51). The behaviour law of reinforcement is elastoplastic with a linear kinetic hardening and a relaxation law.

$$\sigma^r - \sigma_0^r = E^r (\varepsilon^r - \varepsilon^{r,pl} - \varepsilon^{r,m} - \varepsilon^{r,k}) \quad (3-51)$$

Where E^r the reinforcement Young modulus, ε^r the axial strain in the reinforcement, $\varepsilon^{r,pl}$ its plastic strain, $\varepsilon^{r,m}$ its permanent viscous strain and $\varepsilon^{r,k}$ its reversible viscous strain (in a same way than for the concrete as explained in chapter 4). σ_0^r is the possible pre-stress applied to the reinforcement as initial stress (not induced by the computed strain field).

The plastic criterion of reinforcement is uniaxial and it models a linear kinetic hardening:

$$f^r = |\sigma^r - H^r \varepsilon^{r,pl}| \leq f_y^r \quad (3-52)$$

In Eq. (3-52), H^r is the hardening modulus and f_y^r is the elastic limit for the reinforcements.

To evaluate the modelling method of distributed reinforcement (cf. subsection 3. 3. 5.), the full modelling is applied to a reinforced beam which is used firstly in a theoretical case study in the numerical benchmark MECA, in 2003 (Ghavamian and Delaplace, 2003), secondly in

the numerical benchmark CEOS (CEOS.fr, 2009a, 2009b) and by other authors (Richard et al., 2010). The experimental program was conducted in “Ecole Centrale de Nantes”. The test was a three-point bending test and the tensile behaviour of reinforced concrete in term of the load-deflection curve obtained by experiment and model will be compared to validate the numerical implementation of the method. The material characteristics for this experiment are given in Table 3-2 and Table 3-3. The geometry of the beam and its boundary conditions are provided in Figure 3-51. As the probabilistic scale effect is applied (cf. Chapter 5), a hypothesis of double symmetry of problem is not used. As the beam was reinforced against the bending moment by two longitudinal ribbed bars 32 *mm* in diameter, the steel ratio is more important in this direction than in other directions which can be seen clearly in Figure 3-52(a, b, c) (the detail of top longitudinal rebars and the stirrups can be found in (Sellier et al., 2013b)). And a comparison of experimental crack pattern and computed damage pattern for load 90kN is illustrated in Figure 3-52(d). Moreover, the results obtained from the numerical modelling with distributed reinforced method were successfully compared with experimental results in terms of crack pattern and force-deflection curves (Figure 3-53).

Table 3-2 : Concrete characteristics

Parameters	Value
Young modulus E	37 200 MPa
Poisson coefficient ν	0.27
Tensile strength R_t	3.45 MPa
Strain at R_t (ε_t^{peak})	$1.2 R_t / E$
Fracture energy in tension G_f^t	1.10^{-4} MN/m
Compressive strength R_c	36 MPa
Strength at R_c (ε_c^{peak})	2.10^{-3}
Fracture energy in compression G_c^t	1.10^{-2} MN/m
Drucker-Prager parameter δ	0.15

Table 3-3 : Steel characteristics

Parameters	Value
Limit of elasticity	466 MPa
Tensile strength	615 MPa
Young modulus	195 GPa
Poisson coefficient	0.20

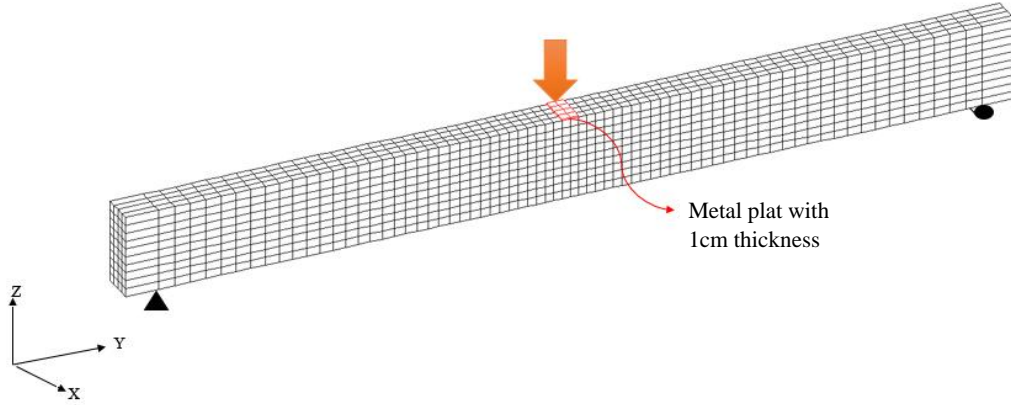


Figure 3-51: Concrete mesh and mechanical boundary conditions

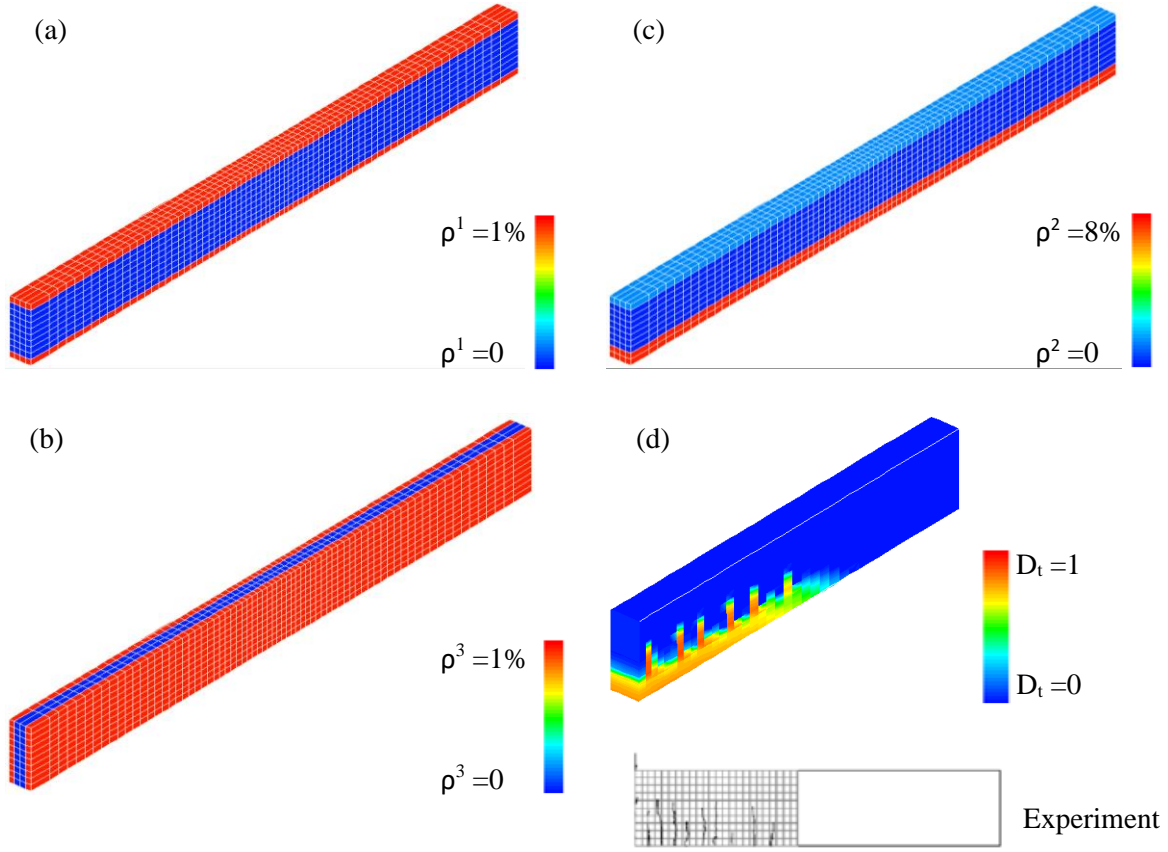


Figure 3-52: (a), (b), (c) Steel ratio in three directions X, Y, Z and (d) Comparison of experimental crack pattern (below) and computed damage pattern (above) for load 90kN

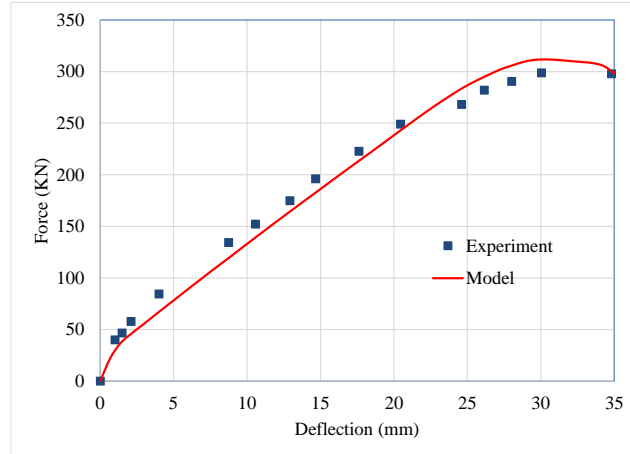


Figure 3-53: Comparison of experimental and calculated force-deflection curves

The new developments made to model are proposed and presented and the part of reinforcement modelling is already validated with the experiment as seen above, but the part of concrete modelling is not yet validated for concrete at high temperature. Therefore, the next paragraph will present the application of model to the MACENA experiments in order to validate the new evolution laws of concrete proposed earlier.

3. 4. Applications of MACENA experiments (LMDC, IPPRA, CERIB)

As previously presented, the model used here is based on the poromechanical framework and implemented in the finite element code CAST3M (CEA, 2015). This paragraph presents the application of model to campaign experiments of MACENA to test its ability to model the effects of temperature and humidity on the concrete behaviour. Noted that the MACENA experiments have been conducted on the VeRCoRs concrete because this MACENA project aims modelling the behaviour of vessel structure VeRCoRs during the LOCA induced conditions. In this work, the continuous lines in the figures are derived from modelling, the points correspond to experimental results.

3. 4. 1. Formulation of VeRCoRs concrete

The experimental tests were performed on the VeRCoRs concrete whose mix design is given in Table 3-4.

Table 3-4: Mix design of VeRCoRs concrete

Component	Mixture proportions (kg/m ³)
Cement CEM I 52.5 N CE CP2 NF « GAURAIN »	320
Dry sand 0/4 REC GSM LGP1 (13% of CaO and 72% of SiO ₂)	830
Gravel (fully saturated) 4/11 R GSM LGP1 (rounded, silicate and limestone)	445
Gravel (fully saturated) 8/16 R Bally (rounded, silicate and limestone)	550
Plasticizer SIKAPLAST TECHNO 80	2.4
Total water	197.5

3. 4. 2. Identification of model and material parameters

During the MACENA project, the concrete used to cast VeRCoRs structure was largely characterised for its instantaneous and delayed behaviour at different laboratories (EDF, LMDC, CERIB, IFSTARR Nantes, and SIAME). These characterisations allowed the THCM model to be fitted.

The three parameters of hydration model (k, r_k, n) have been determined and validated in chapter I and the evolution of hydration development over time obtained by hydration model is shown in Figure 3-54.

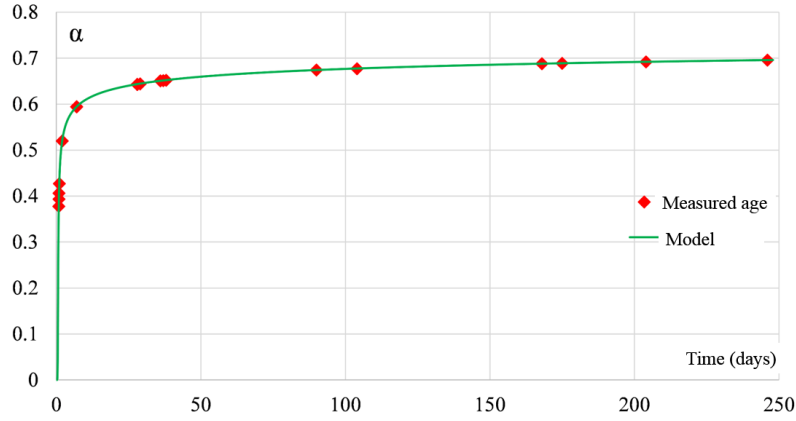


Figure 3-54: Hydration development at centre of 11 x 22 cm specimen obtained from hydration model (points represent ages of concrete used for measures)

In order to obtain the evolution of instantaneous characteristics of concrete (compressive/tensile strength, Young's modulus) according to hydration development, the mechanical tests have to be carried out on the concrete at different ages. In our approach, we consider the evolution law of mechanical properties according to the hydration degree given by Eq. (3-43). The evolution of these characteristics with the hydration degree is presented in Figure 3-55 and the associated parameters are given in Table 3-5.

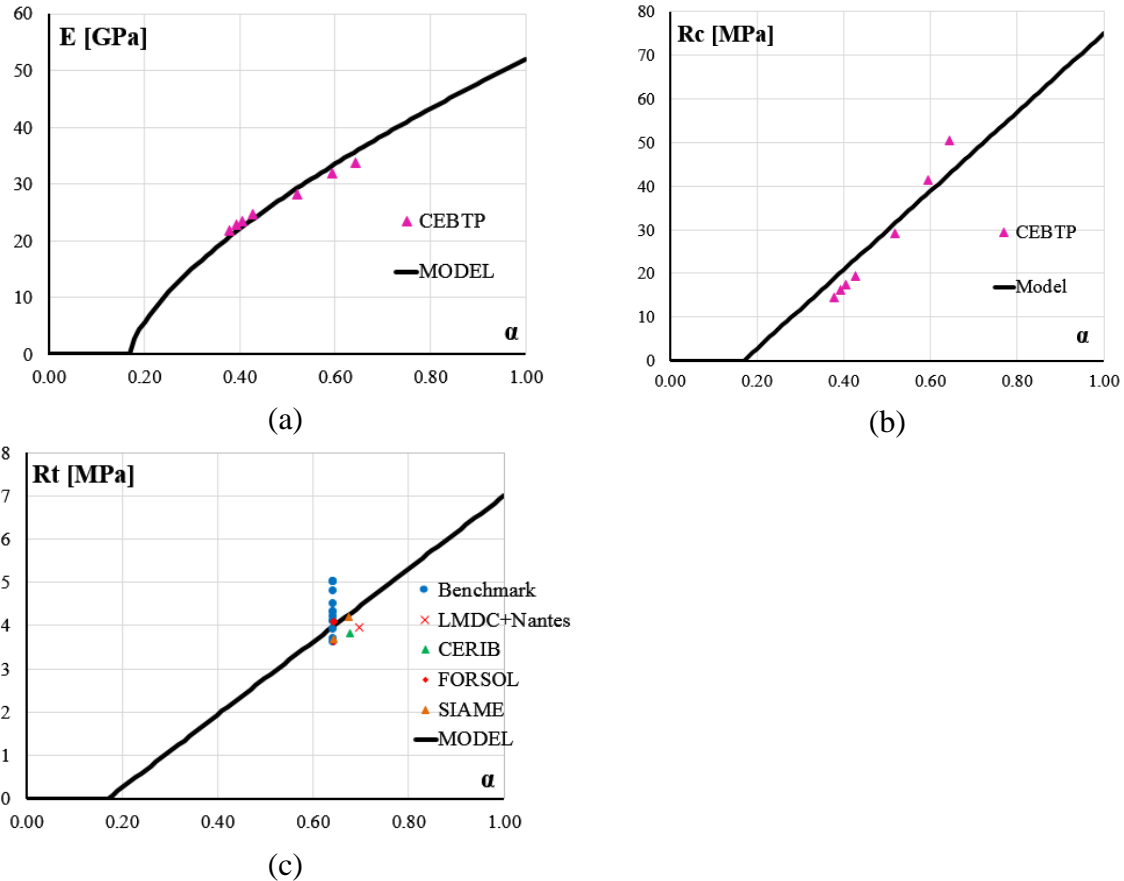


Figure 3-55: Evolution of instantaneous characteristics according to hydration development (a) E , (b) R_c , (c) R_t (experimental results obtained from different laboratories in MACENA project)

The delayed behaviour of concrete i.e. shrinkage and creep were measured on the hardened concrete (Nguyen et al., 2017a) and were used to fit the visco-elastic parameters of rheological model. The creep tests were performed on cylindrical specimen with dimension 11 x 22 cm in compression under a loading at 30% and 60% of R_c . The results of calibrating the creep parameters (found in Table 3-5) on creep and shrinkage tests are presented in Figure 3-56.

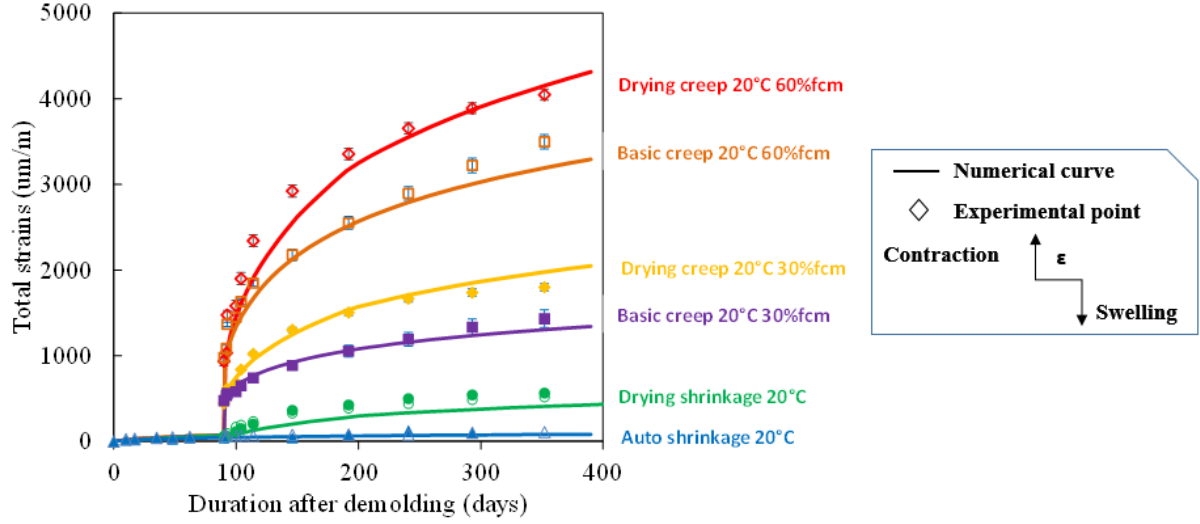


Figure 3-56: LMDC test of concrete creep under uniaxial compression at 20°C ($f_{cm} \approx 52\text{MPa}$)

Once all the parameters are identified for ambient temperature, we can use the model to estimate the concrete behaviour under different thermohydric conditions. In the following paragraph, the response of model will be confronted with the experimental results to validate the new evolution laws relating to the effect of temperature and humidity proposed in this work.

Table 3-5: Model parameters issued from literature (and common for similar concretes) and material parameters for the VeRCoRs's concrete (in **bold and red symbol**)

Parameter	Definition	Unit	Value	References
Basic thermo-elasticity				
α_{th}	Thermal dilation coefficient	-	1.2e-5	(EDF, 2014)
ν	Poisson ratio	-	0.2	(EDF, 2014)
Basic plasticity				
ε_{Rt}^{pk}	Strain at tension peak	-	1.0e-4	Common value for similar concrete (Sellier, 2015)
ε_{Rc}^{pk}	Strain at uniaxial compression peak	-	2.0e-3	
δ	Drucker Prager (DP) confinement coefficient	-	1	
β	Dilatancy for non-associated DP plastic flow	-	0.15	
$\tilde{\sigma}_{rcl}$	Reclosure characteristic stress	MPa	5	
Solidification				
$R_{c,ref}$	Compressive strength for hydrated concrete	MPa	75	Calibration on the evolution of $E(\alpha)$, $R_c(\alpha)$, $R_t(\alpha)$ (Figure 3-55)
$R_{t,ref}$	Tensile strength for hydrated concrete	MPa	7	
E_{ref}	Young's modulus for hydrated concrete	GPa	52	
α_{thr}	Hydration percolation threshold	-	0.17	
Creep				
τ_{ref}^k	Characteristic time for Kelvin module	Day	2	Calibration on creep tests à T_{ref} =20°C (Figure 3-56)
ψ^k	Kelvin stiffness / Young module ratio	Day	5	
τ_{ref}^M	Characteristic time for Maxwell module	Day	15	
ε_{ref}^M	Creep potential characteristic strain	-	25.0e-5	
χ^M	Non-linear creep potential multiplicator at 66% R_c	-	2	Common value for similar concrete (Sellier, 2015)

E_A^M	Activation energy for creep potential amplification in temperature	J/mol.K	2.0e4	Common value for similar concrete (Ladaoui, 2010)
k^{DTT}	Transient thermal creep amplitude constant	-	3.0e-7	Common value for similar concrete (Cagnon, 2015; Ladaoui, 2010)
D_{max}^{cr}	Maximal creep damage	-	0.1	Common value for similar concrete (Sellier, 2015)
Capillary pressure effect				
ϕ	Porosity	m^3/m^3		Results issued from hydration model (cf. Chapter I)
V_w	Water content	m^3/m^3		
b	Biot coefficient (for saturated material and free from stresses)	—	0.6	Calibration on autogenous shrinkage test (Figure 3-56)
M_{shr0}	Reference Van Genuchten modulus	MPa	10	Calibration on isothermal curves at different temperature (cf. Chapter II)
m_{vgn}	Van Genuchten exponent	-	0.26	
T_{kvgn}	Characteristic temperature for isothermal curve at high temperature	°C	40	
σ_{dc}	Desiccation characteristic stress	MPa	14	Calibration on drying creep test (Figure 3-56)
Damage				
T_{thr}	Damage temperature threshold	°C	45	Common value for similar concrete (Ladaoui et al., 2013) (Figure 3-48)
D_{80}^T	Thermal damage at 80°C	-	0.15	
G_t^f	Fracture energy in tension	J/m^2	100	Common value for similar concrete (Sellier, 2015)
G_c^f	Tensile crack reclosure energy	J/m^2	200	
$\varepsilon^{k,s}$	Characteristic plastic strain for DK associated damage	—	2.0e-3	
Effect of water saturation rate on R_t				
S_l^{ref}	Characteristic water saturation rate for R_t	—	0.9	Common value for similar concrete (Bucher et al., 2016; Kallel, 2016) (Figure 3-44)
$C^{w,Rt}$	Coefficient of sensitivity of R_t versus S_l	—	0.85	

3. 4. 3. Validation of new evolution laws with experiments

This part is devoted to the validation of new evolution laws concerning the influence of temperature and humidity on the instantaneous and delayed behaviour of concrete. The experimental results are obtained in the framework of MACENA project.

3. 4. 3. 1. Instantaneous behaviour under effect of temperature and humidity

First of all, we will test the instantaneous behaviour of concrete under different thermohydric conditions. The disk-shaped compact tension (DCT) tests have been chosen and performed by (Kallel et al., 2016) to investigate the mechanical behaviour of concrete under the homogeneous condition of moisture and temperature because the samples have a specific geometry that allows reducing the volume under pressure during the test. The geometry and mesh of DCT specimen are illustrated in Figure 3-57.

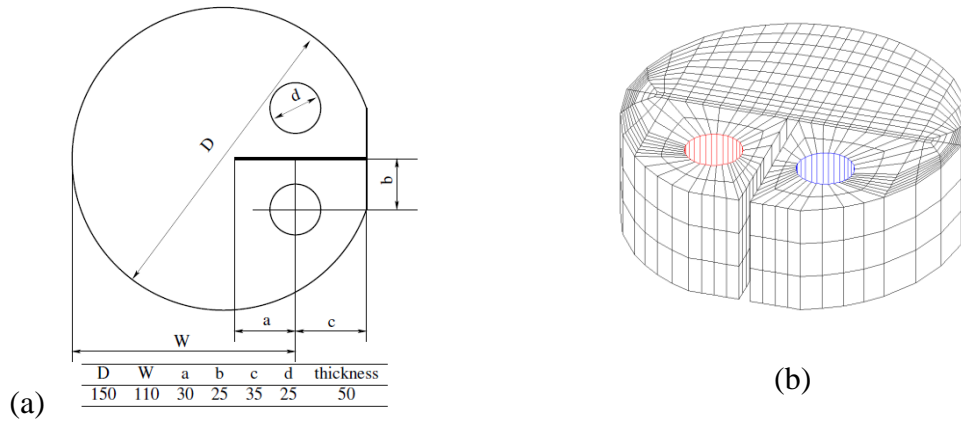


Figure 3-57: DCT specimen (a) and its mesh (b)

The thermal loading is applied by means of a temperature imposed on the whole volume of the specimen. The test was modelled with the damage model in 3D mode. The specimens are placed in a controlled hydrometric condition before carrying out mechanical tests.

Figure 3-58 compares the model responses to the experimental results. We obtain a good agreement for the curve at 20°C with 50% of S_f . Moreover, we observe the degradation of mechanical properties at 140°C and an increase of properties when it is dry. These phenomena are also reproduced by the model. The peak of curves representing the tensile strength of material obtained from model correspond to the ones of experiment. However, the pre-peak slope which corresponds to the elastic modulus of material at 140°C is over-estimated by the model. It should not be neglected that the experiment tests for temperature higher than 100°C are few and complex to perform, therefore subjected to some uncertainty in terms of local displacement measures. So, considering the underlying physical phenomena already considered in the model in one hand, and its ability to retrieve the strengths and creep velocities

at different temperatures and humidity, it was decided to not more complicate the behaviour law while these last experiments are not reiterated.

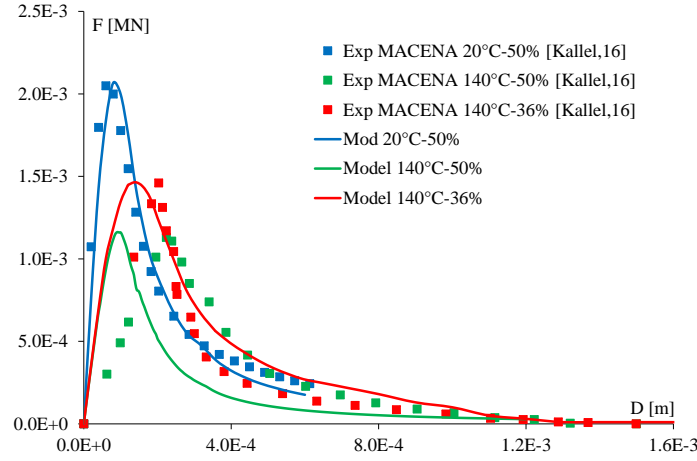


Figure 3-58: Force-displacement evolutions under variable TH conditions

3. 4. 3. 2. Delayed deformations in compression at moderate temperature

Regarding the creep tests at moderate temperature (40 °C), they were performed at LMDC (Nguyen et al., 2017a). The strains of concrete are obtained from cylindrical specimens (11 x 22 cm²) loaded under stress of 30% f_{cm} (about 15 MPa) and then heated to the required temperature level with a heating rate of 0.1°C/minute. Figure 3-59 highlights the evolutions of deformations of concrete at 40°C measured from the moment of loading, in both conditions, endogenous and desiccation with 50% of relative humidity. It shows a good agreement between the model and experiments, except at 60% 40°C for which the creep velocity seems a little bit overestimated. A better fitting is possible reducing the non-linear creep parameter (χ in eq 3.26), but this section concerns the validation and not the fitting, so it was decided to keep the value fitted in last section. For the definitive modelling of VERCORS it is planned to fit the definitive parameters on the overall experimental program available at the end of MACENA project, including this test, but also the pre-stressed beams studied in LMDC and not yet simulated.

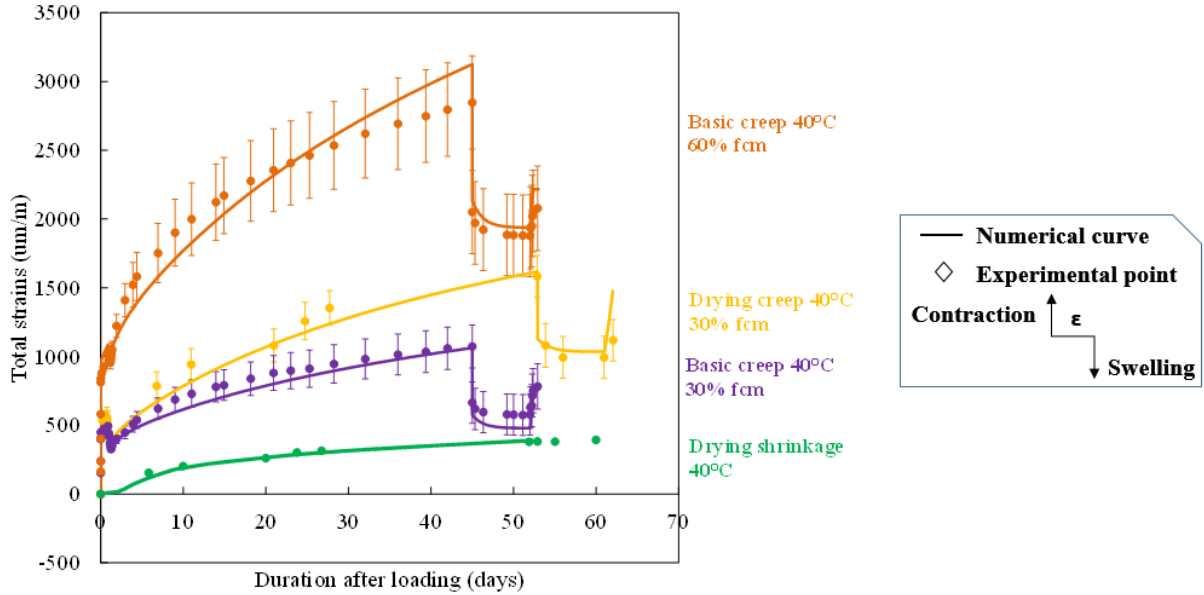


Figure 3-59: Strains of concrete at 40°C

3. 4. 3. 3. Delayed deformations in compression at high temperature

For creep tests in compression at elevated temperatures (100 and 180°C), CERIB (Daval, 2015) carried out tests on cylindrical specimens with a diameter of 10 cm and a length of 30 cm. The specimens are loaded under stress of 30% f_{cm} (13.5 MPa) and then heated with a heating rate of 1°C/minute until the required temperature. It is noted that the average value of compressive strength measured at 28 days given by CERIB is 45 MPa. These tests were performed in an environment where the water state is uncontrolled. Before reaching the stability of required temperature, the concrete specimens obviously undergo a significant drying. So, the decrease of degree of water saturation is not negligible and has been taken into account in the calculation. The thermal loading is applied by mean of an imposed temperature on the whole volume of the specimen. The hypothesis of axisymmetric of the problem is also applied. Figure 3-60 shows the comparison of compressive creep at 40°C, 100°C and 180°C obtained experimentally and numerically. These evolutions are measured from the moment of loading.

The results obtained in Figure 3-60 and Figure 3-61 highlight three important aspects: first, the phenomenon of the transient thermal creep appears when the specimens are loaded before the heating. If we look at the creep evolutions at the first few days, the transient thermal creep occurs simultaneously with thermal expansion and drying shrinkage as soon as the concrete specimens undergo the heating. Secondly, the effect of temperature favours the creep phenomenon. Last but not least, the effect of saturation degree also play an important role on the creep velocity and amplitude as we can see, creep at 40°C is greater than creep at 100°C because when the material is drier, it undergoes less creep strains. It is recalled that the specimens of CERIB at 100°C were very dry compared to those of LMDC at 40°C.

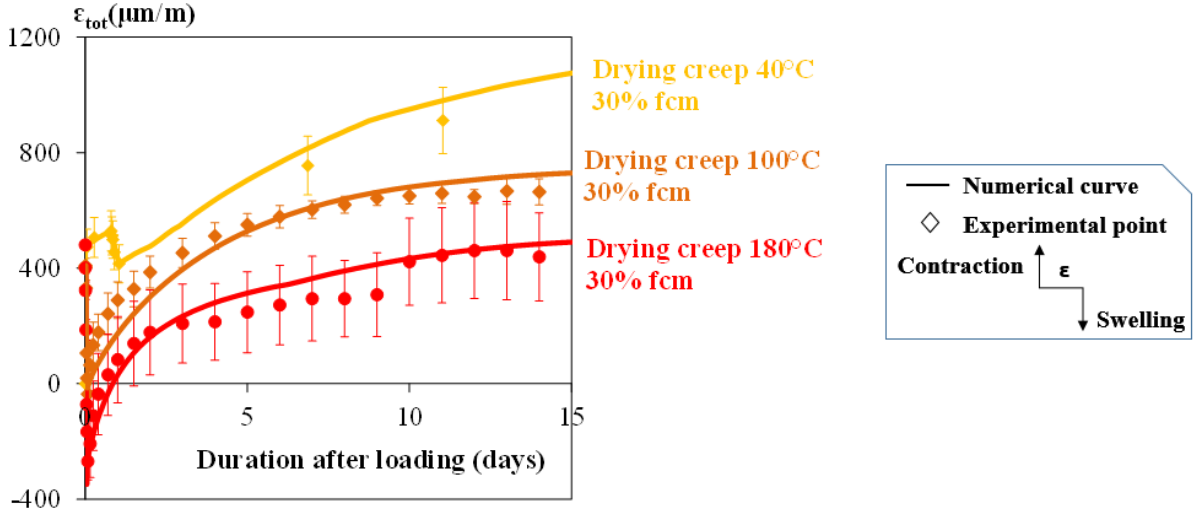


Figure 3-60: Uniaxial drying creeps of concrete in compression at 100 and 180°C (CERIB tests) and at 40°C (LMDC test)

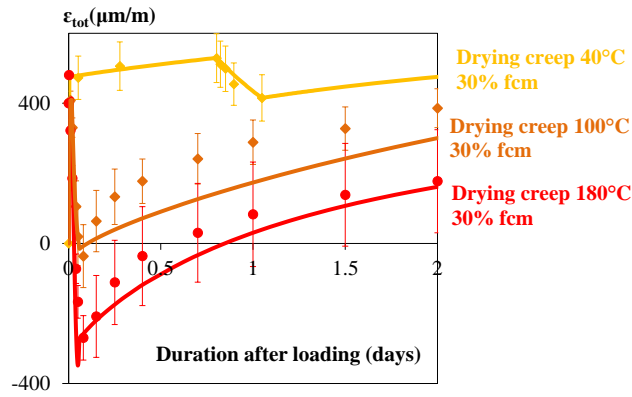


Figure 3-61: Deformation during the 2 first days of creep tests in temperature

3. 4. 3. 4. Delayed deformations in tension at high temperature

The specimens dedicated to the creep tests in tension are cast in specific steel moulds whose form has been optimized in order to limit stress concentrations (Daval, 2015). The latter has a central cylindrical part with a central diameter of 80 mm over a length of 120 mm and two conical ends (extreme diameter of 120 mm) for a total height of 610 mm (Figure 3-62). These tensile tests are carried out in accordance with RILEM TC 129 which follows these steps: first, pre-loading at 1 kN, then heating to the required temperature with a heating rate of 1°C/min and stabilizing the uniform temperature under pre-load about 1 hour. The loading in tension was applied to specimens with a speed of 0.05 MPa/s until it breaks (failure test) or the prescribed force (creep test under 1.15 MPa of loading). The strains were measured throughout the duration of the test. The comparison of tensile creep at 100°C and 180°C obtained from experiment and model is illustrated in Figure 3-63.

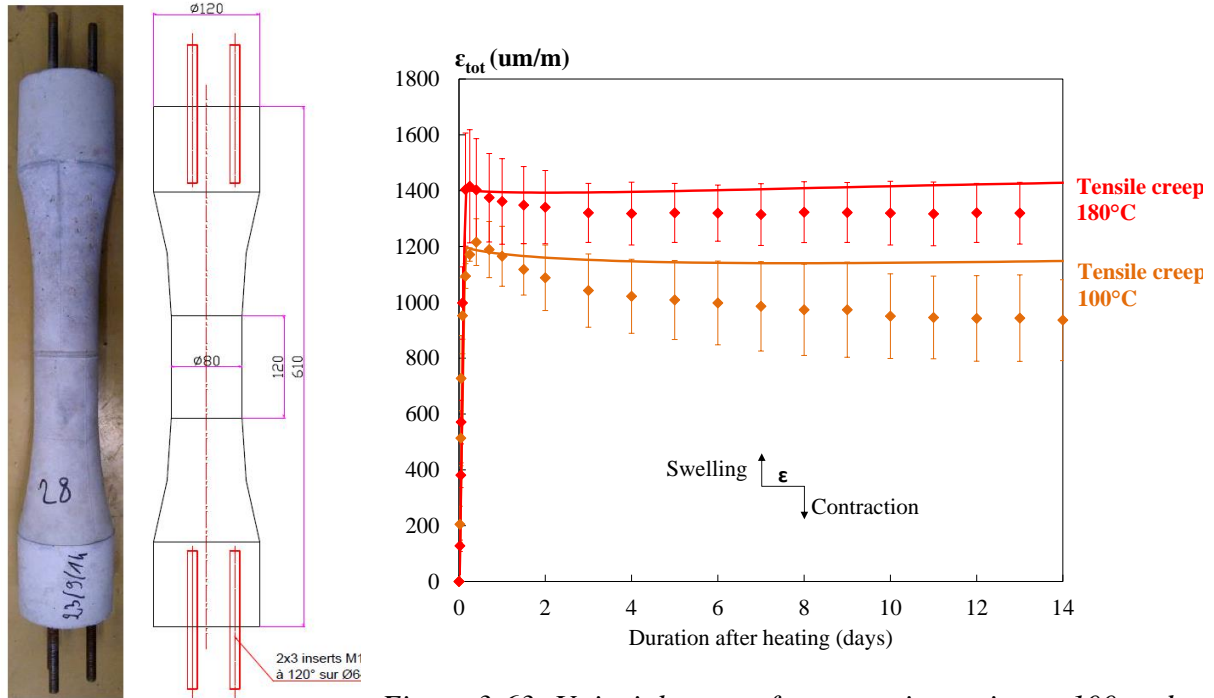


Figure 3-63: Uniaxial creep of concrete in tension at 100 and 180°C (CERIB tests)

Figure 3-62: Geometry of specimen for creep tests in tension (Daval, 2015)

The underestimation of shrinkage at high temperature could be due to a slight misestimation of the mass loss in temperature, which has been assessed approximately from other specimens weighted before and after a similar heating. A parametric study with some variants of mass loss could allow improving the simulation, but the ideal would have been to measure the mass loss during the tests, unfortunately the CERIB's experimental setup did not allow this functionality.

3. 5. Conclusion

This chapter shows that the developed relationships allow to provide a good statistical fit of the available experimental data: All the experiments provided by ANR MACENA and MOSAIC, concerning the effect of temperature and humidity, are referenced. Among these test some were used in order to fit the model while other are used to validate it. The chapter also includes numerous other experimental evidence retrieved in the scientific literature.

A relatively simple damage law, taken into account the influence of temperature and saturation degree of the material, has been proposed to model DCT tests under variable thermohydric conditions. The behaviour of concrete in temperature is in fact relatively complex, and it becomes more complicated when its saturation degree is variable since the two effects are interactive. It would, of course, be necessary to carry out other experimental designs to check whether the law proposed here is applicable to other concretes under well-controlled thermohydric conditions.

The model considers at the structural scale the effects of differential expansion between the concrete components at lower scales (aggregate and paste leading to the thermal damage), the transient thermal creep, the influence of the temperature on capillary pressure, the degree of saturation and the loading rate on the creep rate. The results obtained provide a satisfactory behaviour of the model with respect to the experiment.

The next chapter will supply applications of this model to several RC elements at different scales and in various THM conditions, in order to test its reliability to finally be used at the scale of a whole structure in the last part of the thesis.

CHAPITRE IV

Effect of temperature and prestress ratio on relaxation of prestressing wires

« *Il vaut mieux se disputer avec quelqu'un d'intelligent que parler à un imbécile* » Intelligent & Mieux

4. 1.	Introduction.....	140
4. 2.	State of the art.....	141
4. 2. 1.	Temperature influence on mechanical properties of prestressing wires	141
4. 2. 2.	Temperature influence on the relaxation of prestressing tendons.....	143
4. 3.	Development of relaxation model.....	145
4. 3. 1.	Model principles.....	145
4. 3. 2.	Nonlinear Maxwell level strain.....	146
4. 3. 2. 1.	Non-linear effect of loading ratio.....	147
4. 3. 2. 2.	Temperature effect	148
4. 3. 3.	Kelvin level strain	149
4. 3. 4.	Numerical implementation.....	150
4. 4.	Applications	151
4. 4. 1.	Identification of model and material parameters.....	151
4. 4. 2.	Validation	154
4. 5.	Conclusion	155

4. 1. Introduction

In the context of extending the life of nuclear containment structures, which form the third and last protection barrier of a nuclear reactor building, prestressing steel wires with high elastic limit and high tensile strength are required to improve the tensile strength of the whole concrete structure and to prevent possible leakage of radioactive elements in case of an accident with potential failure of the first two barriers. However, steel wires can undergo a loss of tension (relaxation) when they are subjected to an imposed strain, especially when they are simultaneously subjected to high temperature (Shakya and Kodur, 2016; Hou et al., 2014; Atienza and Elices, 2009; Elghazouli et al., 2009; Li et al., 2003) as could be the case during an accident (Anderson, 2005; Glodowski and Lorenzetti, 1972; Zeren and Zeren, 2003).

In the structures studied in this work (Nuclear vessel in accident conditions), the rebars and tendons of the prestressed concrete containment structure may be subjected to temperatures up to 140°C. The evaluation of the long-term reliability of these structures exposed to such temperature increases, and thus requires a numerical model able to predict the relaxation of prestressing wires considering the impacts of variable temperature and initial loading (prestress). Moreover, as the influence of variation in temperature and loading ratio on the relaxation rate tends to be relatively complex, the necessity for an efficient incremental model to simulate the delayed strain of prestressing wires in different thermomechanical conditions is clear. Adapted from an incremental rheological model of delayed strain in concrete (Sellier et al., 2016), the present model is proposed to take the non-linearity of thermomechanical couplings into account.

This chapter presents a model of prestressing steel relaxation under various levels of loading and temperature. This incremental model enables the delayed strain of prestressing steel wires to be calculated and takes the non-linear coupling of temperature and loading effects into account. The originality of this work lies in a comparison between experimental data and results predicted by the model. Two laboratories collaborated in this work: IFSTTAR/SMC and LMDC. The first part of the chapter briefly recalls the previous studies on the influence of temperature on the mechanical properties and relaxation of prestressing wires. Then, in the second part, the constitutive equations of the proposed model are given, followed by a numerical implementation. In this part, the influence of temperature on relaxation rate is pointed out and the non-linear relation between loading ratio and relaxation rate is also modeled, in the same ways as the thermomechanical coupling. In the third part, various

relaxation tests are simulated and the numerical predictions are compared to experimental results for all the kinds of thermo-mechanical conditions envisioned during experiments. These tests concern stress relaxation at various loading ratios and temperatures, and stepwise cooling/heating in which prestressing steel wires are subjected to unloading/reloading during the temperature changes.

4. 2. State of the art

Prestressed concrete is frequently used for nuclear containment due to its confinement of radioactive material especially in an accident. After 40 years of operation and monitoring, most of reactor containment present the prestressing losses that can be much greater than the design estimation based on the usual standard laws, thus reducing the actual service lifetimes of the structures (Anderson, 2005; Glodowski and Lorenzetti, 1972). Beside this ageing mechanism, previous studies about delayed mechanical behavior of prestressing steel have pointed out an increase of delayed strains inducing relaxation with the temperature rise: the relaxation loss at 20°C can be multiplied by a factor 2 to 8 at 140°C for the initial prestress ratio of 0.7 and 0.8 respectively (Toumi Ajimi et al., 2017), thus coupling between heating and initial tension can accelerate the relaxation phenomenon.

4. 2. 1. Temperature influence on mechanical properties of prestressing wires

In the international literature, the degradation of mechanical properties of prestressing steel in fire have been extensively studied for temperature above 300°C (Abrams and Cruz, 1961; Atienza and Elices, 2009; Fan and Lu, 2001, 2002; Gales et al., 2012; Li et al., 1998; Wang et al., 2010; Xin, 2009; Zheng and Zhang, 2006; Zheng et al., 2006; Zhou et al., 2008). However, many of them are more concerned with fire condition where temperature is above 300°C. According to (Kodur and Dwaikat, 2007), the critical temperature, defined as the temperature at which steel (reinforcement) loses 50% of its ultimate strength, is taken as 426°C for prestressing steel strands and wires. And there are fewer studies carried on temperature between 20°C and 140°C which corresponds to LOCA condition in nuclear reactor containment. The studies of (Elghazouli et al., 2009; Hou et al., 2014; Li et al., 2003; Rostasy et al., 1991) show that low elevated temperature seems to have slight influence on the mechanical tensile properties of prestressing steel. Moreover, in a recent study of (Toumi Ajimi et al., 2017) on the central wire of seven-wires prestressing tendons (ultimate strength of 1860 MPa with a diameter of 15.2 mm) under a temperature range from 40°C to 140°C, it can be observed a

slight decrease of ultimate tensile strength R_m , the characteristic yield stress $R_{p0.1}$ and the elastic modulus E with temperature (Figure 4-1). Only the experimental result of yield stress shows a slight evolution lower than an estimation expected by (Eurocode 2, 2005). The results regarding the evolution of tensile behavior with temperature are given in Table 4-1.

Table 4-1 : Experimental mechanical properties of prestressing wires (tensile tests) (Toumi Ajimi et al., 2017)

Maximum temperature, °C	f_y , MPa	E , GPa
20	1867 +/-3	226.1 +/- 5.0
40	1854 +/-15	226.3 +/- 0.9
100	1793 +/- 4	224.5 +/- 3.4
140	1726 +/- 14	213.4 +/- 1.1

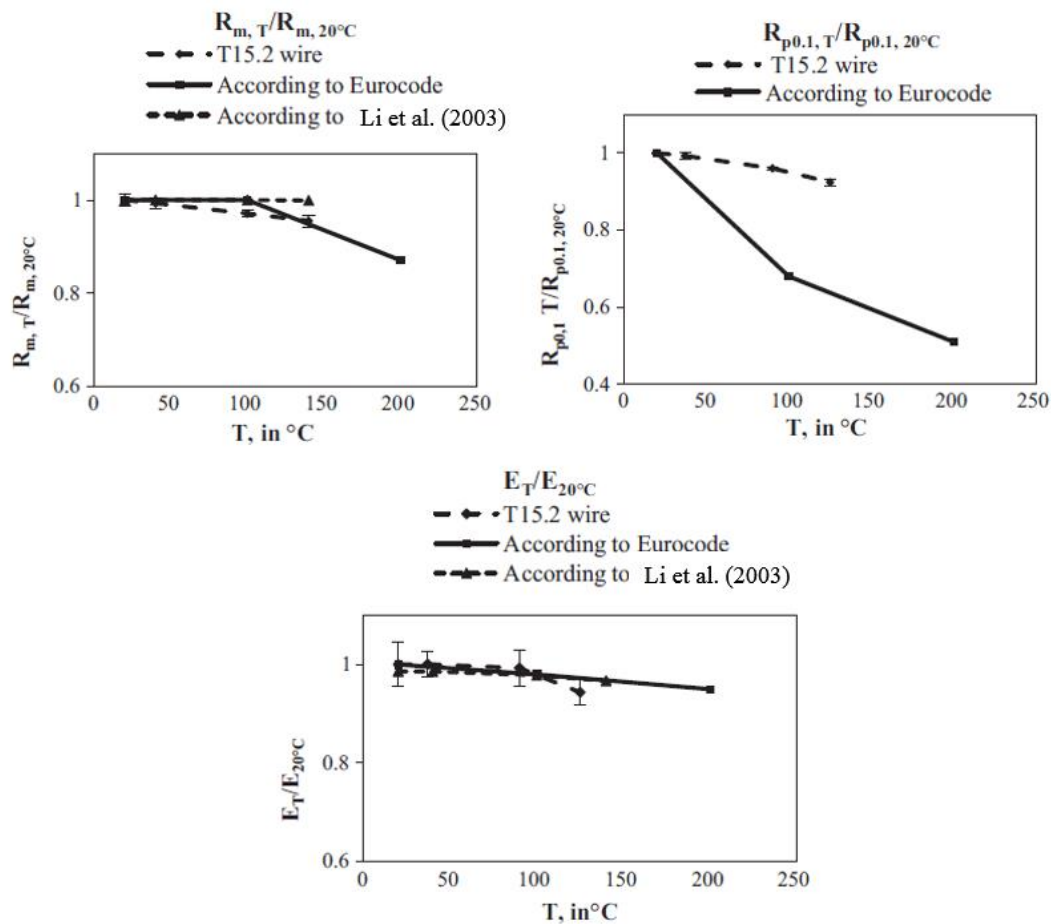


Figure 4-1: Evolution of mechanical tensile behavior of prestressing wires with temperature (Toumi Ajimi et al., 2017) and comparison with (Eurocode 2, 2005) and (Li et al., 2003)

4. 2. 2. Temperature influence on the relaxation of prestressing tendons

Relaxation phenomenon refers to the decrease in stress as a function of time at a constant strain. The relaxation topic has been less deeply investigated than the tensile behavior, especially regarding the influence of the temperature and the prestress ratio.

Predicting the stress relaxation of prestressing steel tendons is usually dealt with in the standard codes by using empirical laws determined for a specific and constant initial load and temperature (BPEL, 1999) (BPEL annex 2, article 3 & BPEL annex 6, article 4.1).

However, the previous studies has investigated that the initial prestress has an significant effect on the relaxation behavior of wires (Magura et al., 1964; Martinez-Perez et al., 2005; Ravera et al., 1984). In the experimental work of (Erdelyi, 1989), it is reported that relaxation value increases from 1.8% to 5.1% for loading ratios varies from 60% to 90% on a prestressing central wire after 5000 hours of test. Several models have been proposed using the code formulas to consider the effect of initial prestress on relaxation (Bazant and Yu, 2013; Eurocode 2, 2005; Magura et al., 1964) but they do not take the effect of temperature into account, despite its strong influence on relaxation rate as reported by (Atienza and Elices, 2009; Raharinaivo, 1978; Rostasy et al., 1991).

That is why , in the framework of ANR PIA-MACENA project, an experimental program was designed on T15.2 prestressing wires at different temperature levels and under different loading ratios, this work is described in (Toumi Ajimi et al., 2017). The stress relaxation tests were performed on central steel wires at constant temperature, using a maximum value of 20°C, 40°C, 100°C or 140°C. In stress relaxation investigations, two levels of initial stress ratio (0.7 and 0.8) were studied for each temperature level. The Figure 4-2 showed that the relaxation was more affected at higher temperature and higher stress ratio. In addition, at 20°C, two other initial stress ratios were investigated: 0.6 and 0.9 (Toumi Ajimi et al., 2017).

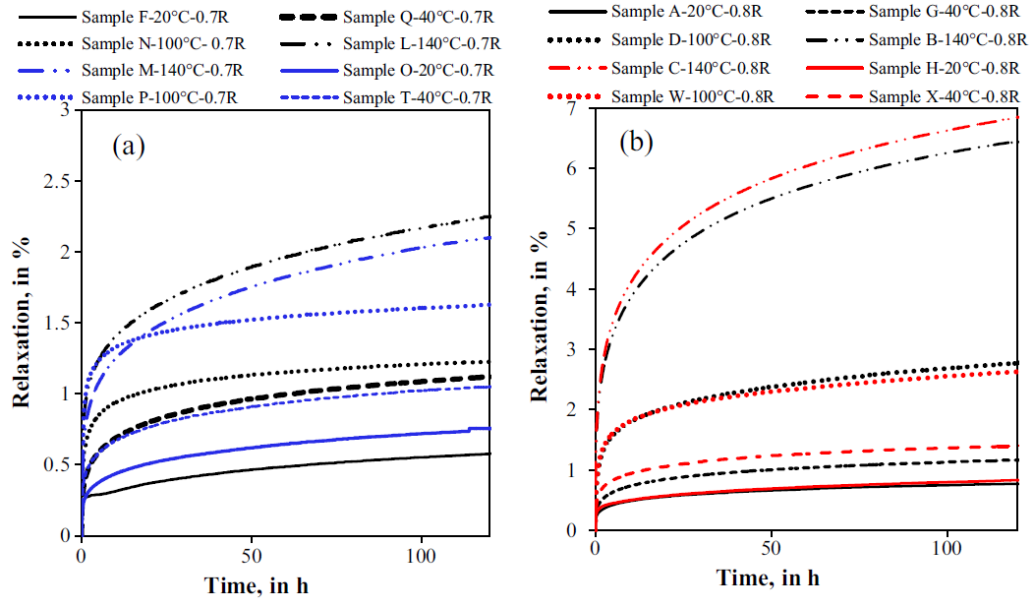


Figure 4-2: Evolution of relaxation with different temperatures and loading ratios (0.7 (a) and 0.8 (b)) (Toumi Ajimi et al., 2017)

It is important to note that, in both cases, the temperature state, although stationary, was not constant along the extensometer (Figure 4-3). However, for each configuration, the average temperature was assessed using temperature sensors. For tensile tests, the average temperatures were 30°C, 79°C and 110 °C for maximal temperatures of 40°C, 100°C and 140°C, respectively. For stress relaxation investigations, they were assessed to be respectively 35 °C, 76°C and 100 °C.

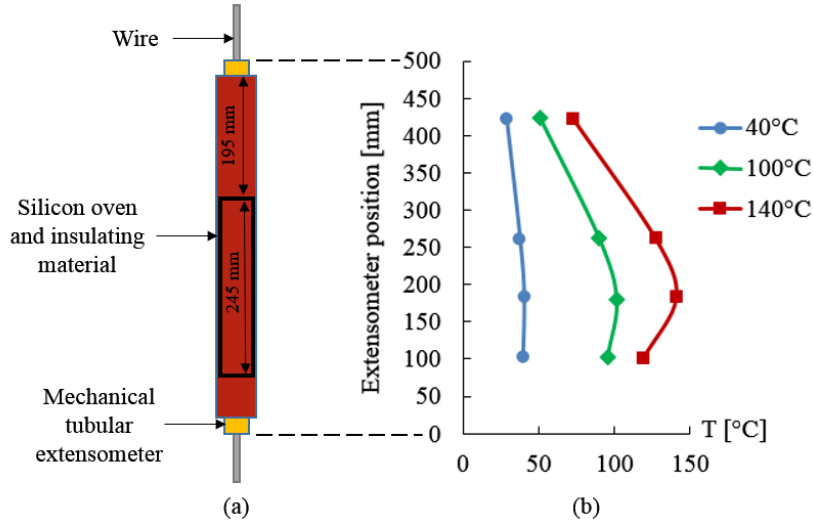


Figure 4-3: Scheme of relaxation sample with the heating device on the prestressing wire (a) and temperature evolution along the heated section (b) (Toumi Ajimi et al., 2017)

In addition, stepwise heating and cooling were performed on the same type of wires under a stress ratio of 0.8. Concerning stepwise temperature variations tests, the first one started at 20°C, rising to 100°C and finally 140°C. Second one started at 140°C, followed by 100°C and finally 20°C. For these two tests, a specific loading/unloading procedure was adopted to

exclude thermal expansion effects from the results. For each step, the wire was unloaded before its temperature state was modified, and was then loaded again with the remaining load obtained from the preceding step. Results are given in Figure 4-7 and Figure 4-8, where they are compared with the model predictions.

Therefore, the relaxation phenomenon which is time-dependent becomes determinant at high temperature and high rate of initial prestress. As the coupled effects of temperature and initial prestress on relaxation have not yet been considered properly in the numerical models, this work aims developing a new finite element model for this purpose.

4. 3. Development of relaxation model

This paragraph is devoted for presenting a new relaxation model developed for modelling the coupling effect of temperature and initial prestress loading on the prestressing loss of cables. We recall that the superscripts "*m*" and "*r*" standing respectively for concrete and reinforcement terms have been used in chapter III, but not in this chapter because there is no any terms belong to concrete. It is reminded that all the parameters presented in this chapter should be presented with superscript "*r*", but for the sake of clarity and ease of reading, we decide to omit this superscript as all the terms here are belong to reinforcement. So some parameters here can be found the same as the parameters of concrete in previous chapter, but they are, of course, belong to reinforcement.

4. 3. 1. Model principles

The relaxation model is based on the rheological model summarized by an idealized scheme in Figure 4-4. It consists of three levels, an elastic part to model instantaneous behavior, a Kelvin module to model viscoelastic strain, and a nonlinear Maxwell module to model permanent strain. This model is formulated to be usable in nonlinear finite element codes able to consider incremental evolution of thermomechanical conditions, so it does not use relaxation functions but stores the material state only through state variables acting on instantaneous characteristics of material, following the recommendations in (Sellier et al., 2016). These state variables are the strain of each level presented in Figure 4-4, the applied stress and the maximum loading rate. To consider the progressive reduction of the relaxation kinetics, the Maxwell level is nonlinear, its viscosity depending on the strain of the Maxwell level (ε^M in Figure 4-4). A nonlinear Maxwell module has already been used successfully, and for the same reason, to model the decrease of concrete creep kinetics (Sellier et al., 2016). Moreover, for the test at decreasing stepwise temperature on Figure 4-7, the recovery stage was not recorded during the experimental work, only the reloading stage was recorded. According to the available data, the

short term delayed strain is observed and stabilized rapidly, which is impossibly explained only by the permanent delayed strain. So, it was decided to treat this rapid delayed strain by the Kelvin module. Note that further measurements during the reloading stage are needed to explain clearly this phenomenon.

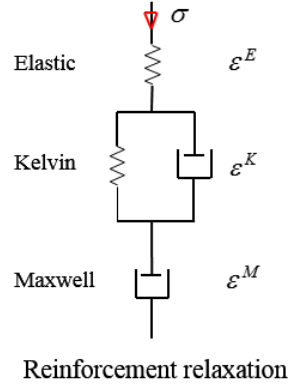


Figure 4-4 : Idealized rheological scheme for relaxation model

4. 3. 2. Nonlinear Maxwell level strain

Permanent relaxation corresponds to the Maxwell strain ε^M of the idealized rheological scheme (see Figure 4-4). The constitutive law of viscous strain, ε^M , for reinforcement is analogous to the one used for concrete by Sellier et al. (Sellier et al., 2016). The viscous strain is proportional to the current elastic strain ε^E and inversely proportional to a characteristic time τ^M through Eq.(4-1). The characteristic time is then affected by a nonlinear function called a “consolidation coefficient” Cc .

$$\frac{\partial \varepsilon^M}{\partial t} = \frac{\varepsilon^E}{\tau^M Cc} \quad (4-1)$$

The consolidation coefficient Cc depends on the current viscous strain and is expressed by Eq.(4-2)

$$Cc = \frac{1}{k} \exp\left(\frac{1}{k} \frac{\varepsilon^M}{\varepsilon^E}\right) \quad (4-2)$$

With k a *relaxation amplitude coefficient* for the current temperature and loading ratio (Eq.(4-3)).

$$k = k_{ref} \cdot k^T \cdot k^M \quad (4-3)$$

k considers the coupled effects of temperature and mechanical nonlinearity involved in the relaxation process. The physical conditions (temperature (T) and loading ratio (M)) affect the relaxation velocity through two functions, k^M and k^T , which will be detailed in 4. 3. 2. 1 and

4. 3. 2. 2, and k_{ref} is a constant proportional to the relaxation capability at reference temperature and reference loading rate. This material constant, k_{ref} , called the “*reference relaxation amplitude coefficient*” is the ratio of a characteristic strain ε_{ref}^K and a reference elastic strain resulting from a *conventional stress level* σ_{ref} corresponding to the loading rate used to fit ε_{ref}^K .

The constant k_{ref} is linked to the previous parameters as follows:

$$k_{ref} = E \frac{\varepsilon_{ref}^K}{\sigma_{ref}} \quad (4-4)$$

In Eq. (4-4), the fitting parameter ε_{ref}^K is called the *reference relaxation potential* due to the fact that the relaxation amplitude is proportional to ε_{ref}^K . And E is the elastic modulus of reinforcement.

4. 3. 2. 1. Non-linear effect of loading ratio

In Eq. (4-3), k^M considers the non-linear amplification of the relaxation rate with the mechanical loading level. Therefore, this coefficient starts from 1 for weakly loading level and diverges when the loading level reaches a critical value causing tertiary delayed strains. k^M is provided by Eq. (4-5):

$$k^M = \frac{\mu^{cr}}{\mu^{cr} - \mu} \quad (4-5)$$

With μ the loading level defined by Eq. (4-6) in which f_y is the elastic limit:

$$\mu = \frac{|\sigma|}{f_y} \quad (4-6)$$

In Eq. (4-5), μ^{cr} is a critical loading level depending on the sensitivity of the material to increase non-linearly its relaxation rate when the load increases; it is linked to a characteristic data χ called *non linearity relaxation factor*, defined such as the relaxation remains linear if $\chi = 1$ and becomes non-linear when $\chi > 1$ as illustrated in Figure 4-5:

$$\mu^{cr} = \frac{2}{3} \frac{\chi}{\chi - 1} \quad (4-7)$$

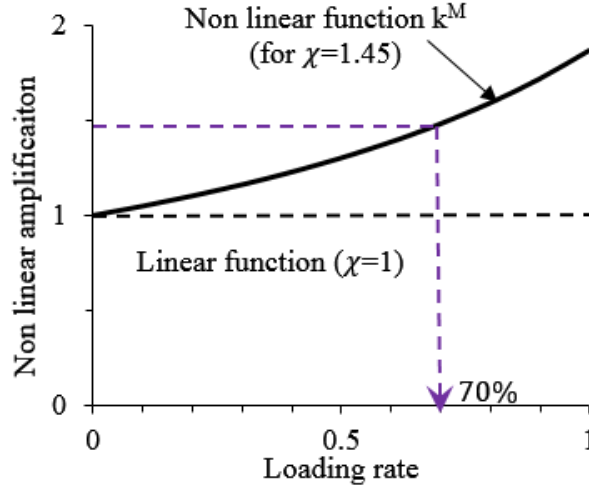


Figure 4-5 : Nonlinear amplification function k^M versus loading level

4.3.2.2. Temperature effect

In Eq. (4-3), k^T accounts for the temperature effect on the relaxation rate. The relaxation phenomenon is accelerated by the temperature increase and coupling with the loading level also exists since an amplification of the temperature effect is observed for loading rates greater than 0.7. To consider the effect of temperature on relaxation, the model uses the thermal activation multiplication coefficient (k^T) of the delayed strain potential (Eq. (4-8)), and to consider that the effect of temperature is amplified in case of high loading rate, coefficient A^T depends on the loading rate (Eq. (4-9)). Several forms of k^T and A^T were tested, and equations (4-8) and (4-9) correspond to the best fit found in the next section. Firstly, an Arrhenius law was tested to consider the thermal activation of relaxation, but the curvature of the curve was not sufficient to obtain the delayed strain potential at 100°C. Therefore, k^T was finally expressed as an exponential function depending on the thermal activation coefficient A^T :

$$k^T = \begin{cases} \exp \left[A^T (T - T_{ref})^n \right] & \text{if } T > T_{ref} \\ \exp \left[-A^T (T_{ref} - T)^n \right] & \text{if } T \leq T_{ref} \end{cases} \quad (4-8)$$

with T the temperature, T_{ref} the reference temperature for which the relaxation characteristic time, τ^M , (Eq. (4-1)) was fitted, and n a fitted parameter. The thermal activation coefficient is given by Eq. (4-9):

$$A^T = A_{ref}^T \exp(\gamma \cdot \mu^{TM}) \quad (4-9)$$

In Eq. (4-9), A_{ref}^T is a fitted constant to account for the effect of temperature on the relaxation rate, γ is a material constant, and μ^{TM} is a loading rate able to change the thermal activation, defined as follows:

$$\mu^{TM}(t + dt) = \max(\mu^{TM}(t), \mu(t + dt), \mu^{thr}) \quad (4-10)$$

where $\mu^{thr} \approx 0.7$ is the minimum loading level able to change the thermal activation, and μ is the loading level given by Eq. (4-6). In fact, the analysis of experimental results shows that the activation energy seems to be definitely changed by the loading rate, even if this loading rate is applied during a short duration that explains the presence of the “max” function in (4-12).

4. 3. 3. Kelvin level strain

Based on experimental results, a rapid delayed strain of the prestressing wires was detected in the tests including unloading and reloading stepwise. The experiments also showed that this rapid and reversible strain evolution, like for the permanent strains, was influenced by the temperature. In the model, the rapid relaxation is then modelled by a Kelvin module (see Figure 4-4 and Eq. (4-11)):

$$\frac{\partial \varepsilon^K}{\partial t} = \frac{1}{\tau^K} \left(\frac{\varepsilon^E}{\psi^K} - \varepsilon^K \right) \quad (4-11)$$

with τ^K the characteristic time for the Kelvin strain and ψ^K the rate of this relaxation relative to the elastic strain. To limit the number of fitting parameters, these two variables depend on the temperature through the same coefficient k^T (Eq. (4-8)) used for the Maxwell element presented above and are given by Eq. (4-12) and (4-13) respectively.

$$\tau^K = \frac{\tau_{ref}^K}{k^T} \quad (4-12)$$

$$\psi^K = \frac{\psi_{ref}^K}{k^T} \quad (4-13)$$

with τ_{ref}^K and ψ_{ref}^K the characteristic time and the rate of reversible relaxation fitted at reference temperature T_{ref} . Ideally, to fit these two parameters, a relaxation test followed by an unloading

phase is needed, but in the present work the recovery stage was not recorded; only the reloading stage for the test at stepwise decreasing temperatures allowed the short term delayed strain modelled by the Kelvin level to be captured.

4. 3. 4. Numerical implementation

The previous equations can be implemented in any finite element code based on a displacement formulation. Here, the model was implemented in the finite element code CAST3M (CEA, 2015). The model is resolved by solving the differential equations (4-1) and (4-11) using the time discretization with a finite-difference time-domain method (θ method). A set of equations involving the elastic strain, Kelvin strain and Maxwell strain is formed, to be solved at each time increment Δt (Eq. (4-14)).

$$\begin{cases} \Delta \varepsilon^{tot} = \Delta \varepsilon^E + \Delta \varepsilon^K + \Delta \varepsilon^M \\ \psi^K \left(\varepsilon^K + \left(\theta + \frac{\tau^K}{\Delta t} \right) \Delta \varepsilon^K \right) = \varepsilon^E + \theta \Delta \varepsilon^E \\ \frac{\tau^M Cc}{\Delta t} \Delta \varepsilon^M = \varepsilon^E + \theta \Delta \varepsilon^E \end{cases} \quad (4-14)$$

where θ is the semi implicit coefficient, taken equal to 1/2 in order to obtain a mid-point method. In these equations, strains ($\varepsilon^E, \varepsilon^K, \varepsilon^M$) are known at the beginning of the time increment (see Eq. (4-15)), while strain increments ($\Delta \varepsilon^E, \Delta \varepsilon^K, \Delta \varepsilon^M$) are unknowns for the current time step Δt , and $\Delta \varepsilon^{tot}$ is the total strain increment imposed. For a material never loaded before, the initial conditions are given by equation (15)

$$(t=0) \begin{cases} \varepsilon^E = \mu f_y / E \\ \varepsilon^K = 0 \\ \varepsilon^M = 0 \end{cases} \quad (4-15)$$

Variations of τ^K, ψ^K, τ^M and Cc due to the variations in thermomechanical conditions are considered explicitly. For instance, the consolidation coefficient Cc (Eq. (4-2)) at the end of the time step is actualized with ε^M , ready for the next step. This approximation is admissible as long as the time step stays relatively small compared to the characteristic time. Alternatively, the consolidation coefficient could be linearized to improve the convergence rate, but this improvement was not necessary for the material studied below. Note that, if the time interval

used by the finite element code user is too large, it can be subdivided (in the subroutine dedicated to this model) in order to avoid inaccuracy. For instance, the following studies were performed with Δt limited to 10% of the characteristic times ($\tau^K, \tau^M Cc$). The method of optimizing the time sub-step has already been used in concrete creep modelling by Sellier et al. (Sellier et al., 2016).

4. 4. Applications

This part presents the applications of the model to the experimental relaxation tests briefly presented in 4. 2. 2 and in greater detail by Toumi Ajimi et al. (Toumi Ajimi et al., 2017). The investigations conducted at constant temperature allowed fitting parameters to be obtained and the ability of the model to simulate the prestress relaxation to be validated in different configurations. In the present section, the comparisons of experimental results for relaxation (points) with numerical results (curve) are presented by the evolution of prestress loss with time. The prestress loss is the ratio of strain at the current time to the initial strain.

4. 4. 1. Identification of model and material parameters

The experiments carried out on the prestressing wires T15.2 which is used for VeRCoRs vessel structure. The relaxation tests can be classified in two series. The model and material parameters used for modelling the relaxation of this cable are listed in Table 4-2. The first series assessed the stress relaxation of steel wires at different temperatures ($T=20^\circ\text{C}$, 40°C , 100°C and 140°C) and different loading ratios ($\mu=0.7$ and 0.8), each kept constant during the test (Figure 4-6). It is of interest to note that, as observed in the literature, the experiments show that relaxation is more affected by higher temperature and higher stress ratio. The other test used to calibrate the model was a test performed at 80% loading rate but with a temperature decreasing by steps during the relaxation test (steel subjected to 140°C , 100°C and 20°C). During the temperature change, samples were unloaded and then heated to reach the next desired temperature before reloading. This was intended to suppress the effects due to thermal expansion of the steel wire.

Both series of tests (variable temperature with reloading and constant T and loading rate) allowed all the model parameters (Kelvin-Voigt level, Maxwell level and parameters related to non-linearity induced by stress and temperature) to be identified. The identified parameters are reported in Table 4-2 and the comparisons with tests are plotted in Figure 4-6 and Figure 4-7.

It should be noted that, due to the dispersion observed on the relaxation at $\mu=0.8$ and 140°C in Figure 4-6, the model only fits perfectly the results $\mu_{0.8_140^{\circ}\text{C_exp}(2)}$ (diamond points in Figure 4-6). The results of incremental temperature needed to fit the Kelvin Voigt parameters are only available for $\mu_{0.8_140^{\circ}\text{C_exp}(3)}$ (circular points in Figure 4-7), for the fitting they were extrapolated to the results of $\mu_{0.8_140^{\circ}\text{C_exp}(2)}$ (diamond empty points in Figure 4-7) after 130 h.

Table 4-2: Model parameters and material parameters (in **bold and red symbol**) for prestressing wires T15.2 at $T_{ref} = 20^{\circ}\text{C}$

Parameter	Definition	Unit	Value
Distributed reinforcement behavior laws			
ρ^i	Reinforcement ratio in direction i	-	
E	Reinforcement Young modulus	GPa	200
f_y	Reinforcement elastic limit	MPa	1860
H	Reinforcement hardening modulus	MPa	1600
τ	Bond stress interface reinforcement concrete	MPa	8.3
τ_{ref}^K	Reinforcement reversible relaxation characteristic time	hour	10
τ^M	Reinforcement irreversible relaxation characteristic time	hour	10
ψ_{ref}^K	Reinforcement reversible relaxation reduction coefficient	-	250
ε^K	Characteristic strain for reinforcement relaxation	-	6.64e-6
χ	Nonlinear relaxation effect		1.45
γ	Coupling coefficient for effect of stress on activation energy	-	6.19
n	Exponent of temperature in thermal activation of relaxation	-	1.216
A_{ref}^T	Reference value of the thermal activation coefficient	-	6.52e-5
σ^K	Characteristic stress for the fitting of ε^K	MPa	1302
μ^{th}	Loading level threshold above which the thermal activation depend on loading	-	0.7
σ_0^r	Initial prestress (imposed as initial stress at first step)	MPa	

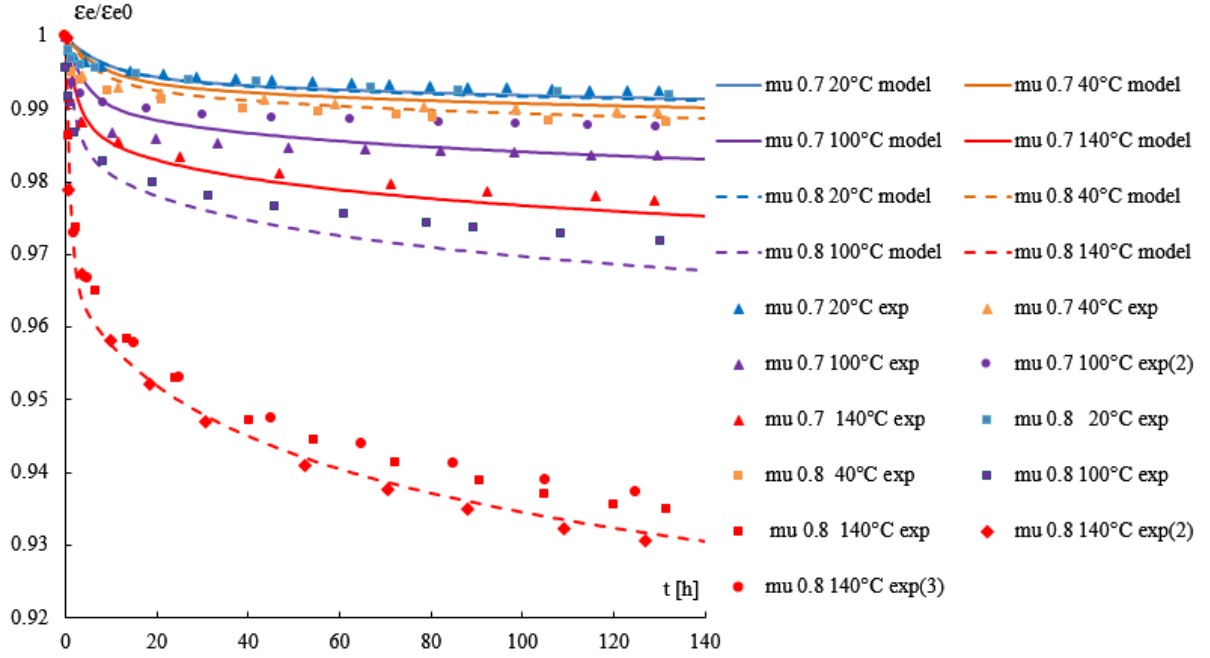


Figure 4-6 : Comparison between model and experimental results of relaxation versus time for different temperatures and loading ratios (0.7 and 0.8)

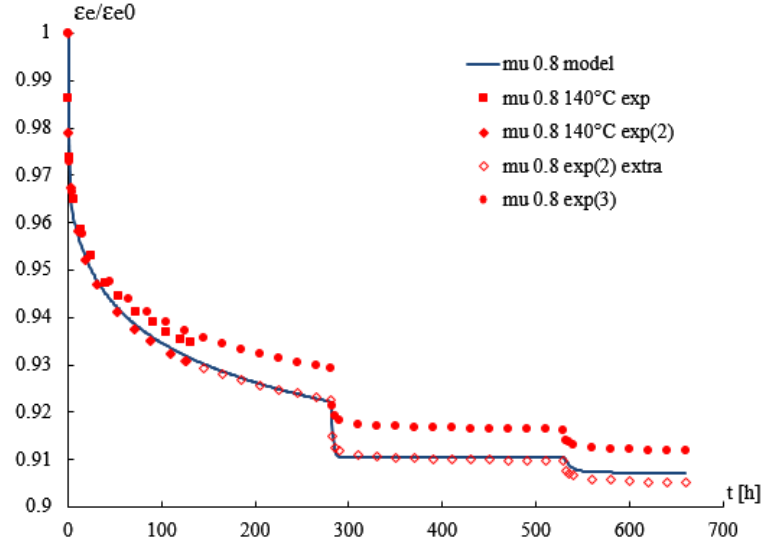


Figure 4-7: Comparison of model with relaxation experiment at stepwise cooling (140°C, 100°C and 20°C)

It is noticeable that the consolidation theory used in the Maxwell module of the model efficiently considers the permanent strain history and takes a large increase of consolidation

coefficient during cooling into account, which results in a significant reduction of the Maxwell relaxation velocity. This is reflected in Figure 4-7 as a plateau that is almost horizontal.

4. 4. 2. Validation

To evaluate the prediction capability of the model, a third test was used. In this test the temperature was increased from 20°C to 140°C as could occur in the vessel wall during an accident. In order to eliminate the effect of thermal strain in steel (and thus evaluate only the capacity of the model to reproduce the nonlinear effect of stress and temperature variation), the temperature was increased in steps (100°C and 140°C) and samples were unloaded and then heated to reach the desired maximal second temperature before reloading. The comparison between the results obtained with the relaxation model proposed above and the experiments is presented in Figure 4-8. It shows the prestress loss versus time using the data given in Table 4-2 (without any additional fitting). The results obtained with the modelling were in quite good agreement with experimental results.

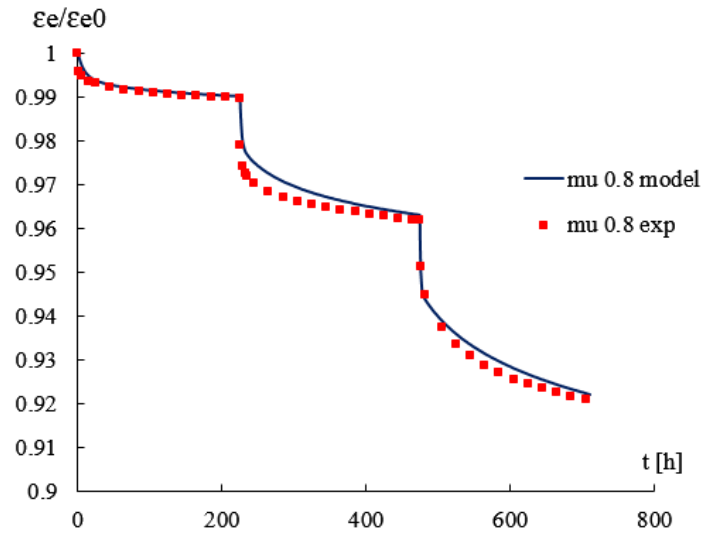


Figure 4-8 : Comparison of model with test of relaxation with a stepwise heating (20°C, 100°C and 140°C)

4. 5. Conclusion

The delayed strain model developed in this part is based on the incremental finite difference method. It was proposed to simulate the relaxation of prestressing steel wires under different conditions of initial loading (prestress) and temperature. As pointed out by Toumi Ajimi et al. (Toumi Ajimi et al., 2017), the existing normative approach from Eurocode 2 does not take temperature into account and does not seem to be consistent with experimental results. Specific experimental investigations with stepwise thermal states were carried out to allow the characteristic parameters of the model to be determined and to be able to validate it with different thermal histories to check that the model does not depend on this issue.

The thermomechanical behaviour of prestressing steel wires has two particularities: first, the delayed strain velocity is not simply proportional to the mechanical loading (prestress) but depends on it nonlinearly when the loading ratio is high and, second, the relaxation is sensitive to the temperature, with a sensitivity that varies with the loading ratio. Therefore, a coupling of the temperature and loading effects was considered in the model via a thermal activation coefficient depending on the maximal loading ratio. Moreover, a short-term delayed strain was observed and modelled. Further research on this topic is needed to verify the reliability of this model for other types of prestressing steel wires in different configurations of loading and temperature. The features of this model seem to be suitable to predict the prestress loss during the life of the massive structure of a nuclear containment building and the envisioned loss-of-coolant accident.

For massive structures in prestressed concrete, the prestress loss due to steel relaxation cannot be separated from the analysis of concrete creep and shrinkage effects. Other experimental and numerical programs were carried out in the MACENA project to quantify the phenomenon of delayed behavior of concrete in this range of temperatures (20°C-180°C). The combination of these research works will be treated in the next section.

CHAPITRE V

Scale effect consideration for application on massive structures

« Il ne faut avoir aucun regret pour le passé, aucun remords pour le présent, et une confiance inébranlable pour l'avenir. » Jean Jaurès

5. 1.	Introduction.....	158
5. 2.	State of the art	158
5. 2. 1.	Size effect phenomena	158
5. 2. 2.	Modelling of probabilistic size effect in tension.....	160
5. 3.	Probabilistic scale effect model	161
5. 3. 1.	Weibull scale effect.....	161
5. 3. 2.	Weakest Link Localization method (WL2).....	162
5. 3. 3.	Numerical implementation.....	163
5. 4.	Application to nuclear wall mock-up PACE 1450	164
5. 4. 1.	Presentation of PACE 1450 structure.....	164
5. 4. 2.	Mesh and boundary conditions	168
5. 4. 3.	Thermal and mechanical results	170
5. 5.	Application to the lower part of vessel mock-up VeRCoRs.....	172
5. 5. 1.	Benchmark VeRCoRs 2015	173
5. 5. 2.	Study of the lower part of the whole vessel containment	176
5. 6.	Conclusion	179

5. 1. Introduction

Prestressed concrete is a complex, composite material used in the construction of almost large-scale structures such as nuclear containments. Prestressed concrete structures are usually designed using regulatory standards or recommendations based on empirical rules and simplified analytical (usually linear) models. But, to predict more accurately the cracking risks which control the durability and service lifetime of the structure (nuclear containment buildings), more complex finite element methods are required to simulate their three dimensional and nonlinear structural behaviour. When the cracking problem is addressed, the estimation of current tensile strength which is linked to the heterogeneity of concrete according to the CEOS.fr conclusions, becomes crucial. Nowadays, numerical tools taking the scale effect, which is a characteristic of heterogeneous materials, into account are progressively enriched. Here, we present the methods found in the literature review to consider this scale effect. One, among these methods, based on WL2 theory will be emphasized and used in the simulation of prestressed concrete structure elements such as PACE 1450 mock-up (nuclear containment wall element) and VeRCoRs mock-up (nuclear containment at 1/3 scale).

5. 2. State of the art

5. 2. 1. Size effect phenomena

There are a lot of numerical approaches in the scientific literature to describe either implicitly or explicitly the cracking of concrete. The assessment of cracking pattern in large reinforced concrete structures is faced with the problem of concrete heterogeneity translated by the tensile strength dependency on the loaded volume, which has been reported via the experimental results (Clément, 1987; Farra, 1994; Mivelaz, 1996; Rossi et al., 1994; Van Vliet and Van Mier, 2000). The variation of tensile strength of concrete specimens and anchors under uniaxial tension has been summarized by (Ghannoum, 2017) and plotted in Figure 5-1. It has been shown the first cracks in a large structure appear under stresses lesser than the tensile strength measured with usual laboratory tests such as split test or direct tension test. As reported by the CEOS.fr project (Buffo-Lacarrière et al., 2016) and Mefisto project (Mefisto, 2012), it underlined a loss of 50% of tensile strength value measured on splitting test can be obtained for large structures such as nuclear containment (Sellier and Millard, 2014). This phenomenon, known as *probabilistic scale effect*, is due to the heterogeneity character of concrete at mesoscale (scale of aggregate), which leads to a decrease of a random field of tensile strength when the size of the solicited volume increases, as presented in Figure 5-2 (Sellier and Millard, 2014). The consideration of scale effect on the reduction of local mechanical properties of concrete has been widely studied in the literature (Bazant, 2004; Bazant and Novak, 2000; Bazant and Yavari, 2005; Carpinteri, 1994; Carpinteri and Chiaia, 2002; Dufour, 2007; Ghannoum, 2017; Mazars et al., 1991; Nader, 2017; Rossi et al., 1994; Sellier and Millard,

2014). For the simulation of large-scale structure, the consideration of diminution of mechanical properties is crucial, mainly for predicting the first cracks, based on the experimental evidence when passing from small-sized specimens to real scale structure. This reduction is induced not only by the size effect phenomenon but also by other aspects such as the geometry, the stress state, the material composition, the boundary effect and the load rate (Bazant, 1999; Bazant and Yavari, 2005; Grégoire et al., 2013; Van Vliet and Van Mier, 2000). Moreover, another origin of the scale effect, for concrete, is the microcracking induced by cement paste shrinkage around large aggregate, therefore this effect is influenced not only by the size of the aggregate (Rossi et al., 1994) but also, possibly, by the hydric state. This last aspect has recently been investigated in the MOSAIC ANR project, the tests performed at LMDC Toulouse on different configurations of un-notched beams pre-dried in different homogenous conditions, show that the scale effect persists whatever the hydric state from 20% until endogenous conditions (Bucher et al., 2017).

According to (Sellier and Millard, 2014), the size effects can be classified into statistical size effect due to material strength randomness treated by weakest link theory (Weibull, 1951) and energetic size effect due to the energy release when a crack develops before the maximum load is reached (treated in the present modelling by the Hillerborgh method (Hillerborg et al., 1976). The statistical size effect is observed on the structures having different volume ΔV and undergoing a quasi-uniform stress field σ , whilst the energetic-statistical size effect is observed on the structures having different volume ΔV and undergoing a non-uniform stress field $\Delta\sigma$.

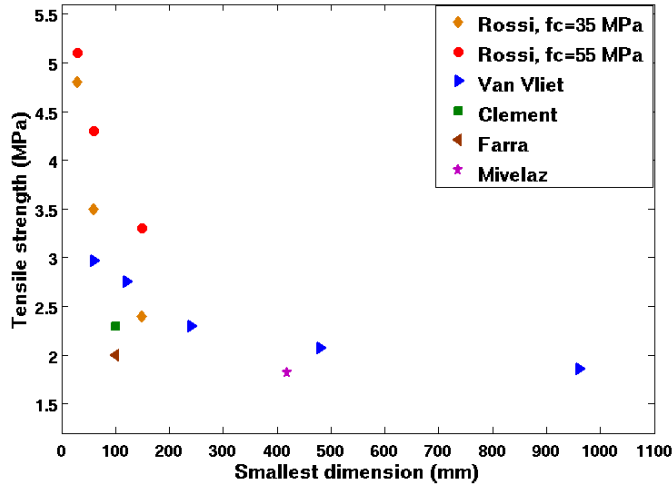


Figure 5-1: Experimental dispersion of concrete tensile strength as function of the smallest dimension of the specimen (Clément, 1987; Farra, 1994; Mivelaz, 1996; Rossi et al., 1994; Van Vliet and Van Mier, 2000) cited by (Ghannoum, 2017)

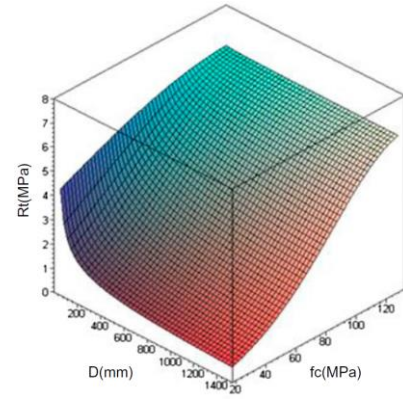


Figure 5-2: Scheme of tensile strength (R_t) vs. specimen diameter (D) and compressive strength (f_c) (Rossi et al., 1994))

5. 2. 2. Modelling of probabilistic size effect in tension

As the scale effect is due to the random properties of the local material, it is often modelled using a direct random field or mesoscopic modelling of heterogeneities. The random field is a statistical method that captures spatial variability of input variables using spatial functions (Matheron, 1973). Matheron proposed a Turning band method (TBM) which is applied, by facilitating the localisation of strains, to assess crack openings in reinforced concrete structures (Matallah et al., 2010; Michou et al., 2015). However, this technique requires very fine meshes (finite elements smaller than the smallest simulated aggregates) and as it belongs to the Monte Carlo methods, it also needs several random samplings to capture a representative behaviour of real structures. Thus it is not suitable for large-scale structures since their modelling is too time-consuming. To avoid resorting to several random samplings and too fine meshes, the weakest-link theory characterized by (Weibull, 1951) is proposed based on the probabilistic aspects. Recently, the Weibull “Weakest link theory” has been developed and transformed into a “Weakest Link and Localization” theory (WL²) (Sellier and Millard, 2014). This new method is capable not only to compute the probability of occurrence of the first crack localisation but also to provide the most likely tensile strength field at each time step of the numerical non-linear analysis. It uses a probabilistic weighting function which depends on the characteristic length l_c (from 0.2 to 0.5 m for concrete and 0.05 to 0.3 m for mortar). Besides, other models are also proposed to consider this size effect (Carpinteri et al., 1995; Hoover and Bazant, 2014; Lamon, 1990; Mazars, 1984; Torrent, 1977) (summarized in (Ghannoum, 2017)). But these methods are based on experimental calibration depending on more than three empirical constants, and are more suitable for analytical analysis than for numerical implementation,

therefore, the analytical probabilistic scale effect WL^2 , clarified in order to be used in an incremental non-linear solver, is used.

5. 3. Probabilistic scale effect model

5. 3. 1. Weibull scale effect

The Weibull theory is used to avoid resorting to a mesoscopic modelling or to a random field sample. Based on the principle of Weibull theory, the tensile strength to be used $R_{t(M)}$ depends on the loaded volume $V_{eq(M)}$ through the scale effect law (Eq. (5-1)). The scale effect is represented by the curve in Figure 5-5 that shows the diminution of tensile strength when the size of volume increases.

$$\frac{R_{t(M)}}{R_t^{ref}} = \left(\frac{V_{ref}}{V_{eq(M)}} \right)^{1/m} \quad (5-1)$$

According to (Sellier and Millard, 2014), in Eq. (5-1), R_t^{ref} is the average tensile strength measured on a cylindrical concrete specimen (11x22 cm) in Brazilian splitting test for which the loaded volume V_{ref} may be taken as 200 cm³. m is the Weibull exponent depending on the coefficient of variation C^v of experimental results (Figure 5-3):

$$m \approx \frac{1}{10} \left(\frac{12}{C^v} - 2 \right) \quad (5-2)$$

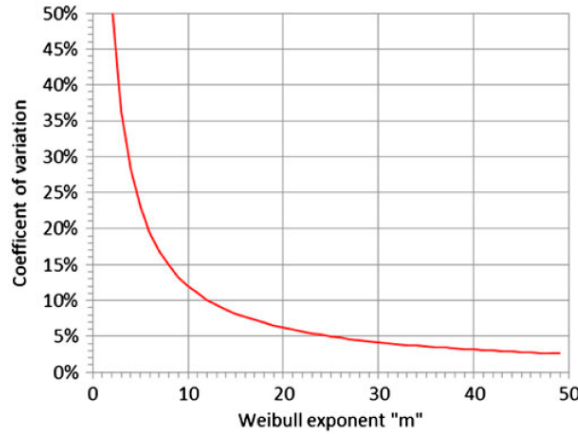


Figure 5-3: Evolution of m as function of C^v (Sellier and Millard, 2014)

For our case study of VeRCoRs structure, a dispersion of measures of tensile strength on concrete at 28 days can be observed in Figure 5-4, leading to a coefficient of variation $C^v \approx 11\%$ and consequently the corresponding value of Weibull exponent $m \approx 10.7$.

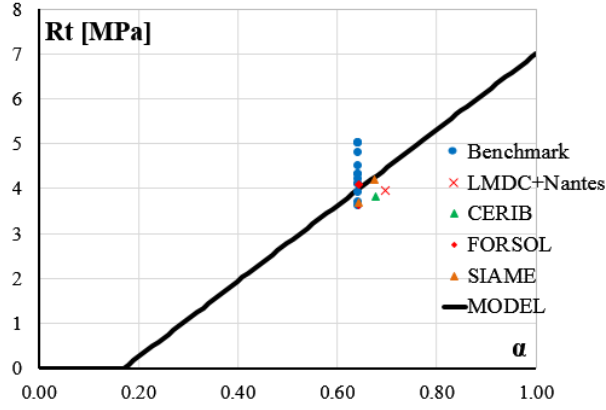


Figure 5-4: Dispersion of measures of tensile strength at 28 days from different laboratories in MACENA project

5. 3. 2. Weakest Link Localization method (WL2)

The WL2 method allows assessing directly the most likely tensile strength. It consists to assess the equivalent loaded volume $V_{eq(M)}$ using a modified Weibull theory. The modification proposed in (Sellier and Millard, 2014) consists to use a weighting function to consider a non-homogeneous probabilistic effect of material points towards each other through the expression (Eq. (5-3)).

$$V_{eq(M)} = \frac{1}{\beta_{\max}} \int_{\Omega} \beta \cdot \psi(M) d\Omega \quad (5-3)$$

With the weighting function $\psi(M)$ which accords a larger probabilistic importance to the vicinity of any material point possibly damageable (Eq. (5-4)), β is the loading index defined at each integration point (Eq. (5-5)), Ω is the structure and $d\Omega$ is a structure infinitesimal volume.

$$\psi(M) = \exp \left[-\frac{1}{2} \left(\frac{d(M)}{l_{cp}} \right)^2 \right] \quad (5-4)$$

Where $d(M)$ the distance between damageable point M and its nearby point, l_{cp} the characteristic length of probabilistic weighting function whose usual value is between 0.2 and 0.5 m for a concrete. This value is in accordance with the experimental investigations of (Bazant, 2004; Hasegawa et al., 1985) showing that the tensile strength is not influenced by the volume of the specimen for specimens having a very large dimension

$$\beta = \left(\frac{\max(\sigma_I, 0)}{R_t^{ref}} \right)^m \quad (5-5)$$

With σ_I the principal tensile stress. If the structure volume Ω is very large compared to the characteristic length l_{cp} , and the stress field is sufficiently homogeneous, the equivalent loaded

volume tends to a maximal equivalent loaded volume $V_{\max(M)}$ impossible to exceed whatever the stress field in the structure and the real size of the structure:

$$V_{\max(M)} = \int_{\Omega} \psi(M) d\Omega \approx \prod_{i=1}^N \left(\min(\dim; l_c \sqrt{2\pi}) \right) \quad (5-6)$$

Where N is the space dimension, and \dim is the dimension i.e. length, width and height of structure.

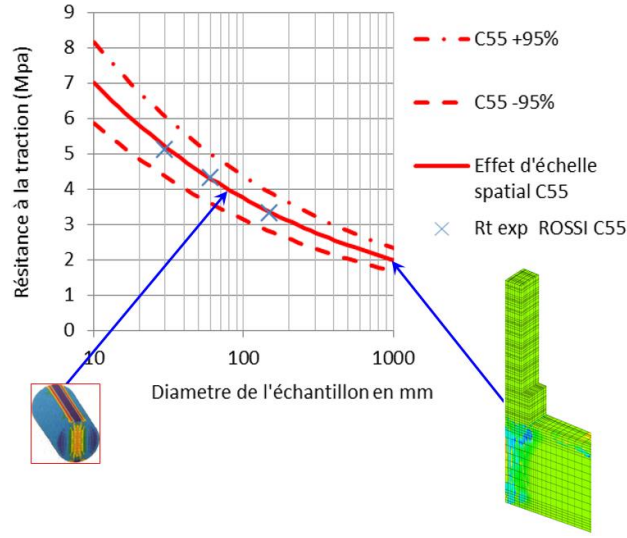


Figure 5-5: Evolution of tensile strength due to scale effect (CEOS.fr, 2016)

5. 3. 3. Numerical implementation

At every time step calculation, the volume $V_{eq(M)}$ is computed to control the most likely tensile strength field. The operation is performed during each loading increment to adapt the tensile strength to the current loading. As the most likely tensile strength depends on the stress field in the undamaged zone but these zones are susceptible to damage during the non-linear analysis, a first approximation of the stress field is applied using the tensile strength field of the previous time step, then a non-local sub-step is performed using this field to assess a more accurate tensile strength field. The definitive calculation is completed with the converged value of this last one.

Moreover, in Eq. (5-3) and (5-5), R_t^{ref} is simplified, which shows that the equivalent loaded volume depends only on the stress field form and not on its amplitude. It means that β can be computed with a non-constant strength field. In fact, Eq. (5-1) provides directly the ratio of the tensile strength linked to its reference value, even if this reference value varies with time; for instance during hydration, it increases with time.

The analytical probabilistic WL^2 approach, THCM models (rheological creep model and damage model), relaxation model and distributed reinforcement method are adapted to the

extension of LMDC model and built in the framework of poromechanics in which all the phenomena are coupled. These methods are merged into a numerical model and implemented in the finite element code Castem (CEA, 2015). The application of model to the real massive structures such as PACE 1450 and VeRCoRs structure will be presented in the next paragraph. It is reminded that the properties of materials used for modelling PACE structure are assumed to be the same as the ones used for modelling VeRCoRs structure. The material and model parameters have been summarised in each chapter.

5. 4. Application to nuclear wall mock-up PACE 1450

5. 4. 1. Presentation of PACE 1450 structure

The design of an intermediate-sized specimen called “PACE 1450” is inspired by a real internal wall of a 1450 MWe nuclear power plant containment under accidental loading conditions (Hermann et al., 2009). The prestressed concrete curved element’s dimensions are 3.5 m in length, 1.8 m in width, and 1.2 m in height which corresponds to the thickness of the original containment wall (see Figure 5-6). The reinforcement layout of the specimen is very similar to the original geometry and consists mainly of meshes of reinforcement bars near the inner and outer surface and four prestressing cables, each of them consisting of 37 strands within ducts in the circumferential direction and one prestressing cable in the vertical direction (see Figure 5-7 and Figure 5-8). An initial prestressing force is applied to a level which leads to a stress state of 12 MPa in the circumferential direction and 1 MPa in the vertical direction of the specimen. The experimental campaign consists of carrying out a test under different loading configurations (called RUNs, see Table 5-1), corresponding to the state of the containment at a different stage during its life cycle. The applied loading will produce a radial displacement and a membrane traction as for the real structure. In order to take into account the creep of the containment during its lifetime, the prestress of the horizontal cables is consequently reduced from 100% in the RUN 1 to 60% in the RUN 4. The main objective of these tests is to measure the crack propagation, as well as the radial leakage rate through the wall. More details can be found in (Hermann et al., 2009).

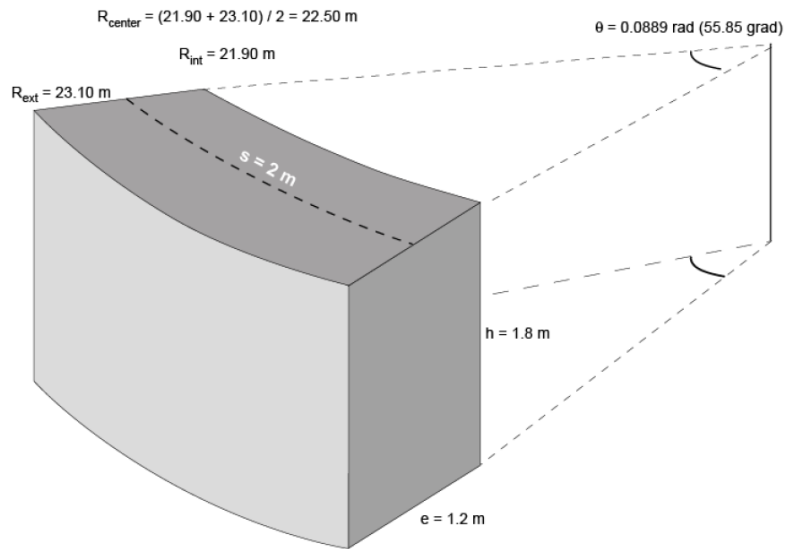


Figure 5-6: Geometry and dimension of specimen PACE 1450 (Hermann et al., 2009)

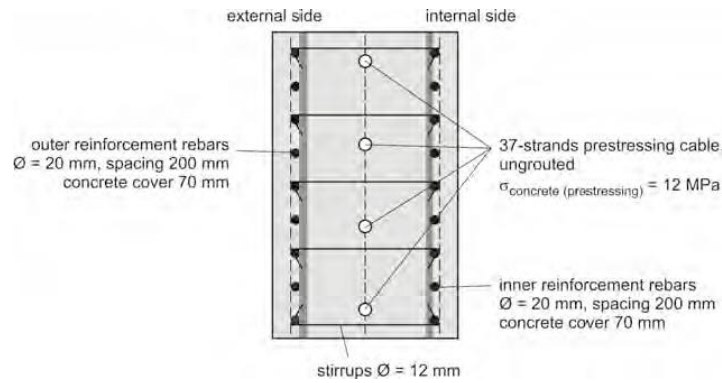


Figure 5-7: Horizontal section of specimen PACE 1450 (Hermann et al., 2009)

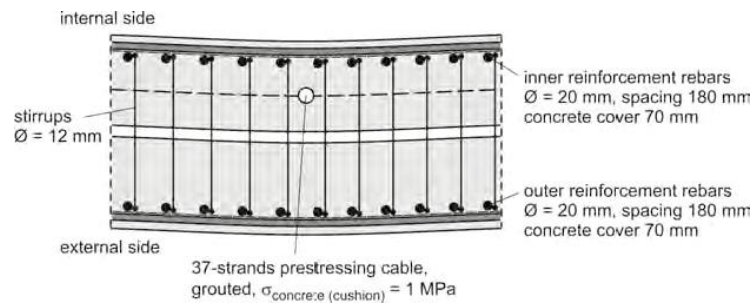


Figure 5-8: Vertical section of specimen PACE 1450 (Hermann et al., 2009)

Table 5-1: Test program (RUNs)(Hermann et al., 2009)

RUN	real age [years]	Press. [bars]	T [°C]	media	pre-stressing [%]	remarks/idea (see also text)
0	0	1.43	20	air	25	testing of the facility
1	0	5.30	20	air	100	first day of plant operation
2	10	5.30	20	air	80	leak tightness test after 10 years of operation
3	35	5.30	20	air	60	leak tightness test after 35 years of operation
4	60	6.00	20	air	60	accident after 60 years of operation/ cracking
5	60	6.00	20	air	60	first leakage test (all cracks)/accident after 60 years of operation
6	60	6.00	20	air	60	second leakage test (all cracks)/accident after 60 years of operation

The mechanical part of the set-up is illustrated in Figure 5-9. The displacements of two lateral surfaces of the specimen are restrained in the circumferential direction and the one of the lower surface of the specimen is also restrained in the vertical direction. The internal pressure is applied to the internal surface of the specimen. The pressure scenario for RUN1 to RUN3 is shown in Figure 5-10 where the starting pressure of 1.15 bars is applied to ensure an exact control of the external force which is coupled to the applied pressure and the pressure increases in step until the peak of 5.3 bars absolute ambient temperature.

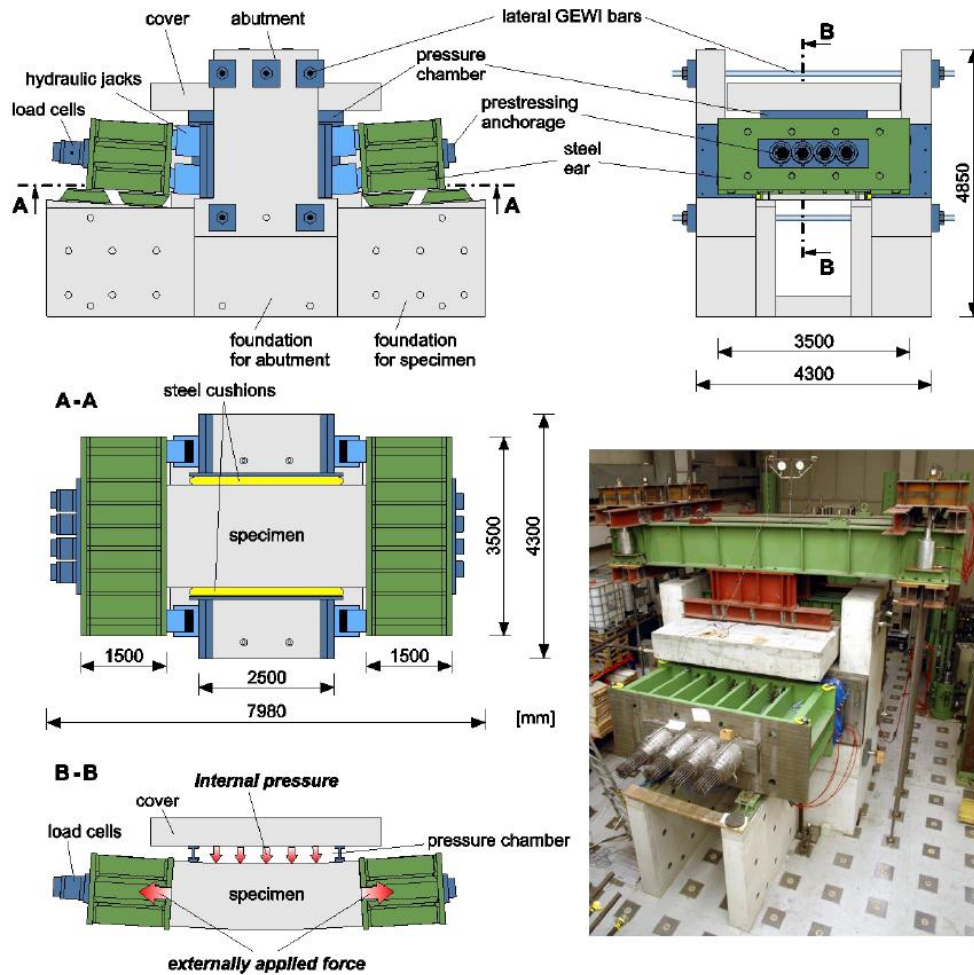


Figure 5-9: Mechanical boundary conditions and photo of the set-up (Hermann et al., 2009)

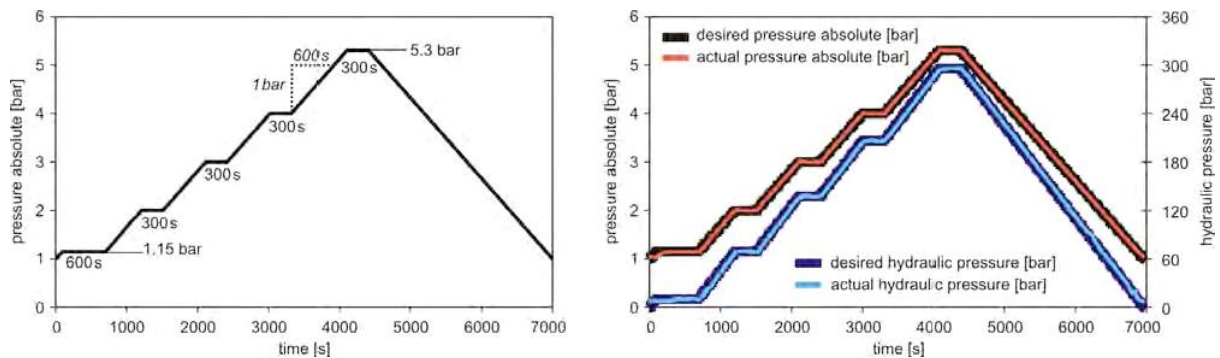


Figure 5-10: Pressure scenario for RUN 1 to RUN 3 (left) and test control (right) (Hermann et al., 2009)

In order to validate our approaches, the PACE structure is modelled since concrete casting to consider realistically the solicitation history state of the structure. As there are many RUNs, we have chosen to compare the results only for two RUNs in this study. It means that we model the hydration and drying of specimen before modelling the two successive RUNs. First, RUN 2 is performed at the ambient temperature under the prestress which is reduced by 20% from the initial prestress. The prestressing force is applied at 149 days after concrete pouring.

Secondly, RUN 6 is carried out at the ambient temperature under the force which is reduced by 40% from the initial prestress. Note that PACE concrete is similar to VeRCoRs concrete, so the model parameters are assumed to be the same.

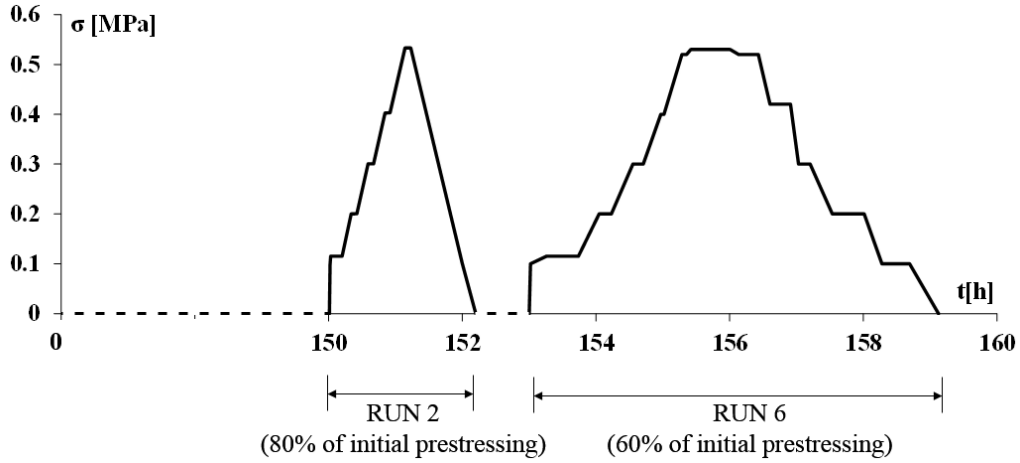


Figure 5-11: Illustration of external loading on PACE mock-up according to time (effect of creep is assumed neglected between RUN 2 and RUN 6)

5. 4. 2. Mesh and boundary conditions

The PACE structure is modelled using a 3D mesh with 1 400 cubic elements (Figure 5-12). As we don't have access to the data of climatic conditions, the lateral surfaces in the radial direction of specimen are assumed to be subjected to the convection with an equivalent convective coefficient equal to $H_{eq} = 8 \text{ W/m}^2 \cdot ^\circ\text{C}$ and the ambient temperature is supposed constant about $25 \text{ }^\circ\text{C}$. As the specimen is considered as a part of nuclear containment wall, there is no thermal flux in other surfaces. For the model and material parameters used for mechanical model can be referred to the summary table of parameters in the previous chapters. The mechanical boundary conditions are illustrated in Figure 5-12. Note that the stress of 1 MPa induced by the vertical prestressing cable is applied directly as external stress to the upper surface of the specimen. Figure 5-13 and Figure 5-14 illustrate respectively the maximal volume V_{max} used for the scale effect and the ratio of reinforcements of specimen in diverse directions used for distributed reinforcement method.

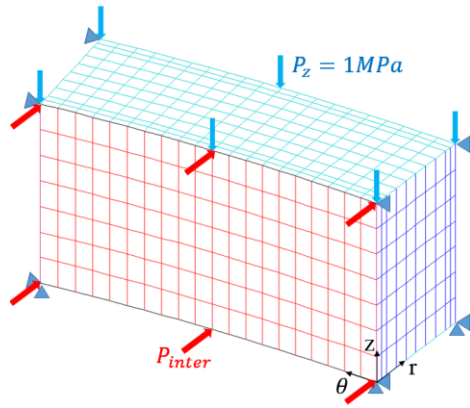


Figure 5-12: Mesh of PACE 1450 and its boundary conditions

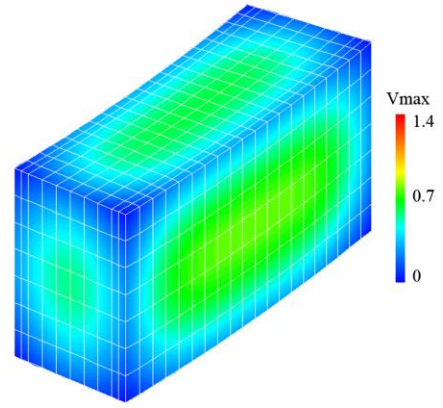


Figure 5-13: Scheme of computed V_{max}

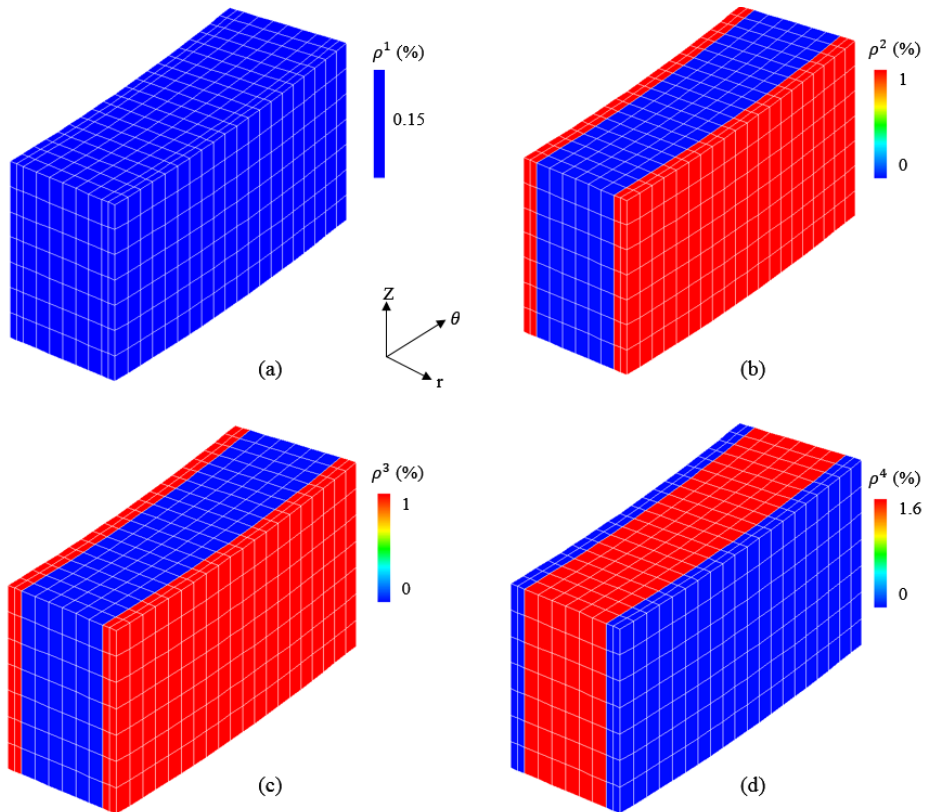


Figure 5-14: Ratio of distributed reinforcement along radial axe (a), circumferential axe (b), vertical axe (c) and prestressing wire along circumferential axe (d)

5.4.3. Thermal and mechanical results

The comparison of thermal results with experiments is shown in Figure 5-15. It demonstrates that the evolution of temperature is well reproduced by the hydration model. The evolution of other parameters such as hydration degree, water content and porosity issued from hydration model will be used directly in the mechanical model.

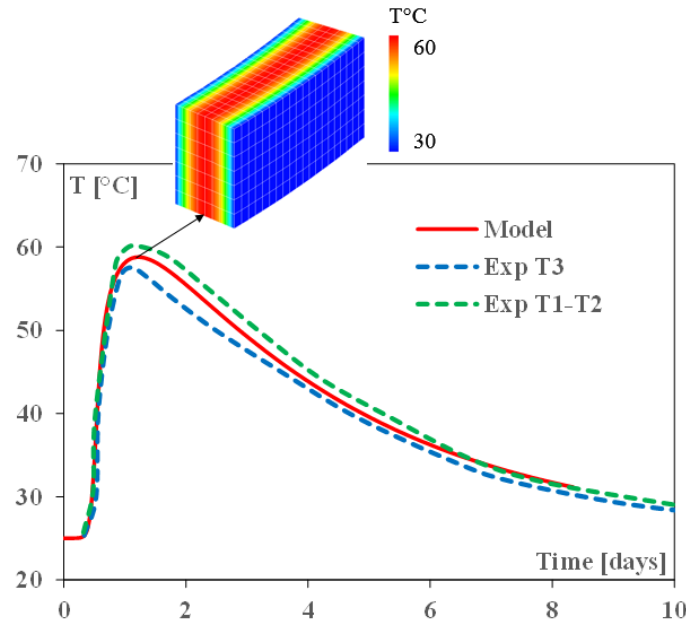


Figure 5-15: Evolution of temperature at the centre of specimen according to time (experimental results obtained from (Rospar, 2016))

Before showing the mechanical results, it is important to ensure that the prestressing force follows exactly the scenario of the internal air pressure. So, the comparison of the prestressing force given by the numerical calculation and by the measure is shown in Figure 5-16. After verifying the change of prestressing force, we will present the comparison of mechanical results from model with experiments. Noted that the internal strain evolution is only given for RUN 2. According to Figure 5-17, we observe that the internal strains of PACE during RUN 2 are well reproduced by the model. Besides this, we will present the comparison of crack patterns for RUN 6.

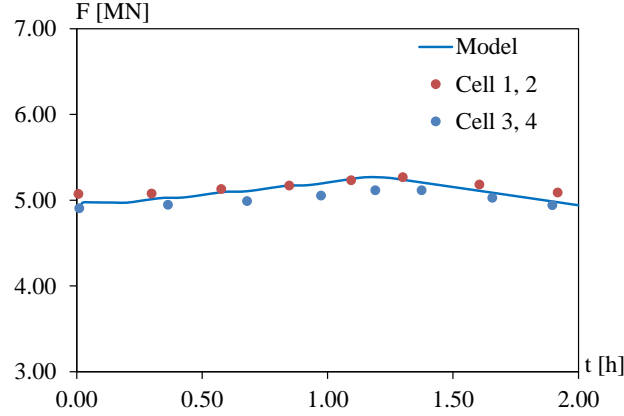


Figure 5-16: Comparison of prestressing force change during RUN 2 (experimental points obtained in (Hermann et al., 2009))

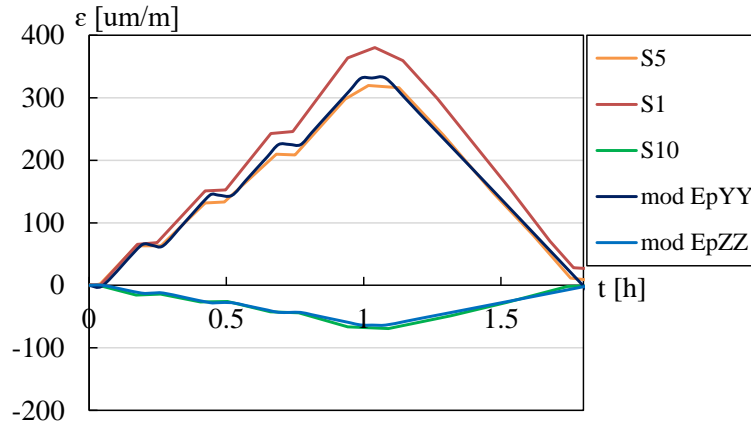


Figure 5-17: Comparison of internal strain during RUN 2 (experimental results S1, S5, S10 obtained in (Hermann et al., 2009))

The crack pattern during the maximal force of RUN 6 test is also globally well reproduced (Figure 5-18). Concerning the crack width, the order of magnitude is respected but the width is underestimated (about 200 μm for numerical results and about 400-500 μm observed experimentally during the maximal force of RUN 6). If we compare the sum of crack width along a horizontal line, its difference become less important because there are fewer, but more open, cracks with the measures while the model provides more, but less open, cracks.

Last but not least, we remind that the current version of the model considers a perfect bond between rebars and concrete and an homogenized model of RC with sliding conditions is under clarification in LMDC in collaboration with CEA Saclay, but these new developments were not yet fully implemented for the present works. So, it is expected that the implementation of the homogenised sliding reinforcements will allow obtaining a less diffuse cracking, and consequently a larger crack opening. Note that the homogenised model already considers the

presence of passive rebars and pre-stressed cables, and is able to find a realistic behaviour of PACE in terms of displacement and crack's positions.

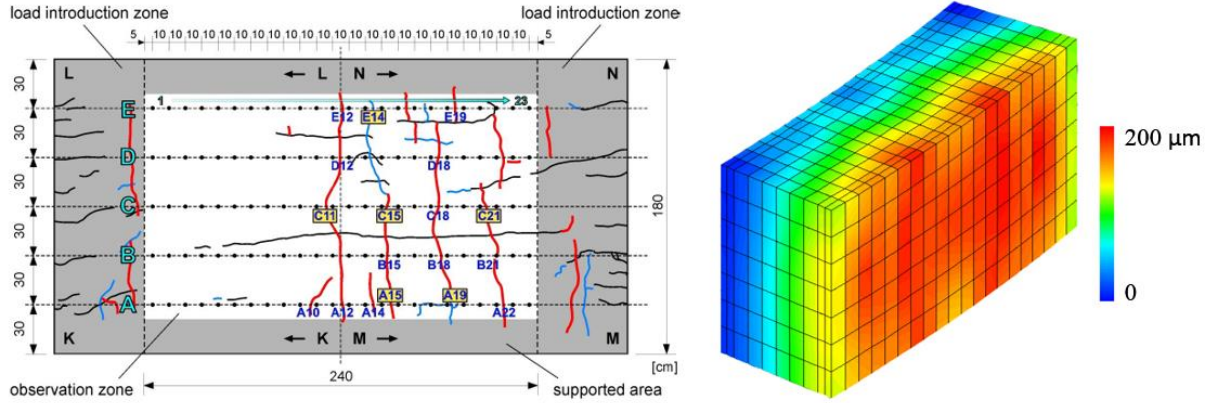


Figure 5-18: Comparison of crack pattern at external surface of PACE during RUN 6 with numerical results (crack measure given by (Hermann et al., 2009))

5. 5. Application to the lower part of vessel mock-up VeRCoRs

VeRCoRs is a 1/3 scale mock-up of a double-wall nuclear containment building, which is made from reinforced and prestressed concrete. In this section, we focus on the prediction of early age behaviour of the first lift of the containment wall (gusset) which contributed to the Benchmark VeRCoRs 2015. During the early age phase, compressive thermal stresses exist during the temperature peak, leading to a shrinkage of solid concrete which passes in tension when it turns back to the ambient temperature so, the strain gradient in the concrete thickness is mainly due to the endogenous and thermal shrinkage and the restrained strains due to the presence of a lower massive basement. Consequently, the risk of cracking in this zone is higher and requires a deep analysis for concrete damage. The prestressing wires have not yet been applied during this period but, following the CEOS.fr recommendations, the structural effect of reinforcement and size effect have been considered in the modelling to reproduce the behaviour of the concrete structure. The mechanical modelling of VeRCoRs uses the results such as the hydration degree, water content and porosity issued from hydration model in Chapter I and the other model and material parameters defined in the summary table of parameters in the previous chapters.

The following paragraph can be distinguished into two case studies. For the first study in the Benchmark VeRCoRs 2015, a representative structural volume (RSV) corresponding to 4.5° of angle was modelled according to the axisymmetric problem (see Figure 5-19). Thereafter, a second study is conducted on the whole containment to predicting realistically the gusset behaviour at early age and to contribute, in the near future, to the next Benchmark VeRCoRs 2018 aiming at study of behaviour of the whole VeRCoRs from pouring time to LOCA.

5. 5. 1. Benchmark VeRCoRs 2015

An International workshop on this benchmark was performed on 7-9 March 2016. The first blind study was performed during this benchmark without assessing to the experimental results in terms of temperature, deformation, and cracking patterns. So, in order to obtain the most realistic behaviour of the gusset, the surrounding structure elements are also taken into consideration such as the second and third lift of containment wall, and the basement. As the basement is a massive structure that is risk for cracking, the pedestal was also modelled in order to realistically consider the mechanical boundary conditions. The modelled RSV is finely meshed and contains the holes for prestressing cables as expected that they would be the weak points for the crack occurrence (Figure 5-19). Concerning the mechanical boundary conditions, the displacements of lateral surfaces of RSV are blocked in the normal direction to represent the symmetry problem and the displacement of the lower surface of RSV is restrained in the vertical direction.

To highlight the effect of distributed reinforcements in this study, two modelling are carried out: one without reinforcement and one with distributed reinforcements. The maximal volume V_{max} for the scale effect and the ratio of distributed reinforcement in the three directions are shown in Figure 5-20.

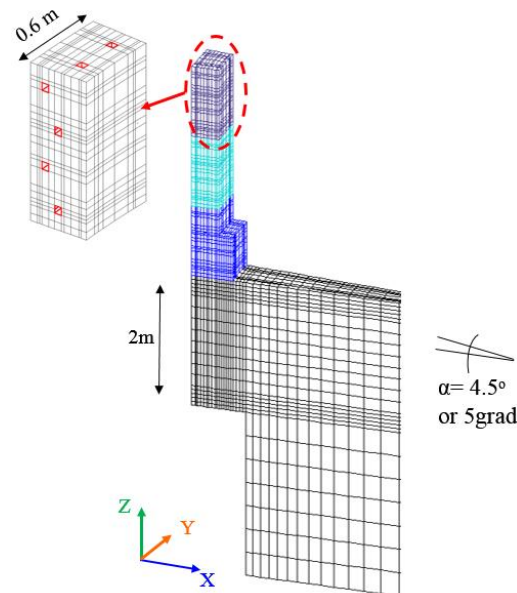


Figure 5-19: Mesh of a piece of VeRCoRs structure (angle about 4.5°)

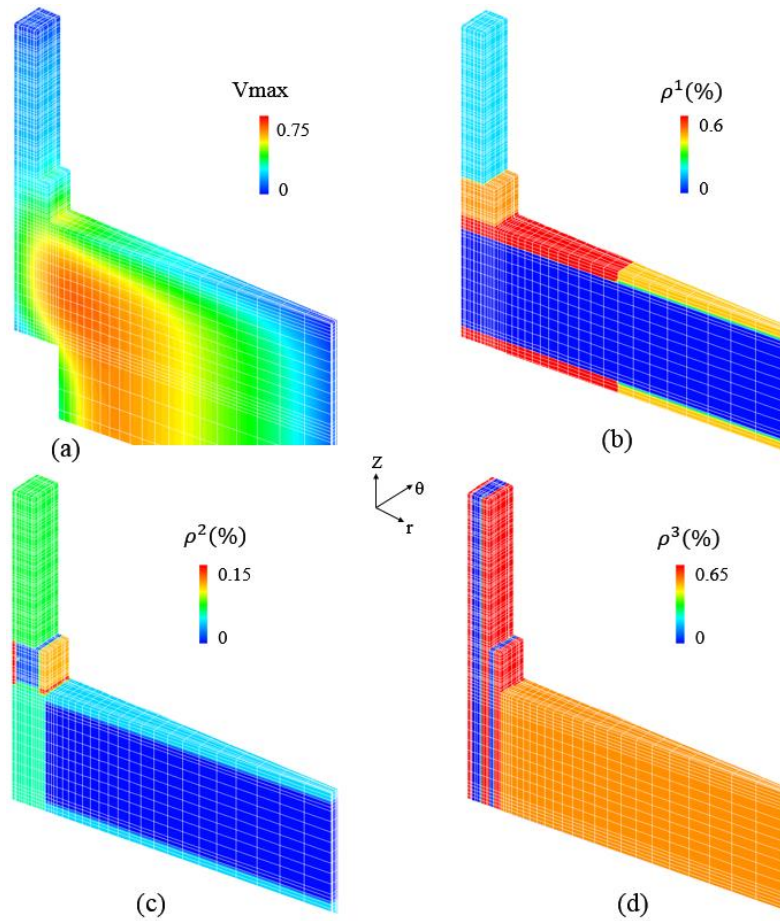


Figure 5-20: Representation of computed V_{max} (a) and ratio of distributed reinforcement in radial (b), tangential (c), vertical (d) direction

The thermal calculation last about 5 h and the mechanical calculation for the first study spend about 4 days on an ordinary personal computer. Note that the thermal results are the same as the results presented in chapter I and in a good agreement with the experiment. Besides this, the mechanical results obtained from the THCM modelling were also successfully compared with experimental results in terms of concrete strains (Figure 5-21). If we compare the results of concrete strains for RSV in concrete (black curve) and for RSV in reinforced concrete (red curve), we see that a significant decrease of strain at 3-4 days after casting, corresponding to the first crack, if we don't consider the reinforcements.

For the crack patterns obtained numerically at 5 days after pouring gusset, Figure 5-22 illustrates the effectiveness of distributed reinforcement method to reproduce globally the structural effect of reinforcement because without modelling the reinforcement, the gusset presents fewer, but more open, cracks. Moreover, the crack width given by RC modelling respect the value of experiment because the maximal crack width observed on the structure is about $100 \mu m$. But the calculation globally overestimates the crack pattern as, considering the symmetry conditions, around 80 cracks are predicted and the approximate valeur of the cumulative crack width (with reinforcement consideration) is about $4000 \mu m$ which is more

than twice from the measure as 15 cracks were observed in the real structure with crack opening lower than $100\ \mu\text{m}$ (which leads to a cumulative crack opening between $750\ \mu\text{m}$ and $1500\ \mu\text{m}$) (see Figure 5-26 and Figure 5-27). This overestimation can be partially explained by the fact that the modelled angle (4.5°) does not induced a representative orthoradial length of the part of the gusset that was modelled. A larger angle should have been chosen enough large to allow the occurring of 2 cracks in order to be representative.

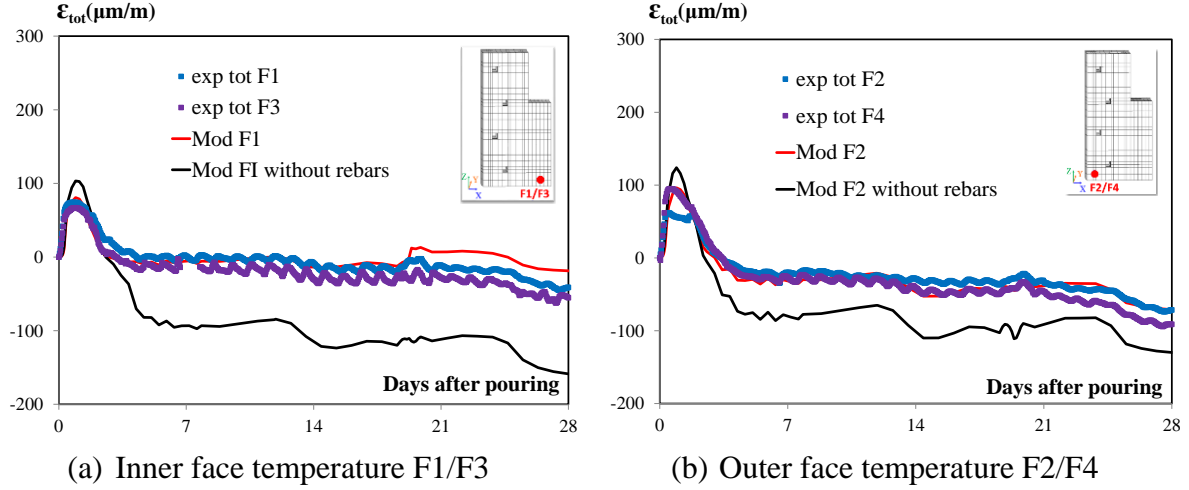


Figure 5-21: Comparison of measured (points) and numerical (curves) deformations at different points (red curve= RC modelling, black curve=Concrete modelling without reinforcement)

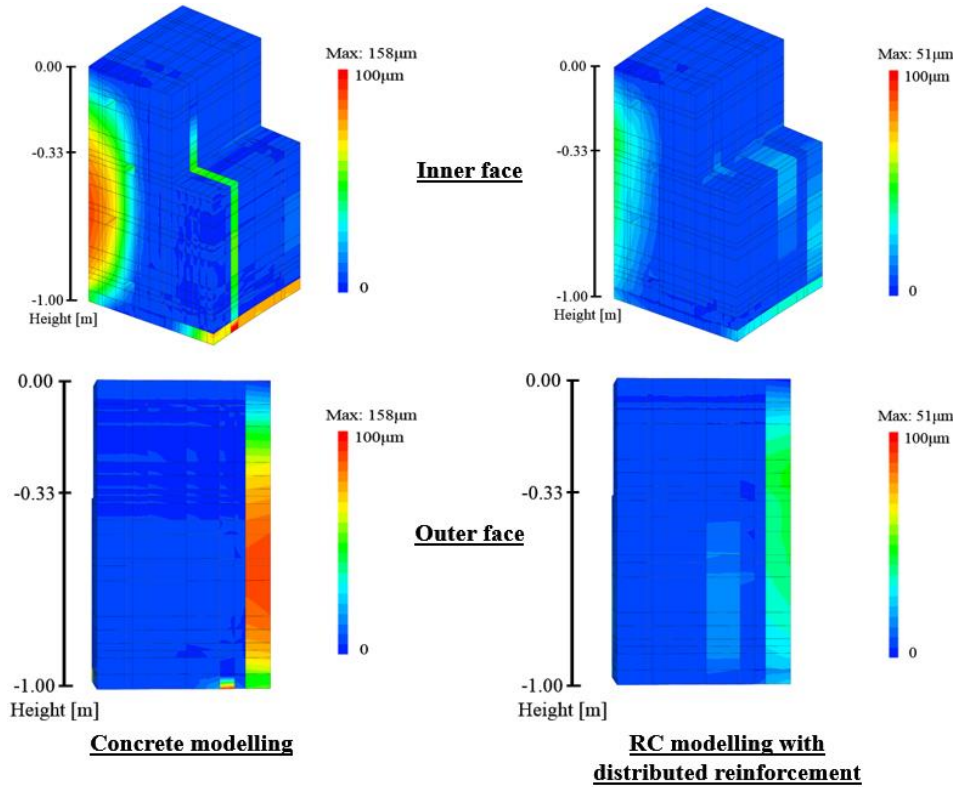


Figure 5-22: Structural effect of distributed reinforcement on the crack pattern of gusset structure

5. 5. 2. Study of the lower part of the whole vessel containment

As previously mentioned, we need a larger dimension to obtain more realistic behaviour of structure. Moreover, as in the next Benchmark 2018 we need to model the whole containment which contains two big holds in the internal wall, this study is carried out on the lower part of the whole structure. Note that after several tests on the effect of mechanical boundary conditions, the soil under the structure is also modelled and assumed to perform with elastic behaviour (see Figure 5-23).

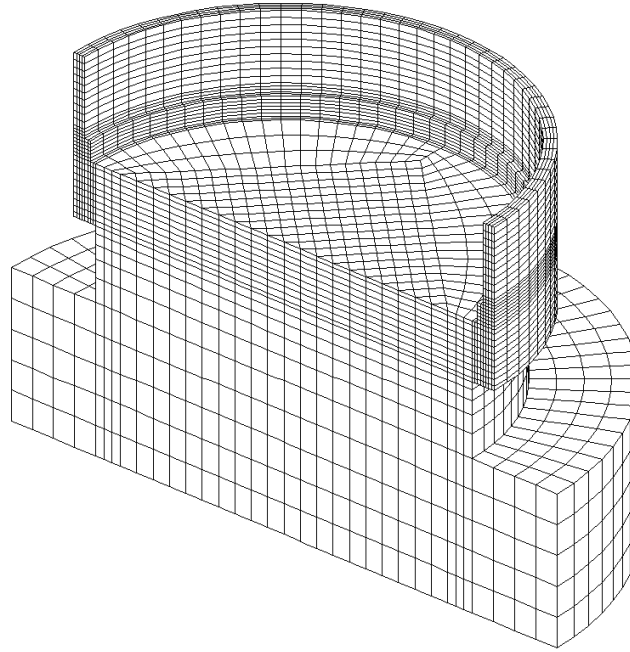


Figure 5-23: 3D mesh of lower part of whole vessel VeRCoRs standing on the soil (only a half of modelled structure is presented here)

Note that this work was granted access to the HPC resources of CALMIP supercomputing centre under the allocation 2016-p16002 (<https://www.calmip.univ-toulouse.fr/>).

The schema in Figure 5-24 shows the maximal volume for the calculation of scale effect and the ratio of distributed reinforcements in three directions (the representation is made only of half of the structure but the entire structure is modelled). Concerning mechanical boundary conditions of this second study, only the vertical displacement and rotation of the lower surface of the soil are blocked.

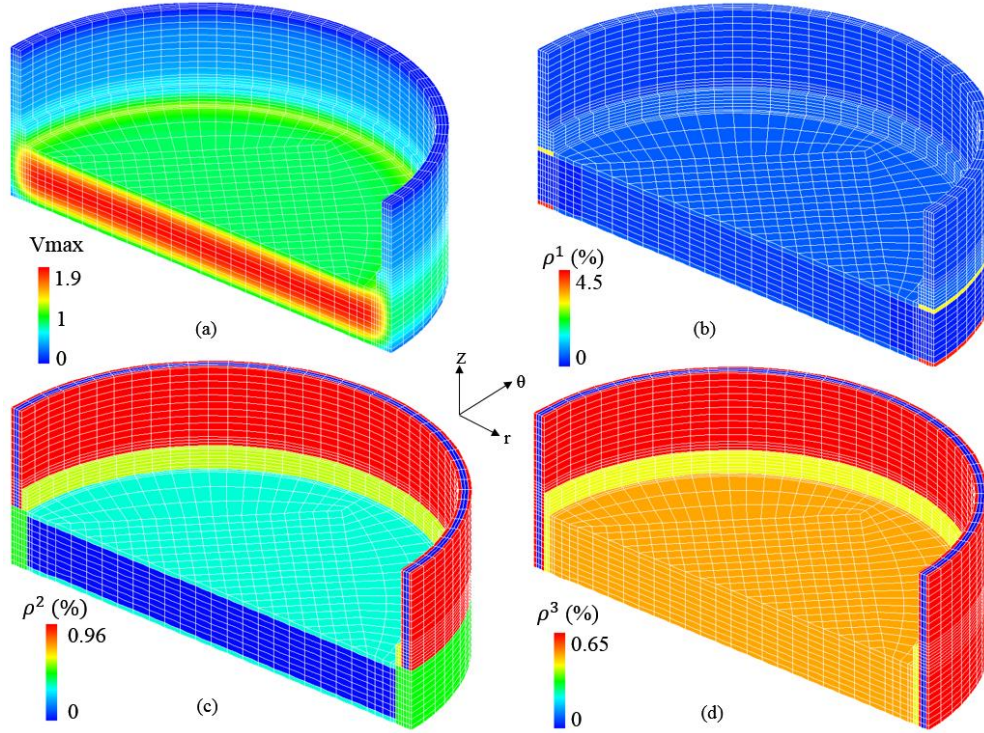


Figure 5-24: Representation of computed V_{max} (a) and ratio of distributed reinforcement in radial (b), tangential (c), vertical (d) direction for a half of modelled structure

The thermal calculation last about 5 h and the mechanical calculation for the second study spend about 5 days on HPC resources of CALMIP supercomputing centre (18 paralyzed processors at 2.4 GHz). The numerical results obtained from the THCM modelling were successfully compared with experimental results in terms of concrete strains (Figure 5-25).

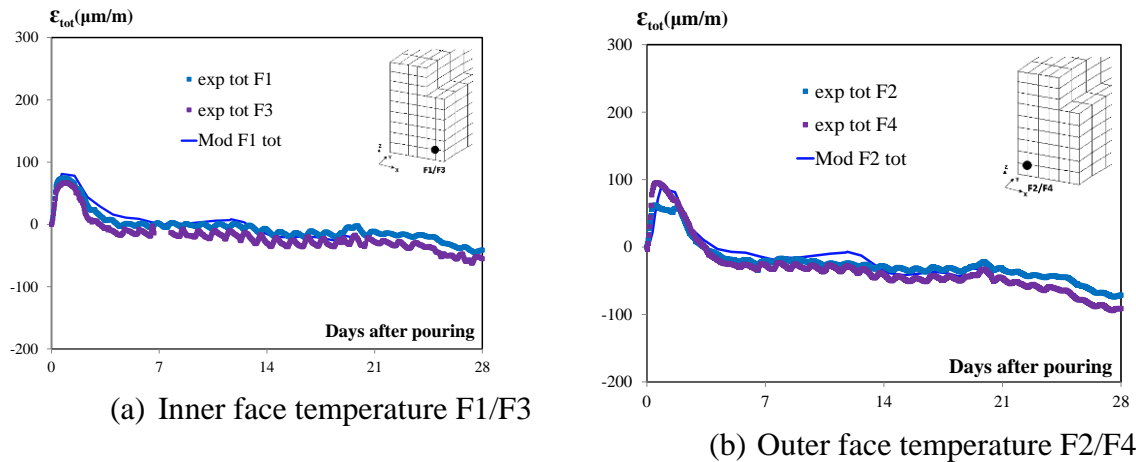


Figure 5-25: Comparison of measured (points) and numerical (blue curve) deformations at different points

As mentioned before, the approximate cumulative crack width experimentally observed is between 750 and 1500 μm along the circumferential line.

For the crack patterns obtained from the modelling (Figure 5-28), it is investigated that there are about 25 cracks with width less than 0.1 mm, leading to an approximate value of 2000 μm in total. Therefore, the crack pattern obtained in this study become closer the experiment.

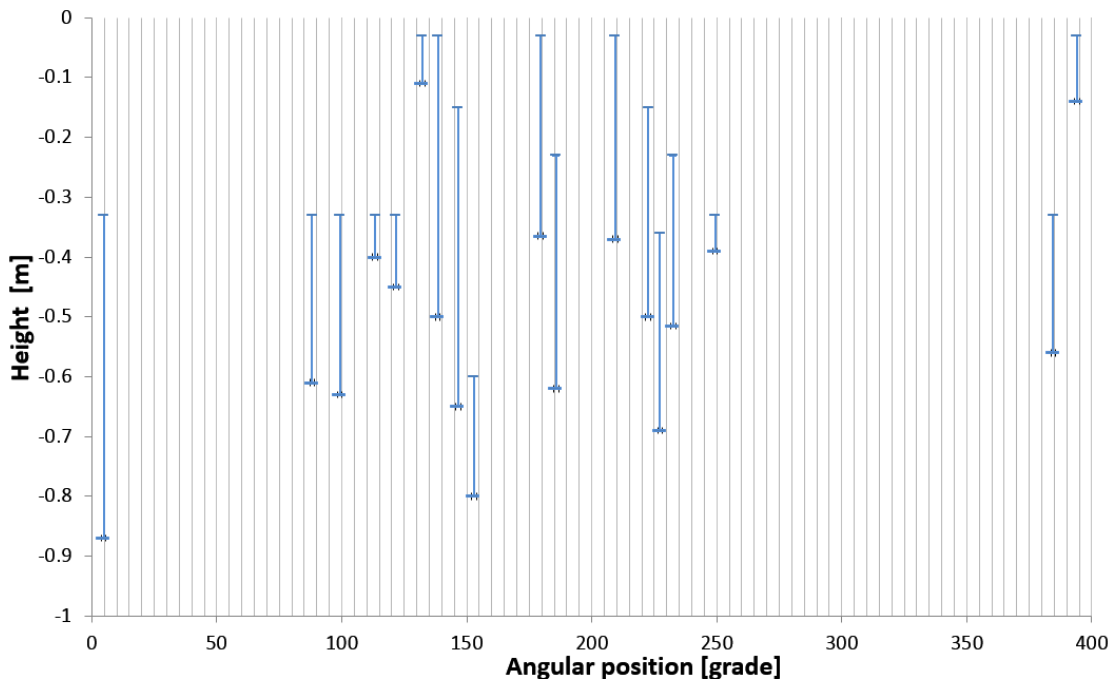


Figure 5-26: Comparison of crack patterns from models (concrete and reinforced concrete) with experimental measurements on intrados of gusset 5 days after casting

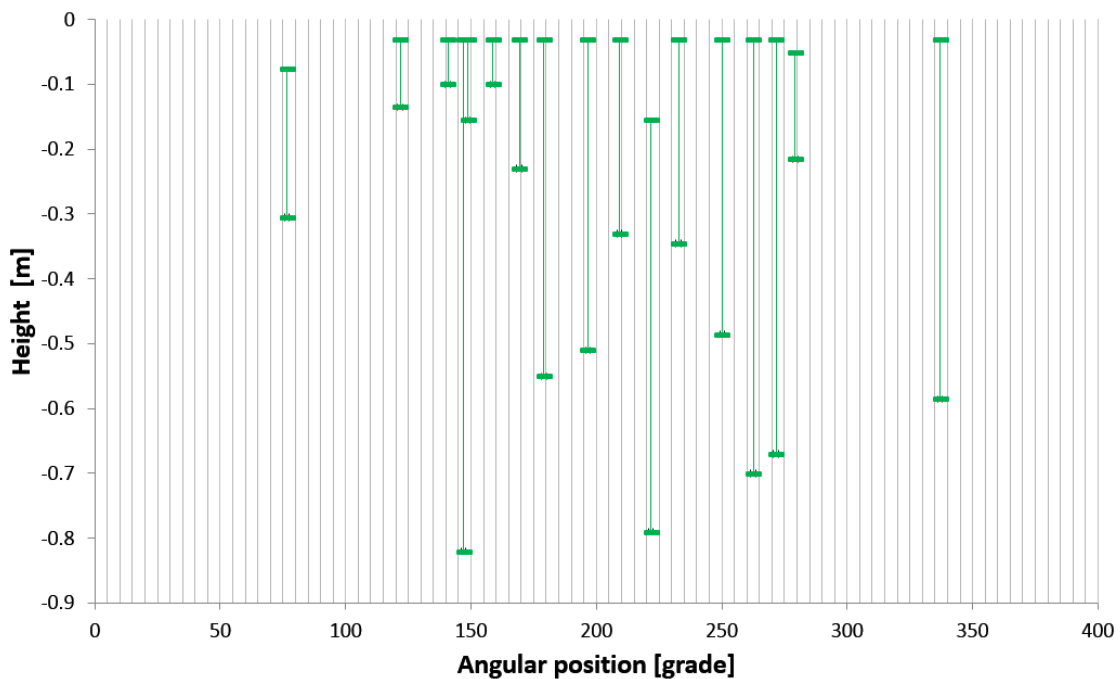


Figure 5-27: Comparison of crack patterns from models (concrete and reinforced concrete) with experimental measurements on extrados of gusset 5 days after casting

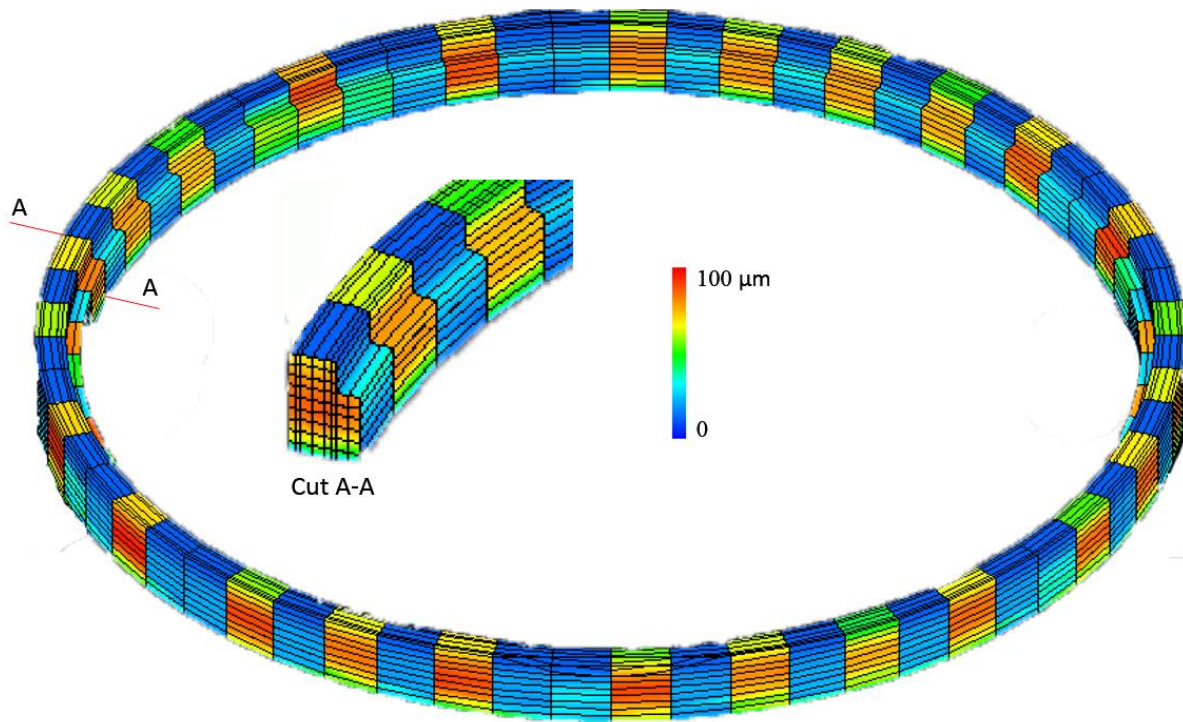


Figure 5-28: Numerical crack pattern of VeRCoRs gusset 5 days after casting (25 cracks in total)

5.6. Conclusion

In conclusion, THCM models developed in this thesis work have been applied to real structures such as PACE 1450 structure and VeRCoRs structure. We note that the scale effect is very important for modelling of massive structures like the vessel containment because the tensile strength can be reduced by 50% from a value measured at specimen scale (splitting tests at the laboratory) when applying to massive structure. The Weakest Link and Localisation (WL^2) method is an efficient method which is well adapted for large-scale structure modelling. Moreover, we also observe that the distributed reinforcement method is able to reproduce the structural effect of reinforcement and suitable for massive structures with a lot of rebars. Besides these, the improvements made to THCM models brought in this thesis work are tested and provided satisfactory results in comparison with experiments. We note that a good agreement with experimental measurements is obtained by considering many phenomena such as the effect of hydration development, the influence of temperature and humidity on the mechanical behaviours, the effect of relaxation of prestressing wires, the structural effect of distributed reinforcement and the scale effect.

General conclusion and perspectives

The safety demonstration of nuclear power plants after long-term operation (more than 50 years old) becomes more demanded following the severe accidents of Chernobyl (in Ukraine, 1986) and Fukushima (in Japan, 2011). In this context, the national project ANR-PIA MACENA (Confinement Assessment of a vessel during an Accident) has been launched since 2013 in order to understand the phenomena that occur during the LOCA induced conditions. The experimental campaigns and modelling works have been designed based on an experimental containment vessel mock-up VeRCoRs.

This PhD work focused exclusively on the computational strategy and numerical modelling of the THCM behaviour of prestressed concrete structures envisioned for LOCA conditions (i.e. increase of temperature up to 180°C and vapour pressure 5 bars maintained several weeks). Based on the experimental results from different partners in the MACENA project and the literature review, the finite element models have been proposed and tested. The computational strategy has consisted in accumulating the damage by a single model from the early age until the LOCA. In this work, several multiphysics models have been studied, improved and tested before their possible use to assess a real structure.

The preliminary prediction of the evolution of chemical, thermal and hydric state of early age concrete from casting has been completed in chapter I using the hydration model. This hydration model allows predicting the hydration degree, temperature, water content and porosity of concrete at early age. As it has been applied to a massive vessel structure, concreting sequence modelling was required and a new strategy has been proposed to adapt with this problem by introducing a new term in order to delay the activation of the hydration model. The interests of using this method for modelling the massive structures are to avoid re-mesh the structure at each stage of casting and to consider realistically the particularities of large structures such as the sequential concreting at different date, the variation of initial temperature of fresh concrete, the daily variation of external temperature, the air convection with/without the presence of formwork. These considerations lead to reproduce the temperature evolution in the gusset of VeRCoRs mock-up and provide the chemo-physical data (i.e. hydration degree, water content and porosity) of concrete for supplying the mechanical model in chapter III.

Then the thermal and hydric state of concrete structure for long-term operation, including the LOCA has been studied in chapter II. The simplified TH model has been developed in this part in order to provide the evolution of temperature and water saturation. The interests of this model for modelling the massive structures that undergo the heating are to consider thermal and hydric states (i.e. saturated and unsaturated) in a single model. Moreover, a new extension of Van Genuchten model has been proposed and integrated into this model to consider the

influence of temperature on the isothermal curves based on the experimental data in the literature review. The originality of this new implementation of heat-mass transport consists in a continuous description of the saturated and unsaturated state through liquid pressure p_l which is the single state variable for the hydric part of model. This requires to express all the parameters as a function of p_l , so a relationship of p_v and p_l has been proposed based on the Kelvin-Laplace's law. Even if it was not done in this first study (for which early age model and TH model for elevated temperature was used separately, this continuous description could be used to model the hydric and thermal behaviour all along the concrete life. For this purpose, the coupling between microstructure development and transport properties must be studied. A way to consider this effect could partly be the use water retention curves depending not only on the temperature but also on the hydration degree (as it was proposed in (Souyris 2012)) and permeability coefficient depending on the microstructure which is still challenging, especially for experimental determination. This coupling with microstructure evolution could also be a way to consider more explicitly the effect of dehydration on transport properties than the way it is done for the moment in literature. Because of the range of temperature studied, these couplings were not considered in this study and the validation was thus made here on the simulation of the evolution of temperature and vapour pressure of the experimental mock-up MAQBETH that is submitted to a variation of temperature until 200°C.

The results of the two previous models provide the data for the mechanical model to estimate the delayed deformations of concrete and the risk of cracking. The mechanical model of reinforced concrete has been presented in chapter III. It includes the rheological and damage models which were initially developed at LMDC. New improvements have been made to these models thanks to experimental campaigns in the framework of MACENA and MOSAIC project that focused on the influence of elevated temperature and humidity on the mechanical behaviour of concrete. A relatively simple damage law has been proposed to consider the effect of temperature and saturation degree and used to model DCT tests under variable thermohydric conditions. The THCM model for delayed deformations at high temperature and humidity is relatively well validated by considering the effect of the differential expansion of concrete components, the transient thermal creep, and the effect of temperature, the saturation degree and the loading rate on the creep rate. It can be noticed that the improvement of the modelling of transient thermal creep applied in this study which was initialised in the PhD work of (Cagnon, 2015) with ANDRA and is currently extended in the PhD work of (Manzoni, 2017) will be usable for the Benchmark VeRCoRs. In fact the transient thermal creep phenomenon leads to, in some conditions, strains as large as the conventional creep but in a very short.

Besides this, a distributed reinforcement method is also proposed in this chapter in order to take into account the structural effect of reinforcement in the massive structure without explicit mesh of rebars. This method has been successfully validated on the three-point bending beam from the benchmark MECA.

The distributed reinforcement method can be used for rebars and prestressing wires. The consideration of relaxation of prestressing steel wires has been treated in chapter IV. A delayed strain model has been developed for prestressing by considering the nonlinear effects of temperature and initial prestress on the relaxation phenomenon. The coupling of these effects has been carried out introducing a thermal activation coefficient that depends on the maximal loading ratio. The experimental results of relaxation of wires under different thermomechanical conditions and stepwise thermal state were successfully reproduced by the relaxation model. The features of this model seem to be suitable to predict the prestress loss during the life of massive structure of a nuclear containment building and the envisioned LOCA.

In the last chapter, these material models have been used to simulate elements of real large structures. In these applications, following the CEOS.fr project conclusions, a particular attention to the probabilistic scale effect is paid. This scale effect reduces the tensile strength significantly in large elements of structure, it is treated thanks to the Weakest Link and Localisation (WL²) approach clarified in the ANR project MEFISTO, this method is based on the Weibull theory coupled with the second gradient one. This method coupled with the other models improved and fitted during the MACENA project allows assessing the most likely tensile strength for the different cracks in the structure. In this work, the probabilistic scale effect is applied since the early age, but intensive study of scale effect on an early age concrete is needed to verify if the scale effect evolves with the cement hydration, and if WL² needs improvements to be applicable in the homogenized RC context (with distributed reinforcements method).

The applications of the model on the prediction of the behaviour of the nuclear wall mock-up PACE 1450 and a part of the vessel mock-up VeRCoRs highlight the capability of the model to globally reproduce the behaviour of reinforced and prestressed concrete under various solicitations (early age temperature increase, pressure ...). But the validation should be completed by the application of the model to mechanical tests on heating or heated reinforced and prestressed concrete elements:

- Bending tests on unnotched beams specimens tested after a long-term storage at different temperatures and saturation rates (LMDC – ANR Mosaic), with a probably rewriting of the laws used to traduce the effect of saturation on mechanical behaviour according to the liquid pressure (to be totally compatible with the thermo-hydric model of chapter II).
- Prestressed and reinforced concrete beams tested under creep loading at different humidity, temperature and creep load (LMDC – MACENA), to validate the relaxation law proposed in chapter IV when the wires are used in concrete beams.

- Pull-out test at different temperatures (IFSTTAR Nantes – MACENA), to verify if the separate effects of temperature on concrete and steel allow reproducing these tests or if the temperature also affects the steel-concrete bond properties.
- RUNs 7 to 10 of PACE structure in which temperature is increased to 140°C, to validate the cumulative approach until the LOCA.

It can next be envisioned to apply the model to the whole VeRCoRs structure in the framework of the numerical benchmark VeRCoRs (deadline March 2018) in which the effect of cumulative damage from the concrete pouring until the end of LOCA will be considered.


To assess with more precision the crack pattern (especially the opening) some improvements of the behaviour laws and numerical models are still needed. As shown in the CEOS.fr project, considering the reinforcement - concrete sliding is needed to improve the assessment of crack openings, particularly in zones meshed with small finite elements, but the mesh of reinforcements frame is always difficult and time-consuming, both during the mesh generation and the numerical analysis; so a method avoiding an explicit meshing of reinforcement, but nevertheless able to consider their effects is needed. This method can be based on the distributed reinforcement model presented in this manuscript (chapter 3 and 5) coupled with a second gradient method (close to the WL^2 one) avoiding meshing the reinforcement frames details, a research on this topic is carried out in LMDC Toulouse, and a software property deposit with Toulouse Tech Transfer ([TTT](#)) is done, but the method must be improved and tested on real structures.

For application to structures subjected to high temperatures, a good assessment of the crack pattern and induced leakage needs the possibility to consider also a diffuse cracking induced by the vapour over-pressure; a way could be to treat it like the overpressure as RAG and RSI in the LMDC endo-poro-plastic model, which allows a combination of several diffuses anisotropic cracking criteria. A strong coupling between anisotropic crack opening and anisotropic permeability tensor was proposed a few years ago by LMDC in the PhD work of Rahal (Rahal et al., 2017). This model could be coupled with the tools developed in MACENA to simulate the post LOCA behaviour.

Finally, as it is well known on this kind of massive structures casted in several phases that a preferential cracking appears at the joint between two lifts, a coupling of our plain RC model with the TH joint model clarified by A. Millard in CEA, in the framework of MACENA, could allow considering particular effects of these lift joints and other initial singularities, this coupling will be possible if common state variables are used in our plain concrete model and in the CEA model.

Annexes

Annexe 1: Technical data sheet of cement



CCB
Italcementi Group

Grand-Route 260
B - 7530 Gaurain-Rumecroix

Tél. ++32 (0) 25 25 11
Fax ++32 (0) 25 25 90

Version du : 02/09/2011
N° Certificat CE : 0965-CPD-00141

Fiche produit de		Gaurain CEM I 52.5 N CE CP2 NF	
-------------------------	--	---	--

Caractéristiques physiques et mécaniques									
Compression en MPa				Eau pâte pure en %	Début de prise Fin de prise en min	Chaleur en J/g à 12h à 41h	Surface Blaine en cm²/g	Masse volumique en g/cm³	Stabilité en mm
1j	2j	7j	28j	28,0	190-210	240-350	4150	3,19	1
23	30	51	65						


Composition élémentaire (%)		Constituants (%)		Caractéristiques des constituants		
Perte au feu	2,1	<u>Principaux</u>		Nature	Caractéristiques	
SiO2	20,8	Clinker (K) de Gaurain	96,0	<u>Clinker (K)</u> Gaurain	CaO/SiO2	3,1
Al2O3	4,5	Laitier (S)			C2S, C3S	79,0
Fe2O3	2,3	Cendres (V)			MgO (%)	2,2
TiO2	0,3	Calcaire (L)			C3S (%)	68
MnO	0,1	Fumées de silice (D)			C2S (%)	10
CaO	63,2	<u>Secondaires</u>			C3A (%)	9
MgO	2,1	Calcaire (L)	4,0		C4AF (%)	7
SO3	3,3	Fillers (F)		<u>Laitier (S)</u>	Laitier vitreux (%) (CaO+MgO)/SiO2 CaO+MgO+SiO2 (%)	
K2O	0,73	Total	100,0		PF (%)	
Na2O	0,36	<u>Sulfate de calcium</u>		<u>Cendres (V)</u>	CaO réactive (%)	
P2O5	0,3	Gypse	3,3		SiO2 réactive (%)	
S=	0,02	Anhydrite		<u>Calcaire (L)</u>	CaCO3 (%)	
Cl=	0,05	<u>Additifs</u>			Ads. bleu	
Insoluble CEN	0,48	Agent de mouture			TDC (%)	
Na2O eq.	0,54	CLOTIER 5903		<u>Fumées de silice (D)</u>	SiO2 amorphe (%)	
		(AXOM) I / T	0,33		PF (%)	
Colorimétrie (L)	65	Agent réducteur			Aire massique	
		FeSO4.H2O	0,18		BET (m²/kg)	

Mouture	
Broyeur(s)	7-8 & 9

Stockage	
Site(s)	cf plan de stockage

Points de vente	Vrac	Sac
Usine de Gaurain	oui	oui
Dépôt de Chercq	oui	non
Dépôt de Gent	oui	non
Dépôt de Gennevilliers	oui	non

Ces valeurs ne sont données qu'à titre indicatif. Les résultats d'autocontrôles sont disponibles sur demande à la Direction Commerciale Assistance et Prescription Clients.



La Compagnie des Ciments Belges CCB s.a.
TVA/BTW B-412443268
CEP/FPA 068 000125138
R.C.B.A. Tournai 75125

Figure A-1: Technical data sheet of cement

Annexe 2: Technical data sheet of aggregates

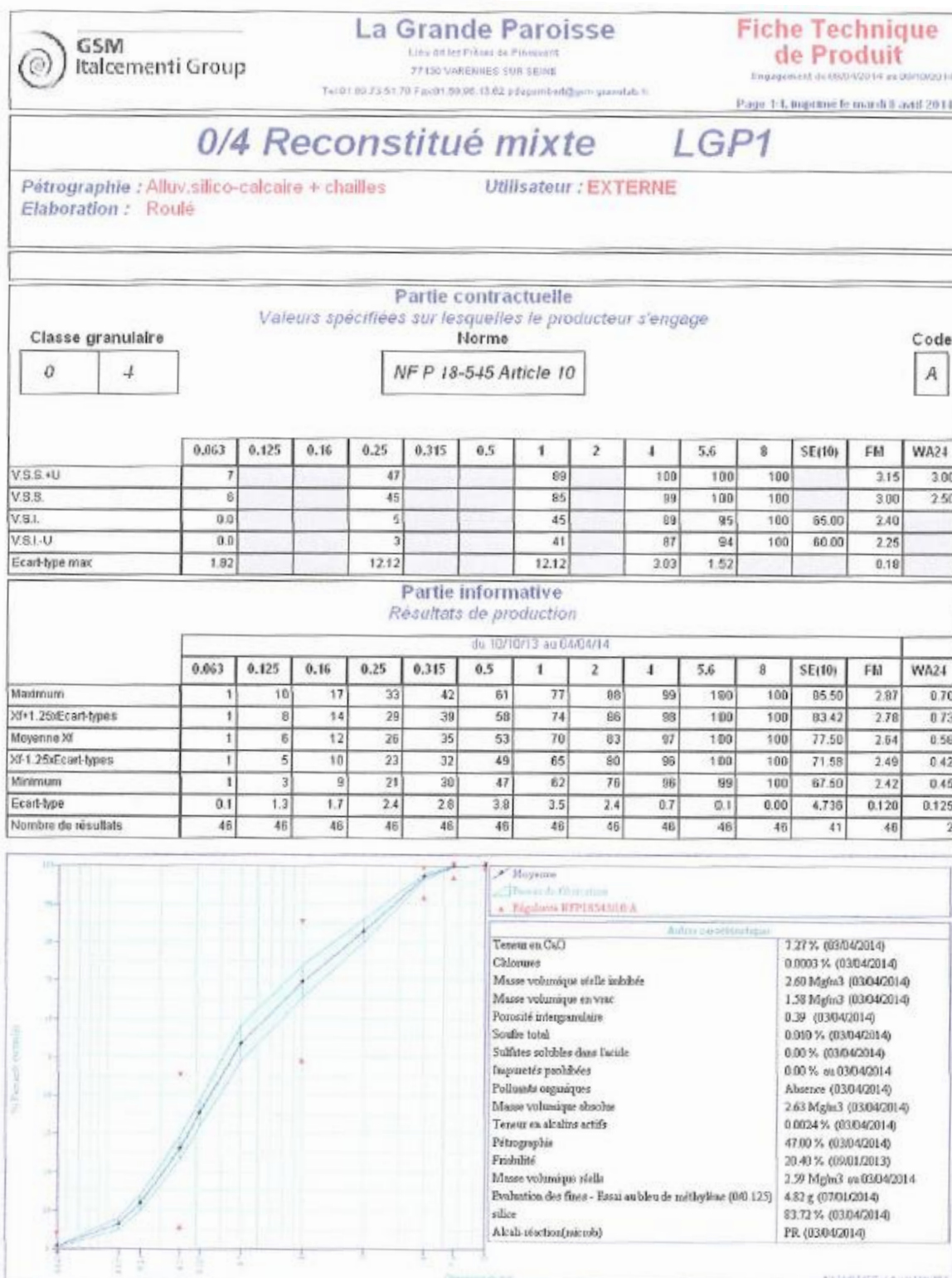


Figure A-2: Technical data sheet of aggregate 0/4

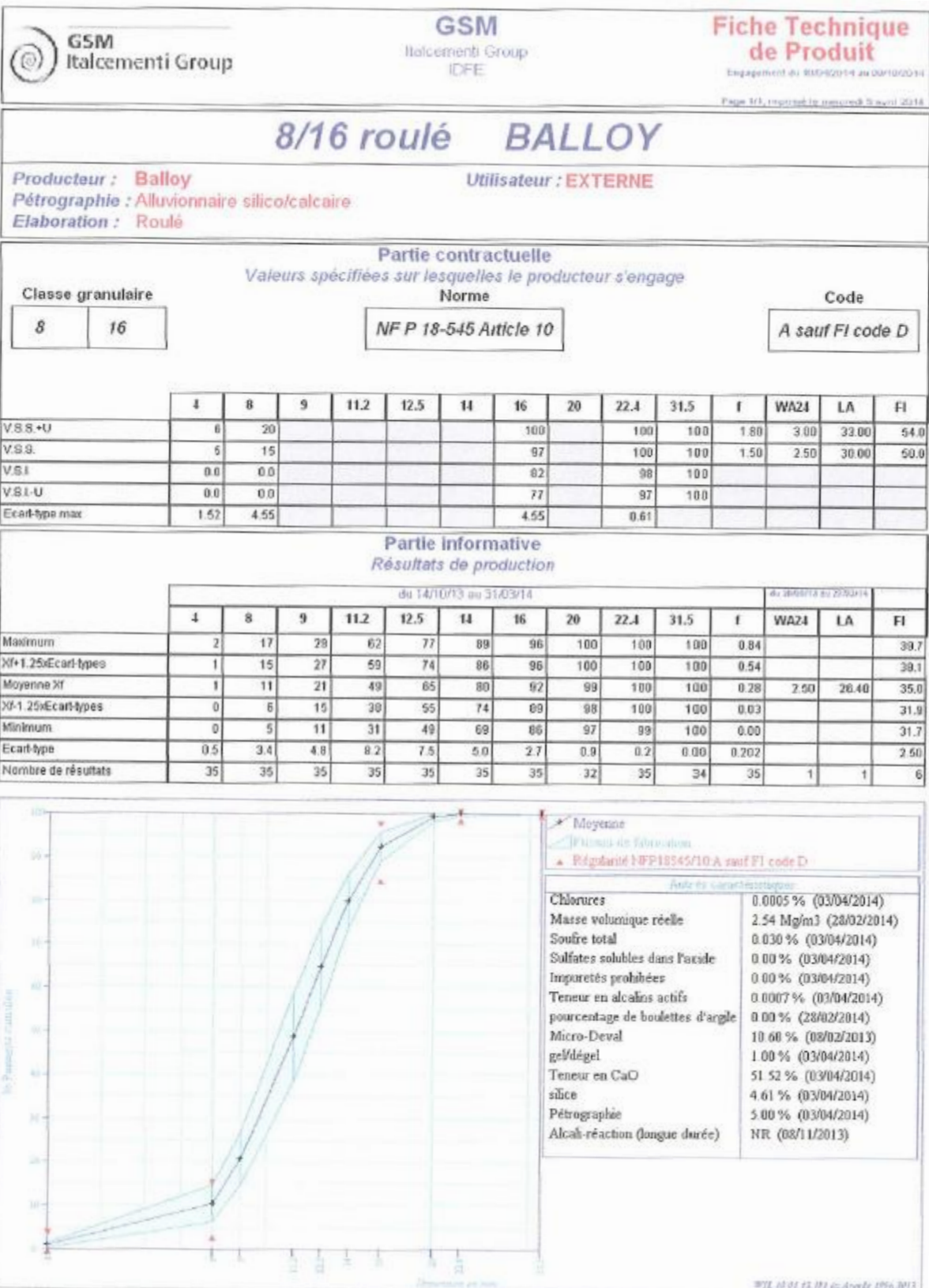


Figure A-4: Technical data sheet of aggregate 8/16

Annexe 3: Technical data sheet of superplasticizer



Construction

Notice produit
Edition Septembre 2015
Numéro 264
Version n° 2015-250
SIKAPLAST® TECHNO 80


SIKAPLAST® TECHNO 80

Plastifiant/Réducteur d'eau de nouvelle génération pour bétons prêts à l'emploi.

Conforme à la Norme NF EN 934-2

Présentation	Le SIKAPLAST® TECHNO 80 est un plastifiant réducteur d'eau non chloré, de nouvelle génération pour bétons prêts à l'emploi, qui se présente sous la forme d'un liquide jaune clair.
Domaines d'application	<p>SIKAPLAST® TECHNO 80 est un plastifiant/réducteur d'eau qui a été développé spécifiquement pour l'utilisation de granulats concassés dans les bétons de consistance S3 et S4. SIKAPLAST® TECHNO 80 confère aux bétons un bon maintien rhéologique (>1h30) sans effet retard sur les résistances initiales.</p> <p>SIKAPLAST® TECHNO 80 permet la fabrication de :</p> <ul style="list-style-type: none"> ■ bétons de consistance S3 et S4, ■ bétons composés de sable et gravillon concassés, ■ bétons utilisant des eaux chargées, ■ bétons pompés sur longues distances. <p>SIKAPLAST® TECHNO 80 confère, pour des bétons S3 et S4, une consistance onctueuse permettant d'utiliser des granulats concassés.</p>
Caractères généraux	<p>Le SIKAPLAST® TECHNO 80 est un plastifiant réducteur d'eau qui confère au béton les propriétés suivantes :</p> <ul style="list-style-type: none"> ■ maintien prolongé de la rhéologie (> 1h30min), ■ haute réduction d'eau, ■ stabilité et homogénéité des bétons composés de sable et gravillon concassés, ■ bonnes résistances initiales et finales, ■ bel aspect de parement au décoffrage.
Caractéristiques	
Aspect	Liquide jaune clair
Conditionnement	<ul style="list-style-type: none"> ■ Vrac ■ Conteneur perdu de 1000 litres ■ Fût de 220 kg
Stockage	<p>A l'abri du gel.</p> <p>En cas de gel accidentel, le produit retrouve ses qualités d'origine une fois dégelé lentement et réhomogénéisé.</p>
Conservation	12 mois dans son emballage d'origine intact



1
SIKAPLAST® TECHNO 80 1/2

Figure A-5: Technical data sheet of superplasticizer (a)

Données techniques

densité 1,055 ± 0,020

pH 4,5 ± 1,0

Teneur en ions Cl⁻ ≤ 0,1 %Teneur en Na₂O Eq. ≤ 1,5 %Extrait sec 23,5 ± 1,1 % (Méthode halogène selon NF 085)
24,0 ± 1,2 % (NF EN 480-8)**Conditions d'application**

Consommation / Dosage Plage d'utilisation recommandée 0,1 à 3,0% du poids de liant ou du ciment selon la fluidité et les performances recherchées.

Mise en œuvre

Le SIKAPLAST® TECHNO 80 est ajouté, soit, en même temps que l'eau de gâchage, soit en différé dans le béton préalablement mouillé avec une fraction de l'eau de gâchage.

Précautions d'emploiEn cas de contact avec la peau, laver abondamment à l'eau.
Consulter la fiche de données de sécurité accessible sur Internet www.sika.fr**Mentions légales**

Produit réservé à un usage strictement professionnel

Nos produits bénéficient d'une assurance de responsabilité civile.

«Les informations sur la présente notice, et en particulier les recommandations relatives à l'application et à l'utilisation finale des produits SIKA, sont fournies en toute bonne foi et se fondent sur la connaissance et l'expérience que la Société SIKA a acquises à ce jour de ses produits lorsqu'ils ont été convenablement stockés, manipulés et appliqués dans des conditions normales. En pratique, les différences entre matériaux, substrats et conditions spécifiques sur site sont telles que ces informations ou toute recommandation écrite ou conseil donné n'impliquent aucune garantie de qualité marchande autre que la garantie légale contre les vices cachés. Nos agences sont à votre disposition pour toute précision complémentaire. Notre responsabilité ne saurait d'aucune manière être engagée dans l'hypothèse d'une application non conforme à nos renseignements. Les droits de propriété détenus par des tiers doivent impérativement être respectés. Toutes les commandes sont acceptées sous réserve de nos Conditions de Vente et de Livraison en vigueur. Les utilisateurs doivent impérativement consulter la version la plus récente de la notice correspondant au produit concerné, qui leur sera remise sur demande.»



Sika France S.A.
84, rue Edouard Vaillant – BP 104
93351 Le Bourget Cedex

Tel. : 01 49 92 80 00
Fax : 01 49 92 80 21

Organisme de certification :
AFNOR CERTIFICATION
11, avenue Francis de Pressensé
93571 Saint-Denis La Plaine cedex
France

Figure A-6: Technical data sheet of superplasticizer (b)

References

3SR Grenoble, CEA, IFSTTAR, IPRA Pau, LMDC Toulouse, CERIB, EDF R&D, NECS and OXAND (2012). MACENA Project.

Abdel-Fattah, H., and Hamoush, S.A. (1997). Variation of the fracture toughness of concrete with temperature. *Constr. Build. Mater.* 11, 105–108.

AbdelRahman, A.K., and Ahmed, G.N. (1996). Computational Heat and Mass Transport in Concrete Walls Exposed to Fire. *Numer. Heat Transf. Part Appl.* 29, 373–395.

Abrams, M.S., and Cruz, C.R. (1961). THE BEHAVIOR AT HIGH TEMPERATURE OF STEEL STRAND FOR PRESTRESSED CONCRETE (Portland Cement Assoc R & D Lab).

ACI 440.3R-04 (2004). Guide Test Methods for Fiber-Reinforced Polymers (FRPs) for Reinforcing or Strengthening Concrete Structures (USA: American Concrete Institute).

ACI Committee 209 (2005). ACI 209.1R-05: Report on Factors Affecting Shrinkage and Creep of Hardened Concrete.

Acker, P., and Ulm, F.-J. (2001). Creep and shrinkage of concrete: physical origins and practical measurements. *Nucl. Eng. Des.* 203, 143–158.

Al Najim, A. (2004). Modélisation et simulation du comportement du béton sous hautes températures par une approche thermo-hygro-mécanique couplée. Thèse de doctorat. Université de Marne-la-Vallée.

Anderberg, Y. (2003). Effect of heat on concrete.

Anderson, P. (2005). Thirty years of measured prestress at Swedish nuclear reactor containments. *Nucl. Eng. Des.* 235, 2323–2336.

ASHRAE (1993). Fundamentals (Atlanta).

Atienza, J.M., and Elices, M. (2009). Behavior of prestressing steels after a simulated fire: Fire-induced damages. *Constr. Build. Mater.* 23, 2932–2940.

Badel, P., and Lorentz, E. (2011). Critères de convergence en mécanique des solides. In 10e Colloque National En Calcul Des Structures, (Giens, France), p. Clé USB.

Baker, G. (1996). The effect of exposure to elevated temperatures on the fracture energy of plain concrete. *Mater. Struct.* 29, 383–388.

Baroghel-Bouny, V. (1994). Caractérisation microstructurale et hydrique des pâtes de ciment et des bétons ordinaires et à très hautes performances. Ecole Nationale des Ponts et Chaussées.

Baroghel-Bouny, V., Mainguy, M., Lassabatere, T., and Coussy, O. (1999). Characterization and identification of equilibrium and transfer moisture properties for ordinary and high-performance cementitious materials. *Cem. Concr. Res.* 29, 1225–1238.

- Bartlett, F.M., and MacGregor, J.G. (1994). Effect of Moisture Condition on Concrete Core Strengths. *Mater. J.* 91, 227–236.
- Bary, B. (1996). Étude du couplage hydraulique-mécanique dans le béton endommagé. Cachan, Ecole normale supérieure.
- Bary, B., Ranc, G., Durand, S., and Carpentier, O. (2008). A coupled thermo-hydro-mechanical-damage model for concrete subjected to moderate temperatures. *Int. J. Heat Mass Transf.* 51, 2847–2862.
- Bary, B., De Morais, M.V.G., Poyet, S., and Durand, S. (2012). Simulations of the thermo-hydro-mechanical behaviour of an annular reinforced concrete structure heated up to 200 °C. *Eng. Struct.* 36, 302–315.
- Bazant, Z.P. (1999). Size effect on structural strength: a review. *Arch. Appl. Mech.* 69, 703–725.
- Bazant, Z.P. (2004). Probability distribution of energetic-statistical size effect in quasibrittle fracture. *Probabilistic Eng. Mech.* 19, 307–319.
- Bazant, Z.P., and Chern, J.C. (1985). Concrete creep at variable humidity: constitutive law and mechanism. *Mater. Struct.* 18, 1–20.
- Bazant, Z.P., and Kaplan, M. (1996). Concrete at high temperature: material behavior and mathematical modeling. 412.
- Bazant, Z.P., and Novak, D. (2000). Probabilistic Nonlocal Theory for Quasibrittle Fracture Initiation and Size Effect. I: Theory. *J. Eng. Mech.* 167–174.
- Bazant, Z.P., and Prat, C. (1988). Effect of Temperature and Humidity on Fracture Energy of Concrete. *ACI Mater. J.* 85.
- Bazant, Z.P., and Thonguthai, W. (1978). Pore Pressure and Drying of Concrete at High Temperature. *J. Eng. Mech. Div.* 104, 1059–1079.
- Bazant, Z.P., and Yavari, a. (2005). Is the cause of size effect on structural strength fractal or energetic–statistical? *Eng. Fract. Mech.* 72, 1–31.
- Bazant, Z.P., and Yu, Q. (2013). Relaxation of Prestressing Steel at Varying Strain and Temperature: Viscoplastic Constitutive Relation. *J. Eng. Mech.* 139, 814–823.
- Bazant, Z.P., Asghari, A.A., and Schmidt, J. (1976). Experimental study of creep of hardened Portland cement paste at variable water content. *Matér. Constr.* 9, 279–290.
- Bazant, Z.P., Cusatis, G., and Cedolin, L. (2004). Temperature Effect on Concrete Creep Modeled by Microprestress-Solidification Theory. *J. Eng. Mech.* 130, 691–699.
- Benboudjema, F. (2002). Modélisation des déformations différées du béton sous sollicitations biaxiales : application aux enceintes de confinement de bâtiments réacteurs des centrales nucléaires. Marne-la-Vallée.

- Benboudjema, F., and Torrenti, J.M. (2008). Early-age behaviour of concrete nuclear containments. *Nucl. Eng. Des.* 238, 2495–2506.
- Benboudjema, F., HEINFLING, G., and Torrenti, J.M. (2001). A Basic Creep Model for Concrete Subjected to Multiaxial Loads. p.
- Benboudjema, F., Meftah, F., and Torrenti, J.M. (2005). Interaction between drying, shrinkage, creep and cracking phenomena in concrete. *Eng. Struct.* 27, 239–250.
- Bentz, D.P. (1997). Three-Dimensional Computer Simulation of Portland Cement Hydration and Microstructure Development. *J. Am. Ceram. Soc.* 80, 3–21.
- Bentz, D.P. (2006). Influence of water-to-cement ratio on hydration kinetics: Simple models based on spatial considerations. *Cem. Concr. Res.* 36, 238–244.
- Bentz, D.P., and Garboczi, E.J. (1991). A Digitized Simulation Model for Microstructural Development.
- Bottin, A. (2017). Bilan énergétique de la France métropolitaine en 2016 - Données provisoires.
- Bouazaoui, L., and Li, A. (2008). Analysis of steel/concrete interfacial shear stress by means of pull out test. *Int. J. Adhes. Adhes.* 28, 101–108.
- Boumiz, A. (1995). Etude comparee des evolutions mecaniques et chimiques des pates de ciment et mortiers a tres jeune age. Developpement des techniques acoustiques. Paris 7.
- BPEL (1999). Règles techniques de conception et de calcul des ouvrages et constructions en béton précontraint, suivant la méthode des états-limites - BPEL 91 révisé 99. Collectif - Commission générale de normalisation-DTU.
- Briffaut, M., Benboudjema, F., Torrenti, J.-M., and Nahas, G. (2012). Concrete early age basic creep: Experiments and test of rheological modelling approaches. *Constr. Build. Mater.* 36, 373–380.
- Brue, F. (2009). Rôles de la température et de la composition sur le couplage thermo-hydro-mécanique des bétons. Ecole Centrale de Lille.
- Bucher, R., Sellier, A., Verdier, J., and Vidal, T. (2016). Effet de la microfissuration de séchage sur les propriétés mécaniques et de transfert des matériaux cimentaires (LMDC).
- Bucher, R., Vidal, T., Sellier, A., and Verdier, J. (2017). EFFET DU SÉCHAGE SUR LES PROPRIÉTÉS MÉCANIQUES DES MATÉRIAUX CIMENTAIRES. (Lille), p.
- Buffo-Lacarrière, L. (2007). Prévision et évaluation de la fissuration précoce des ouvrages en béton. PhD Thesis.
- Buffo-Lacarrière, L., and Sellier, A. (2011). Chemo-Mechanical Modeling Requirements for the Assessment of Concrete Structure Service Life. *J. Eng. Mech.* 137, 625–633.
- Buffo-Lacarrière, L., Sellier, A., Escadeillas, G., and Turatsinze, A. (2007). Multiphasic finite element modeling of concrete hydration. *Cem. Concr. Res.* 37, 131–138.

Buffo-Lacarrière, L., Sellier, A., Turatsinze, A., and Escadeillas, G. (2011). Finite element modelling of hardening concrete: application to the prediction of early age cracking for massive reinforced structures. *Mater. Struct.* 44, 1821–1835.

Buffo-Lacarrière, L., Sellier, A., and Kolani, B. (2014). Application of thermo-hydro-chemo-mechanical model for early age behaviour of concrete to experimental massive reinforced structures with strain-restraining system. *Eur. J. Environ. Civ. Eng.* 18, 814–827.

Buffo-Lacarrière, L., Baron, S., Barré, F., Chauvel, D., Darquennes, A., Dubois, J.-P., Gayete, J., Grondin, F., Kolani, B., Lançon, H., et al. (2016). Restrained shrinkage of massive reinforced concrete structures: results of the project CEOS.fr. *Eur. J. Environ. Civ. Eng.* 20, 785–808.

Burlion, N., Bourgeois, F., and Shao, J.-F. (2005). Effects of desiccation on mechanical behaviour of concrete. *Cem. Concr. Compos.* 27, 367–379.

Cagnon, H. (2015). Influence des variations thermo-hydro-mécaniques sur le comportement différé du béton. phd. Université Toulouse III - Paul Sabatier.

Carpinteri, A. (1994). Fractal nature of material microstructure and size effects on apparent mechanical properties. *Mech. Mater.* 18, 89–101.

Carpinteri, A., and Chiaia, B. (2002). Embrittlement and decrease of apparent strength in large-sized concrete structures. *Sadhana* 27, 425–448.

Carpinteri, A., Chiaia, B., and Ferro, G. (1995). Size effects on nominal tensile strength of concrete structures: multifractality of material ligaments and dimensional transition from order to disorder. *Mater. Struct.* 28, 311.

Carré, H., and Pimienta, P. (2012). Bending test at high temperature. p.

Casanova, A., Jason, L., and Davenne, L. (2012). Bond slip model for the simulation of reinforced concrete structures. *Eng. Struct.* 39, 66–78.

Castellote, M., Alonso, C., Andrade, C., Turrillas, X., and Campo, J. (2004). Composition and microstructural changes of cement pastes upon heating, as studied by neutron diffraction. *Cem. Concr. Res.* 34, 1633–1644.

CEA (2015). CAST3M-Commissariat à l’Energie Atomique CEA.

CEA (2016). CAST3M-Commissariat à l’Energie Atomique CEA.

CEOS.fr (2009a). Benchmark CEOS.fr : Fissuration sous chargement statique monotone, document de lancement du benchmark.

CEOS.fr (2009b). French national research project for the design and assessment of special concrete structure with respect to cracking and shrinkage.

CEOS.fr (2016). Comportement et évaluation des ouvrages spéciaux vis-à-vis de la fissuration et du retrait: Recommandations pour la maîtrise des phénomènes de fissuration (Presses Ponts et Chaussées (IREX)).

- Chen, W., Liu, J., Brue, F., Skoczylas, F., Davy, C.A., Bourbon, X., and Talandier, J. (2012). Water retention and gas relative permeability of two industrial concretes. *Cem. Concr. Res.* 42, 1001–1013.
- Clément, J.-L. (1987). Interface acier-béton et comportement des structures en béton armé : caractérisation, modélisation. Paris 6.
- Coussy, O. (1995). *Mechanics of Porous Continua* (Wiley).
- Coussy, O., Baroghel-Bouny, V., Dangla, P., and Mainguy, M. (2001). Evaluation de la perméabilité à l'eau liquide des bétons à partir de leur perte de masse durant le séchage. *Rev. Fr. Génie Civ.* 5, 269–284.
- Cülfik, M.S., and Özturan, T. (2010). Mechanical properties of normal and high strength concretes subjected to high temperatures and using image analysis to detect bond deteriorations. *Constr. Build. Mater.* 24, 1486–1493.
- Daïan, J.-F. (2001). Evaluation des propriétés de transfert dans les matériaux cimentaires. *Rev. Fr. Génie Civ.* 5, 179–202.
- Dal Pont, S., Schrefler, B.A., and Ehrlacher, A. (2005). Intrinsic Permeability Evolution in High Temperature Concrete: An Experimental and Numerical Analysis. *Transp. Porous Media* 60, 43–74.
- Dal Pont, S., Durand, S., and Schrefler, B.A. (2007). A multiphase thermo-hydro-mechanical model for concrete at high temperatures—Finite element implementation and validation under LOCA load. *Nucl. Eng. Des.* 237, 2137–2150.
- Daval, C. (2015). Etat d'avancement WP 2-2: Essais de fluage sur béton à chaud (CERIB) (CERIB).
- Daval, C. (2016). Rapport intermédiaire : Compression et module élastique à 20°C, 100°C et 180°C – Fluage à 100°C (CERIB).
- Davie, C.T., Pearce, C.J., and Bićanić, N. (2006). Coupled Heat and Moisture Transport in Concrete at Elevated Temperatures—Effects of Capillary Pressure and Adsorbed Water. *Numer. Heat Transf. Part Appl.* 49, 733–763.
- De Morais, M.V.G., Bary, B., Ranc, G., Dal Pont, S., and Durand, S. (2009). Comparative Analysis of Coupled Thermo-Hydro-Mechanical Models for Concrete Exposed to Moderate Temperatures. *Numer. Heat Transf. Part A: Applications*, 654–682.
- De Schutter, G. (1999). Hydration and temperature development of concrete made with blast-furnace slag cement. *Cem. Concr. Res.* 29, 143–149.
- De Schutter, G., and Taerwe, L. (1996). Degree of hydration-based description of mechanical properties of early age concrete. *Mater. Struct.* 29, 335–344.
- Desmorat, R. (2006). Positivité de la dissipation intrinsèque d'une classe de modèles d'endommagement anisotropes non standards. *Comptes Rendus Mécanique* 334, 587–592.

- Diederichs, U., Jumppanen, U.-M., and Penttala, V. (1992). Behaviour of high strength concrete at high temperatures (Espoo-Helsinki University of Technology).
- Djaknoun, S., Ouedraogo, E., and Ahmed Benyahia, A. (2012). Characterisation of the behaviour of high performance mortar subjected to high temperatures. *Constr. Build. Mater.* 28, 176–186.
- Dominguez Ramirez, N.D. (2005). Etude de la liaison acier-béton : de la modélisation du phénomène à la formulation d'un élément fini enrichi "béton armé." École normale supérieure de Cachan - ENS Cachan.
- Dormieux, L., Kondo, D., and Ulm, F.-J. (2006). Microporomechanics.
- Drucker, D.C., and Prager, W. (1952). Soil mechanics and plastic analysis or limit design. *Q. Appl. Math.* 10, 157–165.
- DTU (1987). Comportement au feu des structures en béton.
- Dufour, F. (2007). Size effect in geomaterials. *Rev. Eur. Génie Civ.* 11, 1–15.
- Dufour, F., Giry, C., Mazars, J., and Soufflet, M. (2013). ENGINEERING DAMAGE INDICATORS BASED ON ADVANCED FINITE ELEMENT MODELLING. p.
- EDF (2014). VeRCoRS Project: an experimental mock-up of a reactor containment-building.
- El Bitouri, Y., Buffo-Lacarrière, L., Sellier, A., and Bourbon, X. (2016). Modelling of chemo-mechanical behaviour of low pH concretes. *Cem. Concr. Res.* 81, 70–80.
- Elghazouli, A.Y., Cashell, K.A., and Izzuddin, B.A. (2009). Experimental evaluation of the mechanical properties of steel reinforcement at elevated temperature. *Fire Saf. J.* 44, 909–919.
- Eligehausen, R., Popov, E.P., and Bertero, V.V. (1983). Local bond stress-slip relationships of deformed bars under generalized excitations (Earthquake Engineering Research Center, College of Engineering, University of California, USA).
- England, G.L., and Khoylou, N. (1995). Moisture flow in concrete under steady state non-uniform temperature states: experimental observations and theoretical modelling. *Nucl. Eng. Des.* 156, 83–107.
- Erdelyi, A. (1989). Estimating the relaxation of prestressing tendons. *Period Polytech Civ. Eng* 33, 19–32.
- Eurocode 2 (2004). Design of concrete structures.
- Eurocode 2 (2005). EN 1992-1-2 - Eurocode 2 Design of concrete structures. General rules. Structural fire design.
- Eurocode 4 (1994). Conception et dimensionnement des structures mixtes acier-béton (Paris).
- Fan, J., and Lu, Z.T. (2001). Experimental research on performance of prestressed steel wire in high temperature environment (fire). *Archit. Technol. China Acad. J. Electron. Publ. House* 32, 833–834.

- Fan, J., and Lu, Z.T. (2002). Experimental study on material properties of prestressed steel wire post high temperatures. *Ind. Constr. China Acad. J. Electron. Publ. House* 32, 30–32.
- Farra, B. (1994). Influence du béton et de l'armature sur la fissuration des structures en béton: Rapport des essais de tirants sous déformation imposée de courte durée. Ecole Polytechnique Fédérale de Lausanne.
- Farra, Bicher (1995). Influence de la résistance du béton et de son adhérence avec l'armature sur la fissuration. Ecole Polytechnique Fédérale de Lausanne.
- Felcitti, R., and Gambarova, P.G. (1999). On the residual proprieties of high performance siliceous concrete exposed to high temperatures. *Mech. Quasi-Brittle Mater. Struct.* 167–186.
- Felicetti, R., and Gambarova, P. (1998). Effects of High Temperature on the Residual Compressive Strength of High-Strength Siliceous Concretes. *ACI Mater. J.* 95, 395–405.
- Feraille Fresnet, A., and Ehrlacher, A. (2000). Le rôle de l'eau dans le comportement à haute température des bétons = The role of water in the behaviour of concrete submitted to high temperatures.
- FIB (2000). Bond of Reinforcement in Concrete: State-of-the-art report (Switzerland: fib Fédération internationale du béton).
- Fourier, J. (1822). *Théorie analytique de la chaleur* (Paris, France: Firmin Didot, père et fils).
- Frech-Baronet, J., Sorelli, L., and Charron, J.-P. (2017). New evidences on the effect of the internal relative humidity on the creep and relaxation behaviour of a cement paste by micro-indentation techniques. *Cem. Concr. Res.* 91, 39–51.
- Gales, J., Bisby, L., and Stratford, T. (2012). High Temperature Deformation Behaviour of Prestressing Steel: New Insights into Creep Failure. In *Seventh International Conference on Structures in Fire, SiF 2012*, (Zurich, Switzerland), p.
- Gambarova, P.G., and Rosati, G. (1996). Bond and splitting in reinforced concrete: test results on bar pull-out. *Mater. Struct.* 29, 267.
- Gatuingt, F., Ragueneau, F., and Desmorat, R. (2006). Implantation numérique d'un modèle d'endommagement anisotrope non-local. (REGC), pp. 392–404.
- Gawin, D., Majorana, C.E., and Schrefler, B.A. (1999). Numerical analysis of hygro-thermal behaviour and damage of concrete at high temperature. *Mech. Cohesive-Frict. Mater.* 4, 37–74.
- Gawin, D., Pesavento, F., and Schrefler, B.A. (2002). Simulation of damage–permeability coupling in hygro-thermo-mechanical analysis of concrete at high temperature. *Commun. Numer. Methods Eng.* 18, 113–119.
- Gawin, D., Pesavento, F., and Schrefler, B.A. (2003). Modelling of hygro-thermal behaviour of concrete at high temperature with thermo-chemical and mechanical material degradation. *Comput. Methods Appl. Mech. Eng.* 192, 1731–1771.

- Gawin, D., Alonso, C., Andrade, C., and Pesavento, F. (2005a). Effect of damage on permeability and hygro-thermal behaviour of HPCs at elevated temperatures: Part 1. Experimental results. *Comput. Concr.* 2, 189–202.
- Gawin, D., Majorana, C.E., Pesavento, F., and Schrefler, B.A. (2005b). Effect of damage on permeability and hygro-thermal behaviour of HPCs at elevated temperatures: Part 2. Numerical analysis. *Comput. Concr.* 2, 203–214.
- Gawin, D., Pesavento, F., and Schrefler, B.A. (2011a). What physical phenomena can be neglected when modelling concrete at high temperature? A comparative study. Part 1: Physical phenomena and mathematical model. *Int. J. Solids Struct.* 48, 1927–1944.
- Gawin, D., Pesavento, F., and Schrefler, B.A. (2011b). What physical phenomena can be neglected when modelling concrete at high temperature? A comparative study. Part 2: Comparison between models. *Int. J. Solids Struct.* 48, 1945–1961.
- van Genuchten, M.T. (1980). A Closed-form Equation for Predicting the Hydraulic Conductivity of Unsaturated Soils1. *Soil Sci. Soc. Am. J.* 44, 892.
- Ghannoum, M. (2017). Effets des hétérogénéités des matériaux sur le comportement mécanique de structures en béton armé à plusieurs échelles. Thèse de doctorat. Université Grenoble Alpes.
- Ghavamian, S., and Delaplace, A. (2003). Modèles de fissuration de béton, Projet MECA. *Rev. Fr. Génie Civ.* 7, 172.
- Giry, C., Dufour, F., and Mazars, J. (2011). Stress-based nonlocal damage model. *Int. J. Solids Struct.* 48, 3431–3443.
- Glodowski, R.J., and Lorenzetti, J.J. (1972). A METHOD FOR PREDICTING PRESTRESS LOSSES IN A PRESTRESSED CONCRETE STRUCTURE. *Precast. Concr. Inst.* 17, 17–31.
- Goto, Y. (1971). Cracks Formed in Concrete Around Deformed Tension Bars.
- Grasberger, S., and Meschke, G. (2004). Thermo-hygro-mechanical degradation of concrete: From coupled 3D material modelling to durability-oriented multifield structural analyses. *Mater. Struct.* 37, 244–256.
- Grégoire, D., Rojas-Solano, L., and Pijaudier-Cabot, G. (2013). Failure and size effect for notched and unnotched concrete beams. *Int. J. Numer. Anal. Methods Geomech.* 37, 1434–1452.
- Gross, H. (1973). On high temperature creep of concrete. In 2nd SMIRT, (Berlin), p.
- Hager, I. (2013). Behaviour of cement concrete at high temperature. *Bull. Pol. Acad. Sci. Tech. Sci.* 61, 145–154.
- Hager, I.G. (2004a). Comportement à haute température des bétons à haute performance : évolution des principales propriétés mécaniques. Thèse de doctorat. École nationale des ponts et chaussées (France).

- Hager, I.G. (2004b). Comportement à haute température des bétons à haute performance - évolution des principales propriétés mécaniques. Thèse de doctorat. ENPC Paris.
- Hamarthy, T.A. (1965). Effect of moisture on the fire endurance of building elements. *ASTM J. Mater.* 385.
- Hameed, R. (2010). Apport d'un renfort de fibres sur les performances des structures en béton armé pour les applications parasismiques. Université Toulouse 3 Paul Sabatier.
- Hamon, F., and Mazars, J. (2012). Modèle d'endommagement 3D Pour le béton sous chargement cyclique. In XXXe Rencontres AUGC-IBPSA, (Chambéry, Savoie), p.
- Handika, N. (2017). Multi-fissuration des structures en béton armé : analyse par corrélation d'images et modélisation. Toulouse, INSA.
- Haniche, R. (2011). Contribution à l'étude des bétons portés en température / Evolution des propriétés de transfert / Etude de l'éclatement. INSA de Lyon.
- Hansen, T.C. (1986). Physical structure of hardened cement paste. A classical approach. *Mater. Struct.* 19, 423–436.
- Harada, T., Takeda, J., Yamane, S., and Furumura, F. (1972). Strength, Elasticity and Thermal Properties of Concrete Subjected to Elevated Temperatures. pp. 377–406.
- Harmathy, T.Z. (1967). A Comprehensive Creep Model. *J. Basic Eng.* 89, 496–502.
- Hasegawa, T., Shioya, T., and Okada, T. (1985). Size effect on splitting tensile strength of concrete. pp. 309–312.
- Hassen, S. (2006). Etude du comportement du béton à hautes températures: Une nouvelle approche thermo-hygro-mécanique couplée pour la modélisation du fluage thermique transitoire. Presses Academiques Francophones.
- He, Z., and Qian, C. (2011). Internal relative humidity and creep of concrete with modified admixtures. *Prog. Nat. Sci. Mater. Int.* 21, 426–432.
- HEINFLING, G. (1998). Contribution à la modélisation numérique du comportement du béton et des structures en béton armé sous sollicitations thermomécaniques à hautes températures. Thèse de doctorat. INSA de Lyon.
- Hermann, N., Gerlach, L., Muller, H.S., and Kiefer, D. (2009). PACE 1450 - Experimental investigation of the crack behaviour of prestressed concrete containment walls considering the prestressing loss due to ageing. p. 1671.
- Hettema, M.H.H. (1996). The thermo-mechanical behaviour of sedimentary rock: an experimental study. PhD Thesis. Delft University.
- Hilaire, A., Benboudjema, F., Darquennes, A., Berthaud, Y., and Nahas, G. (2014). Modeling basic creep in concrete at early-age under compressive and tensile loading. *Nucl. Eng. Des.* 269, 222–230.

- Hillerborg, A., Mod  r, M., and Petersson, P.-E. (1976). Analysis of crack formation and crack growth in concrete by means of fracture mechanics and finite elements. *Cem. Concr. Res.* 6, 773–781.
- Hoover, C.G., and Bazant, Z.P. (2014). Universal Size-Shape Effect Law Based on Comprehensive Concrete Fracture Tests. *J. Eng. Mech.* 140, 473–479.
- Hou, X., Zheng, W., Kodur, V., and Sun, H. (2014). Effect of temperature on mechanical properties of prestressing bars. *Constr. Build. Mater.* 61, 24–32.
- Hover, K.C. (2011). The influence of water on the performance of concrete. *Constr. Build. Mater.* 25, 3003–3013.
- Huang, Z. (2010). Modelling the bond between concrete and reinforcing steel in a fire. *Eng. Struct.* 32, 3660–3669.
- IAEA (2016). INTERNATIONAL ATOMIC ENERGY AGENCY, Nuclear Power Reactors in the World, Reference Data Series No. 2.
- Ishida, T., Maekawa, K., and Kishi, T. (2007). Enhanced modeling of moisture equilibrium and transport in cementitious materials under arbitrary temperature and relative humidity history. *Cem. Concr. Res.* 37, 565–578.
- Jennings, H.M., and Johnson, S.K. (1986). Simulation of Microstructure Development During the Hydration of a Cement Compound. *J. Am. Ceram. Soc.* 69, 790–795.
- Jennings, H., Masoero, E., Pinson, M., Strekalova, E., Bonnaud, P., Manzano, H., Ji, Q., Thomas, J., Pellenq, R., Ulm, F.-J., et al. (2013). Water Isotherms, Shrinkage and Creep of Cement Paste: Hypotheses, Models and Experiments. (ASCE), pp. 134–141.
- Jiang, Z., Sun, Z., and Wang, P. (2005). Autogenous relative humidity change and autogenous shrinkage of high-performance cement pastes. *Cem. Concr. Res.* 35, 1539–1545.
- Jordaan, I.J., and Illston, J.M. (1969). The creep of sealed concrete under multiaxial compressive stresses. *Mag. Concr. Res.* 21, 195–204.
- Ju, J. W., and Zhang, Y. (1998). Axisymmetric thermomechanical constitutive and damage modeling for airfield concrete pavement under transient high temperature. *Mech. Mater.* 29, 307–323.
- Kachanov, L.M. (1958). Damage Model for Ductile Fracture. In *Introduction to Continuum Damage Mechanics*, (Springer Netherlands), pp. 97–113.
- Kalifa, P., and Menneteau, F. (2000). Mesures de pression, temp  ratures et perte en masse dans les b  tons    hautes temp  ratures.
- Kallel, H. (2016). Influence de la temperature et de l’hygrom  trie sur le comportement instantan   du b  ton. Universit   de Pau.
- Kallel, H., Carre, H., La Borderie, C., Masson, B., and Tran, N.C. (2016). Influence of Moisture and Temperature on Mechanical Properties of the Concrete. p.

- Kallel, H., Carré, H., La Borderie, C., Masson, B., and Tran, N.C. (2017). Effect of temperature and moisture on the instantaneous behaviour of concrete. *Cem. Concr. Compos.* 80, 326–332.
- Kameche, Z.A., Ghomari, F., Choinska, M., and Khelidj, A. (2014). Assessment of liquid water and gas permeabilities of partially saturated ordinary concrete. *Constr. Build. Mater.* 65, 551–565.
- Kanema, M. (2007). Influence des paramètres de formulation sur le comportement à haute température des bétons. Cergy.
- Kanema, M., and De Morais, M. V. G. (2007). Experimental and numerical studies of thermo-hydrous transfers in concrete exposed to high temperature. 44, 149–164.
- Kang, J., Yoon, H., Kim, W., Kodur, V., Shin, Y., and Kim, H. (2016). Effect of Wall Thickness on Thermal Behaviors of RC Walls Under Fire Conditions. *Int. J. Concr. Struct. Mater.* 10, 19–31.
- Katz, A., Berman, N., and Bank, L.C. (1999). Effect of High Temperature on Bond Strength of FRP Rebars. *J. Compos. Constr.* 3, 73–81.
- Khoury, G.A., Majorana, C.E., Pesavento, F., and Schrefler, B.A. (2002). Modelling of heated concrete. *Mag. Concr. Res.* 54, 77–101.
- Kim, K.-H., Jeon, S.-E., Kim, J.-K., and Yang, S. (2003). An experimental study on thermal conductivity of concrete. *Cem. Concr. Res.* 33, 363–371.
- Kishi, T., and Maekawa, K. (1994). Thermal and mechanical modelling of young concrete based on hydration process of multi-component cement materials, Thermal cracking in concrete at early age. In *RILEM Proc.* 25, pp. 11–19.
- Klinkenberg, L. (1941). The Permeability Of Porous Media To Liquids And Gases. In *Drilling and Production Practice*, (1941: American Petroleum Institute), pp. 200–213.
- Kodur, V. (2014). Properties of Concrete at Elevated Temperatures. *Int. Sch. Res. Not.* 2014.
- Kodur, V.K.R., and Dwaikat, M. (2007). Performance-based Fire Safety Design of Reinforced Concrete Beams. *J. Fire Prot. Eng.* 17, 293–320.
- Kolani, B. (2012). Comportement au jeune âge des structures en béton armé à base de liants composés aux laitiers. phd. Université de Toulouse, Université Toulouse III - Paul Sabatier.
- Kolani, B., Buffo-Lacarrière, L., Sellier, A., Escadeillas, G., Boutillon, L., and Linger, L. (2012). Hydration of slag-blended cements. *Cem. Concr. Compos.* 34, 1009–1018.
- Kollek, J.J. (1989). The determination of the permeability of concrete to oxygen by the Cembureau method—a recommendation. *Mater. Struct.* 22, 225–230.
- La Borderie, C. (1991). Phénomènes unilatéraux dans un matériau endommageable: Modélisation et application à l'analyse de structures en béton. Thèse de doctorat. Université Pierre et Marie Curie.

- La Borderie, C., Lawrence, C., and Menou, A. (2007). Approche mésoscopique du comportement du béton. *Rev. Eur. Génie Civ.* *11*, 407–421.
- Ladaoui, W. (2010). Etude expérimentale du comportement Thermo-Hydro-Mécanique à long terme des BHP destinés aux ouvrages de stockage des déchets radioactifs. phd. Université de Toulouse, Université Toulouse III - Paul Sabatier.
- Ladaoui, W., Vidal, T., Sellier, A., and Bourbon, X. (2013). Analysis of interactions between damage and basic creep of HPC and HPFRC heated between 20 and 80 °C. *Mater. Struct.* *46*, 13–23.
- Lamon, J. (1990). Ceramics Reliability: Statistical Analysis of Multiaxial Failure Using the Weibull Approach and the Multiaxial Elemental Strength Model. *J. Am. Ceram. Soc.* *73*, 2204–2212.
- Lawson, J.R., Phan, L.T., and Davis, F.L. (2000). Mechanical properties of high performance concrete after exposure to elevated temperatures (USA: National Institute of Standards and Technology).
- Lemaitre, J., and Chaboche, J.-L. (1985). *Mécanique des matériaux solides* (Paris: Dunod).
- Lemaitre, J., Chaboche, J.-L., Benallal, A., and Desmorat, R. (2009). *Mécanique des matériaux solides* (Paris).
- Li, G. (2004). THE EFFECT OF MOISTURE CONTENT ON THE TENSILE STRENGTH PROPERTIES OF CONCRETE. University of Florida.
- Li, G.-Q., Jiang, S.-C., Yin, Y.-Z., Chen, K., and Li, M.-F. (2003). Experimental Studies on the Properties of Constructional Steel at Elevated Temperatures. *J. Struct. Eng.* *129*, 1717–1721.
- Li, K., Stroeve, P., Stroeve, M., and Sluys, L.J. (2015). Liquid water permeability of partially saturated cement paste assessed by dem-based methodology. *Proc. 11th Int. Symp. Brittle Matrix Compos.* *11*, 28–30.
- Li, M., Zhu, Y.J., and Wang, Z.L. (1998). The Mechanical Behaviors of Prestressed and Non-Prestressed Steel Rebars under High Temperature. *J. Chongqing Jianzhu Univ. China Acad. J. Eletronic Publ. House* *20*, 73–77.
- Llau, A. (2016). Méthodes de simulation du comportement mécanique non linéaire des grandes structures en béton armé et précontraint : condensation adaptative en contexte aléatoire et représentation des hétérogénéités. Thèse de doctorat. Université Grenoble Alpes.
- Llau, A., Jason, L., Dufour, F., and Baroth, J. (2016). Finite element modelling of 1D steel components in reinforced and prestressed concrete structures. *Eng. Struct.* *127*, 769–783.
- Luikov, A.V. (1975). Systems of differential equations of heat and mass transfer in capillary-porous bodies (review). *Int. J. Heat Mass Transf.* *18*, 1–14.
- Lutz, L.A., and Gergely, P. (1967). Mechanics of Bond and Slip of Deformed Bars in Concrete. *J. Proc.* *64*, 711–721.

- MAEKAWA, K., CHAUBE, R.P., and KISHI, T. (1996). Coupled Mass Transport, Hydration and Structure Formation theory for Durability Design of Concrete Structures. Integr. Des. Environ. Issues Concr. Technol. K Sakai Ed 83–98.
- Magura, D.D., Sozen, M.A., and Siess, C.P. (1964). A study of stress relaxation in prestressing reinforcement. J. Prestress. Concr. Inst. 9, 13–57.
- Maia, L., Azenha, M., Faria, R., and Figueiras, J. (2012). Identification of the percolation threshold in cementitious pastes by monitoring the E-modulus evolution. Cem. Concr. Compos. 34, 739–745.
- Mainguy, M. (1999). Modèles de diffusion non linéaire en milieux poreux. Applications a la dissolution et au séchage des matériaux cimentaires. Ecole Nationale des Ponts et Chaussées.
- Mainguy, M., Coussy, O., and Baroghel-Bouny, V. (2001). Role of Air Pressure in Drying of Weakly Permeable Materials. ASCE J. Eng. Mech. 127, 582–592.
- Mang, C., Jason, L., and Davenne, L. (2015). A new bond slip model for reinforced concrete structures: Validation by modelling a reinforced concrete tie. Eng. Comput. 32, 1934–1958.
- Manzoni, F. (2017). Comportement thermo-hydro-mécanique des structures en béton. Thèse de doctorat. Université Toulouse III - Paul Sabatier.
- Marechal, J.C. (1970). Contribution à étude des propriétés thermiques et mécaniques du bétonnet en fonction de la température. Ann. Inst. Tech. Bâtim. Trav. Publics 274, 122–146.
- Marechal, J.C. (1972). Variations in the modulus of elasticity and Poisson's ratio with temperature. (Detroit: American Concrete Institute), pp. 495–503.
- Martinez-Perez, M.L., Borlado, C.R., Mompean, F.J., Garcia-Hernandez, M., Gil-Sevillano, J., Ruiz-Hervias, J., Atienza, J.M., Elices, M., Peng, R.L., and Daymond, M.R. (2005). Measurement and modelling of residual stresses in straightened commercial eutectoid steel rods. Acta Mater. 53, 4415–4425.
- Matallah, M., La Borderie, C., and Maurel, O. (2010). A practical method to estimate crack openings in concrete structures. Int. J. Numer. Anal. Methods Geomech. 34, 1615–1633.
- Matheron, G. (1973). The Intrinsic Random Functions and Their Applications. Adv. Appl. Probab. 5, 439–468.
- Matsuzawa, K., Kitsutaka, Y., Abe, M., Kasami, H., Tayama, T., and Nishi, H. (2016). Effects of Exposure Term on the Strength and Elasticity of Concrete Subjected to Elevated Temperature up to 175°C. Key Eng. Mater. 711, 519–524.
- Mazars, J. (1984). APPLICATION DE LA MECANIQUE DE L'ENDOMMAGEMENT AU COMPORTEMENT NON LINEAIRE ET A LA RUPTURE DU BETON DE STRUCTURE. Université Pierre et Marie Curie.
- Mazars, J. (1986). A description of micro- and macroscale damage of concrete structures. Eng. Fract. Mech. 25, 729–737.

- Mazars, J., Pijaudier-Cabot, G., and Saouridis, C. (1991). Size effect and continuous damage in cementitious materials. *Int. J. Fract.* *51*, 159–173.
- Mefisto (2012). *Maîtrise durable de la Fissuration des InfraStructures en béton*.
- Menou, A. (2004). *Etude du comportement thermomécanique des bétons à haute température. : Approche multi échelles de l'endommagement thermique*. Pau.
- Menou, A., Mounajed, G., Boussa, H., Pineaud, A., and Carre, H. (2006). Residual fracture energy of cement paste, mortar and concrete subject to high temperature. *Theor. Appl. Fract. Mech.* *45*, 64–71.
- Mensi, R., Acker, P., and Attolou, A. (1988). Séchage du béton: analyse et modélisation. *Mater. Struct.* *21*, 3–12.
- Michou, A. (2015). *Analyse expérimentale et modélisation du comportement de structures précontraintes*. Université Pierre et Marie Curie.
- Michou, A., Hilaire, A., Benboudjema, F., Nahas, G., Wyniecki, P., and Berthaud, Y. (2015). Reinforcement-concrete bond behavior: Experimentation in drying conditions and meso-scale modeling. *Eng. Struct.* *101*, 570–582.
- Millard, A., and Vivier, M. (2006). Modelling of tests performed in order to evaluate the residual strength of corroded beams in the framework of the benchmark of the rance beams. *J. Phys. IV Proc.* *136*, 151–158.
- Mindeguia, J.-C. (2009). *Contribution expérimentale à la compréhension des risques d'instabilité thermique des bétons*. phdthesis. Université de Pau et des Pays de l'Adour.
- Mindeguia, J.-C., Pimienta, P., Carre, H., and La Borderie, C. (2012). On the influence of aggregate nature on concrete behaviour at high temperature. *Eur. J. Environ. Civ. Eng.* *16*, 236–253.
- Mindess, S., Young, J.F., and Darwin, D. (2002). *Concrete* (Prentice Hall, Pearson Education, Inc. Upper Saddle River, NJ 07458, U.S.A.).
- Mivelaz, P. (1996). *Etanchéité des structures en béton armé: Fuite au travers d'un élément fissuré*. Ecole Polytechnique Fédérale de Lausanne.
- Monlouis-Bonnaire, J.P., Verdier, J., and Perrin, B. (2004). Prediction of the relative permeability to gas flow of cement-based materials. *Cem. Concr. Res.* *34*, 737–744.
- Morabito, P. (1989). Measurement of the thermal properties of different concretes. *High Temp High Press* *21*, 51–59.
- Mounajed, G., and Obeid, W. (2004). A new coupling F.E. model for the simulation of thermal-hydro-mechanical behaviour of concretes at high temperatures. *Mater. Struct.* *37*, 422–432.
- Mualem, Y. (1976). A new model for predictinag the hydraulic conductivity of nsaturated porous media. *Water Resour. Res.* *12*, 513–522.

- Nader, C. (2017). A Multi-Scale Strategy for the Probabilistic Modeling of Reinforced Concrete Structures. Thesis. Université Paris-Est.
- Naus, D.J. (2006). The Effect of Elevated Temperature on Concrete Materials and Structures — A Literature Review.
- Neville, A. (2000). Propriétés des bétons.
- NF EN ISO 13788 (2013). NF EN ISO 13788 - Performance hygrothermique des composants et parois de bâtiments - Température superficielle intérieure permettant d'éviter l'humidité superficielle critique et la condensation dans la masse - Méthodes de calcul.
- Nguyen, M.D. (2009). Modélisation des couplages entre hydratation et dessiccation des matériaux cimentaires à l'issue du décoffrage. Étude de la dégradation des propriétés de transfert. Ecole nationale des ponts et chaussées - ENPC PARIS / MARNE LA VALLEE.
- Nguyen, V. thai (2013). Comportement des bétons ordinaire et à hautes performances soumis à haute température : application à des éprouvettes de grandes dimensions. Université de Cergy Pontoise.
- Nguyen, V.N., Cagnon, H., Vidal, T., Torrenti, J.M., and Sellier, A. (2017a). Effet des couplages Thermo-Hydro-Mécaniques sur le comportement différé du béton précontraint. (Lille), p.
- Nguyen, V.N., Cagnon, H., Vidal, T., and Torrenti, J.M. (2017b). Comportement différé du béton précontraint en conditions accidentelles: Etude expérimentale et modélisation (Toulouse).
- Noumowé, N.A. (1995). Effet de hautes températures (20-600 0C) sur le béton : Cas particulier du béton à hautes performances. Thèse de doctorat. INSA de Lyon.
- Oh, B.H., and Cha, S.W. (2003). Nonlinear Analysis of Temperature and Moisture Distributions in Early-Age Concrete Structures Based on Degree of Hydration. *Cem. Concr. Res.* 100, 361–370.
- Perre, P., and Degiovanni, A. (1990). Simulation par volumes finis des transferts couplés en milieux poreux anisotropes: Séchage du bois à basse et à haute température. *Int. J. Heat Mass Transf.* 33, 2463–2478.
- Pesavento, F. (2000). Non linear modelling of concrete as multiphase porous material in high temperature conditions. University of Padova.
- Phan, L.T., and Carino, N.J. (2003). Code provisions for high strength concrete strength-temperature relationship at elevated temperatures. *Mater. Struct.* 36, 91–98.
- Philip, J.R., and De Vries, D.A. (1957). Moisture movement in porous materials under temperature gradients. *Eos Trans. Am. Geophys. Union* 38, 222–232.
- Picandet, V. (2001). Influence d'un endommagement mécanique sur la perméabilité et sur la diffusivité hydrique des bétons. phdthesis. UNIVERSITÉ DE NANTES.
- Pierre PERROT (1992). Propriétés thermodynamiques de l'eau.

- Pihlajavaara, S.E. (1974). A review of some of the main results of a research on the ageing phenomena of concrete: Effect of moisture conditions on strength, shrinkage and creep of mature concrete. *Cem. Concr. Res.* 4, 761–771.
- Pijaudier-Cabot, G., and Bazant, Z.P. (1987). Nonlocal Damage Theory. *J. Eng. Mech.* 113, 1512–1533.
- Pimienta, P. (1999). Evolution des caractéristiques des BHP soumis à des températures élevées (tranche 1), résistances en compression et modules d’élasticité.
- Popovics, S. (1986). Effect of Curing Method and Final Moisture Condition on Compressive Strength of Concrete. *J. Proc.* 83, 650–657.
- Pothisiri, T., and Panedpojaman, P. (2012). Modeling of bonding between steel rebar and concrete at elevated temperatures. *Constr. Build. Mater.* 27, 130–140.
- Powers, T.C., and Brownnyard, T.L. (1947). Studies of the Physical Properties of Hardened Portland Cement Paste. *ACI J. Proc.* 43, 933–992.
- Poyet, S. (2009). Experimental investigation of the effect of temperature on the first desorption isotherm of concrete. *Cem. Concr. Res.* 39, 1052–1059.
- Radjy, F., Sellevold, E.J., and Hansen, K.K. (2003). Isosteric Vapor Pressure – Temperature Data for Water Sorption in Hardened Cement Paste: Enthalpy, Entropy and Sorption Isotherms at Different Temperatures (Technical University of Denmark, Department of Civil Engineering).
- Rahal, S., Sellier, A., and Casaux-Ginestet, G. (2017). Finite element modelling of permeability in brittle materials cracked in tension. *Int. J. Solids Struct.* 113–114, 85–99.
- Raharinaivo, A. (1978). Influence de la contrainte et de la température sur la relaxation et le fluage des files d’acier de précontrainte de qualité 5-III-TBR.
- Ramtani, S. (1990). Contribution à la modélisation du comportement multiaxial du béton endommagé avec description du caractère unilatéral. Université de Paris 6.
- Ranaivomanana, H. (2010). Transferts dans les milieux poreux réactifs non saturés : application à la cicatrisation de fissure dans les matériaux cimentaires par carbonatation. phd. Université de Toulouse, Université Toulouse III - Paul Sabatier.
- Ranc, G., Sercombe, J., and Rodrigues, S. (2003). Comportement à haute température du béton de structure: Impact de la fissuration sur les transferts hydriques. *Rev. Fr. Génie Civ.* 7, 397–424.
- R. T. Tenchev, J.A.P., L.Y. Li (2001). Finite Element Analysis of Coupled Heat and Moisture Transfer in Concrete Subjected to Fire. *Numer. Heat Transf. Part Appl.* 39, 685–710.
- Ravera, P.P., Firrao, D., and Colombo, R.L. (1984). Influence of aging on the relaxation and internal friction properties of cold drawn pearlites. *Scr. Metall.* 18, 1313–1318.
- Raznjevic, K. (1970). Tables et diagrammes thermodynamiques.

- Reid, R.C. (1987). *The Properties of Gases and Liquids* (McGraw-Hill).
- Richard, B., Ragueneau, F., Cremona, C., and Adelaide, L. (2010). Isotropic continuum damage mechanics for concrete under cyclic loading: Stiffness recovery, inelastic strains and frictional sliding. *Eng. Fract. Mech.* 77, 1203–1223.
- Rolland, A. (2015). *Comportement mécanique et durabilité de structures en béton renforcées par des armatures composites internes*. phdthesis. Université Paris-Est.
- Rospars, C. (2016). *Rapport Etape WP1-WP4 task 1 R2* (Institut National Polytechnique de Grenoble).
- Rossi, P., Wu, X., Maou, F.L., and Belloc, A. (1994). Scale effect on concrete in tension. *Mater. Struct.* 27, 437–444.
- Rossi, P., Tailhan, J.-L., and Le Maou, F. (2013). Comparison of concrete creep in tension and in compression: Influence of concrete age at loading and drying conditions. *Cem. Concr. Res.* 51, 78–84.
- Rostasy, F.S., Thienel, K. -ch., and Schütt, K. (1991). On prediction of relaxation of cold drawn prestressing wire under constant and variable elevated temperature. *Nucl. Eng. Des.* 130, 221–227.
- Rouquand, A., and Pontiroli, C. (2007). A model for geologic materials (rock, soil and concrete), presentation and validation for a large range of dynamic loads. pp. 201–221.
- Sa, C.D. (2007). *Etude hydro-mécanique et thermo-mécanique du béton. Influence des gradients et des incompatibilités de déformation*. phdthesis. École normale supérieure de Cachan - ENS Cachan.
- Schneider, U. (1988). Concrete at high temperatures — A general review. *Fire Saf. J.* 13, 55–68.
- Schrefler, B.A., Majorana, C.E., Khoury, G.A., and Gawin, D. (2002). Thermo-hydro-mechanical modelling of high performance concrete at high temperatures. *Eng. Comput.* 19, 787–819.
- Schutter, G.D., and Taerwe, L. (1996). Degree of hydration-based description of mechanical properties of early age concrete. *Mater. Struct.* 29, 335–344.
- Sellier, A. (2015). *Model FLUENDO3D Version 20-P for Castem 2012, Tentative Handbook*, LMDC Internal Document (Toulouse).
- Sellier, A., and Buffo-Lacarrière, L. (2009). Towards a simple and unified modelling of basic creep, shrinkage and drying creep of concrete. *Eur. J. Environ. Civ. Eng.* 13, 1161–1182.
- Sellier, A., and Millard, A. (2014). Weakest link and localisation WL 2 : a method to conciliate probabilistic and energetic scale effects in numerical models. *Eur. J. Environ. Civ. Eng.* 18, 1177–1191.

- Sellier, A., Casaux-Ginestet, G., Buffo-Lacarrière, L., and Bourbon, X. (2013a). Orthotropic damage coupled with localized crack reclosure processing. Part I: Constitutive laws. *Eng. Fract. Mech.* 97, 148–167.
- Sellier, A., Casaux-Ginestet, G., Buffo-Lacarrière, L., and Bourbon, X. (2013b). Orthotropic damage coupled with localized crack reclosure processing: Part II: Applications. *Eng. Fract. Mech.* 97, 168–185.
- Sellier, A., Vidal, T., Cagnon, H., Buffo-Lacarrière, L., and Multon, S. (2016a). Requirements for the modeling of medium-term behavior of Nuclear containment concrete for a “Loss of Coolant Accident” analysis. *Key Eng. Mater.* 711, 916–923.
- Sellier, A., Multon, S., Buffo-Lacarrière, L., Vidal, T., Bourbon, X., and Camps, G. (2016b). Concrete creep modelling for structural applications: non-linearity, multi-axiality, hydration, temperature and drying effects. *Cem. Concr. Res.* 79, 301–315.
- Sercombe, J., Gallé, C., and Ranc, G. (2001). Modélisation du comportement du béton à haute température: Transferts des fluides et de chaleur et déformations pendant les transitoires thermiques, Note Technique SCCME.
- Shakya, A.M., and Kodur, V.K.R. (2016). Effect of temperature on the mechanical properties of low relaxation seven-wire prestressing strand. *Constr. Build. Mater.* 124, 74–84.
- Shoukry, S.N., William, G.W., Downie, B., and Riad, M.Y. (2011). Effect of moisture and temperature on the mechanical properties of concrete. *Constr. Build. Mater.* 25, 688–696.
- Sogbossi, H. (2017). Etude de l'évolution de la perméabilité du béton en fonction de son endommagement : transposition des résultats de laboratoire a la prédiction des débits de fuite sur site. Thèse de doctorat. Université Paul Sabatier.
- Stablon, T., Sellier, A., Domede, N., Plu, B., and Dieleman, L. (2012). Influence of building process on stiffness: numerical analysis of a masonry vault including mortar joint shrinkage and crack re-closure effect. *Mater. Struct.* 45, 881–898.
- Stefan, L., Benboudjema, F., Torrenti, J.-M., and Bissonnette, B. (2010). Prediction of elastic properties of cement pastes at early ages. *Comput. Mater. Sci.* 47, 775–784.
- Stefano Dal Pont (2004). Lien entre la perméabilité et l'endommagement dans les bétons à haute température. Ecole des Ponts ParisTech.
- Tamtsia, B.T., and Beaudoin, J.J. (2000). Basic creep of hardened cement paste A re-examination of the role of water. *Cem. Concr. Res.* 30, 1465–1475.
- Taylor, H.F.W. (1990). *Cement chemistry* (London: Academic Press).
- Thiery, M., Baroghel-Bouny, V., Bourneton, N., Villain, G., and Stéfani, C. (2007). Modélisation du séchage des bétons. *Rev. Eur. Génie Civ.* 11, 541–577.
- Thomas, H., and Sansom, M. (1995). Fully Coupled Analysis of Heat, Moisture, and Air Transfer in Unsaturated Soil. *J. Eng. Mech.* 121, 392–405.

- Tognevi, A. (2012). Modélisation multi-échelle et simulation du comportement thermo-hydro-mécanique du béton avec représentation explicite de la fissuration. Ecole normale supérieure de Cachan.
- Topçu, I.B., and Karakurt, C. (2008). Properties of Reinforced Concrete Steel Rebars Exposed to High Temperatures. *Adv. Mater. Sci. Eng.*
- Torrent, R. (1977). A general relation between tensile strength and specimen geometry for concrete-like materials. *Matér. Constr.* 10, 187–196.
- Torrenti, J.M., and Benboudjema, F. (2005). Mechanical threshold of cementitious materials at early age. *Mater. Struct.* 38, 299–304.
- Toumi Ajimi, W., Chataigner, S., and Gaillet, L. (2015). Influence de la température sur le comportement de l'interface acier/béton (IFSTTAR Nantes).
- Toumi Ajimi, W., Chataigner, S., and Gaillet, L. (2017). Influence of low elevated temperature on the mechanical behavior of steel rebars and prestressing wires in nuclear containment structures. *Constr. Build. Mater.* 134, 462–470.
- Ulm, F.-J., and Acker, P. (1998). Le point sur le fluage et la recouvrance des bétons. *Bull. Lab. Pans Chaussees Spec.* XX 73–82.
- Ulm, F.-J., and Coussy, O. (1998). Couplings in early-age concrete: From material modeling to structural design. *Int. J. Solids Struct.* 35, 4295–4311.
- Van Breugel, K. (1995). Numerical simulation of hydration and microstructural development in hardening cement-based materials (I) theory. *Cem. Concr. Res.* 25, 319–331.
- Van Vliet, M.R.A., and Van Mier, J.G.M. (2000). Experimental investigation of size effect in concrete and sandstone under uniaxial tension. *Eng. Fract. Mech.* 65, 165–188.
- Vandamme, M., Zhang, Q., Ulm, F.-J., Le Roy, R., Zuber, B., Gartner, E., and Termkhajornkit, P. (2013). Creep Properties of Cementitious Materials from Indentation Testing: Significance, Influence of Relative Humidity, and Analogy Between C-S-H and Soils. (American Society of Civil Engineers), pp. 48–61.
- Vidal, T., Sellier, A., Ladaoui, W., and Bourbon, X. (2014). Effect of Temperature on the Basic Creep of High-Performance Concretes Heated between 20 and 80°C. *J. Mater. Civ. Eng.* 27.
- Vidal, T., Sellier, A., Cagnon, H., Ladaoui, W., and Bourbon, X. (2016). EXPERIMENTAL INVESTIGATION AND MODELLING OF TEMPERATURE EFFECTS ON BASIC CREEP OF CONCRETE.
- Villain, G., Baroghel-Bouny, V., Kounkou, C., and Hua, C. (2001). Mesure de la perméabilité aux gaz en fonction du taux de saturation des bétons. *Rev. Fr. Génie Civ.* 5, 251–268.
- Vodák, F., Černý, R., Drchalová, J., Hošková, Š., Kapičková, O., Michalko, O., Semerák, P., and Toman, J. (1997). Thermophysical properties of concrete for nuclear-safety related structures. *Cem. Concr. Res.* 27, 415–426.

- de Vree, J.H.P., Brekelmans, W.A.M., and van Gils, M.A.J. (1995). Comparison of nonlocal approaches in continuum damage mechanics. *Comput. Struct.* 55, 581–588.
- Waller, V. (1999). Relations entre composition des betons, exothermie en cours de prise et resistance en compression. Thèse de doctorat. ENPC Paris.
- Wang, J. (2016). Modeling of concrete dehydration and multiphase transfer in nuclear containment concrete wall during loss of cooling accident. phd. Université de Toulouse, Université Toulouse III - Paul Sabatier.
- Wang, X.-Y., Lee, H.-S., Park, K.-B., Kim, J.-J., and Golden, J.S. (2010a). A multi-phase kinetic model to simulate hydration of slag–cement blends. *Cem. Concr. Compos.* 32, 468–477.
- Wang, Y., Shen, Z., and Li, Y. (2010b). Experimental study of mechanical properties of prestressed steel wire at elevated temperatures. In *Sixth International Conference on Structures in Fire, SiF 2010*, (Michigan State University, U.S.), p.
- Weibull, W. (1951). A Statistical Distribution Function of Wide Applicability. *J. Appl. Mech.* 18, 293–297.
- Wittmann, F. (1970). EFFECT OF MOISTURE CONTENT ON THE CREEP OF HARDENED CEMENT. *Rheol. Acta* 9, 282–287.
- Xi, Y., Bazant, Z.P., Molina, L., and Jennings, H.M. (1994). Moisture diffusion in cementitious materials Moisture capacity and diffusivity. *Adv. Cem. Based Mater.* 1, 258–266.
- Xin, J.J. (2009). Experimental investigation of material properties of 1860 MPa prestressing seven-wire strand at stress and high temperature. Master of Engineering Thesis. Qingdao Technological University.
- Xing, Z. (2011). Influence de la nature minéralogique des granulats sur leur comportement et celui du béton à haute température. phdthesis. Université de Cergy Pontoise.
- Yao, X., and Wei, Y. (2014). Design and verification of a testing system for strength, modulus, and creep of concrete subject to tension under controlled temperature and humidity conditions. *Constr. Build. Mater.* 53, 448–454.
- Yuen, R.K.K., Kwok, W.K., Lo, S.M., and Liang, J. (2007). Heat and Mass Transfer in Concrete at Elevated Temperature. *Numer. Heat Transf. Part Appl.* 51, 469–494.
- Zeren, A., and Zeren, M. (2003). Stress relaxation properties of prestressed steel wires. *J. Mater. Process. Technol.* 141, 86–92.
- Zhang, B. (2011). Effects of moisture evaporation (weight loss) on fracture properties of high performance concrete subjected to high temperatures. *Fire Saf. J.* 46, 543–549.
- Zheng, W., and Zhang, H. (2006). An experimental study on the creep and stress relaxation properties of 1770-φP5 prestressing steel wires at high temperatures. *China Civ. Eng.* 39, 7–13.

Zheng, W., Hu, Q., and Zhang, H. (2006). Experimental research on the mechanical property of prestressing steel wire during and after heating. *J. Build. Struct. China Acad. J. Electron. Publ. House* 27, 120–128.

Zhou, H.T., Li, G.Q., and Jiang, S.C. (2008). Experimental Studies on the Properties of Steel Strand at Elevated Temperatures. *J. Sichuan Univ. China Acad. J. Electron. Publ. House* 40, 106–110.

(1992). *ASCE Manuals and Reports on Engineering Practice: Structural Fire Protection No 78* (New York, N.Y: American Society of Civil Engineers).